To the memory of my grandfather, Emilio Guinea

Reflectors in Cherenkov Detectors

Martin Emilio Moorhead
New College, Oxford
Thesis submitted for the degree of Doctor of Philosophy
Hilary Term 1992

Abstract

Current solar neutrino experiments indicate the possibility of neutrino oscillations $\nu_e \rightarrow \nu_\mu$ or ν_τ. These flavour oscillations should either be confirmed or refuted by the Subdury Neutrino Observatory (SNO), a 1,000 ton heavy water Cherenkov detector presently under construction. This detector should measure the ^{8}B ν_e flux and energy spectrum via a pure charge current reaction, and *independently* the ^{8}B *total* ν flux via a pure neutral current reaction. The experiment is thus self-normalizing and does not rely on the predictions of solar models to search for oscillations.

Light reflecting concentrators have been developed for SNO and will be fitted to each of the 9,500 photomultipliers in the detector. These concentrators will enhance the light collection from the heavy water volume by a factor of at least 1.6, improving the energy resolution and the statistical component of the vertex reconstruction accuracy by a factor of 1.3, and also suppressing the high energy tail of the dominant low energy background events by an order of magnitude.

The real and imaginary parts of the complex refractive index, $\tilde{n} = n + ik$, and the thickness, d, of the K_2CsSb photocathode (used in SNO) have been reliably determined ($n = 2.7$, $k = 1.5$, $d = 23$ nm) from a measurement at 442 nm of the angular dependence of the reflectivity of an EMI 9124 photomultiplier immersed in water. A reanalysis of previous measurements of other optical properties of this photocathode has established the wavelength dependence of n and k in the 390 to 800 nm range. From the three parameters n, k and d one can calculate the optical properties (reflectivity, transmissivity and absorptivity) of this photocathode as a function of the angle of incidence at the photomultiplier window and for a given refractive index of the medium in contact with the window.

The theory of light concentration onto 3D flat absorbers and 2D curved absorbers has been extended to the case of 3D curved absorbers (the near-hemispherical photocathodes of large photomultipliers). For cylindricaly symmetric concentrators with flat entrance apertures, it is found that the Liouville theorem imposes a more stringent limit on the 3D case of a curved photocathode than on the corresponding 2D case of the 2D cross-section of the photocathode. Moreover, conservation of angular momentum imposes an even more stringent limit on the 3D case of a curved photocathode than either of these Liouville limits. Together, these three limits effectively specify the theoretical performance of concentrators for 3D curved photocathodes.

The performance of such concentrators has been measured both in air and in water and is found to be consistent with the expected theoretical performance, including the optical properties of the K_2CsSb photocathode derived from the parametrization discussed above. Two manufacturing methods have been identified for producing 9,500 concentrators which according to accelerated ageing tests should not degrade after 10 years continuous immersion in high purity water.

Acknowledgements

I am greatly indebted to a large number of people who have contributed in many ways to this thesis. I would like to thank my supervisor, Neil Tanner, whose experience and inventiveness have been the guiding influences throughout this work; Nick Jelley and Chris Waltham who have contributed enormously to the practical development of concentrators; David Sinclair, an early proponent of concentrators, who has taught me much about the SNO detector; Donald Perkins for much encouragement and for taking an interest in the project; David Wark who has never tired of illuminating me on the subjects of solar neutrinos and American politics; Peter Trent for injecting much needed doses of reality and for the leaching measurements; George Doucas for remaining calm as ever in sometimes troubled waters; John Barton for numerous radioactivity measurements; Barrie Knox for daily assistance on practical matters; Andy Ferraris who wrote the original version of the analysis program for bialkali photocathodes; Robert Boardman for much help with the electronics set-up for concentration factor measurements and generally on photomultipliers; Robert Black who measured many reflectivities for accelerated ageing tests; Peter Thornewell who calculated the Euler strut shapes of petals.

I would like to acknowledge many useful discussions with the late Walter Welford, one of the founding fathers of the theory of concentrators.

I am very grateful for the interest and time given by many people at Thorn EMI, Kendal Hyde and Omitec OEC and would like to thank, in particular, Jim Wardley and Peter Wright for many useful discussions on photomultipliers; and David Hyde and Ron Marsh for much advice and help on evaporating Al onto glass domes and for putting up with never ending pleas for thicker dielectric coatings.

I would also like to thank the support staff of the nuclear physics department and in particular Bill Costar, Dave Burdis and Maurice Lacosta who respectively made the apparatus for concentration factor measurements, the apparatus for reflectivity measurements and the jigging for depositing Al onto glass domes; Bill Linford who designed the above pieces of equipment; Keith Nobbs who CNC machined the male formers for polygonal concentrators and their petals; Alan Holmes for much advice on engineering; Chris Goodwin for much advice on vacuum deposition; Beverly Rogers who with customary efficiency typed up Chapter 7; Irmegarde Smith who, contending admirably well with lots of dithering, drew most of the figures; and the wonderful Tea-Ladies whose daily quips and flexible credit facilities have kept me going (and who have threatened violence if they don't get mentioned).

My studies at Oxford have been funded by CERN and the extreme generosity of my parents without whom none of this would have been possible.

Last, but certainly not least, I would like to thank all my family and especially my girlfriend, Delia Kempley, for all their help and encouragement, not to mention patience, which have been essential for the completion of this thesis.

Contents

Chapter 1

Solar Neutrinos

1.1 Introduction

Nuclear fusion provides the energy source which sustains the Sun's luminosity and keeps it from collapsing under gravity. Most of this energy is produced by the proton-proton (pp) chain of reactions (see Figure 1.1) with a small contribution ($\sim 1.5\%$) from the CNO cycle. Every termination of the pp chain (and also the CNO cycle) can be represented by the exothermic process

$$4\mathrm{p} + 2\mathrm{e}^- \rightarrow \alpha + 2\nu_e + 4\gamma, \qquad \mathrm{Q} = 27.7\,\mathrm{MeV} \tag{1.1}$$

which is the sum of several reactions, including beta+ decay and electron capture reactions which produce electron neutrinos. On average, very little of the kinetic energy is carried away by the neutrinos and hence the overall rate of terminations in the Sun is directly proportional to the Sun's luminosity. The integrated flux of solar neutrinos at the Earth can thus be approximated by

$$\phi(\nu_e) = \frac{L_\odot}{13\,\mathrm{MeV}} \times \frac{1}{4\pi D^2} = 6.6 \times 10^{10}\,\nu_e/\mathrm{cm}^2/\mathrm{sec} \tag{1.2}$$

where $L_\odot$ is the solar luminosity ($3.86 \pm 0.004 \times 10^{33}$ erg/sec) and D is the Sun-Earth distance (1.5×10^{11} m). However the *individual* fluxes from the different neutrino producing reactions in the sun can only be predicted by modelling the sun in painstaking detail.

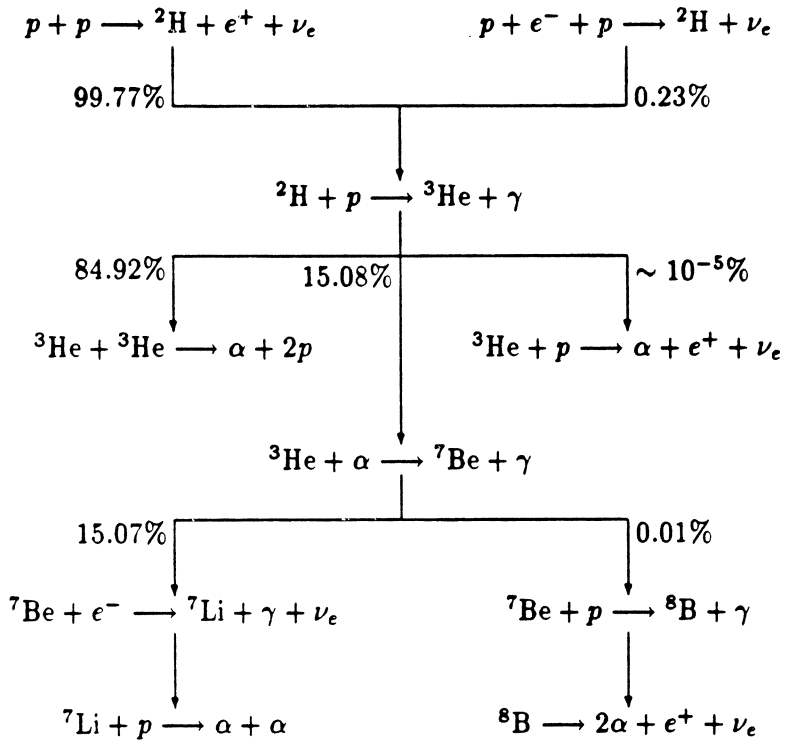

Figure 1.1: The Proton-Proton chain [6].

The long-standing discrepancy between the measured ν_e capture rate in ^{37}Cl [1] and the predicted rates from solar models, and the more recent results from Kamiokande-II [2] and SAGE [3] indicate that neutrino oscillations could be taking place. These experiments, which are sensitive only to electron neutrinos[1], seem to detect fewer neutrinos than are predicted by solar models. The neutrino oscillation hypothesis is that the 'missing' neutrinos have oscillated into different flavour neutrinos which are not detected.

Another hypothesis, first proposed by Cisneros [4], is that the left handed ν_e's are spin flipped into sterile right handed neutrinos by the interaction of their magnetic moment with the magnetic field of the Sun. The magnitude of the neutrino magnetic moment required for producing a significant probability of spin flip ($0.3\text{–}1.0 \times 10^{-10}\mu_B$) is just inside the existing experimental limit ($\leq 2 \times 10^{-10}\mu_B$ [5]). However, these values are many orders of magnitude greater than typical theoretical values obtained from

[1]Except Kamiokande-II which is about 1/6th as sensitive to ν_μ's or ν_τ's as it is to ν_e's.

calculations with relatively conventional models and so the spin flip hypothesis is not as appealing as the oscillation hypothesis. Nevertheless if either of these hypotheses is shown to be actually correct then the Sun will have provided a clue as to what lies beyond the standard model.

In this chapter the assumptions of solar models will be briefly reviewed, with emphasis on the limitations of the models and how these affect the predicted neutrino fluxes. Then the possible signatures of neutrino oscillations in solar neutrino experiments will be examined. In the light of these considerations, the three results from current solar neutrino experiments will be discussed. Finally, the outlook for the next generation of solar neutrino experiments and what might be learned from them will be summarized.

1.2 Solar Models

Several groups [6], [7], [8], [9], [10], [11] and [12] have developed codes which model the Sun in sufficient detail to make quantitative predictions of the solar neutrino spectrum. Most of these groups predict a neutrino spectrum which is very similar to that of [6] (Figure 1.2) but one group [7] predicts a significantly lower flux for the high energy ^{8}B neutrinos which dominate most solar neutrino experiments. Throughout this chapter we will refer to [6] as representative of the majority and to [7] as the lowest prediction (for the high energy neutrinos). The underlying assumptions of all of the above models can be summarized as follows:

1. **Hydrostatic Equilibrium**: Gravitational attraction is balanced by particle and radiation pressures.

2. **Energy Transport**: Energy is transported by photon diffusion or, if the classical Schwarzchild criterion is satisfied, by convection. This results in a large central region dominated by photon diffusion with a convective zone near the surface. Hence the calculated radiative opacity as a function of temperature, density and elemental abundances plays a major role in the models as it determines the temperature profile in the central region of the Sun where the fusion reactions take place.

3. **Energy Generation**: Energy is generated locally by the nuclear fusion reactions of the pp chain and the CNO cycle with a very small contribution from gravitational effects. The rates of these fusion reactions are calculated by averaging the energy dependent cross-sections

$$\sigma(E) = \frac{S(E)}{E} \exp(-2\pi Z_1 Z_2 e^2/\hbar v) \tag{1.3}$$

over Maxwell–Boltzmann velocity distributions. The exponential quantity in the above equation is known as the Gamow penetration factor (barrier tunneling) where v is the relative velocity of the interacting nuclei with atomic numbers Z_1 and Z_2. At the temperatures of the solar interior the product of the exponential Gamow factor and the exponential factor from the Maxwell–Boltzmann distribution peaks relatively sharply at around 10 KeV. The value of $S(E)$ at these low energies is taken to be equal to the zero energy s-factor, S_0.

4. **Elemental Abundances**: The Sun began as a homogenous mixture with the same relative abundances of 'heavy elements' (above helium) and the same ratio of hydrogen abundance to the total abundance of heavy elements as is presently measured on the surface. The initial abundance ratio of hydrogen to helium is a free parameter of the model. Elemental abundances evolve through the energy generating nuclear reactions, by convective mixing and (in some cases) by diffusion.

The solution to the system of coupled nonlinear differential equations which embody the above assumptions is evolved in an iterative fashion up to the present age of the Sun (4.55×10^9 years). The model is then compared to the Sun's measurable parameters: radius and luminosity; the mass being already fixed (no mass-loss). The free input parameters of the model (the initial hydrogen to helium abundance ratio and another entropy-like parameter) are adjusted, and the iterative evolution repeated, until satisfactory agreement with the present radius and luminosity is obtained.

The model can then be used to predict the present radial distribution of physical variables: temperature, pressure, density and elemental abundances, the spectrum of acoustic waves and the neutrino spectrum. Table 1.1 shows the predicted neutrino

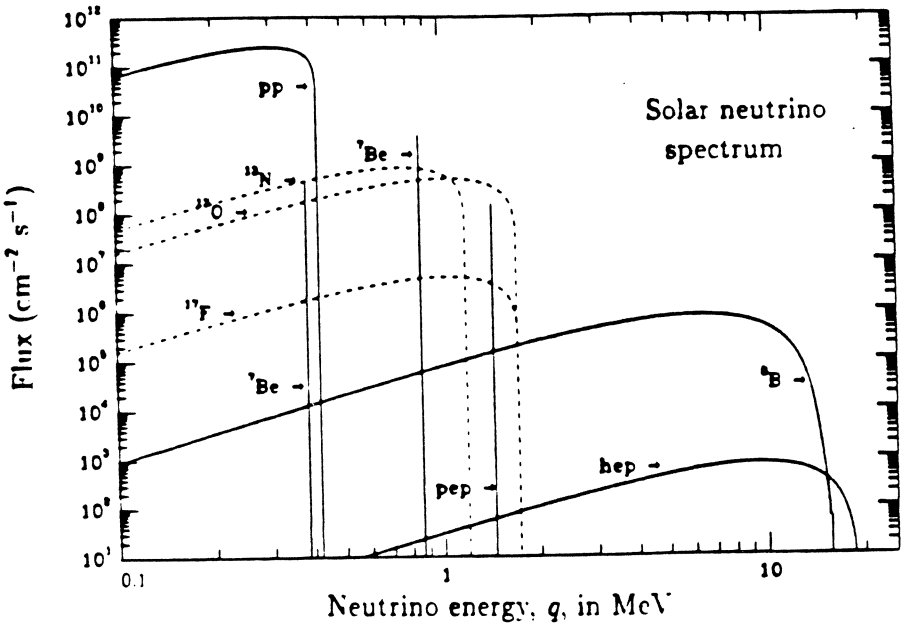

Figure 1.2: Predicted solar neutrino spectrum from [6]. The neutrino fluxes from continuum sources are given in units of number per cm^2 per second per MeV at one astronomical unit (the average Sun-Earth distance) and the line sources are given in units of number per cm^2 per second. The spectra from the pp chain are drawn in solid lines and the CNO spectra are drawn in dotted lines.

fluxes, for the different neutrino producing reactions in the Sun, from [6] and [7]. From the point of view of solar neutrino experiments, the pp, ^{7}Be and ^{8}B neutrinos dominate the solar neutrino spectrum (see Figure 1.2). They contribute nearly all of the event rates in current or planned detectors. In the predictions of their fluxes, Bahcall & Ulrich [6] quote errors which they call the 'total theoretical range'. These are roughly equivalent to three sigma errors and throughout this work they will be divided by three in order to facilitate the comparison with the calculations of Turck-Chieze *et al.* [7] and with measurements which are all presented in standard one sigma notation.

There are three major sources of uncertainty in the predicted neutrino fluxes from solar models:

1. The assumed initial abundance ratio of hydrogen to heavy elements which is deduced from spectroscopic measurements of the Sun's surface and chemical analyses of meteorites. This ratio has a strong effect on the opacity as a result of the dis-

Neutrino Source	Bahcall & Ulrich [6]	Turck-Chieze *et al.* [7]
pp	$6.0(1 \pm 0.007)$	$5.98(1 \pm 0.03)$
pep	$1.40 \times 10^{-2}(1 \pm 0.017)$	1.30×10^{-2}
hep	7.6×10^{-7}	n.a.
^{7}Be	$4.7 \times 10^{-1}(1 \pm 0.05)$	4.18×10^{-1}
^{8}B	$5.8 \times 10^{-4}(1 \pm 0.12)$	$3.8 \times 10^{-4}(1.0 \pm 0.29)$
^{13}N	$6.1 \times 10^{-2}(1 \pm 0.17)$	n.a.
^{15}O	$5.2 \times 10^{-2}(1 \pm 0.19)$	n.a.
^{17}F	$5.2 \times 10^{-4}(1 \pm 0.15)$	n.a.

Table 1.1: Predicted neutrino fluxes at the Earth (in units of $10^{10}\,\mathrm{cm}^{-2}\mathrm{s}^{-1}$) from the different neutrino producing reactions in the Sun.

proportionate influence of the heavy elements which contribute about 40% of the inner core opacity.

2. The actual calculation of opacity, for a given elemental abundance, which is an extremely complex calculation.

3. The S_0 values for the ^{1}H(p,e$^{+}\nu_e$)^{2}H, ^{3}He(^{3}He,2p)^{4}He, ^{3}He(^{4}He,γ)^{7}Be and ^{7}Be(p,γ)^{8}B reactions. The latter three are *extrapolated* from measurements at higher energies ($\sim$ MeV's) where the Gamow penetration factor is not dominant. In particular the ^{7}Be(p,γ)^{8}B cross-section is notoriously difficult to measure because of the radioactivity of the target.

All of these uncertainties translate into uncertainties in the 'branching ratios' of the pp chain (Figure 1.1) which are directly proportional to the relative fluxes of the different neutrino types. In particular the $\psi(^{7}\mathrm{Be})/\psi(^{8}\mathrm{B})$ flux ratio is extremely sensitive to the temperature in the solar core as the ^{7}Be(p,γ)^{8}B reaction rate is a strong function of temperature (through the Gamow penetration factor) whereas the ^{7}Be(e, ν_e)^{7}Li reaction rate is only weakly dependent on temperature. Bahcall [13] estimates, from analysing the output of 1000 different solar models where small changes are made to the input parameters, that the temperature dependence of the three major neutrino fluxes can be represented by a power law, $\phi \approx T^{\beta}$, where β is -1.2 for pp neutrinos, 8 for ^{7}Be

neutrinos and 18 for ^{8}B neutrinos. Thus the ^{8}B flux is the least certain of these three fluxes. The ^{7}Be flux is less sensitive to the uncertainties of solar models and the pp flux is well constrained — essentially by the luminosity. It should be pointed out that when the different solar models are corrected for different input parameters their ^{8}B flux predictions all agree (within errors).

So far, only the so-called 'standard solar models' have been considered, where the physical assumptions and input parameters of the model are all generally accepted. There exist many other 'non-standard solar models' where one or more of these assumptions or parameters is changed in an *ad hoc* fashion which is contrary to current knowledge. These models have mostly been invented with the aim of lowering the temperature in the Sun's core and hence decreasing the expected ^{8}B and ^{7}Be fluxes to accommodate the measured capture rate in ^{37}Cl. They have not gained general acceptance and have recently become disfavoured by results from helioseismology [14] (the spectrum of acoustic waves) which favour the standard solar models.

1.3 Neutrino Oscillations

Pontecorvo [15] [16] was the first to suggest that the electron neutrinos produced in the Sun might be oscillating into different flavour neutrinos along their voyage to the Earth. However, in the vacuum oscillations which were proposed, the three neutrino flavours would have to be maximally mixed in order to account for the factor of three suppression measured in ^{37}Cl, and this seems unnatural. In 1987, Mikheyev & Smirnov [17] [18], following the theoretical framework of Wolfenstein [19] [20], proposed a beautiful mechanism (now called the MSW effect) in which very large suppressions are more natural. This has given new impetus to the search for neutrino oscillations in the Sun. In this chapter the essential features of this MSW effect will be reviewed, starting with the vacuum oscillations which form the basis of the theory.

1.3.1 Vacuum Oscillations

To simplify the discussion we will consider just two Dirac neutrinos $|\nu_e\rangle$ and $|\nu_x\rangle$ of equal momentum and of which at least one is massive. These flavour eigenstates of the weak interaction are not necessarily equal to the mass eigenstates $|\nu_1\rangle$ and $|\nu_2\rangle$ which propagate in the vacuum (for example, the quark eigenstates of the weak and strong interactions are not the same but are related to each other by the famous CKM matrix [21]). A mixing angle θ_v ($\leq \pi/4$ by convention) describes the transformation from one basis to the other:

$$\begin{aligned} |\nu_e\rangle &= \cos\theta_v|\nu_1\rangle + \sin\theta_v|\nu_2\rangle \\ |\nu_x\rangle &= -\sin\theta_v|\nu_1\rangle + \cos\theta_v|\nu_2\rangle. \end{aligned} \tag{1.4}$$

As a function of time (or distance travelled) an arbitrary neutrino state vector $|\nu(t)\rangle$ can be expressed in either basis by

$$\begin{aligned} |\nu(t)\rangle &= c_e(t)|\nu_e\rangle + c_x(t)|\nu_x\rangle \\ &= c_1(t)|\nu_1\rangle + c_2(t)|\nu_2\rangle. \end{aligned} \tag{1.5}$$

The time development of this neutrino, in the vacuum, is governed by the Schrodinger equation:

$$i\frac{d}{dt}\begin{pmatrix} c_1(t) \\ c_2(t) \end{pmatrix} = \begin{pmatrix} E_1 & 0 \\ 0 & E_2 \end{pmatrix}\begin{pmatrix} c_1(t) \\ c_2(t) \end{pmatrix} \tag{1.6}$$

where the energy eigenvalues are given by

$$E_i = \sqrt{p^2 + m_i^2} \cong p + \frac{m_i^2}{2p} \tag{1.7}$$

assuming that $m \ll p$, the ultrarelativistic limit (natural units are used throughout the discussion of vacuum and MSW oscillations). The solutions of this equation are $c_1(t) = c_1(0)e^{-iE_1t}$ and $c_2(t) = c_2(0)e^{-iE_2t}$.

If the state at $t = 0$ is ν_e, i.e. $c_1(0) = \cos\theta_v$ and $c_2(0) = \sin\theta_v$, then the state at a later time t is given by

$$|\nu(t)\rangle = \cos\theta_v e^{-iE_1t}|\nu_1\rangle + \sin\theta_v e^{-iE_2t}|\nu_2\rangle. \tag{1.8}$$

The probability that this state is still ν_e at time t (or at a distance $L = ct$) is given by

$$P(\nu_e \rightarrow \nu_e) = |\langle \nu_e | \nu(t) \rangle|^2 = 1 - \sin^2 2\theta_v \sin^2(\pi L/L_v) \tag{1.9}$$

where $L_v = 2\pi/|E_2 - E_1| = 4\pi p/\Delta m^2$ is the vacuum oscillation length[2] and $\Delta m^2 = |m_2^2 - m_1^2|$. Similarly, the probability of oscillation into the state $|\nu_x\rangle$ is given by

$$P(\nu_e \rightarrow \nu_x) = |\langle \nu_x | \nu(t) \rangle|^2 = \sin^2 2\theta_v \sin^2(\pi L/L_v). \tag{1.10}$$

It is more convenient to rewrite the distance-dependent dimensionless argument of the sine function as follows:

$$\frac{\pi L}{L_v} = 1.9 \times 10^{11} \left(\frac{1\,\mathrm{MeV}}{E}\right) \left(\frac{\Delta m^2}{\mathrm{eV}^2}\right) \left(\frac{L}{1\,\mathrm{AU}}\right) \tag{1.11}$$

where 1 AU is the average Sun-Earth distance. For most parameters of interest ($\Delta m^2 > 5 \times 10^{-10}\mathrm{eV}^2$) this dimensionless argument will run through many factors of 2π when averaging over the beta-decay spectrum of most solar neutrinos (but not of course for the line spectra of electron capture neutrinos). Thus the $\sin^2(\pi L/L_v)$ factor in the oscillation probability averages out to 0.5. There is a small parameter space ($2 \times 10^{-12}\mathrm{eV}^2 < \Delta m^2 < 5 \times 10^{-10}\mathrm{eV}^2$) where some 'fine tuning' is possible and the averaged $\sin^2(\pi L/L_v)$ factor can be greater than 0.5. Thus the signature of vacuum oscillations in a solar neutrino experiment is a reduction in the $|\nu_e\rangle$ flux, by a factor $(1 - 0.5 \sin^2 2\theta_v)$, without distorting the energy spectrum, except in the case of fine tuning where the energy dependent oscillation term can cause pronounced distortions in the ν_e spectrum.

The ν_x's into which the ν_e's oscillate are most likely to be ν_μ or ν_τ. Other sterile neutrinos have been postulated but this seems unlikely. Thus the flavour independent flux measured by a *pure neutral current interaction* would be unaffected by oscillations. This provides a way for searching for oscillations which is independent from solar models. The measured ν_e flux from a charge current interaction is normalised to an *independent*

[2]Strictly speaking, this derivation of the vacuum length is incorrect since the assumption that the two different mass eigenstates have the same momenta violates conservation of energy and linear momentum in the, say, electron capture reaction which produces the neutrino. However, a more rigorous derivation [22] which includes the phase difference $\exp[i(p_1 - p_2)x]$ and in which the vacuum length is given by $L_v = 2\pi/|p_2 - p_1 - E_2 + E_1|$ produces the same result.

measurement of the *total* ν flux from a neutral current interaction. This method is very attractive given the inherent uncertainties in solar model flux predictions, particularly for ^{8}B neutrinos.

1.3.2 Matter Oscillations

When neutrinos propagate through matter an extra term is introduced in the Hamiltonian which determines the time development of the neutrino state vector. This term, which was first derived by Wolfenstein [19], arises from the coherent forward scattering of neutrinos through their charged current and neutral current interactions with electrons. In the flavour basis the neutral current component of this term is proportional to the identity matrix (all neutrinos scatter equally) and the charged current component is given by $\sqrt{2}G_F n_e|\nu_e\rangle\langle\nu_e|$ (only ν_e's scatter off electrons by W exchange) where G_F is the Fermi coupling constant and and n_e is the number density of electrons.

After rewriting (1.6) in the flavour basis and inserting this interaction term, the propagation through matter of an arbitrary neutrino state is given by

$$i\frac{d}{dt}\begin{pmatrix} c_e(t) \\ c_x(t) \end{pmatrix} = \frac{m_1^2+m_2^2}{4p}\begin{pmatrix} 1 & 0 \\ 0 & 1 \end{pmatrix}\begin{pmatrix} c_e(t) \\ c_x(t) \end{pmatrix} + \frac{1}{4p}\begin{pmatrix} -\Delta m^2\cos 2\theta_v + \sqrt{2}G_F n_e p & \Delta m^2 \sin 2\theta_v \\ \Delta m^2 \sin 2\theta_v & \Delta m^2\cos 2\theta_v - \sqrt{2}G_F n_e p \end{pmatrix}\begin{pmatrix} c_e(t) \\ c_x(t) \end{pmatrix} \tag{1.12}$$

where another term proportional to the identity matrix which contains the neutrino's momentum and neutral current interaction has been discarded since it only contributes an overall phase which does not affect oscillation probability amplitudes. The $(m_1^2 + m_2^2)/4p$ term which is also proportional to the identity matrix has been included to help illustrate the physical interpretation of this equation [23]. In this equation $\Delta m^2 = m_2^2 - m_1^2$ so that it can be either positive or negative depending on which neutrino state is heavier.

The eigenfunctions, $|\nu_{1m}\rangle$ and $|\nu_{2m}\rangle$, of this Hamiltonian are called the *matter* mass

eigenstates and are related to the flavour states through the *matter* mixing angle θ_m:

$$\begin{aligned} |\nu_e\rangle &= \cos\theta_m|\nu_{1m}\rangle + \sin\theta_m|\nu_{2m}\rangle \\ |\nu_\mu\rangle &= -\sin\theta_m|\nu_{1m}\rangle + \cos\theta_m|\nu_{2m}\rangle \end{aligned} \tag{1.13}$$

where θ_m is given by

$$\sin 2\theta_m = \frac{\Delta m^2 \sin 2\theta_v}{\left[(\Delta m^2 \cos 2\theta_v - \sqrt{2}G_F n_e p)^2 + (\Delta m^2 \sin 2\theta_v)^2\right]^{1/2}} \tag{1.14}$$

and the *matter* oscillation length, L_m, is given by

$$L_m = \frac{2\pi}{|E_2 - E_1|} = \frac{4\pi p}{\left[(\Delta m^2 \cos 2\theta_v - \sqrt{2}G_F n_e p)^2 + (\Delta m^2 \sin 2\theta_v)^2\right]^{1/2}} \tag{1.15}$$

in analogy with the vacuum oscillation length. The eigenvalues of the two matter eigenstates are given by

$$\frac{m_\nu^2}{2p} = \frac{1}{4p}(m_1^2 + m_2^2 + \sqrt{2}G_F n_e p) \pm \frac{1}{4p}\left[(\Delta m^2 \cos 2\theta_v - \sqrt{2}G_F n_e p)^2 + (\Delta m^2 \sin 2\theta_v)^2\right]^{1/2} \tag{1.16}$$

where the plus sign corresponds to $|\nu_{2m}\rangle$ and the negative sign to $|\nu_{1m}\rangle$. They are shown in Figure 1.3 as a function of electron density, assuming that $m_2^2 > m_1^2$. At resonance, defined by the condition $\Delta m^2 \cos 2\theta_v = \sqrt{2}G_F n_e p$, the energy difference between the two eigenstates reaches a minimum of $\Delta m^2 \sin^2\theta_v/2p$. Notice that resonance can only occur if $m_2^2 > m_1^2$.

In a medium of constant electron density the neutrino mass eigenstates $|\nu_{1m}\rangle$ and $|\nu_{2m}\rangle$ propagate with the different phases given by the above eigenstates, just as the vacuum mass eigenstates $|\nu_1\rangle$ and $|\nu_2\rangle$ propagate in the vacuum. For such a medium of constant density there are three regions of interest:

1. Well below resonance ($\sqrt{2}G_F n_e p \ll \Delta m_2 \cos 2\theta_v$) where the matter mixing angle and matter oscillation length are very close to their vacuum values and hence $P(\nu_e \rightarrow \nu_x) = \sin^2 2\theta_v \sin^2(\pi L/L_v)$ as before.

2. At resonance ($\Delta m^2 \cos 2\theta_v = \sqrt{2}G_F n_e p$) where $\theta_m(\text{res}) = \pi/4$ and $L_m(\text{res}) = L_v/\sin 2\theta_v$ so that $P(\nu_e \rightarrow \nu_x) = \sin^2[\pi L \sin(2\theta_v)/L_v]$ which typically yields 0.5 when averaged over the neutrino energy spectrum.

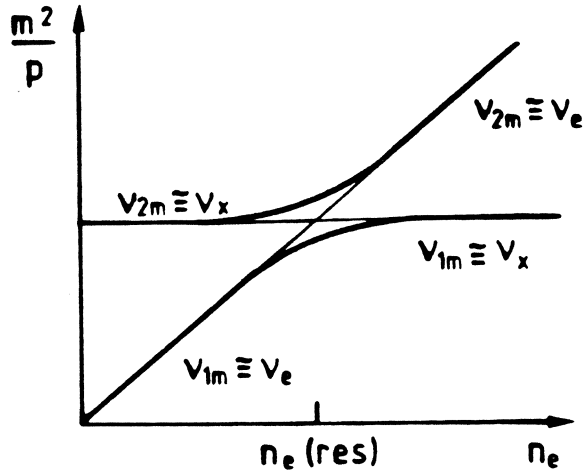

Figure 1.3: The *matter* mass eigenstates $|\nu_{1m}\rangle$ and $\nu_{2m}\rangle$ are shown as a function of electron number density, n_e, for the case $m_2^2 > m_1^2$.

3. Far above resonance ($\sqrt{2}G_F n_e p \gg \Delta m_2 \cos 2\theta_v$) where $\theta_m \cong \pi/2$ and the matter oscillation length is much smaller than the vacuum oscillation length. In this case the oscillation probability can be written $P(\nu_e \rightarrow \nu_x) = (L_m/L_v)^2 \sin^2 2\theta_v \sin^2(\pi L/L_m)$ where the factor $(L_m/L_v)^2$ is considerably suppressing oscillations.

The full power of matter oscillations only emerges when one considers a medium of *varying* electron density. Mikheyev & Smirnov [17] were the first to realise the significance of matter oscillations in the case of the slowly varying electron density of the solar interior. Let us rewrite the resonance condition in terms of the electron density required for resonance

$$n_e(\text{res}) = \frac{\Delta m^2 \cos 2\theta_v}{2\sqrt{2}G_F E} \simeq 66 N_A \cos 2\theta_v \left(\frac{\Delta m^2}{10^{-4}\,\text{eV}^2}\right)\left(\frac{10\,\text{MeV}^2}{E}\right). \qquad (1.17)$$

Now if the energy of the neutrino, E, and the parameter Δm^2 are such that the electron density at the center of the Sun is larger than the resonance density, i.e. $E/\Delta m^2 > 5\,\text{MeV}/10^{-4}\,\text{eV}^2$, then the $|\nu_e\rangle$ produced in the center of the Sun will be predominantly in the $|\nu_{2m}\rangle$ state since $\theta_m \cong \pi/2$ at these densities. As this neutrino travels out of the Sun it will pass through a medium in which the electron density decreases exponentially over approximately four orders of magnitude. At some point it will pass through a region where the electron density is equal to the resonance density for this neutrino (see Figure

1.3). If in this region the electron density is changing sufficiently slowly (the adiabatic condition) then the wavefunction has sufficient time to follow the rapidly rotating mass eigenstate $|\nu_{2m}\rangle$ and the probability of 'level jumping', i.e. the transition from one mass eigenstate to the other, is negligible. Thus the neutrino emerges from the Sun in the $|\nu_{2m}\rangle$ state which in the vacuum is mostly $|\nu_x\rangle$ (for small θ_v).

Mathematically the adiabatic condition is prescribed by requiring the physical width of the resonance, Δr, to be larger than the matter oscillation length at resonance, $L_m(\text{res})$. The physical width of the resonance is defined as the distance Δr over which the change in electron density causes the eigenvalues to separate by an amount equal to the intrinsic energy difference at resonance, i.e.

$$\sqrt{2}G_F\Delta r\left|\frac{dn_e}{dr}\right|_{res} = \Delta m^2 \sin 2\theta_v/2E. \tag{1.18}$$

In the non-adiabatic regime, when $\Delta r \approx L_m(\text{res})$, the probability of jumping from one mass eigenstate to another can be calculated using an approximation developed by Landau and by Zener, (see for example [24]). The result can be written

$$P_{jump} = \exp\left[-\frac{\pi\Delta m^2 \sin^2 2\theta_v}{4E\cos 2\theta_v}\left(\frac{n_e}{|dn_e/dr|}\right)_{res}\right] = \exp\left[-\frac{\pi^2\,\Delta r}{2\,L_m(\text{res})}\right] \tag{1.19}$$

from which it is clear that $P_{jump} \to 0$ in the adiabatic limit of $\Delta r > L_m(\text{res})$.

Assuming that the $|\nu_e\rangle$ produced in the Sun is initially in the $|\nu_{2m}\rangle$ state, i.e. $E/\Delta m^2$ is greater than the critical value $5\,\text{MeV}/10^{-4}\,\text{eV}^2$, then the probability that this neutrino will emerge from the Sun as $|\nu_e\rangle$ is given by

$$P(\nu_e \to \nu_e) = |\langle\nu_e|\nu(t)\rangle|^2 \cong \sin^2\theta_v + P_{jump}(E)\cos 2\theta_v \tag{1.20}$$

where the $\sin^2\theta_v$ term represents the $|\nu_e\rangle$ component of a $|\nu_{2m}\rangle$ state which has emerged into the vacuum without jumping. This equation is valid for both the adiabatic and non-adiabatic regimes.

The effect of matter oscillations on the solar neutrino spectrum is shown in Figure 1.4 where the probability $P(\nu_e \to \nu_e)$ is plotted as a function of $p/\Delta m^2$ for two values of $\sin^2 2\theta_v$. If $p/\Delta m^2$ is *smaller* than the critical value ($5\,\text{MeV}/10^{-4}\,\text{eV}^2$) then the electron density required for resonance, $n_e(\text{res})$, is *greater* than the electron density at the center

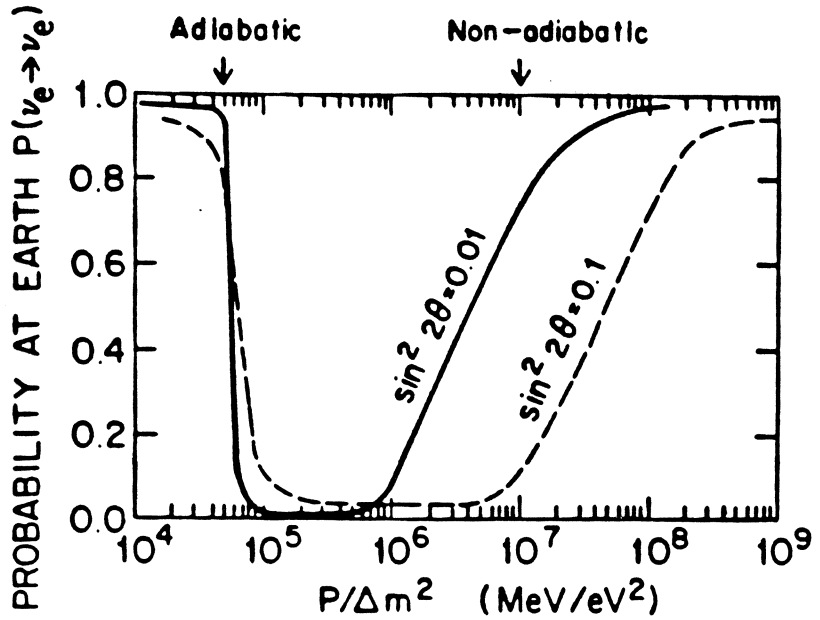

Figure 1.4: Probability $P(\nu_e \rightarrow \nu_e)$ that an electron neutrino created in the center of the Sun reaches the Earth in the $|\nu_e\rangle$ state, as a function of $p/\Delta m^2$ for two given values of $\sin^2 2\theta_v$.

of the Sun and so the neutrinos do *not* pass through resonance as they emerge from the Sun and so cannot be converted (apart from vacuum oscillations). Conversely, if $p/\Delta m^2$ is *greater* than the critical value then the neutrinos *necessarily* pass through resonance. Let us first consider the behaviour of the $\sin^2 2\theta_v = 0.1$ case. In this case the adiabatic condition, $\Delta r > L_m(\text{res})$, is easily fulfilled for neutrinos with energies just above the critical value. As $p/\Delta m^2$ increases from the critical value the quantity $\Delta r/L_m(\text{res})$ decreases (proportionally) until it reaches unity (the non-adiabatic regime) and the probability of level jumping, given by (1.19), becomes non-negligible. As $p/\Delta m^2$ increases further, $\Delta r/L_m(\text{res})$ continues to decrease and P_{jump} increases exponentially towards unity. If $\sin^2 2\theta_v$ is an order of magnitude smaller (the other case presented in Figure 1.4) then the quantity $\Delta r/L_m(\text{res})$ is decreased everywhere by a factor of ten and the non-adiabatic regime is shifted down a decade to lower energies. This narrows the energy range over which the adiabatic condition is fulfilled. Nevertheless even if $\sin^2 2\theta_v = 0.001$ there is still a narrow energy window in which $|\nu_e\rangle$'s can be totally converted to $|\nu_x\rangle$'s.

Thus the signatures of the MSW effect in solar neutrino experiments would be an overall reduction of the ν_e signal and (possibly) a distortion of the ν_e energy spectrum with respect to the parent beta-decay shapes and the relative strengths of the different solar neutrino sources. Many different reduction factors and distortions are possible according to the values of $\sin^2 2\theta_v$ and Δm^2, i.e. how the solar neutrino spectrum which spans about two decades (0.2–20 MeV) is related to the oscillation probability spectrum shown in Figure 1.4. The range in Δm^2 over which the two spectra overlap ($10^{-7}\text{eV}^2 < \Delta m^2 < 10^{-4}\text{eV}^2$ for $\sin^2 2\theta_v = 0.1$) is inaccessible to terrestrial experiments and is made plausible by some grand unified theories which predict neutrino masses of the order 10^{-3} eV.

The same technique of normalizing a measured ν_e flux to an *independent neutral current measurement* as discussed for vacuum oscillations is equally applicable and attractive here.

1.4 The ^{37}Cl Experiment

The ^{37}Cl experiment is a radiochemical experiment where the neutrino absorption reaction

$$\nu_e + {}^{37}\text{Cl} \rightarrow {}^{37}\text{Ar} + e^- \tag{1.21}$$

is used to measure an *integral* flux of solar neutrinos. The threshold for this reaction is 0.814 MeV which is above the endpoint of the predominant pp neutrinos and so these neutrinos are not detected. The event rate, in solar neutrino units (SNUs) where 1 SNU is 1 event per 10^{36} target atoms per second, can be calculated by integrating the energy dependent cross-section over the predicted solar neutrino spectrum (Figure 1.2). For the two predictions of solar neutrino fluxes discussed in Section 1.2 the total capture rate is 7.9 ± 0.9 SNU (Bahcall & Ulrich [6]) and 5.8 ± 1.2 SNU (Turck-Chieze *et al.* [7]). The breakdown of these total capture rates into individual components of the solar neutrino spectrum is given in Table 1.2. About 70% of the total capture rate comes from the high energy ^{8}B neutrinos which can react via the superallowed transition to the excited (5.2

Neutrino Source	Bahcall & Ulrich [6]	Turck-Chieze *et al.* [7]
pp	0.0	0.0
pep	0.2	0.2
hep	0.03	n.a.
^{7}Be	1.1	1.0
^{8}B	6.1	4.0
^{13}N	0.1	n.a.
^{15}O	0.3	n.a.
^{17}F	0.003	n.a.
Total	7.9 ± 0.9	5.8 ± 1.2

Table 1.2: Predicted capture rates in a ^{37}Cl experiment (in SNUs).

MeV) analogue state in ^{37}Ar. Thus the large uncertainty in the ^{8}B flux prediction (see Section 1.2) carries over into a large error in the predicted capture rate for ^{37}Cl.

The target material is 615 tons of liquid perchloroethylene, C_2Cl_4, contained in a single tank located 4850 ft underground in the Homestake Gold mine. The number of ^{37}Cl atoms in this tank is such that 5.35 SNU is equivalent to the production of one ^{37}Ar atom per day.

At the beginning of each exposure, 0.05 to 0.10 cm^3 of isotopically pure ^{36}Ar is introduced into the tank to act as a carrier. A couple of months later this sample of ^{36}Ar, together with the few atoms of ^{37}Ar produced by solar neutrinos, are removed from the tank by helium purging and collected in a charcoal trap. The volume of this recovered Ar serves as a measure of the efficiency of the extraction process (typically 90–95%). The Ar is then mixed with tritium-free methane and loaded into a small (0.3 to 0.5 cc) proportional counter which detects the Auger electrons from the electron capture decay of ^{37}Ar.

Several tests have been performed to try and check the validity of the assumption that the efficiency for recovering gaseous ^{36}Ar (or ^{38}Ar) is the same as the efficiency for extracting the neutrino induced ^{37}Ar which is initially created as an $^{37}Ar^{+}$ ion with considerable momentum (certainly enough to break free from its parent C_2Cl_4 molecule). The most convincing of these tests (see [25] and [26]) is one where tetrachloroethylene

labeled with ^{36}Cl was introduced into the tank. The beta-decay of ^{36}Cl produces a $^{36}Ar^{+}$ ion with approximately the same recoil momentum as the $^{37}Ar^{+}$ ions from neutrino events. The efficiency of the extraction of this ^{36}Ar, by the usual helium purge, was measured by activation analysis to be $100 \pm 3\%$.

For each extraction of neutrino induced ^{37}Ar, data from a proportional counter is collected over about an eight month period, i.e. several times the 35 day half-life of ^{37}Ar. The few counts which fall in a prescribed window in the pulse height vs. rise time[3] plane are fitted, by a maximum likelihood method, to a flat background and an exponential decay with a half life of 35 days. For the 61 runs from 1970.8 to 1989.5 the combined result is an inferred production rate of 0.49 ± 0.04 ^{37}Ar atoms per day in the 615 ton tank. Both the chemical extraction efficiency and the counting efficiency ($\simeq 50\%$, estimated by Monte-Carlo and measured by counting known quantities of ^{37}Ar) are already included in this number. One of the outstanding checks of systematics in this experiment is the verification that these two efficiencies are indeed well understood by measuring the production rate of ^{37}Ar from a calibrated neutrino source. Unfortunately, this extremely difficult and expensive measurement has never been accomplished.

Background induced ^{37}Ar is primarily produced by the $^{37}Cl(p,n)^{37}Ar$ reaction where cosmic ray muons are the principle source of energetic protons in the tank. This background has been estimated by two independent methods: (1) by exposing 600 gallon tanks of C_2Cl_4 at higher levels in the mine and then extrapolating the ^{37}Ar production rate back down to the 4850 ft level; and (2) from a theoretical estimate of the average ^{37}Ar yield per muon. These two estimates are in agreement and yield 0.08 ± 0.03 ^{37}Ar atoms per day.

Subtracting this rate from the inferred production rate from the maximum likelihood analysis yields the neutrino induced production rate which can be converted to a capture rate of 2.19 ± 0.24 SNU. Dividing this rate by the predicted capture rates from solar models gives the ratios of $0.28(1 \pm 0.16)$ for [6] and $0.38(1 \pm 0.23)$ for [7] where we

[3]Signals from k-capture in ^{37}Ar tend to have faster rise times than background signals of the same pulse height.

have added the experimental errors and theoretical uncertainties in quadrature. This discrepancy has been dubbed the 'solar neutrino problem'.

The *possible* time correlation between the measured ^{37}Cl capture rate and the inverse of the sun-spot number, which has an 11 year period, has attracted much attention. If such a correlation were confirmed by future experiments with higher statistics then it would indicate new neutrino properties since it is highly improbable that the neutrino generating processes, which have an equilibrium time constant of the order 10^7 years, could exhibit such a periodicity. A much more plausible explanation would be that the ν_e flux is modulated by the Sun's magnetic field which is known to peak at times of maximum sun-spot activity. This would imply some sort of spin flip mechanism induced by a neutrino magnetic moment (and/or electric dipole moment).

1.5 The ^{71}Ga Experiments

These radiochemical experiments detect solar neutrinos via the reaction

$$\nu_e + {}^{71}\mathrm{Ga} \rightarrow {}^{71}\mathrm{Ge} + e^- . \tag{1.22}$$

The very low threshold (0.2332 MeV) of this reaction enables the detection of the abundant pp neutrinos. About 50% of the total capture rate is from pp neutrinos, with a further 25% from ^{7}Be neutrinos. Since the fluxes of these neutrinos are relatively well constrained by solar model calculations the uncertainty in the total capture rate (132 ± 7 SNU from Bahcall & Ulrich [6] and 125 ± 5 SNU from Turck-Chieze *et al.* [7]) is much less than for the ^{37}Cl experiment. In fact the dominant source of uncertainty is the inferred values (from (p,n) measurements) of matrix elements to excited levels of ^{71}Ge[4]. The minimum capture rate in ^{71}Ga is 80 SNU [13] assuming that only pp neutrinos (for which the capture cross-section is smallest) are generated in the Sun and that they are generated at a rate which sustains the Sun's luminosity.

Two separate groups are presently taking solar neutrino data with ^{71}Ga: the Soviet

[4]The superallowed transition does not contribute very much to the measured capture rate in ^{71}Ga because the analogue state in ^{71}Ge decays mostly (> 90%) by particle emission.

American Gallium Experiment (SAGE) in Baksan and a European experiment, Gallex, located in the Gran Sasso laboratory near Rome. Both of these experiments measure the electron capture decay of ^{71}Ge ($t_{1/2}$ = 11.4 days) by detecting the Auger electrons in proportional counters which are very similar to those used in the ^{37}Cl experiment. The data analysis by a maximum likelihood method is also common to both these experiments. The principle difference between SAGE and Gallex is in the method of extraction of the ^{71}Ge, although both deduce their efficiency for extracting neutrino induced ^{71}Ge from the measured efficiency for recovering inert Ge carrier.

In SAGE the gallium is kept in four reactors containing each about 7.5 tons of gallium metal. After a typical exposure time of 4 weeks, concentrated HCl is added to the liquid metal and the two are thoroughly mixed in the presence of hydrogen peroxide, resulting in the extraction of Ge into the acid solution. This solution is then siphoned off from the reactors and reduced by a series of extractions and back extractions to about 1 litre of weakly basic solution. The counting gas GeH_4, germane, is then synthesized and purified by gas chromatography. The overall efficiency is typically 80% [3].

In Gallex the gallium is held in a single tank of concentrated $GaCl_3$–HCl solution. The $GeCl_4$ which forms in this solution is extracted by a nitrogen purge into a small volume of H_2O from which germane is synthesized and purified. This process yields an overall extraction efficiency at least as good as SAGE and probably slightly better [27].

Both SAGE and Gallex intend to perform an overall calibration of their experiments by measuring the production rate of ^{71}Ge from a calibrated ^{51}Cr neutrino source.

So far, only SAGE has reported any results [3]. The combined result of five extractions in early 1990 is a ^{71}Ga capture rate of 20^{+15}_{-20}(stat)$\pm$32(syst) SNU, assuming that the chemical extraction efficiencies for the Ge carrier and the neutrino induced ^{71}Ge are the same. This translates into the following upper limits on the ^{71}Ga capture rate: $<$ 55 SNU (68% C.L.) and $<$ 79 SNU (90% C.L.). Once more there is an indication of a deficit in comparison with the predicted capture rates from solar models. However it is premature to suggest that this is firm evidence for new neutrino properties. It will be interesting to see what Gallex reports in the near future. These experiments, particu-

larly if their calibrations with ^{51}Cr neutrinos are successful, provide an opportunity of clearly demonstrating that new neutrino properties are required.

1.6 Kamiokande-II

In 1985, the Kamiokande-I detector, which was originally built for searching for proton decay, was upgraded with the addition of a 4π 1.5 m thick H_2O anticounter and the installation of new improved electronics [28]. These improvements have enabled Kamiokande-II [29], [2] to measure the high energy ^{8}B solar neutrino flux through the electron scattering reaction

$$\nu_{e,\mu,\tau} + e^- \rightarrow \nu_{e,\mu,\tau} + e^-. \tag{1.23}$$

The differential cross-section for this scattering process is given by [30]

$$\frac{d\sigma}{dT_e} = \frac{2G_F^2 m_e}{\pi}\left[g_L^2 + g_R^2\left(1 - \frac{T_e}{E_\nu}\right)^2 - g_L g_R\left(\frac{m_e T_e}{E_\nu^2}\right)\right] \tag{1.24}$$

$$(g_L = \pm\frac{1}{2} + \sin^2\theta_W,\ g_R = \sin^2\theta_W \text{ and } \sin^2\theta_W = 0.23),$$

where G_F, m_e, E_ν and T_e are respectively the Fermi coupling constant, the electron rest mass, the incoming neutrino energy and the electron recoil kinetic energy. The upper sign in g_L applies for ν_e's (charged and neutral current interaction) and the lower sign for ν_μ's and ν_τ's (neutral current interaction).

The *spectrum averaged* differential cross-section is obtained by integrating the above differential cross-section over the normalised neutrino spectrum $\lambda(E_\nu)$ from the minimum neutrino energy necessary to produce a recoil electron of kinetic energy T_e to the maximum neutrino energy in the spectrum. The *total* cross-section for an experiment with a given electron recoil energy threshold, T_e(thresh), is then determined by integrating the spectrum averaged differential cross-section over T_e from T_e(thresh) to the maximum possible T_e produced by the maximum neutrino energy in the spectrum. If the *detection efficiency* as a function of T_e is folded into this second integration then the *effective* total cross-section is calculated. For any threshold of interest to solar neutrino

experiments the ratio of the total cross-section for ν_e scattering to that of ν_μ or ν_τ scattering is between 6:1 and 7:1. The angular distribution of recoil electrons is strongly peaked in the forward direction, e.g. if T_e(thresh) = 9 MeV then 90% of the electrons are scattered within 8° of the neutrino's initial direction.

Kamiokande-II is a water Cherenkov detector in which 948 fifty centimeter photomultipliers (PMTs), equally spaced on the surface of a cylinder of diameter 14.4 m and height 13.1 m, look inwards at a volume of 2140 tons. This volume is completely surrounded by a 1.5 m thick layer of water which is viewed by 123 PMTs and acts both as an anticoincidence counter and as shielding from high energy gammas and neutrons from the walls of the cavity. The cavity itself is located in the Kamioka mine with an overburden of 2400 mWe (meters of water equivalent).

In June 1988 the gain of the PMTs was increased by a factor of 2 with the addition of new improved electronics. Before this change the energy scale of the detector was 26 photoelectrons for 10 MeV of recoil energy and afterwards it was 30 photoelectrons per 10 MeV. Both these absolute energy scales have been calibrated to within 3% accuracy by three separate measurements: (1) the energy spectrum of recoil electrons produced by Compton scattering from (up to) 9 MeV gammas from the reaction Ni(n,γ)Ni; (2) the Michel spectrum from stopped muons decaying in the tank; and (3) the beta-spectra of various nuclei which are spallation products of through-going muons. The rms energy resolution of $22\%/(T_e/10\ \text{MeV})$, the rms angular resolution (28° for T_e = 10 MeV) and the rms vertex-position resolution (1.7 m for T_e = 10 MeV) are all obtained from Monte-Carlo simulations which reproduce quite well the above measured spectra and the angular and spatial distributions (with respect to the Nickel gamma source) of the Comptons. The poor rms angular resolution is mostly caused by multiple scattering in the water of the recoil electron which smears the Cherenkov cone.

In the analysis of 450 + 590 days of data (January 87–May 88: sample 1 [29] and June 88–April 90: sample 2 [2]) four different cuts are made to reduce as far as possible the number of background events: (a) only events with less than 30 photoelectrons in the anticoincidence counter are selected (contained events) and the time interval from

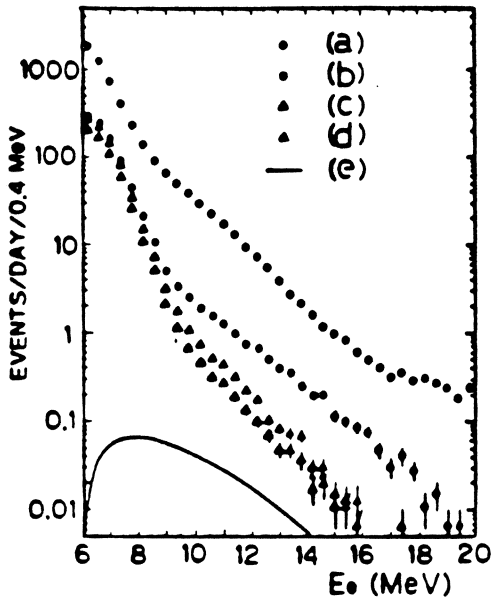

Figure 1.5: Differential energy distribution for Kamiokande-II events from sample 1 [29] after the following cuts: (a) the anti-coincidence veto; (b) the reduced fiducial mass from 2140 t to 680 t; (c) the spallation cut; and (d) the γ-ray cut, (see text for more details). Curve (e) represents the anticipated electron recoil spectrum from a Monte-Carlo simulation with the same cuts as above and based on a predicted ^{8}B flux [6].

any preceeding event must be longer than 100 μsec, to exclude electrons from muon decays; (b) the fiducial volume is restricted to the inner 618 tonnes in order to increase the thickness of water attenuating the high energy gammas from the rock; (c) events which are near in time ($\leq$ 100 msec) and distance ($\leq$ 3 m) to through-going muons are rejected as possible beta-decays of muon spallation products; and finally (d) events in the outer 1 m of the 618 ton volume are rejected if they point inwards from the nearest wall ($\cos\theta > 0.67$ where θ is the angle between the reconstructed direction of the event and the normal to the closest part of the wall), to further reduce the number of γ events from the wall. The data reduction afforded by each of these four cuts is shown in Figure 1.5 where the final energy spectrum of the reduced data is still well above the predicted event rate from ^{8}B neutrino scattering. However the neutrino scattering events point away from the Sun — within the angular resolution of the experiment — as can be seen in Figure 1.6 where the number events above a threshold of 9.3 MeV are plotted against $\cos\theta_{Sun}$ where θ_{Sun} is the angle between the electron's reconstructed direction

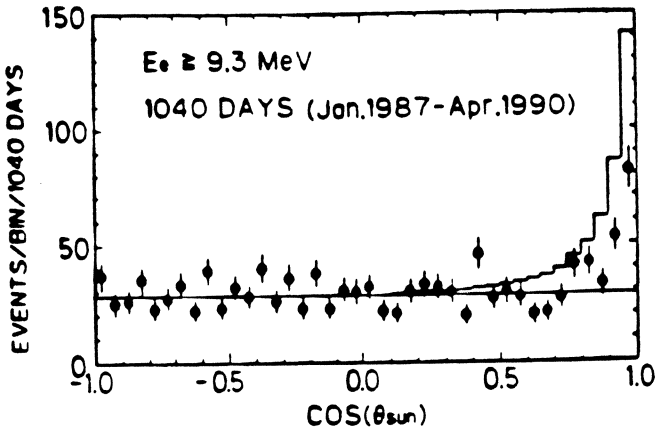

Figure 1.6: Distribution in $\cos\theta_{\rm Sun}$ for the reduced Kamiokande-II data (samples 1 and 2) above a threshold of 9.3 MeV [2]. The histogram represents the anticipated distribution from a Monte-Carlo simulation based on a predicted ^{8}B flux [6].

and the direction away from the Sun. This distribution in $\cos\theta_{\rm Sun}$ has been fitted to a flat background plus the expected angular distribution of the neutrino signal, simulated by Monte-Carlo.

The results are expressed as a ratio of the measured value of the ^{8}B solar neutrino flux, for $T_e \geq 9.3$ MeV in data sample 1 and $T_e \geq 7.5$ MeV in data sample 2, to the predicted value from Bahcall & Ulrich [6]:

$$\frac{\text{Kam-II data}}{\text{Bahcall \& Ulrich}} = 0.46 \pm 0.05(\text{stat}) \pm 0.06(\text{syst}) \pm 0.05(\text{solar}) \qquad (1.25)$$

where we have included the 11% uncertainty from the normalisation to Bahcall & Ulrich's solar model. Normalizing the Kamiokande-II data to the predicted ^{8}B flux from Turck-Chieze *et al.* [7] gives the following result

$$\frac{\text{Kam-II data}}{\text{Turck-Chieze } et\ al.} = 0.70 \pm 0.08(\text{stat}) \pm 0.09(\text{syst}) \pm 0.20(\text{solar}) \qquad (1.26)$$

which is about 1.3 sigma away from unity, combining all errors quadratically. Therefore it is concluded that the evidence for a $|\nu_e\rangle$ deficit is dependent on the assumptions of solar models.

As mentioned in Section 1.3.2 one possible signature of the MSW effect is a distortion in the energy spectrum of the $|\nu_e\rangle$'s detected at the Earth. Figure 1.6 shows the energy distribution of the *electron* recoil signal, i.e. the number of events per energy bin in the

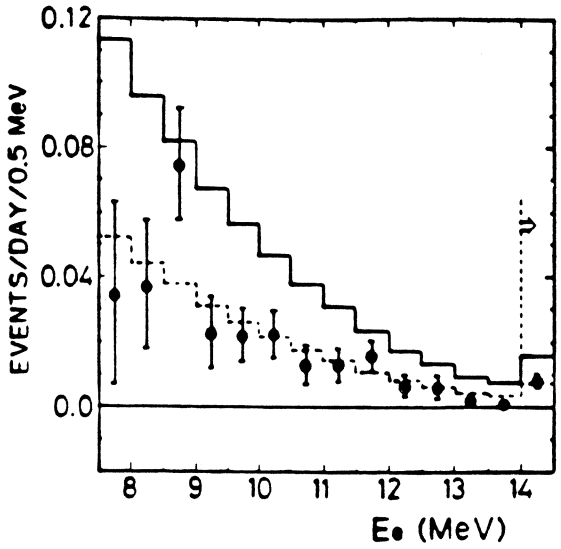

Figure 1.7: Energy distributions of electron recoil signals from solar neutrinos for the combined 1040 days of Kamiokande-II data (samples 1 + 2) [2]. The solid line is the Monte-Carlo generated signal for the ^{8}B flux prediction of [6] and the dotted line is the Monte-Carlo signal for the inferred flux, i.e. 0.46 × this prediction.

forward peak after subtracting the flat background. This distribution is (unavoidably) integrated over the incoming neutrino spectrum. The statistical accuracy of the data is insufficient to differentiate this spectrum and infer the *neutrino* spectrum.

Searches were made for day/night effects, seasonal variations and sun-spot correlations. No time variations were found but the statistics do not exclude the possibility of such time variations with reduced amplitudes.

1.7 Outlook

At best, the combined ^{37}Cl, SAGE and Kamiokande-II results can be regarded as a possible indication of neutrino oscillations. If in the next few years both SAGE and Gallex measure a significantly smaller capture rate in ^{71}Ga than can possibly be accounted for by even the most extreme solar model (i.e. < 79 SNU [13]) *and* these experiments have undergone successful calibrations with ^{51}Cr neutrino sources, then there would be considerable evidence for new neutrino properties. Even then, it would be impossible to infer the precise nature of these new properties (the oscillation parameters and/or

magnetic moments) from the limited spectral information and low statistical accuracy data that would be available.

Numerous second generation experiments have been proposed which have one or more of the following advantages over current experiments for testing the neutrino oscillation and spin flip hypotheses: (1) increased statistics, (2) spectral information and (3) neutral current measurements. The discussion here will be restricted to Super Kamiokande, Borexino and the Sudbury Neutrino Observatory (SNO).

As the name suggests, Super Kamiokande will be a larger version of Kamiokande-II. The fiducial volume, number of PMTs and coverage will be increased from 680 t, 948 PMTs and 20% coverage to 22,000 t, 11,200 PMTs and 40% coverage. The ^{8}B ν_e–e^- scattering signal is expected to increase from 180/year to 6200/year, whilst the backgrounds from internal radioactivity and external gammas are expected to decrease due to improved water purification, more H_2O shielding from the rock and the much improved characteristics of the 50 cm PMTs which will increase the vertex reconstruction accuracy and to a lesser extent the angular and energy resolutions. On the other hand, the detector will be situated at the same depth as the Kamiokande-II detector and the beta-decay rate of spallation nuclei from through-going muons is expected to be approximately 3500/year (after cuts).

One can expect a precise measurement of the ^{8}B ν_e flux above a threshold of about 5 MeV and a reasonably well inferred ν_e energy spectrum from the measured electron recoil spectrum. However, neither of these is certain to produce conclusive evidence for neutrino oscillations given the inherent uncertainties in the solar model predictions of this flux and the numerous oscillation scenarios which produce minimal distortion in the ν_e spectrum over the 5–14 MeV range of the measurements. Nevertheless the spectral information might prove very useful for confirming the oscillation hypothesis if a severe distortion is observed. The difference in electron recoil spectra between ν_e scattering and ν_μ or ν_τ scattering is not significant enough to provide a signature for oscillations but will further complicate the interpretation of the differentiated electron recoil spectrum.

Borexino will be a 200 t spherical scintillator detector shielded with H_2O and/or

glycerol and viewed with a few hundred 20 cm PMTs. The amplification of electron recoil signals obtained by scintillation compared to the signal from the Cherenkov process should allow the detection of the ^{7}Be neutrino line at 0.861 MeV. The flux of these neutrinos is roughly three orders of magnitude greater than the ^{8}B flux. With a threshold of 250 KeV one can expect about 50 events/day from solar model predictions. This large count rate would allow a very precise search for any time correlations in the signal. In fact, the 7% annual variation due to the Earth's eccentricity should provide a useful check on the origin of the signal. The ^{7}Be flux can be predicted to $\pm 5\%$ accuracy [6] but it should be noted that the difference between the predicted fluxes from [6] and [7] is 11%. Thus a measurement of this flux would provide useful information for pinning down a possible MSW distortion in the solar neutrino spectrum. The key to reaching these physics goals will be the radiopurity of the scintillator since the scintillation process will also amplify the internal backgrounds. A level of 10^{-16} g/g of Th and U contamination is required, (see discussion of internal backgrounds in Chapter 2).

The SNO detector and its physics capabilities will be discussed in detail in Chapter 2. However at this point it is worth mentioning that SNO is the only funded experiment which can detect solar neutrinos by both a charged current reaction and an *independent* neutral current reaction. The experiment is thus self-normalizing and does not rely on the predictions of solar models to search for neutrino oscillations. Conversely, the ^{8}B flux measured by the neutral current reaction is an excellent test of solar models, irrespective of flavour oscillations.

Chapter 2

Sudbury Neutrino Observatory

2.1 Detector

The Sudbury Neutrino Observatory (SNO) [31] is a heavy water Cherenkov detector (presently under construction) for measuring the ^8B ν_e energy spectrum and flux via a charge current reaction and the ^8B total ν flux via an independent neutral current rection. One thousand tons of 99.85% enriched D_2O will be contained in a 5 cm thick spherical acrylic vessel of 12 m diameter. This sphere will be suspended in the middle of a barrel shaped cavity (30 m high and 22 m in diameter) filled with 7,300 tons of ultrapure H_2O (see Figure 2.1). A minimum thickness of 5 m of H_2O will shield the D_2O from the walls of the cavity. At present, the cavity is being excavated at the 2070 m level in the INCO nickel mine in Sudbury, Ontario. This overburden of rock (6200 m.w.e.) attenuates the flux of cosmic ray muons to a minimal level of $\sim$ 100 $m^{-2}year^{-1}$ which is more than two hundred times smaller than in Kamiokande-II.

The central volume of D_2O will be viewed by 9,600 Hamamatsu R1408 photomultipliers located on a concentric sphere (the photomultiplier sphere) of 16.8 m diameter, i.e. 2.4 m radially outwards from the acrylic vessel. Each of these 20 cm diameter PMTs will be equipped with a light reflecting concentrator which will increase its effective area by a factor of at least 1.6 and restrict its field of vision to the central volume of D_2O and the surrounding 1 m shell of H_2O (500 tons), i.e. a spherical fiducial volume of 14 m

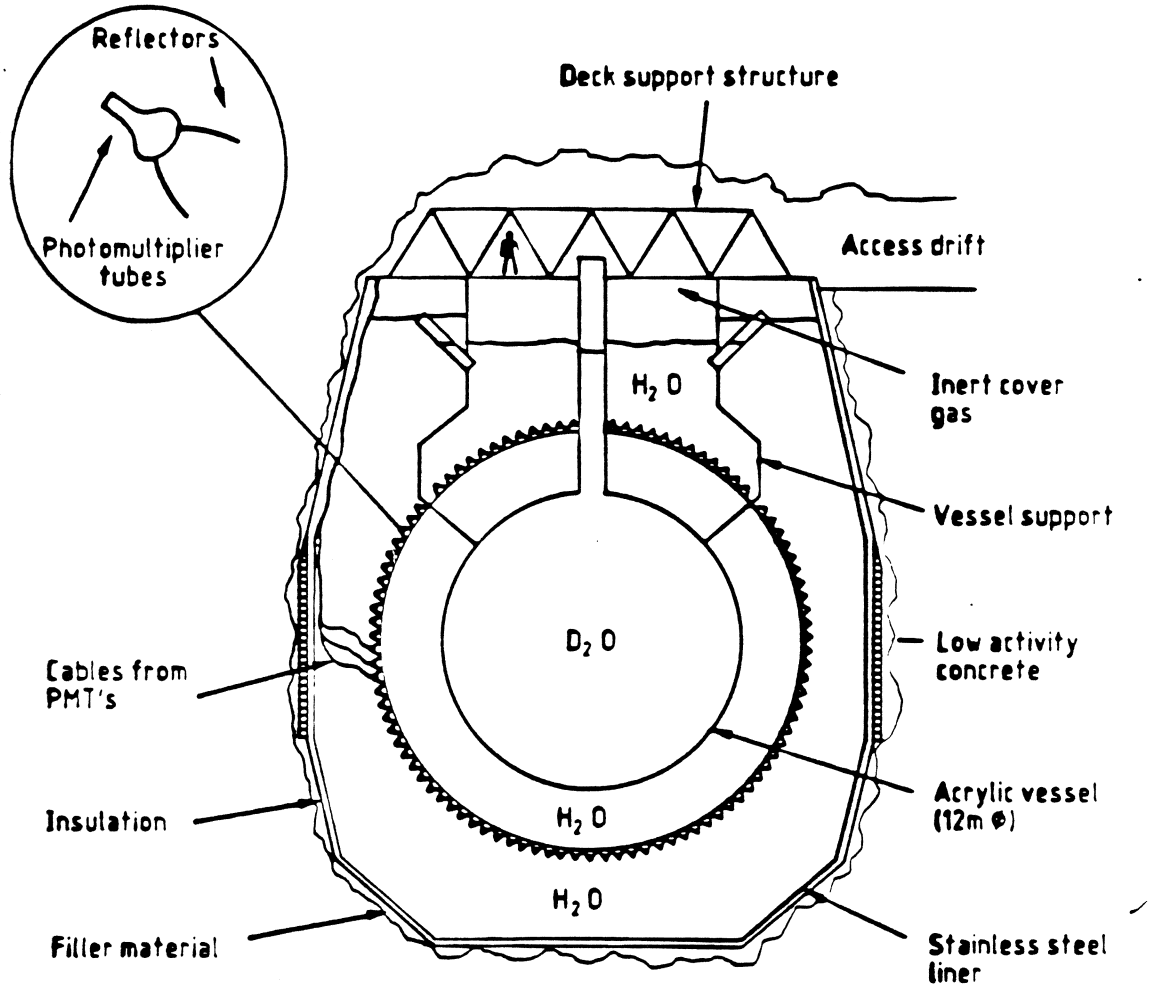

Figure 2.1: Schematic representation of the SNO detector.

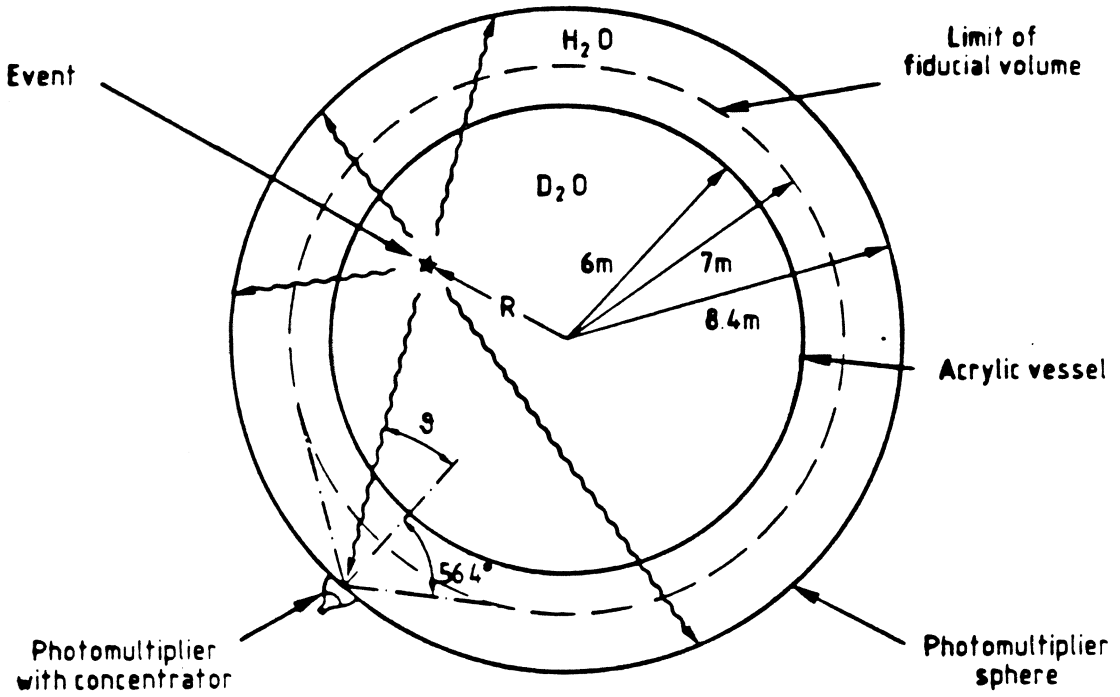

Figure 2.2: The fiducial volume of the SNO detector subtends a cone of half angle 56.4° at the entrance aperture of the concentrators. The Cherenkov light from an event at radius R is incident on a particular concentrator entrance aperture at polar angle θ. The rest of the Cherenkov light is incident on the photomultiplier sphere at angles from 0° to $\sin^{-1}(R/8.4\text{ m})$

diameter, see Figure 2.2. The effective coverage (PMT equivalent) of the photomultiplier sphere which will be achieved with the concentrators is about 55%.

2.2 Neutrino Reactions

Three neutrino reactions will be used to detect ^{8}B (and perhaps hep) solar neutrinos in the fiducial volume of SNO. Firstly, the charge current (CC) reaction

$$\nu_e + d \rightarrow p + p + e^-, \qquad Q = -1.44\,\text{MeV} \tag{2.1}$$

will be used to measure the ^{8}B ν_e flux above an expected electron recoil threshold of about 5 MeV. The recoil energy of the 2 protons is negligible and so the recoil energy of the electron is given by $T_e = E_\nu - 1.44$ MeV. The cross-section for this reaction, as a function of neutrino energy, is shown in Figure 2.3. Integrating this cross-section

over the ^{8}B neutrino spectrum between E_ν = 6.44 MeV and the endpoint of the beta spectrum ($\sim$ 14 MeV) gives an expected event rate of 4,300 events per year per kiloton (kt), assuming the ^{8}B ν_e flux measured in Kamiokande-II, i.e. 2.7 x 10^6 cm^{-2} s^{-1}. The accuracy with which the ^{8}B ν_e flux can be measured by this reaction is limited by the $\pm$10% uncertainty in the absolute cross-section [32]. The direct relation between E_ν and T_e and the relatively high event rate should allow an accurate measurement of the ^{8}B ν_e spectrum above 6.5 MeV. This might provide clear evidence for neutrino oscillations if a severe distortion with respect to the beta decay spectrum is observed, or, if no distortion is observed, restrict the available parameter space for oscillations. The angular distribution of recoil electrons is given by $W(\theta_{\rm Sun}) = 1 - 1/3\cos\theta_{\rm Sun}$, i.e. a 2-1 backward to forward asymmetry.

The second reaction for detecting ^{8}B neutrinos is the electron scattering (ES) reaction

$$\nu_{e,\mu,\tau} + e^- \rightarrow \nu_{e,\mu,\tau} + e^- \qquad (2.2)$$

which has already been discussed in Section 1.6, in connection with the Kamiokande-II detector. The slightly larger fiducial volume (1.5 kt vs. 680 t) and lower expected threshold (5 MeV vs. 7.5 MeV) of the SNO detector compared with Kamiokande-II, should result in a larger event rate of 730 per year, vs. 180 per year, for the same flux of 2.7 x 10^6 cm^{-2}s^{-1}. It may be possible to deduce the $\nu_{\mu,\tau}$ component of this event rate by subtracting the ν_e component inferred from the 'pure' ν_e flux measured by the CC reaction. The accuracy of this procedure will be limited by the $\pm$10% uncertainty in the absolute cross-section of the CC reaction and the fact that the cross-section for $\nu_{\mu,\tau}$-e^- scattering is about 1/7th that for ν_e-e^- scattering. Nevertheless the deduced $\nu_{\mu,\tau}$ flux from the combination of the CC and ES reactions might indicate the existence of neutrino oscillations.

The 'pure' neutral current (NC) reaction

$$\nu_{e,\mu,\tau} + d \rightarrow \nu_{e,\mu,\tau} + p + n, \qquad Q = -2.23\,\text{MeV} \qquad (2.3)$$

should provide a more accurate test for neutrino oscillations. The free neutron from this reaction can be detected by the γ-ray emission (8.5 MeV) from neutron capture on ^{37}Cl

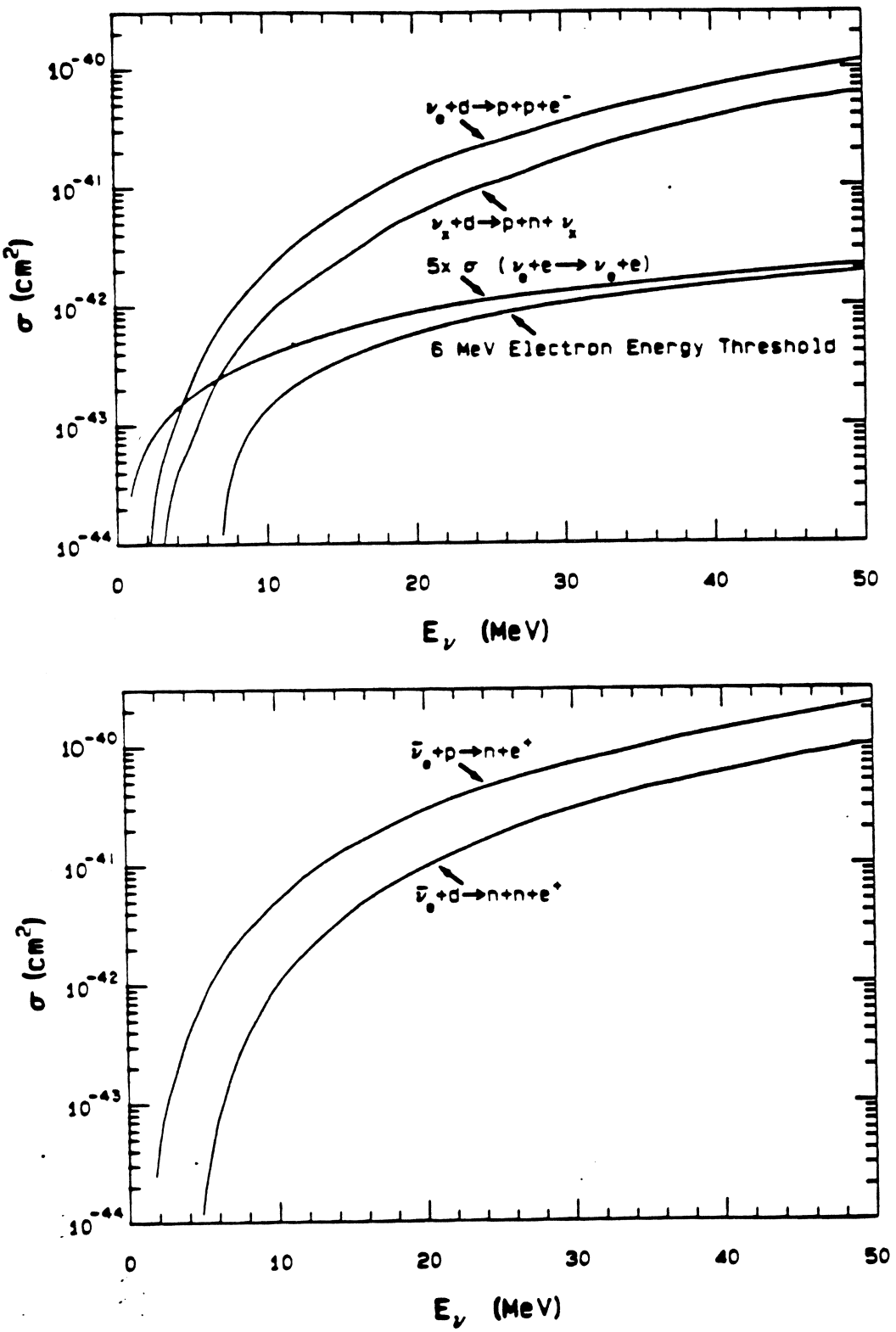

Figure 2.3: Cross-sections for the principle neutrino reactions in SNO, as a function of neutrino energy. The cross-section for ν_e-e^- scattering is scaled up by the electron/deuteron ratio in D_2O.

when NaCl is added to the D_2O. Although the absolute cross-section for the NC reaction (see Figure 2.3) is known to $\pm 10\%$ accuracy, the ratio of this cross-section to that of the CC reaction is known to within 0.5% [33]. Therefore the ratio of the fluxes measured from these two reactions is an accurate test for neutrino oscillations, *independent of solar models.*

If no salt is added to the D_2O then approximately 25% of the NC neutrons will capture on deuterium producing 6.25 MeV γ's of which less than half would be detected above the expected *electron* threshold of about 5 MeV. The rest of the neutrons will be captured by hydrogen producing 2.2 MeV γ's which will be well below threshold. If 2.5 t of NaCl are added to the D_2O then approximately 84% of the NC neutrons will be captured on ^{37}Cl releasing 8.5 MeV of γ energy. More than half of these captures would be detected above the expected 5 MeV threshold. For a *total* ^8B $\nu_{e,\mu,\tau}$ flux of 2.7×10^6 $cm^{-2}s^{-1}$, i.e. the same flux as measured by Kamiokande-II assuming no oscillations, about 1,200 NC events per year should be detected (above threshold) with the salt and about 200 without the salt. The angular distribution of these events will of course be isotropic.

The current experimental schedule is to start with D_2O and *no* salt in the acrylic vessel for about a year. This should allow a high statistics measurement of the ν_e spectrum from the CC reaction (see Figure 2.6) and a search for neutrino oscillations by comparing the yields of the CC reaction and of the ES reaction which should be easily identified by its strong forward peaking. In the second year 2.5 t of NaCl will be added to the D_2O to enhance the NC signal by a factor of about 6 (see Figure 2.7). Assuming that the CC signal is constant (with time) one can infer the NC signal in the second year by subtracting the CC signal measured in the first year from the sum of the CC and NC signals measured in the second year (they have similar energy distributions). Alternatively one could use the 2–1 backward to forward asymmetry of the CC signal to decouple these two signals. At some later stage in the experiment the D_2O will be replaced with H_2O to measure *directly* some of the backgrounds associated with the CC and NC signals (see Figure 2.5). Originally this exercise was planned first but because

	Reaction	Target Medium	ν_e Burst	Cooling Phase
(2.1)	$\nu_e + d \rightarrow p + p + e^-$	D_2O	10	33
(2.2)	$\nu_{e,\mu,\tau} + e^- \rightarrow \nu_{e,\mu,\tau} + e^-$	D_2O/H_2O	1.5	24
(2.3)	$\nu_{e,\mu,\tau} + d \rightarrow \nu_{e,\mu,\tau} + p + n$	D_2O	6	760
(2.4)	$\bar{\nu_e} + d \rightarrow n + n + e^+$	D_2O	0	20
(2.5)	$\bar{\nu_e} + p \rightarrow n + e^+$	H_2O	0	60

Table 2.1: Predicted number of events in the 1.5 kt fiducial volume of the SNO detector from the ν_e burst and cooling phases of a stellar collapse at 10 kpc, assuming 100% detection efficiency.

of fears of the acrylic vessel crazing during a water change, it has been rescheduled to a later time, after the critical data with the D_2O has been obtained.

There are two other neutrino reactions in the fiducial volume of SNO that do not concern solar neutrinos but would produce detectable signals in the event of a supernova occurring in our galaxy. These are the charge current reactions

$$\bar{\nu_e} + d \rightarrow n + n + e^+, \qquad Q = -4.0\,\text{MeV} \tag{2.4}$$

and

$$\bar{\nu_e} + p \rightarrow n + e^+, \qquad Q = -1.8\,\text{MeV}. \tag{2.5}$$

The first reaction could be recognised from the triple coincidence of the e^+ signal and the two neutron capture signals (for some events), within 10 msec (neutron capture time) and 70 cm (neutron mean free path in D_2O *with* salt). The second reaction is limited to the outer 500 t of H_2O and its neutron would be captured by hydrogen producing a 2.2 MeV gamma which is well below threshold. The cross-sections for these two neutrino reactions are shown in Figure 2.3.

For a supernova at 10 kpc (the distance to the center of our galaxy) one can expect the number of events given in Table 2.1 for each of the five neutrino reactions in SNO. From the time distribution of the 10 prompt ν_e events (from the neutronisation of the core) one can expect to set a limit of about 3 eV on the mass of ν_e. The several hundred NC events from the cooling phase would allow the possible determination of the ν_μ and/or ν_τ masses within the range 50 eV$< m_\nu <$100 KeV. Below about 50 eV the

spread in time would be masked by the inherent (10 sec) time span of the cooling phase and above 100 KeV the events would be spread over more than 6 months and would be hard to distinguish from the solar neutrino 'background'. The present experimental limits on the ν_μ and ν_τ masses are respectively 270 KeV and 35 MeV [34].

2.3 Optics

Neutrino interactions in SNO are detected via the Cherenkov radiation of relativistic electrons (or positrons). This radiation is emitted when a charged particle traverses a medium of refractive index n at a velocity v which is greater than c/n (the speed of light in the medium). The number of Cherenkov photons emitted per unit track length per unit wavelength is given by [35]

$$\frac{\mathrm{d}^2N}{\mathrm{d}x\mathrm{d}\lambda} = 2\pi\alpha Z^2\left(1-\frac{1}{n^2\beta^2}\right)\frac{1}{\lambda^2} \tag{2.6}$$

where α is the fine structure constant, $\beta = v/c$, and Z is the charge of the relativistic particle. The light is emitted at the Cherenkov cone angle, $\theta_C = \cos^{-1}(1/n\beta)$, relative to the momentum vector of the relativistic particle.

For an electron (or positron) in water with 5–15 MeV of kinetic energy about 220 Cherenkov photons are emitted per MeV between 250 and 600 nm wavelength, with a $1/\lambda^2$ wavelength spectrum and at a Cherenkov cone angle of about 42°. The percentage of these photons which will actually be detected by the PMTs in SNO, as electronic pulses above a discriminator threshold (photoelectrons), will be determined by (i) the effective coverage of the photomultiplier sphere; (ii) the anode efficiency (quantum efficiency × first dynode collection efficiency × discriminator efficiency) of the R1408 PMTs; and (iii) the light transmission of the H_2O, D_2O and acrylic vessel.

At present, one can estimate these quantities from measurements of (i) the optical performance of concentrators (Chapter 6); (ii) the anode efficiency of R1408 PMTs [36]; and (iii) the attenuation lengths in high purity H_2O and D_2O [37] and U.V. transmitting acrylic [38] as a function of wavelength. Monte-Carlo simulations [39], [40], [41] and [42], which include these measurements but do *not* take into account the wavelength

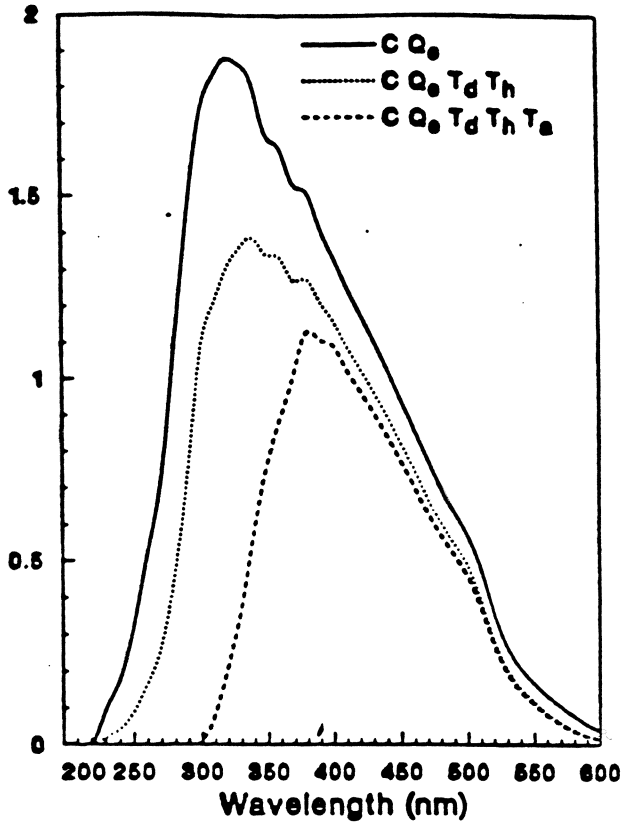

Figure 2.4: Effective wavelength spectrum for the detected Cherenkov light from events *inside* the acrylic vessel, where (C) is the $1/\lambda^2$ spectrum of Cherenkov radiation, (Q_e) is the measured quantum efficiency of an R1408 PMT (including attenuation in the glass envelope) and (T_d), (T_h) and (T_a) are the average transmissions of the D_2O, H_2O and acrylic vessel.

dependence of the reflectivity of the concentrators, indicate that for events in the D_2O one can expect about 8–10 photoelectrons per MeV. The effective wavelength spectrum of this detected light for D_2O events (without including the wavelength dependence of the reflectivity of the concentrators) is shown in Figure 2.4. The cut-off at short wavelengths (half-way point at 340 nm) is caused by attenuation in the acrylic vessel.

Events *outside* the acrylic vessel are expected to show an $\sim$ 30% increase in the number of photoelectrons per MeV, due to less absorption in the acrylic vessel. This estimate should decrease slightly when the wavelength dependence of the concentrators (which have reduced reflectivity below 340 nm) is included in the simulations. Both of these energy scales will eventually be calibrated with gammas of known energy and ^{90}Sr

Cherenkov sources, (see Section 2.5).

2.4 Event Simulation and Reconstruction

The energy, position and initial direction of 5–15 MeV electrons will be deduced from the number of photoelectrons, N_{pe}, and their hit pattern in space and time at the PMTs. Monte-Carlo simulations [40], [41] and [42], using EGS4 [43] to track electrons and photons in the 200 KeV–20 MeV energy range, show that the energy resolution one can expect for events inside the D_2O is $\pm 110\%/\sqrt{N_{pe}}$ (the extra 10% is caused by delta-ray production along the electron track). This has been verified by measuring the energy resolution of 2–10 MeV monoenergetic electrons injected from a Linac into a small test detector filled with water [44]. The linearity of N_{pe} with electron energy was also confirmed in this experiment.

The vertex position of an event will be reconstructed from the distribution in space and time of the PMTs hit. The accuracy of this reconstruction will be limited by (i) the inherent timing jitter (3 ns FWHM) of the R1408 PMTs, (ii) the few PMT noise hits which will occur during an event and (iii) the fact that up to 20% of the detected light will be Rayleigh scattered in the water. Using the simplest possible algorithm in the Monte-Carlo simulations one obtains a 30 cm (1 sigma) vertex reconstruction accuracy. This accuracy improves with increasing N_{pe} but the dependence is complicated by the systematic effects of noise hits and Rayleigh scattering.

The initial direction of the electron will be deduced from the vector sum of N_{pe} unit vectors from the reconstructed vertex to each of the PMTs hit. The inherent error in this procedure is dominated by the multiple scattering of the electron along its track which smears the Cherenkov cone. For a 7 MeV electron the direction reconstruction accuracy should be about 25°, and this should improve slightly with energy.

Gammas in the detector produce showers of relativistic electrons and positrons through Compton scattering and pair production. The Cherenkov yield for these γ's is less than the yield for an electron of the same energy because each charged particle

in the shower ceases to radiate as it drops below Cherenkov threshold ($\beta = 1/n$, $\sim$ 250 KeV for electrons in water). Monte-Carlo simulations with EGS4 show that 6 MeV γ's produce 18% less photoelectrons and have a 30% worse energy resolution than 6 MeV electrons.

The neutron transport in SNO has been calculated [45] using a Monte-Carlo code, a discrete ordinate code and one-group diffusion theory. The results of all three calculations are in agreement. In 99.85% enriched D_2O one can expect that 24% of the neutrons from the NC reaction will be captured on deuterium releasing 6.25 MeV gammas and 22% will be captured on hydrogen releasing 2.2 MeV gammas. The rest will leak out into the H_2O where they will be captured on hydrogen. If 2.5 tonnes of NaCl are added to the D_2O then 84% of the NC neutrons will be captured releasing up to 8.5 MeV in gammas. The mean distance traveled by a thermal neutron in 99.85% D_2O is about 300 cm and with 2.5 t of NaCl it is about 70 cm. In H_2O thermal neutrons travel 7 cm, on average, before capture.

2.5 Calibration

Ideally one would introduce a collimated beam of monoenergetic electrons into the detector and measure, as a function of position, direction and electron energy, the average number of photoelectrons per electron (energy scale), the width of this distribution (energy resolution) and the the accuracy of the vertex and initial direction reconstructions. Unfortunately, no practical method of introducing such a beam has been found.

Instead, gamma sources from (n, γ) reactions will be introduced into the D_2O and H_2O to calibrate the absolute energy scales for γ's at several energies. Gammas from ^{37}Cl (8.6 MeV), ^{2}H (6.25 MeV) and ^{3}He (22 MeV) are presently anticipated [46]. Since the gamma showering processes are well understood, this calibration can be used to infer, by Monte-Carlo, the absolute energy scale for single electrons. The gamma sources could also be collimated to provide a check on the *direction* reconstruction accuracy of gamma events. This reconstruction accuracy is closely related to that of electron events

and the relation between the two can be inferred by Monte-Carlo. Similarly, the *vertex* reconstruction accuracy for gamma events can be (roughly) checked by comparing the measured spatial distribution of gamma events around a gamma source to the simulated spatial distribution from the known gamma attenuation lengths and the expected vertex reconstruction accuracy.

Many other small light sources are being developed. A light diffusing sphere will be used for the day to day relative calibration of the PMTs. A ^{90}Sr beta-decay Cherenkov source is being developed for checking the absolute calibration efficiency of the PMTs (anode efficiency). The light output of this source can be calculated to within $\pm 5\%$ [47] and it has the correct $(1/\lambda^2)$ wavelength spectrum. Its small size ($\simeq$ 5 cm diameter) makes it ideal for measuring the energy scale of the detector as a function of *position*. However, the energy of the decay (end point 2.3 MeV), is too low to reconstruct individual events so that this source cannot be used to check any of the reconstruction parameters. A small ^{241}Am/scintillator source with enough light output to simulate 7–10 MeV electron events is being considered for checking the vertex reconstruction accuracy. However the wavelength spectrum and angular distribution (isotropic) of this source are not ideal for simulating the Cherenkov radiation from electron events.

The calibration of the absolute energy scale in the H_2O is much more difficult as this energy scale will depend strongly on the initial direction of the electrons (and gammas). Electrons pointing towards the center of the detector will produce up to four times less photoelectrons than electrons pointing away from the center. This distortion is mostly due to the difference between double attenuation in the acrylic vessel and no attenuation in the acrylic vessel.

The rate of stopped muon decays in SNO ($<$ 1/day) will be too small to use the Michel spectrum for calibration, as is possible in Kamiokande-II. Moreover, too few beta-emitting spallation nuclei will be produced to use their beta-decay spectra for calibration.

The neutron transport code can be calibrated by introducing calibrated neutron sources into the centre of the D_2O. The efficiency of neutron capture and the mean free path, in 99.85% D_2O, can be checked by measuring the yield and radial distribution of

6.25 MeV gammas. Similarly, the improved capture efficiency and reduced mean free path, when 2.5 t of NaCl are added, can be measured from the radial distribution of (up to) 8.5 MeV gammas. At the same time, the mean number of photoelectrons and the energy resolution of these two gamma signals can be measured.

2.6 Backgrounds

The angular distributions of the CC and NC reactions do not allow the subtraction of a dominant flat background as is possible for the ES reaction, (c.f. Kamiokande-II). Therefore, the event rates from these reactions must be well above background. This implies a background of less than a few events per day in the D_2O, above a threshold of about 5 MeV. The required background levels for the 1 m shell of H_2O are much less stringent because of the distinctive signature of the ES reaction.

Muon induced background will be much less of a trouble in SNO than in Kamiokande. Only about 24 muons per day will penetrate the photomultiplier sphere and on average about 1.5 of these will produce beta-emitting spallation nuclei. These beta-decays will be easily identified from the preceeding muon track.

High energy gammas (up to 10 MeV) are produced in $(\alpha, p\gamma)$ and (α, n) followed by (n, γ) reactions in the rock surrounding the cavity. The α's which initiate these reactions come from the decays of naturally occurring radionuclides: ^{232}Th, ^{235}U, ^{238}U and their daughters. The flux of these high energy gammas (> 5 MeV) has been measured in three separate locations in the half-excavated cavity. After attenuation in the H_2O shielding, it is expected that less than 4/day will penetrate into the fiducial volume and less than 0.2/day will reach the D_2O.

The PMTs, concentrators and their support structure will also be a source of high energy gammas from $(\alpha, p\gamma)$ and (n, γ) reactions. Although this source will be much closer to the fiducial volume its contamination level of radionuclides and mass will be much smaller. It is estimated that a similar flux of gammas will reach the D_2O and fiducial volume from this source as from the walls of the cavity. The total flux of high

energy gammas from both of these sources will be measured during a light water fill of the vessel (see Figure 2.5).

The dominant background for the CC reaction will come from low energy coincident β-γ decays in the ^{238}U and ^{232}Th chains. In the ^{238}U chain, ^{214}Bi decays to ^{214}Po by β-γ (or β only) releasing 3.26 MeV of kinetic energy; and in the ^{232}Th chain, ^{208}Tl decays to ^{208}Pb by β-γ releasing 5 MeV. Although the 'effective' energies of these decays are below 5 MeV, the tail of their energy distributions might go beyond 5 MeV because of the rather poor energy resolution of the detector, or, by two or more of these events occurring in coincidence. The β-γ background has been classified into two categories: (i) the 'internal' β-γ background from ^{208}Tl and ^{214}Bi decays in the D_2O, acrylic and H_2O; and (ii) the 'external' β-γ background from ^{208}Tl and ^{214}Bi decays in the PMTs, concentrators and their support structure which are reconstructed as events occurring in the D_2O (a few of these occur in coincidence with ^{208}Tl or ^{214}Bi decays elsewhere in the detector but most are singles).

Both of these categories of β-γ background have been simulated for the expected concentration levels of ^{238}U and ^{232}Th in the various detector components. The results are shown in Figure 2.5 together with the expected electron recoil spectrum from the ES reaction. This figure corresponds to one year's data with H_2O in the acrylic vessel. Notice that above a threshold of 6 MeV the ES signal itself should be above background and should be easily identified by its strong directional signature. The expected energy distribution of one year's data with D_2O and *no* salt in the acrylic vessel is shown in Figure 2.6. The CC signal should be clear from background above a threshold of about 5 MeV.

The NC reaction has two types of background: (i) the CC and ES reactions and the β-γ and high energy γ backgrounds; and (ii) photodisintegration of the deuteron

$$\gamma + d \rightarrow p + n, \qquad Q = -2.2\,\mathrm{MeV} \tag{2.7}$$

which produces free neutrons that will be indistinguishable from the free neutrons produced by the NC reaction.

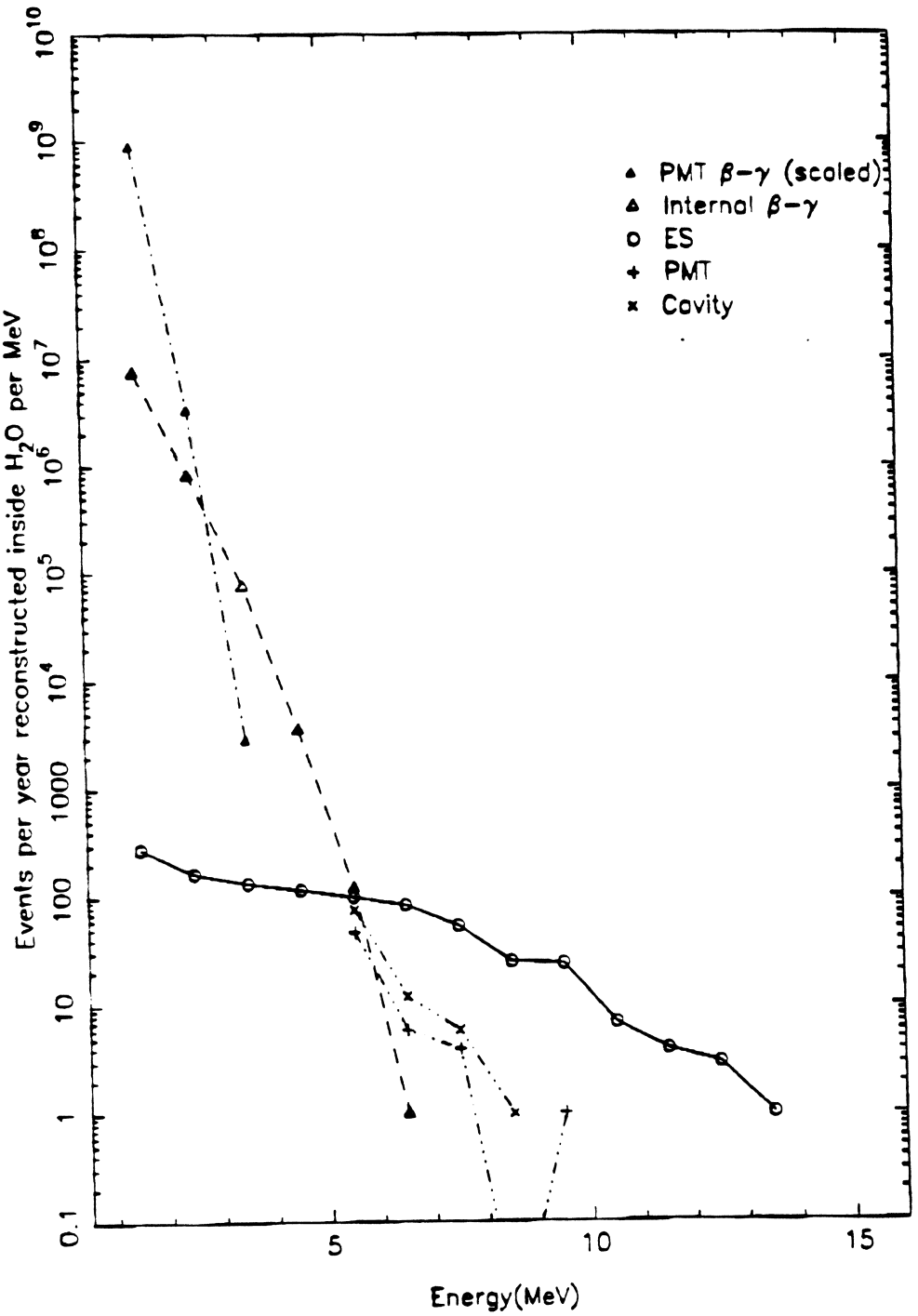

Figure 2.5: Energy distribution of one year's data with H_2O in the acrylic vessel. PMT β-γ = external β-γ background; ES = electron scattering signal; PMT = high energy (> 5 MeV) γ background from the PMTs, concentrators and their support structure; Cavity = high energy (> 5 MeV) γ background from the surrounding rock.

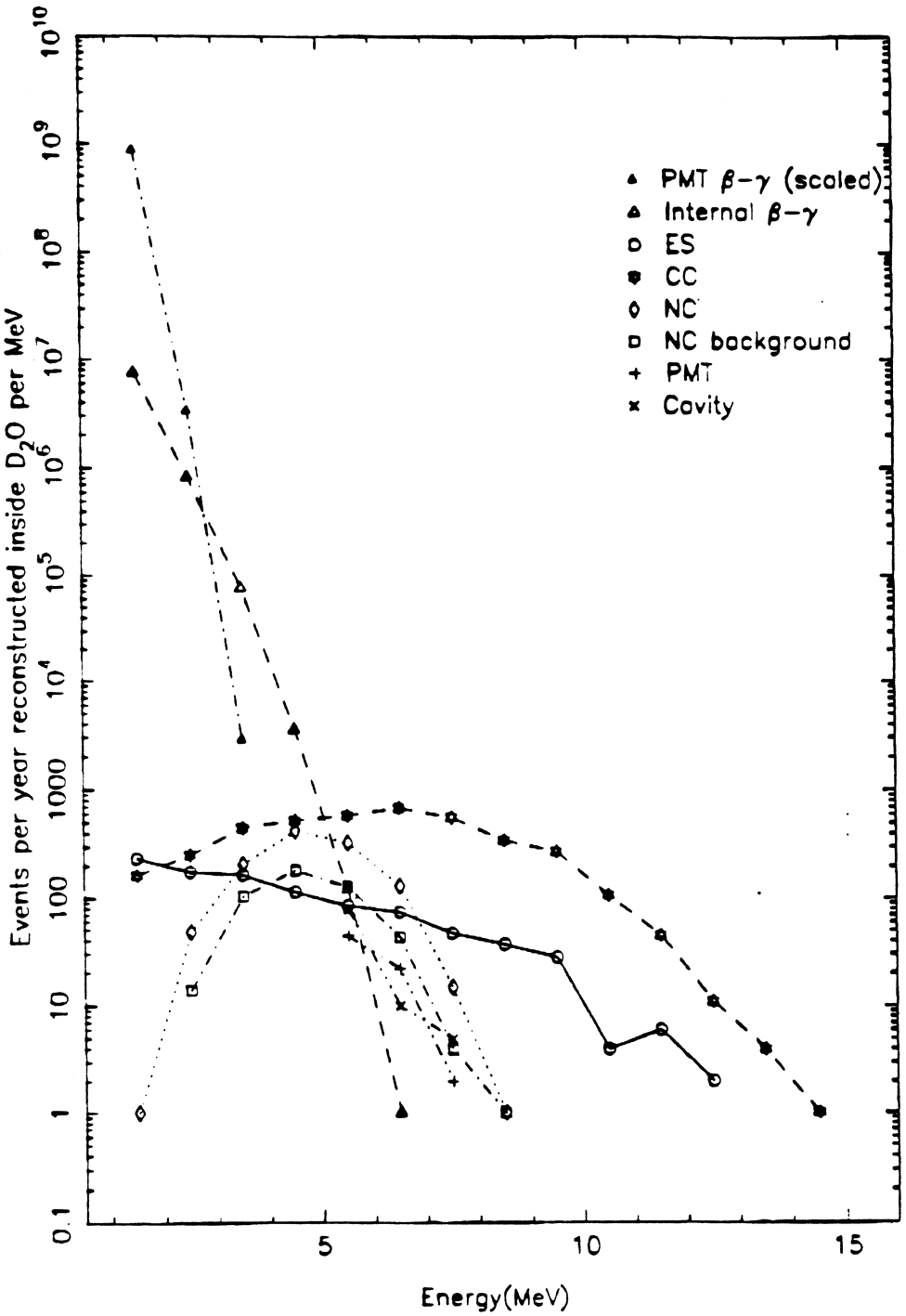

Figure 2.6: Energy distribution of one year's data with D_2O and *no salt* in the acrylic vessel. PMT β-γ = external β-γ background; ES = electron scattering signal; CC = charge current signal; NC = neutral current signal; NC background = photodisintegration background; PMT = high energy (> 5 MeV) γ background from the PMTs, concentrators and their support structure; Cavity = high energy (> 5 MeV) γ background from the surrounding rock.

The first category of background can be measured *directly* by taking D_2O data for a year *without* adding salt, when the NC signal will be substantially suppressed (Figure 2.6). When 2.5 tons of NaCl are added to the heavy water the NC signal (+ photodisintegration background) will be enhanced by a factor of about 6 (Figure 2.7). Hence it should be possible to deduce the NC signal (+ photodisintegration background) in salt by subtracting the CC and ES signals (above 5 MeV) that have been measured in the previous year without salt. The validity of this subtraction can be checked from the different angular distributions of these three signals.

The photodisintegration background will be more difficult to assess. There are two naturally occurring γ's, with significant rates, which have sufficient energy (> 2.23 MeV) to disintegrate the deuteron: (i) the 2.615 MeV γ in the decay of ^{208}Tl to ^{208}Pb which occurs at the bottom of the ^{232}Th chain; and (ii) the 2.445 MeV γ in the decay of ^{214}Bi to ^{214}Po at the bottom of the ^{238}U chain. Assuming equilibrium in both these chains, a concentration of 3.7×10^{-15} g/g of ^{232}Th and 4.5×10^{-14} g/g of ^{238}U in the D_2O corresponds to one free neutron per chain per kt per day. This is to be compared with a NC production rate of 3.4 neutrons per kt per day assuming a ^{8}B $\nu_{e,\mu,\tau}$ flux of 2.7×10^6 $cm^{-2}s^{-1}$. A water purification system has been developed to attain these extremely low levels of concentration. At present the system is being refined and tested.

The two γ's which cause the photodisintegration background come from the same radioactive decays that produce the β-γ background. It may be possible to determine the rate of these decays in the D_2O by monitoring the β-γ background at low energies (3–5 MeV). This would enable a direct measurement of the photodisintegration background since the branching ratios of the troublesome γ's and the ratios of the photodisintegration cross-sections to the Compton scattering cross-sections are all well known. However, at the low energies necessary to monitor these decays there are other backgrounds, e.g. external backgrounds, which will complicate the task enormously. Furthermore, other systematic effects may make it impossible to interpret these low energy measurements reliably.

Another possibility for monitoring the ^{232}Th and ^{238}U chains is to analyse samples

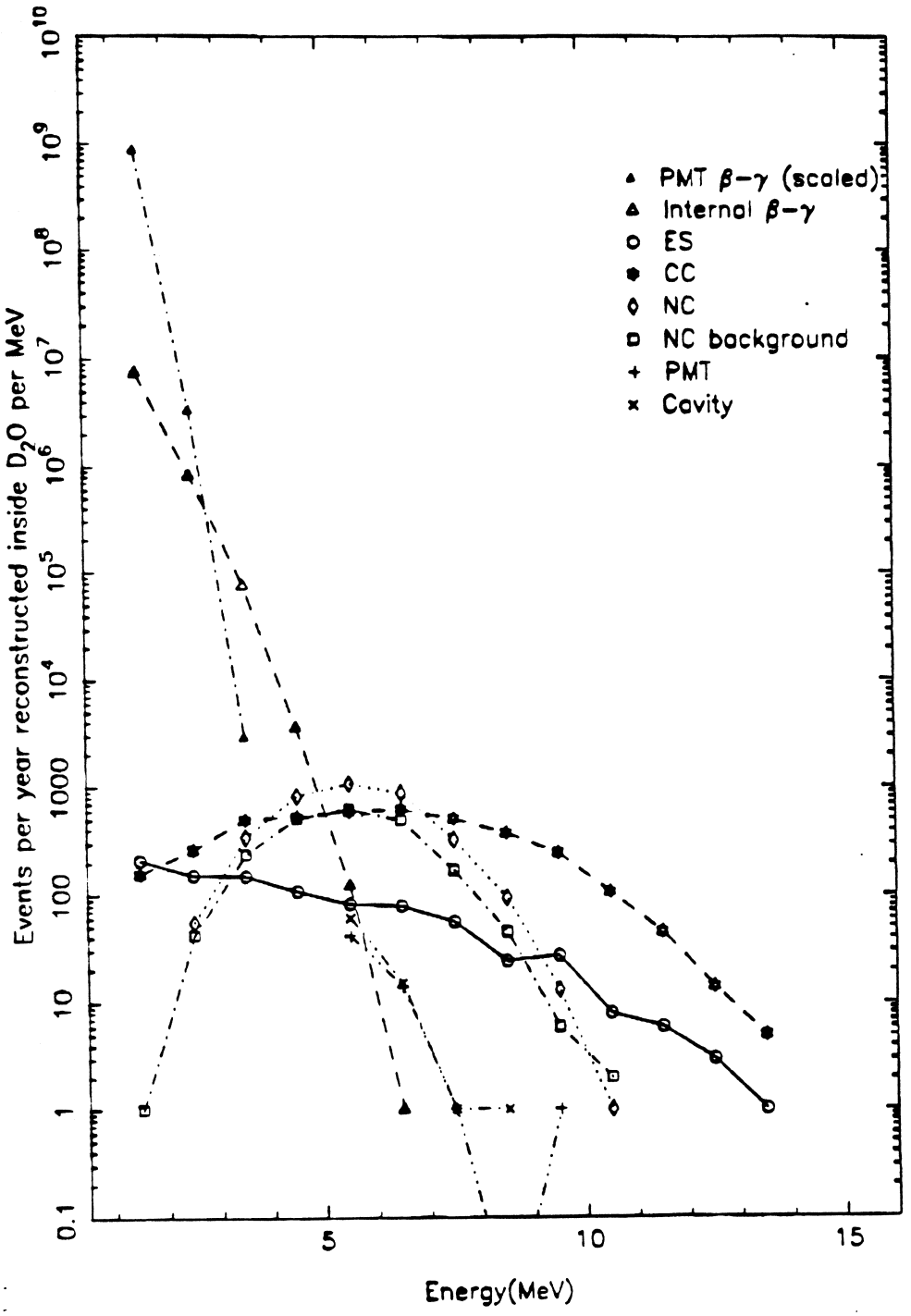

Figure 2.7: Energy distribution of one year's data with D_2O + 2.5 t of NaCl in the acrylic vessel. PMT β-γ = external β-γ background; ES = electron scattering signal; CC = charge current signal; NC = neutral current signal; NC background = photodisintegration background; PMT = high energy (> 5 MeV) γ background from the PMTs, concentrators and their support structure; Cavity = high energy (> 5 MeV) γ background from the surrounding rock.

of D_2O by mass spectroscopy. The concentration levels of ^{232}Th and ^{238}U are just beyond the limits of this technology but recent improvements may render this technique feasible. Even then, there is a caveat in that there may be disequilibrium in the chains (with various other long lived isotopes along both chains) and the measurement of the concentration levels of the parent nuclei does not unambiguously determine the activity levels at the bottom of the chains.

The SNO collaboration has developed two methods [48], one for monitoring the activity level at the bottom of the ^{232}Th chain, and the other for monitoring the ^{238}U chain. In both these methods, the *daughter* of the *last long-lived* isotope of the chain will be extracted from a sample volume of the D_2O and concentrated into a counter which will measure directly the activity at the bottom of the chain. From this measured activity, the photodisintegration background neutron rate can be deduced, provided that the chemical extraction and counting efficiencies are known. These efficiencies can be measured in separate tests with samples of 'spiked' water. These methods can be used to monitor the ^{232}Th and ^{238}U chains in both the H_2O and the D_2O. They could also be used to track down any possible changes in the internal β-γ background, e.g. after a change of water.

The only other possible source of photodisintegrating gammas is the acrylic vessel (the PMTs, concentrators, etc. are too far away). This source is not so significant because of its reduced mass and because only about 25% of the neutrons which are produced by external γ's are captured in the D_2O (with 2.5 t of NaCl). These neutrons are produced so close ($\sim$ 20 cm) to the edge of the D_2O that they tend to leak out (m.f.p. $\simeq$ 70 cm) into the H_2O where they are very quickly captured (m.f.p. $\simeq$ 7 cm). Moreover, about 75% of the neutrons which are captured in the D_2O will be captured in the outer 0.5 m shell of D_2O where only 25% of the NC neutrons are captured. Hence the photodisintegration background from the acrylic vessel can be further reduced by making a fiducial cut inside the D_2O. The expected concentration levels of ^{232}Th and ^{238}U in the acrylic vessel are 1.9×10^{-12} g/g and 3.6×10^{-12} g/g which would produce 2 captured neutrons per day in the whole D_2O.

2.7 Role of Concentrators

The concentrators are low cost devices for maximizing the light collection from the fiducial volume and at the same time decreasing the light collection from external background sources such as the PMT β-γ's. The number of photoelectrons from events inside the fiducial volume will be increased (relative to an identical detector without concentrators) by a factor of at least 1.6. This will improve the energy resolution by a factor $\sqrt{1.6} = 1.27$ and the statistical contribution to the vertex reconstruction accuracy by a similar factor. The improvement in energy resolution and the reduction in light collection from events outside the fiducial volume have a strong effect on the high energy tail of the β-γ background. This background will be suppressed by a factor of about 10 pushing it across to lower energies by about 1 MeV. Thus the expected β-γ threshold is $\sim$ 5 MeV with concentrators (Figure 2.7) whereas it would be $\sim$ 6 MeV without concentrators. Having a low threshold is important for extracting the NC γ signal which looks like a 6 MeV electron signal (when salt is added) with a broad energy distribution.

It is also important that the concentrators collect light *uniformly* from the fiducial volume. Otherwise, they will cause distortions in the energy calibration as a function of position and direction in the detector. However, there is already a 30% discontinuity in the energy calibration across the acrylic vessel. Outside the acrylic vessel the energy calibration is a strong function of direction and does depend on position, but *inside* the vessel it is a reasonably flat function of position and direction. Therefore it is essential that inside the vessel, where the vast majority of neutrino events will occur, the concentrators do not significantly distort the flat energy calibration. Keeping this function as flat as possible will greatly simplify the data analysis in the future. Outside the vessel, where fewer neutrino events will occur and some distortions are already present, it is not quite as imperative to avoid any distortions in the energy calibration.

Chapter 3

Optical Principles of Light Concentration

3.1 The Liouville Theorem: Conservation of Phase Space

For a detector of given fiducial volume subtending a cone of half angle θ_i at a photomultiplier (see Figure 3.1) the concentration which can be achieved optically is limited by the Liouville theorem of statistical mechanics, viz., the phase space density of particles (photons) cannot be increased without doing work on the system, but can be decreased of course by absorption or scattering.

The phase space acceptance of any photomultiplier $\Psi_{\rm cath}$ is defined by the double integral

$$\Psi_{\rm cath} = \int\int_0^{\pi/2} \pi\, n_2^2\, E_{\rm cath}(\theta_2,\, \mathbf{r}_{\rm cath})\, \sin(2\theta_2)\, d\theta_2\, dA_{\rm cath} \qquad (3.1)$$

where θ_2 is the angle of incidence at an area element $dA_{\rm cath}$ of the photocathode, n_2 is the refractive index of the medium (usually glass) directly in front of the photocathode and $E_{\rm cath}(\theta_2,\, \mathbf{r}_{\rm cath})$ is the efficiency of the photocathode as a function of angle of incidence and point of incidence at the photocathode (see Figure 3.2). In practice $E_{\rm cath}(\theta_2,\, \mathbf{r}_{\rm cath})$ is more or less constant over the useful surface area of the photocathode $A_{\rm cath}$ and for all angles of incidence within some maximum angle $\theta_{\rm max} \simeq \pi/2$ where it cuts-off relatively sharply to zero. Hence the double integral reduces to $\Psi_{\rm cath} = \pi\, n_2^2\, E_{\rm cath}\, A_{\rm cath}\, \sin^2\theta_{\rm max}$.

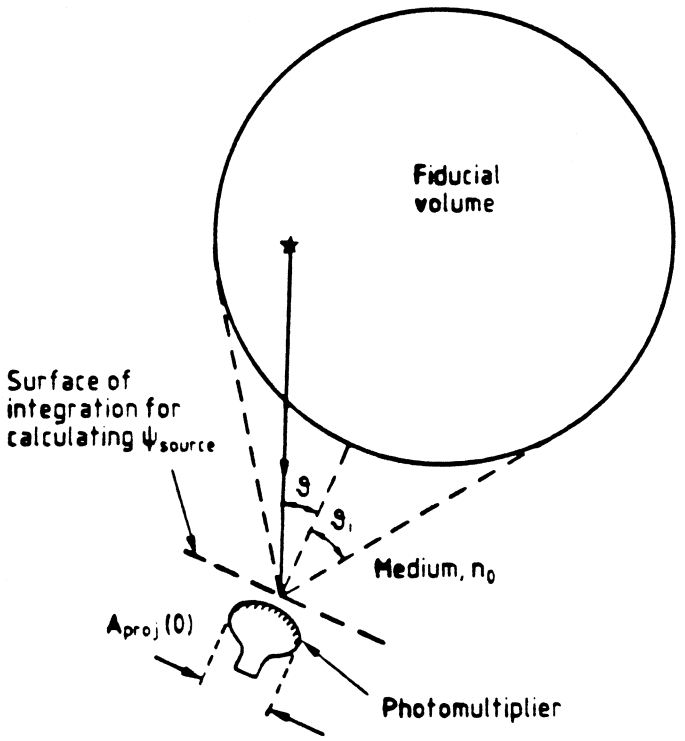

Figure 3.1: Geometry of detector fiducial volume and photomultiplier.

However in the configuration of Figure 3.1 only a fraction of this available phase space acceptance is actually being used. The source occupies a phase space volume Ψ_{source} given by the double integral

$$\Psi_{source} = \int\int_0^{\theta_1} \pi\, n_0^2\, E_{cath}(\theta_2, \mathbf{r}_{cath}) \sin 2\theta \, d\theta \, dA_{surf} \tag{3.2}$$

where θ is the (polar) angle of incidence at an element dA_{surf} of a *flat* surface directly in front of the photomultiplier and n_0 is the refractive index of the medium in which the photomultiplier is immersed (see Figure 3.1). In this equation the angle of incidence and point of incidence at the photocathode, θ_2 and $\mathbf{r}_{cath}$, are functions of the angle of incidence and point of incidence at the flat surface, θ and $\mathbf{r}_{surf}$. It is implicitly assumed that the photomultiplier is cylindrically symmetric, so that the integration over ϕ reduces to 2π. Assuming that the dimensions of the photomultiplier are small in comparison with the distance separating it from the fiducial volume, the integration over area can

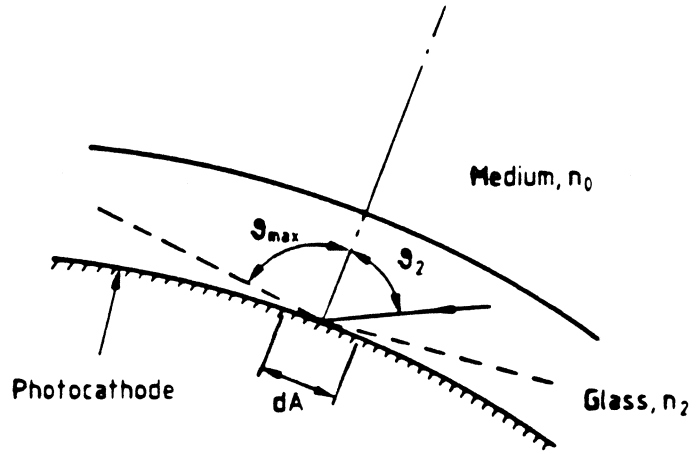

Figure 3.2: Phase space acceptance of an area element dA of the photocathode.

be performed *first*, leaving the following integral over angle

$$\Psi_{source} = \int_0^{\theta_i} \pi\, n_0^2\, E_{cath}\, A_{proj}(\theta)\, \sin 2\theta\, d\theta \tag{3.3}$$

where $A_{proj}(\theta)$ is the useful area of the photocathode *projected* onto the surface of integration at a given angle θ. In most cases, where the photocathode is not excessively curved and θ_i is not too great, $A_{proj}(\theta)$ is constant or very nearly so in the range $0 \rightarrow \theta_i$ so that Ψ_{source} is approximately $\pi\, n_0^2\, E_{cath}\, A_{proj}(0)\, \sin^2\theta_i$. Hence the fraction of the photocathode's available phase space acceptance which is actually being used is given by the ratio

$$\frac{\Psi_{source}}{\Psi_{cath}} \simeq \frac{n_0^2\, A_{proj}(0)\, \sin^2\theta_i}{n_2^2\, A_{cath}\, \sin^2\theta_{max}} \tag{3.4}$$

which can be quite small.

In principle at least, an optical system can be arranged to modify the phase space filled by the source and allow the use of the full phase space acceptance of the photocathode. Such a 'Liouville-exact' concentrator is schematically represented in Figure 3.3. All light incident at the entrance aperture at less than θ_i is transmitted to the photocathode at an angle of incidence $\theta_2 \leq \theta_{max}$. Conversely all light incident at the entrance aperture at greater than θ_i is not transmitted to the photocathode at an angle of incidence less than θ_{max} and is hence rejected by the concentrator/photocathode system — the concentrator is said to have an 'ideal' transmission-angle characteristic (see Figure 3.4).

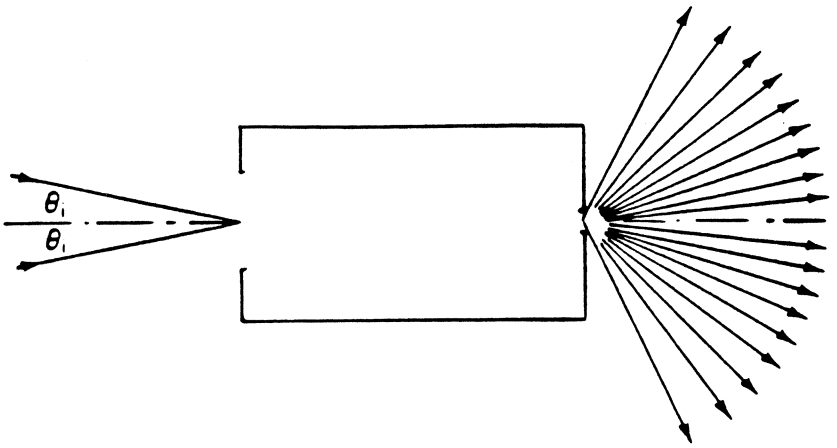

Figure 3.3: Schematic representation of a Liouville-exact concentrator which transmits to the photocathode (at less than θ_{max}) all rays incident at the entrance aperture at angles $< \theta_i$ and none incident at $> \theta_i$ [49]. The ratio of the entrance aperture area A_{conc} to the photocathode area A_{cath} is given by (3.5) and hence a source of half angle θ_i occupies the full phase space acceptance of the photocathode.

Furthermore the ratio of the entrance aperture area A_{conc} of this Liouville-exact concentrator to the area of the photocathode A_{cath} is given by

$$\frac{A_{conc}}{A_{cath}} = \frac{n_2^2 \sin^2 \theta_{max}}{n_0^2 \sin^2 \theta_i} \tag{3.5}$$

so that the phase space acceptance of the concentrator Ψ_{conc} is equal to that of the photocathode. This can be proved by evaluating the double integral

$$\Psi_{conc} = \int\int_0^{\pi/2} \pi\, n_0^2\, T(\theta, r_{conc})\, E_{cath} \sin 2\theta \, d\theta \, dA_{conc} \tag{3.6}$$

where θ is the (polar) angle of incidence at an area element dA_{conc} of the concentrator entrance aperture and where $T(\theta, r_{conc})$ is the probability of transmission to the photocathode (at less than θ_{max}) as a function of both angle of incidence and point of incidence at the entrance aperture of the concentrator (it is implicitly assumed that the concentrator is cylindrically symmetric so that the integration over ϕ reduces to 2π). Since the concentrator has the ideal transmission-angle characteristic, i.e. $T(\theta, r_{conc})$ is 1 for all r_{conc} and $\theta < \theta_i$ and 0 for all r_{conc} and $\theta > \theta_i$, Ψ_{conc} reduces simply to $\pi\, n_0^2\, E_{cath}\, A_{conc} \sin^2 \theta_i$ which is only equal to Ψ_{cath} if (3.5) holds true. Hence (3.5) represents the *maximum concentration ratio* allowed by the Liouville theorem.

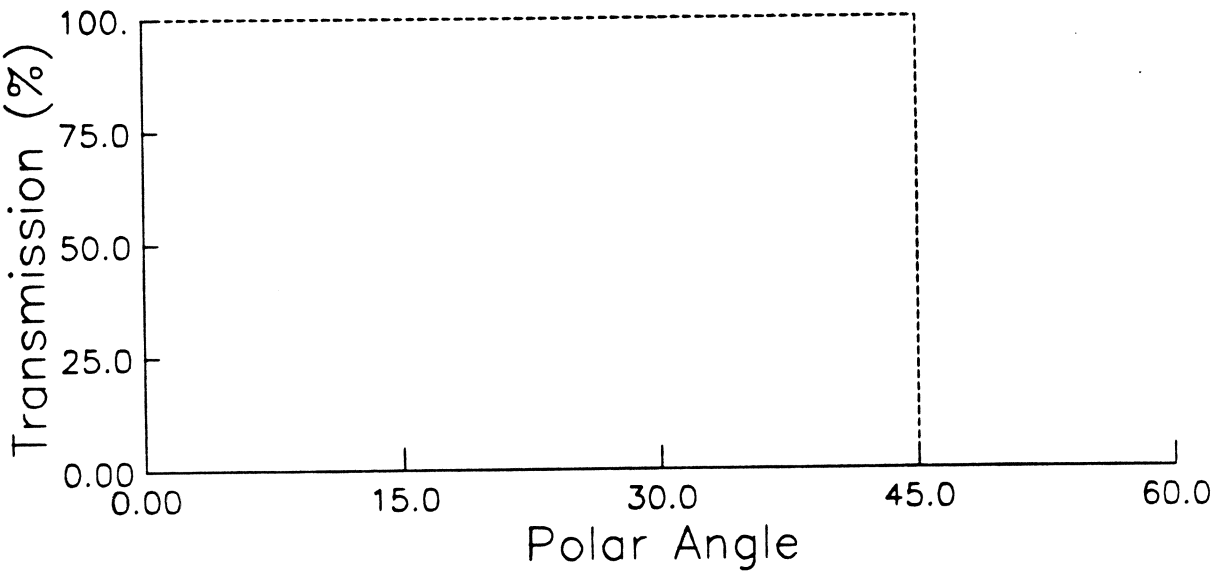

Figure 3.4: Ideal transmission-angle curve of a concentrator with a limiting angle $\theta_i = 45°$. The probability of transmission to the photocathode (at an angle of incidence $\theta_2 < \theta_{max}$), $T(\theta, \mathbf{r}_{conc})$, is averaged over the entrance aperture of the concentrator.

Let us define the concentration *factor* $C(\theta)$ as the efficiency of the PMT *with* the concentrator E_{conc} as a function of polar angle θ and divided by the efficiency of the *bare* PMT E_{pmt} at polar angle $\theta = 0$. We write

$$C(\theta) = \frac{E_{conc}(\theta)}{E_{pmt}(0)\cos\theta} = \frac{\int T(\theta, \mathbf{r}_{conc})\, E_{cath}(\theta_2, \mathbf{r}_{cath})\, dA_{conc}}{\int E_{cath}(\theta_2, \mathbf{r}_{cath})\, dA_{surf}} \tag{3.7}$$

where the $\cos\theta$ term has been included to compensate for the reduction in effective area of the concentrator aperture as a function of polar angle (it varies as $\cos\theta$ since the aperture is flat). In this equation the angle of incidence and point of incidence at the photocathode (θ_2 and $\mathbf{r}_{cath}$) are, in the numerator, functions of the angle of incidence and point of incidence at the concentrator aperture (θ and $\mathbf{r}_{conc}$); and, in the denominator, functions of the angle of incidence and point of incidence at a flat surface directly in front of the photomultiplier ($\theta = 0$ and $\mathbf{r}_{surf}$, see Figure 3.1).

For a Liouville-exact concentrator (ideal transmission-angle characteristic and concentration ratio given by (3.5)) the concentration factor (3.7) reduces to

$$C(\theta \le \theta_i) = \frac{A_{conc}}{A_{proj}(0)} = \frac{n_2^2\, A_{cath} \sin^2\theta_{max}}{n_0^2\, A_{proj}(0) \sin^2\theta_i} \tag{3.8}$$

and $C(\theta > \theta_i) = 0$, after using (3.5) to substitute for A_{conc}. Thus (3.8) represents the *maximum concentration factor* allowed by the Liouville theorem. Notice that it is the *reciprocal* of the fraction of the photocathode's available phase space acceptance used in the geometry of Figure 3.1 *without* a concentrator, (3.4).

For flat photocathodes (where $A_{cath}/A_{proj} = 1$ and the concentration ratio (3.5) is equal to the concentration factor (3.8)) the optical system is realised to a good approximation by the reflecting 'Winston cone' which is universally used for the concentration of light from gas Cherenkov counters onto photomultipliers. The peculiar non-imaging optics necessary to approach the Liouville limit of concentration have been studied in detail and presented with great clarity by Welford and Winston [49]. The principles laid down by Welford and Winston and the two dimensional applications represent the starting point for the developments described in this thesis. Generally the practical three dimensional concentrators which approach the Liouville limit, e.g. the Winston cone, are figures of revolution of two dimensional Liouville-exact concentrators (assuming 'ideal' reflecting surfaces, i.e. 100% reflectivity). In fact there is a Liouville-exact three dimensional refracting solution, the Luneburg lens [50], but that requires a spatial variation of refractive index which is not easily achieved. Conventional lens systems with large f-numbers fail because of the gross and unfavourable aberrations [49].

3.2 The Compound Parabolic Concentrator or Winston Cone

The Liouville-exact two dimensional reflecting concentrator from which the Winston cone is generated is an off-axis parabola called the compound parabolic concentrator ('CPC'). All the rays which are incident at the concentrator entrance aperture at the limiting angle θ_i are focussed by the parabola onto the edge of the plane photocathode (see Figure 3.5). This construction by the so-called 'edge-ray principle' ensures that all rays incident at the concentrator aperture at $\leq \theta_i$ necessarily reach the photocathode whilst those at $> \theta_i$ cannot find their way to the photocathode and are hence rejected

(see Figure 3.6). Thus the ideal transmission-angle characteristic is obtained.

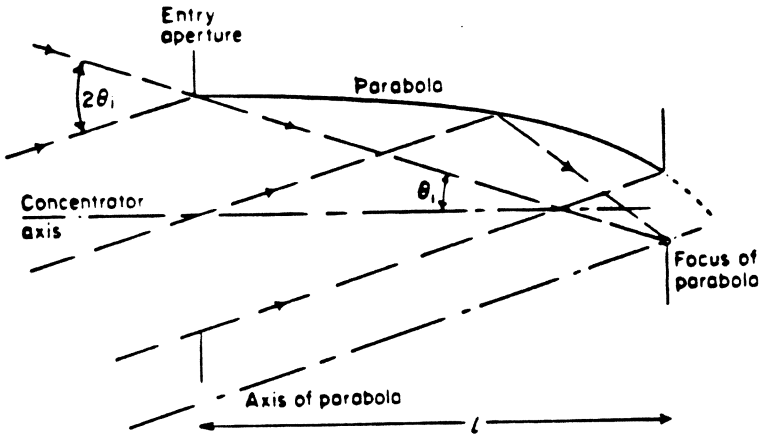

Figure 3.5: Construction of a 2D CPC profile from the edge-ray principle [49].

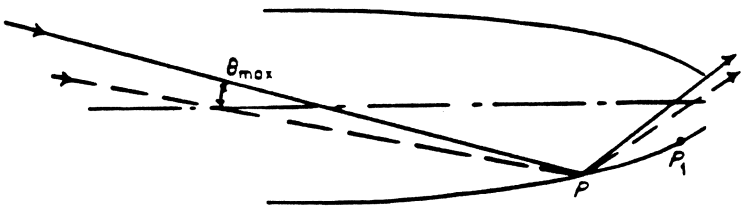

Figure 3.6: To prove that a 2D CPC has an ideal transmission-angle curve [49].

The concentration ratio of this 2D CPC, i.e. the ratio of half its entrance aperture length, l_{conc}, to half the length of the photocathode, l_{cath} (see Figure 3.5) can be shown to be

$$\frac{l_{conc}}{l_{cath}} = \frac{1}{\sin\theta_i} \tag{3.9}$$

which is the maximum concentration ratio allowed (in 2D) by the Liouville theorem assuming that the index of refraction is constant throughout the optical system and that the photocathode is uniformly efficient at all angles of incidence, i.e. $\theta_{max} = \pi/2$.

The celebrated Winston cone is the figure of revolution of the 2D CPC. It also has the maximum concentration ratio allowed (in 3D) by the Liouville theorem:

$$\frac{A_{conc}}{A_{cath}} = \frac{1}{\sin^2\theta_i} \tag{3.10}$$

But its transmission-angle curve (averaged over the entrance aperture) is not quite ideal. Instead of cutting off perfectly at θ_i the transmission cuts-off more gently over a small

range of angles centered about θ_i (see Figure 3.7). The steepness of the cut-off can be quantified by the change in angle ($\Delta\theta$) in going from 90% to 10% transmission. Approximate values of $\Delta\theta$ for several 3D CPCs are [49]

θ_i	2°	10°	16°	20°	40°	60°
$\Delta\theta$	0.4°	1.5°	2°	2.5°	2.7°	2.0°

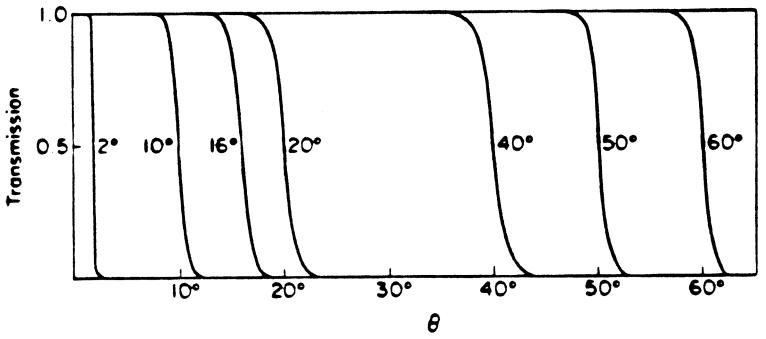

Figure 3.7: Transmission-angle curves for 3D CPCs with θ_i from 2° to 60° [49].

For a photocathode which detects light uniformly up to a maximum angle of incidence $\theta_{max} < \pi/2$ the edge-ray construction has to be modified. This refinement of the 2D CPC in which all rays incident at the entrance aperture at angles $< \theta_i$ are constrained to intersect the photocathode at angles no greater than θ_{max} is described in Chapter 5 of [49]. With this construction the ideal transmission-angle characteristic is still achieved and the 2D concentration ratio is now given by

$$\frac{l_{conc}}{l_{cath}} = \frac{\sin\theta_{max}}{\sin\theta_i} \tag{3.11}$$

which is the maximum ratio allowed by the Liouville theorem for a photocathode efficient out to an angle θ_{max}.

Another interesting development of the CPC is the dielectric-filled CPC presented in Chapter 5 of [49]. This CPC (see Figure 3.8) relies on total internal reflection which operates for all rays in the acceptance cone provided that $\sin\theta_i' \leq 1-(2n_0^2/n_1^2)$ or $\sin\theta_i \leq n_1/n_0 - (2n_0/n_1)$ where θ_i is the limiting angle outside the dielectric, θ_i' is the limiting angle inside the dielectric, n_1 is the refractive index of the dielectric and n_0 is the refractive index of the medium directly in front of the dielectric. The 3D concentration

ratio of this concentrator is given by

$$\frac{A_{\text{conc}}}{A_{\text{cath}}} = \frac{\sin^2\theta_{\max}}{\sin^2\theta_i'} = \frac{n_1^2\sin^2\theta_{\max}}{n_0^2\sin^2\theta_i} \tag{3.12}$$

where $\theta_{\max}$ is the maximum angle of incidence (at the photomultiplier window) at which the photocathode effectively detects light when the photomultiplier window is placed in contact with a medium of refractive index n_1.

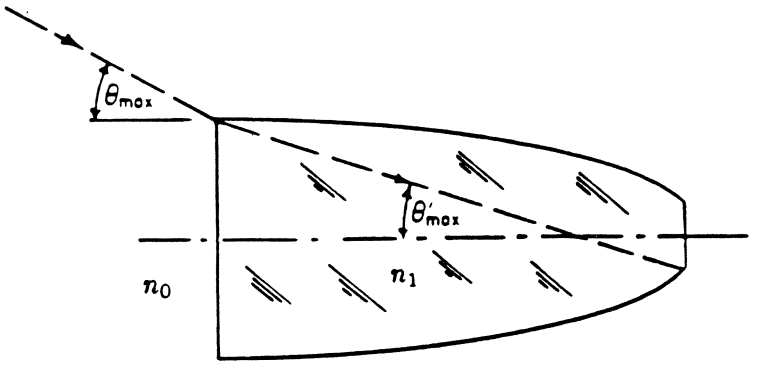

Figure 3.8: A dielectric-filled CPC. The figure is drawn with $\theta_i' = 18°$ and $n_1/n_0 = 1.5$ so that $\theta_i = 27.6°$ and the 3D concentration ratio is 10.5 (assuming $\theta_{\max} = \pi/2$) [49].

3.3 The CPC Design for Off-Axis Rays

So far the 3D CPC has always been generated from the profile of a Liouville-exact 2D CPC. Appendix F of [49] describes a method for constructing the 2D profile of a 3D CPC which has an ideal transmission-angle characteristic for a particular set of off-axis rays of given skewness h. The skewness of a ray is proportional to its axial component of angular momentum and is given by

$$h = n(\mathbf{r}\times\hat{\mathbf{t}}).\hat{\mathbf{z}} \tag{3.13}$$

where $\mathbf{r}$ is the vector from the origin to a point R along the path of the ray; n and $\hat{\mathbf{t}}$ are the refractive index and the unit vector in the direction of propagation of the ray at the point R and $\hat{\mathbf{z}}$ is the unit vector in the z-direction (the axis of symmetry). It can be shown that for any optical system of cylindrical symmetry (about $\hat{\mathbf{z}}$) the skewness of a ray is an *invariant* with respect to either reflection or refraction throughout the whole optical system (c.f. conservation of the z-component of angular momentum).

The first order nonlinear differential equation which is developed in Appendix F of [49] for constructing the profiles of these 3D CPCs for non-zero skewness is restricted to flat photocathodes and is based on the edge-ray principle, viz., that all rays of skewness h incident at the concentrator aperture at the limiting angle θ_i are reflected onto the edge of the photocathode (see Figure 3.9). It can be shown that these 'skew' CPCs have the maximum concentration ratio allowed by Liouville (3.8) and the ideal transmission-angle characteristic for the particular set of rays of given skewness h. However, just as in the case of the Winston cone which is optimised for the meridional rays ($h = 0$), the 3D transmission-angle curves (averaged over the entrance aperture) of these skew CPCs are not quite ideal. In fact the greater the value of h for which the concentrator has been optimized, the worse is its 3D transmission cut-off. Some 3D transmission-angle curves for skew CPCs are shown in Figure 3.10.

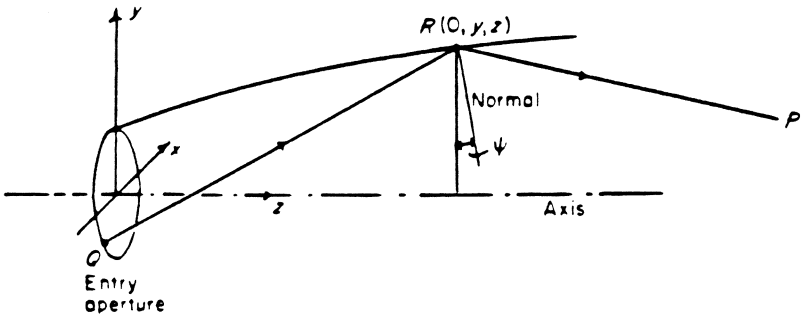

Figure 3.9: Constructing the 2D profile of a skew CPC by reflecting the rays of skewness h and polar angle θ_i onto the edge of the photocathode. [49].

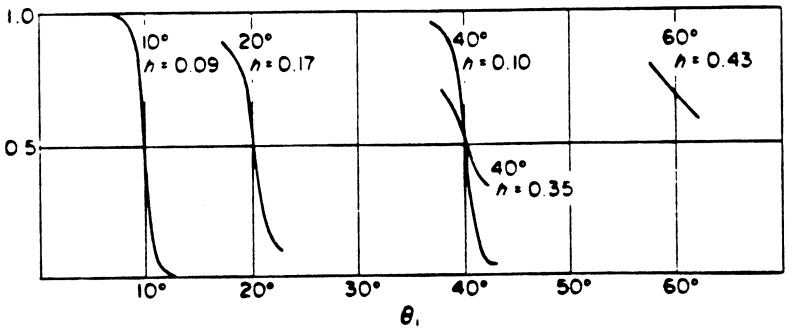

Figure 3.10: Transmission-angle curves for skew CPCs (optimised for non-zero skewness h). All the concentrators are designed for photocathodes of diameter unity and $\theta_{max} = \pi/2$. [49].

3.4 The Tangent-Ray Principle

In Chapter 6 of [49] the edge-ray principle is generalized to the 'tangent-ray principle' which enables the construction of Liouville-exact 2D concentrators for *non-plane* photocathodes. We shall refer to these concentrators as compound tangential concentrators ('CTC's) in order to differentiate them from CPCs which are constructed for *plane* photocathodes by the edge-ray principle. In the tangent-ray construction the rays which are incident at the entrance aperture at the limiting angle θ_i are reflected to be tangent to the photocathode (see Figure 3.11). For generating the portion of the concentrator profile which is shadowed by the photocathode from rays of polar angle θ_i the tangent-ray principle is modified. Here the rays of polar angle $< \theta_i$ which are tangent to the photocathode are reflected to remain tangent to the photocathode, i.e. the normal to the concentrator is tangent to the photocathode. Hence this portion of the concentrator profile is the involute of the portion of the photocathode which is also shadowed from rays of polar angle θ_i (see Figure 3.11).

Any 2D CTC constructed in this manner is easily shown to have the ideal transmission-angle characteristic by considering rays of polar angle slightly greater than or slightly less than the limiting angle θ_i incident at any point P on the concentrator profile (see Figure 3.11). Furthermore it can be shown to have the maximum concentration ratio allowed by the Liouville theorem:

$$\frac{l_{\text{conc}}}{l_{\text{cath}}} = \frac{1}{\sin\theta_i} \tag{3.14}$$

where l_{conc} is half the entrance aperture length of the CTC and l_{cath} is half the *arc-length* of the 2D photocathode. Once more the assumptions are being made that the photocathode is uniformly efficient at all angles of incidence up to $\pi/2$ and that the refractive index is constant throughout the optical system.

The development of the 2D CTC was mainly motivated by the design of trough-like 2D CTCs for concentrating solar energy onto tubular absorbers of circular section. Hence its development was not extended to the 3D case (by taking the surface of revolution) as it was with the 2D CPC which is the basis of the Winston cone. However, before

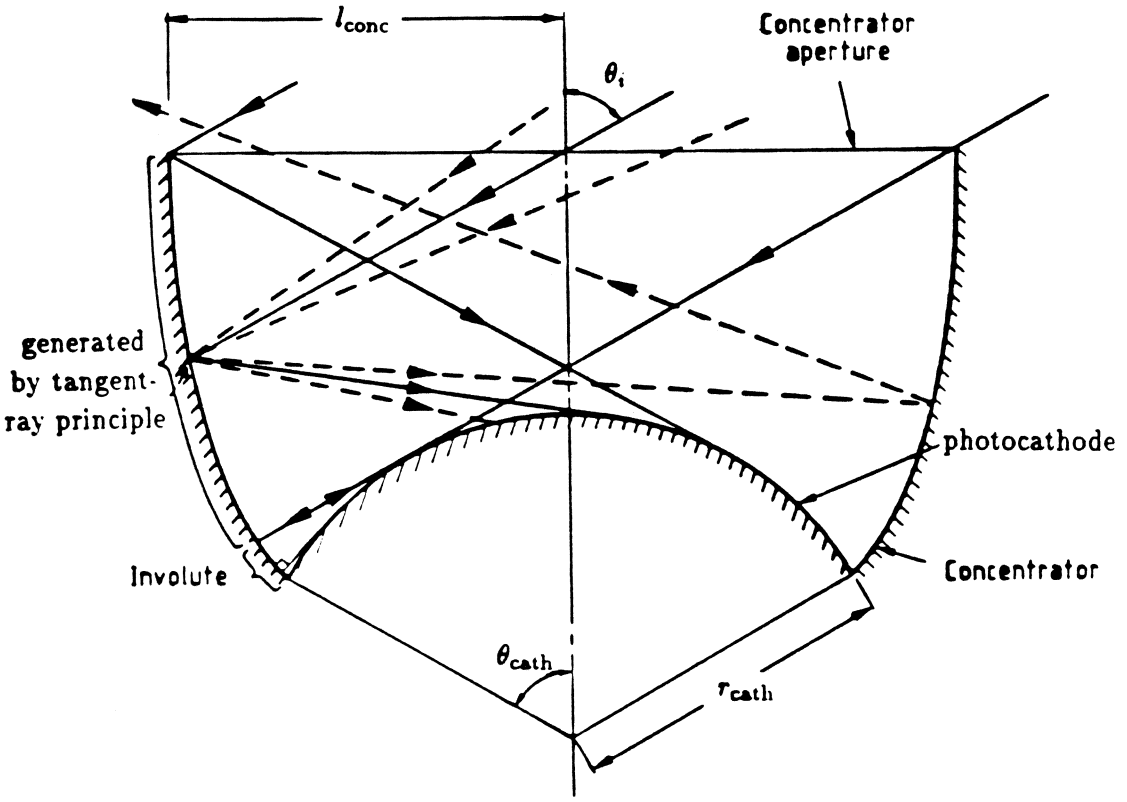

Figure 3.11: Liouville-exact 2D CTC constructed according to the tangent-ray principle. The (solid) rays incident at the concentrator entrance aperture at the limiting angle θ_i are reflected to be tangent to the photocathode. The portion of the concentrator profile which is shadowed from these rays is an involute of the photocathode profile which is also shadowed from these rays. The (dashed) rays with polar angle $< \theta_i$ which intersect any point P on the concentrator necessarily intersect the photocathode whilst those of polar angle $> \theta_i$ are rejected from the concentrator.

embarking on this development which is the main subject of this thesis we will direct our attention to the optical properties of the photocathode itself which are crucial to the arguments relating to conservation of phase space. The main question is what is the value of θ_{max}, the maximum angle of incidence at the PMT window at which the photocathode effectively detects light, and how does θ_{max} vary as the PMT window is placed in contact with media of different refractive index?

Chapter 4

Optical Properties of the K_2CsSb Bialkali Photocathode

4.1 Introduction

Despite the extensive use of the K_2CsSb bialkali photocathode for scintillation and Cherenkov counters, surprisingly little is known of its optical properties. When laid down on borosilicate glass it typically has the spectral response shown in Figure 4.1 [36] where the cut-off at about 300 nm is caused by absorption in the glass envelope of the photomultiplier. Shorter wavelengths can be detected at the cost of a high purity silica window. The only two published measurements [51], [52] of the real and imaginary parts of its complex refractive index report widely differing results, and both of these experiments determine the complex refractive index from measurements of the photocathode's reflectivity and transmissivity at near-normal incidence. This method is open to considerable uncertainty from an inherent ambiguity in the interpretation of the measurements.

The situation has been clarified by measuring the angular dependence of the reflectivity of this photocathode when the photomultiplier window is immersed in water. This measurement has allowed an unambiguous determination of the three photocathode parameters: real and imaginary parts of the complex refractive index and thickness, which

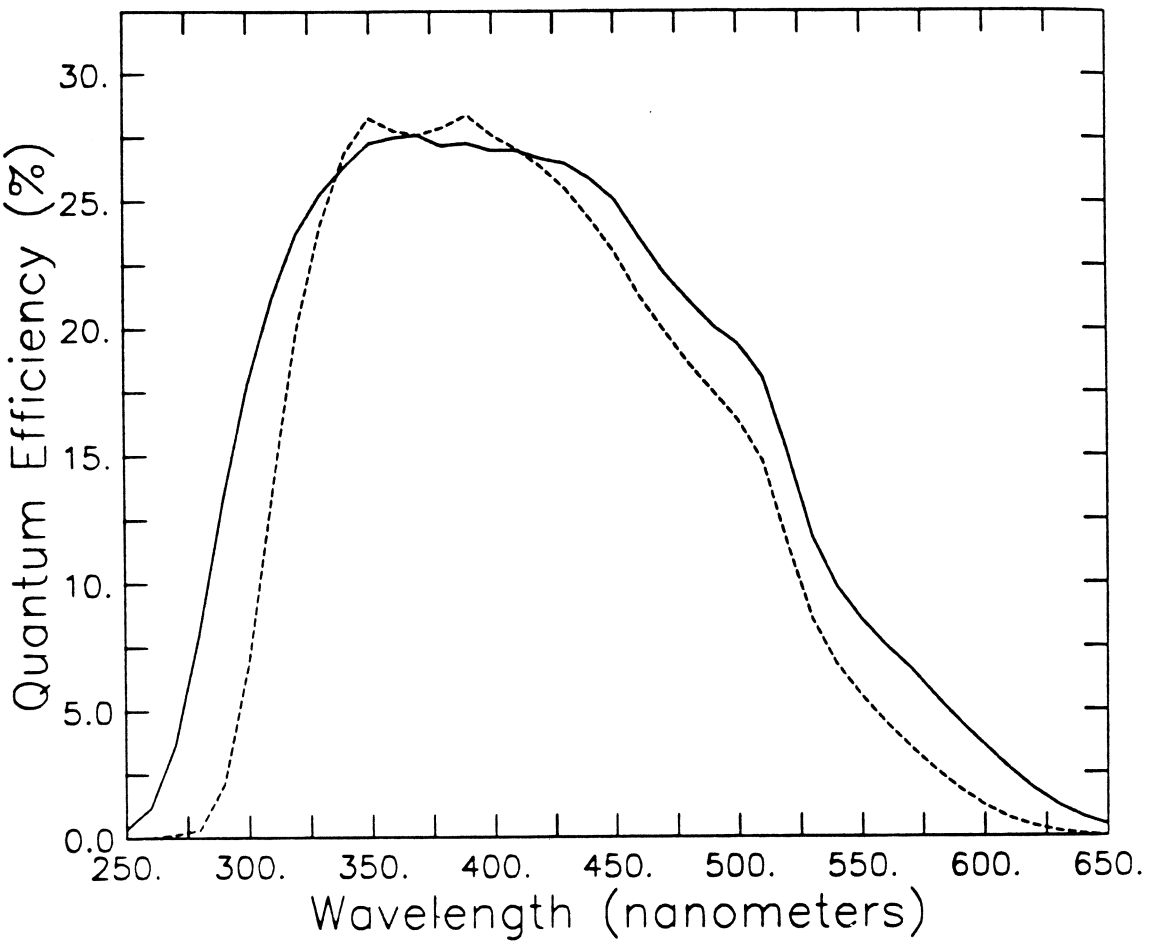

Figure 4.1: Typical wavelength dependence of the quantum efficiency of the K_2CsSb bialkali photocathode [36] measured from a Hamamatsu R1408 20 cm photomultiplier (——) and an EMI 9351 20 cm photomultiplier (– – –). The different cut-offs at short wavelengths are caused by the different quality of borosilicate glass in the envelopes of the PMTs; whereas at long wavelengths the difference might be due to different photocathode thicknesses.

are shown to be consistent with the measurements (but not the analysis) of [51].

From these three parameters one can predict the angular dependencies of the photocathode reflectivity, transmissivity, absorptivity and quantum efficiency. The first two can be directly calculated from the three parameter model of the photocathode [53]. The absorptivity is then easily inferred from the first two since by definition these three quantities always add up to unity. Lastly, the quantum efficiency is expected to have the same angular dependence as the absorptivity since it is the product of the absorptivity and the probability of the photo-electron escaping to the vacuum which should be

independent of the angle of incidence of the photons.

Greschat et al [55] measured the angular dependencies of the reflectivity, transmissivity and quantum efficiency of the Cs_3Sb photocathode. They established that the angular behaviour of the reflectivity, transmissivity and hence absorptivity could indeed be reproduced by the three parameter model and that the quantum efficiency and absorptivity had the same angular dependencies.

Later work by Chyba and Mandel [56] on the multialkali photocathode (Na_2KSb:Cs, S20), where the same quantities as in [55] were measured, showed that the angular behaviour of the reflectivity (and hence absorptivity) in the region of total internal reflection could not be completely reproduced by the three parameter model. They further observed that the angular dependence of the quantum efficiency which could be reproduced by the three parameter model was different to that of the absorptivity and concluded that another mechanism, not included in the three parameter model, was absorbing 20% of the parallel polarization photons at large angles of incidence without inducing any photo-electron emission.

Our measurement of the angular dependence of the reflectivity of the bialkali photocathode establishes that the three parameter model gives a valid description of the photocathode's optical properties. There is some evidence for a $3.6 \pm 1.5\%$ departure from the three parameter model but this departure is certainly much smaller than the departure which was observed in the multialkali photocathode [56] and does not significantly effect the optical properties of the bialkali photocathode.

Furthermore, the angular dependence of the absorptivity of the bialkali photocathode, calculated from the parametrization obtained here, compares favorably with a measurement of the angular dependence of the quantum efficiency [60] despite several differences between the assumptions of the parametrization and the conditions of the measurement.

Finally, the angular dependence of the optical properties of the bialkali photocathode are calculated with the photomultiplier window in contact with media of refractive indices 1.0 (gases), 1.34 (water) and 1.49 (scintillator, oil, glycerol etc.).

4.2 Experiment

The intensity of the multiple reflections from the front window of an EMI 9124 (30 mm) photomultiplier (see Figure 4.2) were measured as a function of the angle of incidence at the PMT window, θ_1. The K_2CsSb photocathode of this photomultiplier is evaporated onto a 2 mm thick borosilicate glass window.

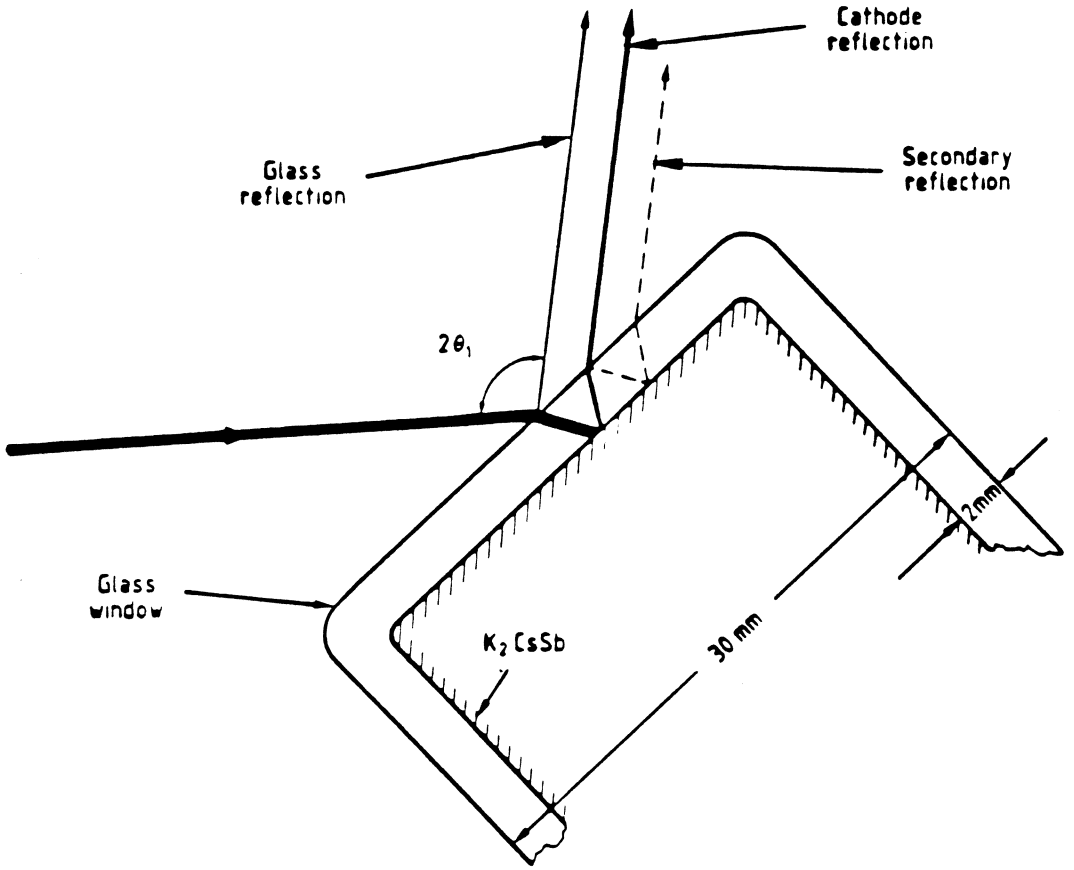

Figure 4.2: Multiple reflections from the front window of an EMI 9124 photomultiplier.

A schematic layout of the apparatus is shown in Figure 4.3. A Liconix Helium-Cadmium laser provided a polarized beam of diameter 1.1 mm and wavelength 442 nm. The beam intensity was continuously monitored with a beam-splitter and photodiode arrangement. A Perspex cylinder, of diameter 150 mm was located on a rotating table with its centerline coincident with the vertical axis of rotation of the table. The photo-

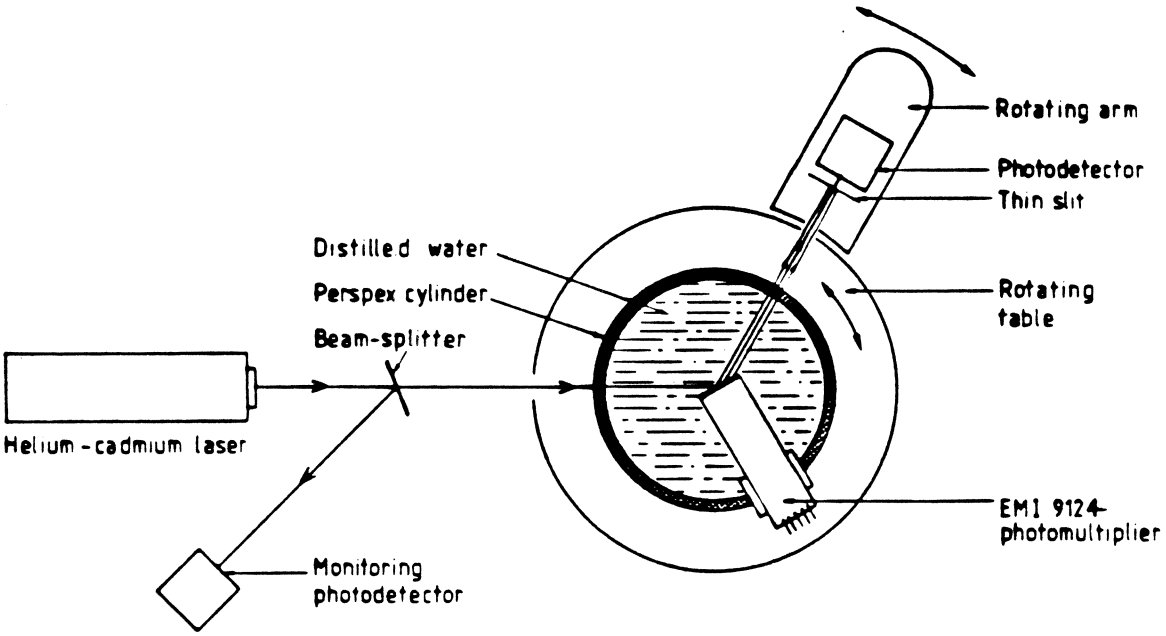

Figure 4.3: Schematic representation of the apparatus.

multiplier tube was mounted through the side of the Perspex cylinder with the centre of its front window at the axis of rotation of the table. The horizontal laser beam was aligned to be incident at the centre of the photomultiplier window. The Perspex cylinder was filled with deionized (Millipore) water, completely immersing the photomultiplier.

A photodiode on an independently rotating arm (with the same axis of rotation as the table) measured the intensity of the reflections from the photomultiplier. All the reflection measurements were normalised to the beam intensity which was measured with the same rotating photodiode by pulling the photomultiplier back in its mounting and allowing the beam to pass straight through the Perspex cylinder. Both the straight-through beam and the photomultiplier reflections suffer the same losses from reflection at the Perspex cylinder. Hence these losses factor out upon normalization. However, a variable percentage of the beam was scattered by small defects on the Perspex cylinder. The r.m.s. fluctuation of the photomultiplier reflections caused by the passage *twice* through the walls of the scattering Perspex cylinder was measured from the r.m.s. fluctuation

of the straight through beam which also passes twice through the Perspex. This r.m.s. fluctuation of $\pm 1.5\%$ was the limiting random error of the reflection measurements.

The multiple reflections emerged parallel from the photomultiplier window, separated from one another by a distance of order 2 mm (the thickness of the window — see Figure 4.4). Since the laser beam was 1.1 mm wide it was possible to resolve the multiple reflections into individual components: glass reflection, primary photocathode reflection, secondary photocathode reflection, etc. Moreover, the ability to resolve the multiple reflections was greatly enhanced by the focussing effect of the water-filled Perspex cylinder which acted as a thick cylindrical lens. This lens focussed the parallel laser beam into a vertical line at a distance $n_1 r/2(n_1 - 1) \simeq 2r$ from the centre of the lens where n_1 is the refractive index of water (1.34 at 442 nm) and r is the radius of the lens, i.e. the radius of the Perspex cylinder. Hence at a distance r from the Perspex cylinder the straight-through beam appeared as a vertical line and the multiple reflections as a series of parallel vertical lines. The focussing also caused the multiple reflections to converge together, but with only *half* the focussing power of the lens, since the multiple reflections were produced parallel to each other *inside* the lens. They were brought together at a distance $n_1 r/(n_1 - 1) \simeq 4r$ from the centre of the lens. Therefore at a distance r from the Perspex cylinder their separation had only decreased by a third from the initial $\sim$ 2 mm whereas each individual reflection was focussed into a $\simeq$ 0.1 mm wide line and hence could easily be resolved by placing a 0.15 mm wide vertical slit in front of the rotating photodiode, as in Figure 4.3.

Measurements were made of both the glass reflection and the primary photocathode reflection as a function of the angle of incidence θ_1 at the PMT window, for both polarizations independently, i.e. electric field vector perpendicular or parallel to the plane defined by the incident and the reflected beams, (respectively TE and TM waves).

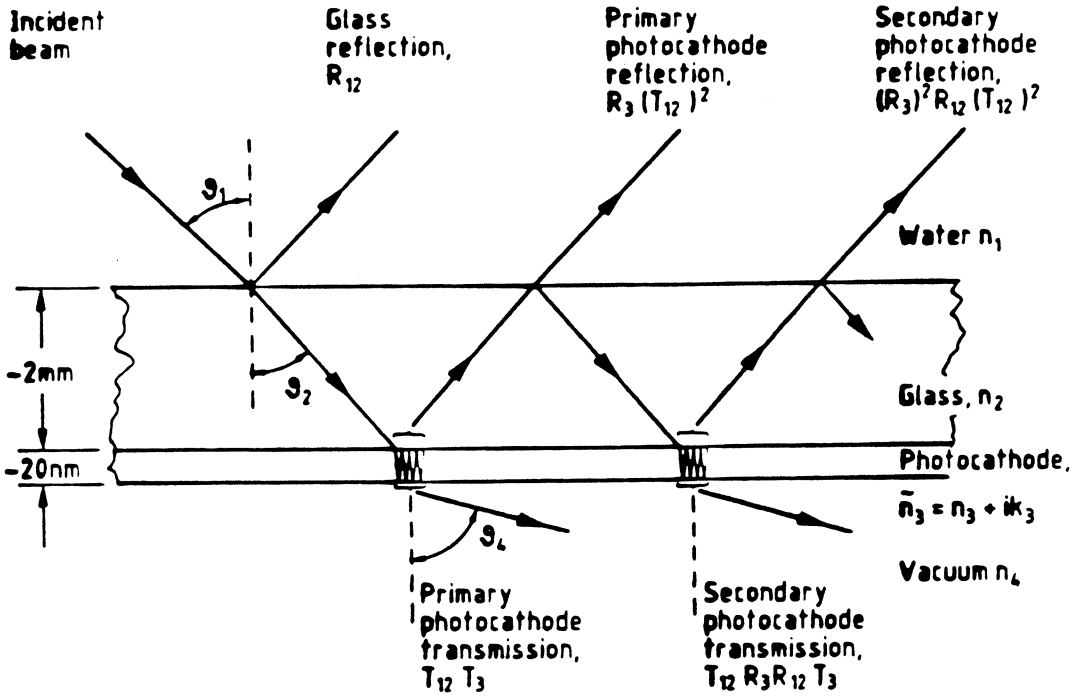

Figure 4.4: The multiple reflections which occur inside the glass window of the photomultiplier do not interfere with each other. They emerge parallel, separated by a distance of order 2 mm which depends on the angle of incidence and the thickness of the window. By contrast, the multiple reflections which occur inside the thin (~20 nm) photocathode overlap each other and interfere coherently with each other. Their amplitudes must be summed, taking into account their relative phases, in order to calculate the total amplitudes of the reflected and transmitted waves.

4.3 Theory, Results and Discussion

Measuring the glass reflection and photocathode reflection separately simplifies the analysis and provides a useful check on the systematics of the experiment as the glass reflection is well understood. We shall discuss the glass reflection first and the photocathode reflection later.

The coefficients of reflection (R_{12}) and transmission (T_{12}) of the water/glass boundary are easily calculated from the well known Fresnel equations which can be written, for the perpendicular polarization (TE waves)

$$R_{12} = \left(\frac{n_1 \cos\theta_1 - n_2 \cos\theta_2}{n_1 \cos\theta_1 + n_2 \cos\theta_2} \right)^2 \tag{4.1}$$

$$T_{12} = \left(\frac{2n_1 \cos\theta_1}{n_1 \cos\theta_1 + n_2 \cos\theta_2} \right)^2 \frac{n_2 \cos\theta_2}{n_1 \cos\theta_1} \tag{4.2}$$

and for the parallel polarization (TM waves)

$$R_{12} = \left(\frac{n_2 \cos\theta_1 - n_1 \cos\theta_2}{n_2 \cos\theta_1 + n_1 \cos\theta_2}\right)^2 \tag{4.3}$$

$$T_{12} = \left(\frac{2n_1 \cos\theta_2}{n_2 \cos\theta_1 + n_1 \cos\theta_2}\right)^2 \frac{n_2 \cos\theta_1}{n_1 \cos\theta_2} \tag{4.4}$$

where n_1 is the refractive index of water, n_2 is the refractive index of the borosilicate glass window, θ_1 is the angle of incidence at the photomultiplier window and θ_2 is the angle of transmission into the window (see Figure 4.4) given by Snell's law:

$$n_1 \sin\theta_1 = n_2 \sin\theta_2 \tag{4.5}$$

The only variable in the calculation of R_{12} is n_2 and hence its value can be determined from the best fit to the glass reflection data which is obtained by minimizing the r.m.s. fluctuation about the theory, Δ_{rms}, given by

$$\Delta_{rms}(n_2) = \left[\frac{1}{N}\sum_{\theta_1}\left(\frac{\text{measured glass reflection}}{\mathrm{R}_{12}} - 1\right)^2\right]^{1/2} \tag{4.6}$$

where N is the number of data. The minimum Δ_{rms} occurred at $n_2 = 1.495$ and was 2.2% which is slightly more than the r.m.s. fluctuation of $\pm 1.5\%$ from the double transmission through the Perspex cylinder. This difference can be explained by the systematic error caused by scattered light from the primary photocathode reflection finding its way through the slit during the glass reflection measurements. This increase in the measured glass reflection leads to a slight overestimate of the value of n_2. It has a proportionally greater effect when the glass reflection intensity is smaller. This can be seen in Figure 4.5 where the glass reflection data is plotted against a theoretical fit with $n_2 = 1.490$ for which Δ_{rms} is 2.5%. The reason why this value for n_2 is chosen is that it is the inferred value from the theoretical fit to the photocathode reflection data.

The coefficients of reflection and transmission of the photocathode are given by an extension of the Fresnel equations where the absorptive properties of the photocathode are incorporated into the theory by giving the photocathode a complex refractive index, $\tilde{n}_3 = n_3 + ik_3$ [54]. A further complication arises because the multiple reflections which occur inside the thin photocathode ($\sim$ 20 nm) overlap each other and interfere coherently

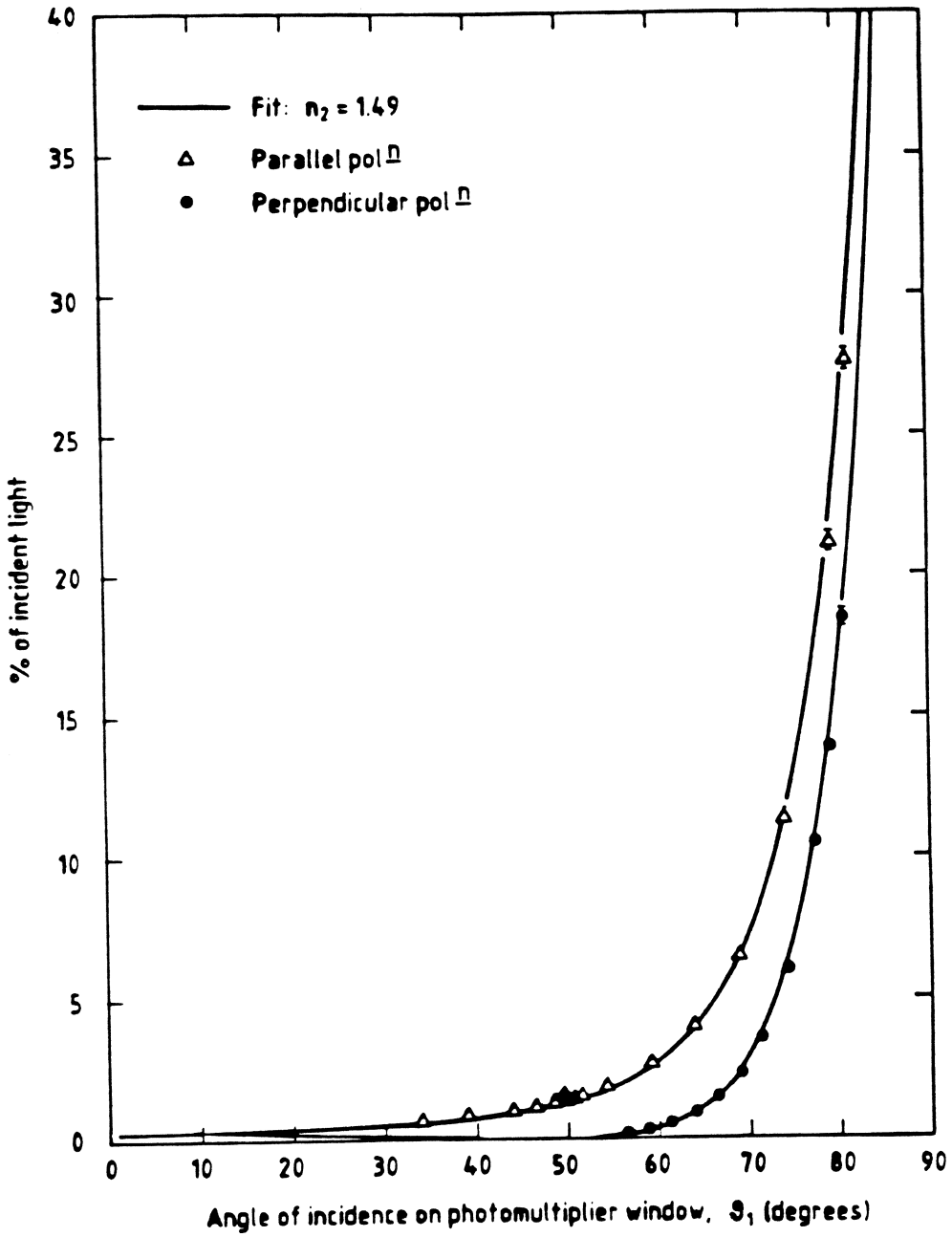

Figure 4.5: Glass reflection data fitted to $n_2 = 1.490$ ($\Delta_{rms} = 2.5\%$). This value for n_2 which is the best fit to the photocathode reflection data is chosen rather than 1.495, the best fit to the glass reflection data, as n_2 is more strongly constrained by the photocathode reflection data than by the glass reflection data.

with each other (see Figure 4.4). Their *amplitudes* must be summed, taking into account their relative phases, in order to calculate the total amplitudes of the reflected and transmitted waves. The formalism developed for this summation is clearly presented in [53] where the intensities of the reflected wave, R_3, and the transmitted wave, T_3 are given by

$$R_3 = \frac{|\tilde{r}_{23}|^2 e^{2v\eta} + |\tilde{r}_{34}|^2 e^{-2v\eta} + 2|\tilde{r}_{23}||\tilde{r}_{34}| \cos(\arg \tilde{r}_{34} - \arg \tilde{r}_{23} + 2u\eta)}{e^{2v\eta} + |\tilde{r}_{23}|^2|\tilde{r}_{34}|^2 e^{-2v\eta} + 2|\tilde{r}_{23}||\tilde{r}_{23}| \cos(\arg \tilde{r}_{23} + \arg \tilde{r}_{34} + 2u\eta)} \tag{4.7}$$

$$T_3 = \frac{g|\tilde{t}_{23}|^2|\tilde{t}_{34}|^2}{e^{2v\eta} + |\tilde{r}_{23}|^2|\tilde{r}_{34}|^2 e^{-2v\eta} + 2|\tilde{r}_{23}||\tilde{r}_{23}| \cos(\arg \tilde{r}_{23} + \arg \tilde{r}_{34} + 2u\eta)} \tag{4.8}$$

where for the perpendicular polarization (TE waves)

$$g = \frac{n_4 \cos\theta_4}{n_2 \cos\theta_2}. \tag{4.9}$$

$$\tilde{r}_{23} = \frac{n_2 \cos\theta_2 - \tilde{n}_3 \cos\tilde{\theta}_3}{n_2 \cos\theta_2 + \tilde{n}_3 \cos\tilde{\theta}_3} \tag{4.10}$$

$$\tilde{r}_{34} = \frac{\tilde{n}_3 \cos\tilde{\theta}_3 - n_4 \cos\theta_4}{\tilde{n}_3 \cos\tilde{\theta}_3 + n_4 \cos\theta_4} \tag{4.11}$$

$$\tilde{t}_{23} = \frac{2n_2 \cos\theta_2}{n_2 \cos\theta_2 + \tilde{n}_3 \cos\tilde{\theta}_3} \tag{4.12}$$

$$\tilde{t}_{34} = \frac{2\tilde{n}_3 \cos\tilde{\theta}_3}{\tilde{n}_3 \cos\tilde{\theta}_3 + n_4 \cos\theta_4} \tag{4.13}$$

and for the parallel polarization (TM waves)

$$g = \frac{n_4 \cos\theta_2}{n_2 \cos\theta_4}. \tag{4.14}$$

$$\tilde{r}_{23} = \frac{\tilde{n}_3 \cos\theta_2 - n_2 \cos\tilde{\theta}_3}{\tilde{n}_3 \cos\theta_2 + n_2 \cos\tilde{\theta}_3} \tag{4.15}$$

$$\tilde{r}_{34} = \frac{n_4 \cos\tilde{\theta}_3 - \tilde{n}_3 \cos\theta_4}{n_4 \cos\tilde{\theta}_3 + \tilde{n}_3 \cos\theta_4} \tag{4.16}$$

$$\tilde{t}_{23} = \frac{2n_2 \cos\theta_2}{\tilde{n}_3 \cos\theta_2 + n_2 \cos\tilde{\theta}_3} \tag{4.17}$$

$$\tilde{t}_{34} = \frac{2\tilde{n}_3 \cos\tilde{\theta}_3}{n_4 \cos\tilde{\theta}_3 + \tilde{n}_3 \cos\theta_4} \tag{4.18}$$

Here $\eta = 2\pi d/\lambda_0$ where λ_0 is the vacuum wavelength of the incident light and d is the thickness of the photocathode. We have made the standard substitution

$$u + iv = \tilde{n}_3 \cos\tilde{\theta}_3 \tag{4.19}$$

where $\tilde{n}_3 = n_3 + ik_3$ is the complex refractive index of the photocathode and $\tilde{\theta}_3$, the complex angle in the photocathode is given by Snell's law:

$$n_2 \sin\theta_2 = \tilde{n}_3 \sin\tilde{\theta}_3 \tag{4.18}$$

Finally, $n_4 = 1.0$ is the refractive index of the vacuum inside the photomultiplier tube and θ_4 is the angle of transmission into this vacuum (see Figure 4.4) also given by Snell's law:

$$\tilde{n}_3 \sin\tilde{\theta}_3 = n_4 \sin\theta_4 \tag{4.19}$$

From the above equations the reflectivity of the photocathode, R_3, can be calculated as a function of the three photocathode parameters (n_3, k_3 and d), the angle of incidence at the photocathode from the glass side (θ_2) and the refractive index of the glass envelope (n_2). However, the primary photocathode reflection was measured as a function of the angle of incidence at the photomultiplier window, θ_1. It is therefore necessary to use Snell's law (4.5) to transform θ_2 into θ_1 in order to calculate R_3 as a function of θ_1. Furthermore, the primary photocathode reflection passed twice through the water/glass boundary (see Figure 4.4) and is hence given by $R_3(T_{12})^2$, where T_{12}, the transmissivity of the water/glass boundary, can be calculated from (4.2), (4.4) and (4.5), for a given value of n_2.

A computer program was written to calculate $R_3(T_{12})^2$ as a function of θ_1, the three photocathode parameters, and n_2. It was used to search the 4D parameter space (n_2, n_3, k_3 and d) for a best fit to the photocathode reflection data by minimizing the r.m.s. fluctuation about the theory:

$$\Delta_{rms}(n_2, n_3, k_3, d) = \left[\frac{1}{N}\sum_{\theta_1}\left(\frac{\text{measured primary photocathode reflection}}{R_3(T_{12})^2} - 1\right)^2\right]^{1/2} \tag{4.20}$$

where n_2 was varied from 1.475 to 1.495 in steps of 0.005; n_3 from 1.0 to 6.0 in steps of 0.05; k_3 from 0.0 to 5.0 in steps of 0.05 and d from 5 nm to 50 nm in steps of 0.5 nm.

The best fit occurred at $n_2 = 1.49$, $n_3 = 2.7$, $k_3 = 1.5$, $d = 23$ nm and is illustrated in Figure 4.6 with the data. It reproduces closely the angular behaviour of the photocathode reflectivity. The most striking features of this angular behaviour are the pronounced

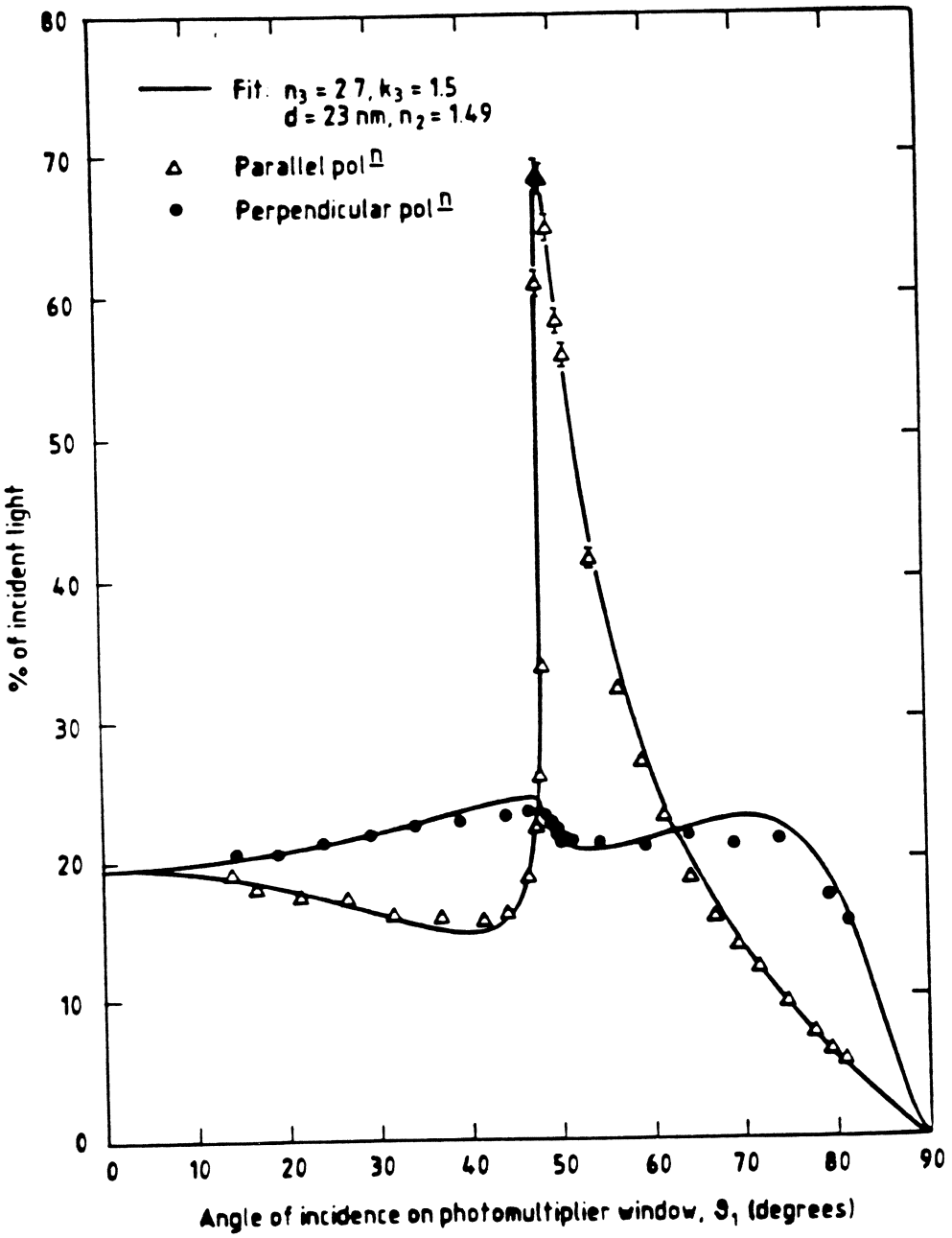

Figure 4.6: Best fit to the primary photocathode reflection data ($\Delta_{rms} = 3.6\%$).

peak in the parallel polarization and the small but steep drop in the perpendicular polarization, both occurring at about 48° incidence. These abrupt changes in reflectivity coincide with the onset of total internal reflection at the photocathode/vacuum boundary. The critical angle for this total internal reflection is easily derived by considering Snell's law at all the boundaries between the water and the vacuum:

$$n_1 \sin\theta_1 = n_2 \sin\theta_2 = \tilde{n}_3 \sin\tilde{\theta}_3 = n_4 \sin\theta_4 \tag{4.21}$$

Hence total internal reflection begins at an angle of incidence at the photomultiplier window given by $\theta_{1,c} = \sin^{-1}(1/n_1) = 48.3°$ which depends only on the refractive index of the medium in which the photomultiplier window is immersed. Although the abruptness of the features at 48.3° incidence is explained by the onset of total internal reflection, their precise nature (e.g. pronounced peak or slight drop) is determined by the interference effects between the multiple reflections inside the photocathode.

The best theoretical fit has a Δ_{rms} of 3.6% which is greater than the 1.5% r.m.s. fluctuation from the double transmission through the Perspex and cannot be accounted for by scattered light from another reflection increasing the measured photocathode reflection. There may be some extra mechanism, not included in the theory, which absorbs only parallel polarization photons, as has been suggested by Chyba and Mandel [56]. Nevertheless the $3.6 \pm 1.5\%$ departure from the three parameter model is certainly much smaller than the departure found in the multialkali photocathode [56].

The four parameters determined from the best fit to the photocathode reflection data are strongly constrained by these data. Δ_{rms} increases quite steeply as one moves away from its minimum in the 4D parameter space (n_2, n_3, k_3, d). However, there is a line in this 4D space running through the best fit along which Δ_{rms} rises the least steeply from its minimum. This line is characterised by approximately constant values of n_2, n_3/k_3 and $|\tilde{n}_3|^2 d$. Along it, the normal incidence reflectivity of the photocathode remains constant which explains why Δ_{rms} does not increase so steeply. But, even so, near the critical angle for total internal reflection the reflectivity does change significantly, especially the peak in the parallel polarization. This can be seen in Figure 4.7 where

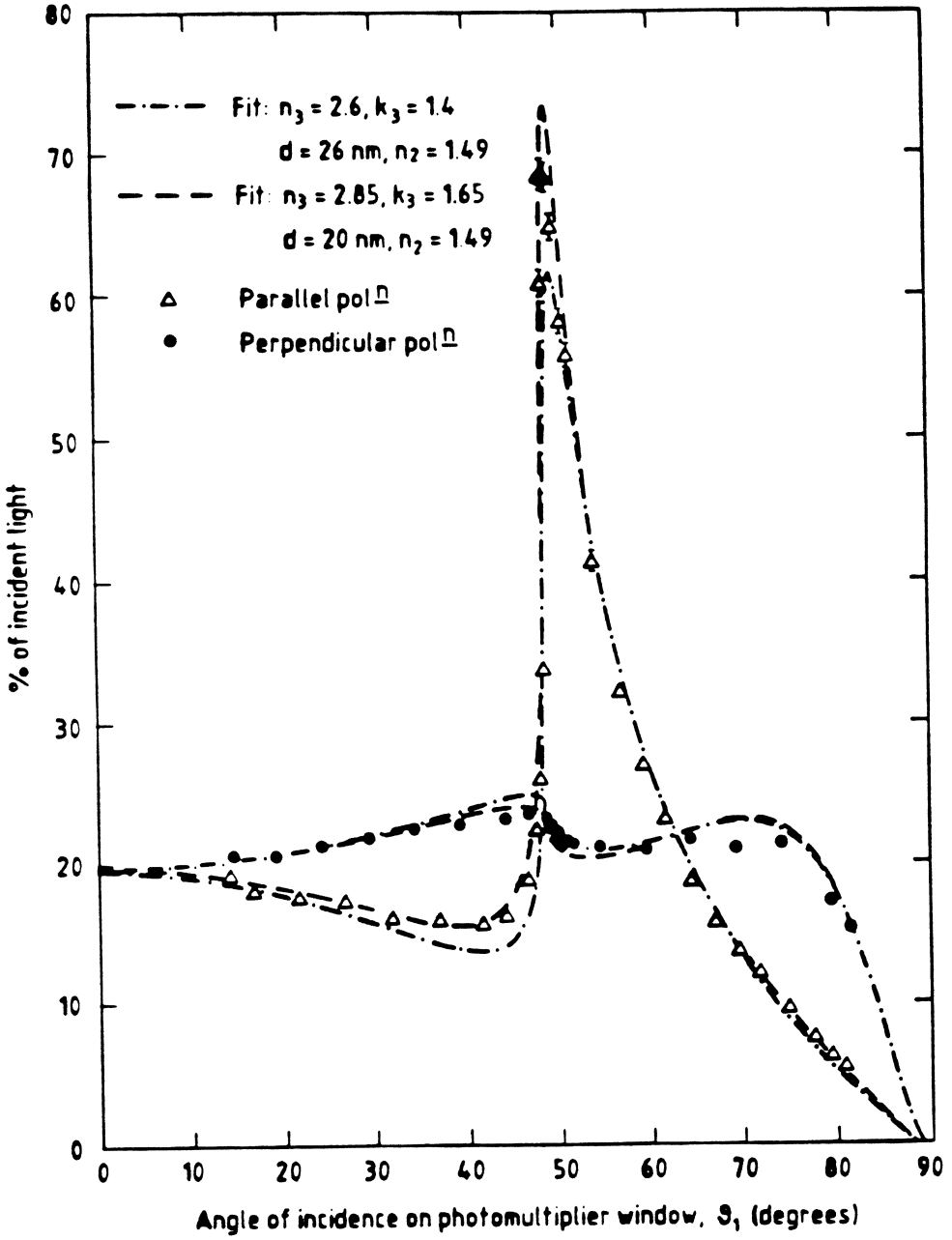

Figure 4.7: Two fits to the primary photocathode data from the line in the 4D parameter space (n_2, n_3, k_3, d) along which Δ_{rms} increases the least quickly from its true minimum since the normal incidence reflectivity along this line is more or less constant. The parameter values of these fits have been obtained by minimizing Δ_{rms} for fixed values of d (20 nm and 26 nm) and n_2 (1.49). The respective Δ_{rms} values are 5.5% and 5.9%.

two fits on this line from either side of the true minimum (the two best fits at d = 20 nm and d = 26 nm, keeping n_2 = 1.490) are plotted with the data. These two fits do not reproduce the measured height of the peak in the parallel polarization and hence they have high Δ_{rms} values (5.5% and 5.9% respectively) and can be discounted. Thus the measurement of the height of this peak is critical for determining a unique set of values for n_3, k_3 and d. The best value for n_2 is determined by the the data at large angles where $(T_{12})^2$ becomes a significant factor. We conclude that for the particular photomultiplier investigated $n_2 = 1.490 \pm 0.005$, $n_3 = 2.70 \pm 0.05$ and $k_3 = 1.50 \pm 0.05$ at 442 nm wavelength, and $d = 23 \pm 1$ nm. This parametrization of the photocathode shall be referred to as P1.

4.4 Other Measurements

Timan [51] has measured the optical parameters of the K_2CsSb bialkali photocathode and reports values of 4.5 and 0.8 for the real and imaginary parts of the refractive index at 454 nm, and 40.8 nm for the thickness. It is hard to reconcile these values with those of P1. However it appears that the discrepancy between the two results is caused by an unfortunate numerical error.

Timan used the 'three intensities method' in which the reflectivities of the photocathode from the glass side, R_f, and the vacuum side, R_v, and the transmissivity of the photocathode, T, are all measured at near-normal incidence. These three quantities (corrected for reflection losses at all air/glass boundaries) can be calculated as a function of the three photocathode parameters: n_3, k_3 and d, e.g. R_f and T are equal to R_3 and T_3 in the notation of Section 4.3 and can hence be calculated from (4.7)–(4.21) whereas R_v is equal to R_3 if n_2 is substituted by n_4 and vice-versa in (4.7)–(4.21). Different equations [57] were used which are strictly only valid at normal incidence but the approximation is justified for unpolarized light in the 10° to 20° range of the measurements. Numerically these equations agree with (4.7)–(4.21) in the limit where $\theta_2, \tilde{\theta}_3, \theta_4 \rightarrow 0$, but Timan's values for R_f, R_v and T quoted for a specific set of parameters n_3, k_3 and d

do not agree with the values we calculate for the same parameters using either system of equations[1]. Although the discrepancy is small it has affected the results of the analysis. A new analysis of Timan's measurements is presented in this section.

The three intensities were measured at five different wavelengths (390, 453.5, 505, 601.5 and 798 nm) for two K_2CsSb bialkali photocathodes which shall be referred to as B1 and B3, using Timan's notation. Particular attention will be paid to the measurements at 453.5 nm which is close to P1 (442 nm), and to those at 390 nm which is close to the peak of the effective wavelength spectrum of SNO (380 nm, see Figure 2.4).

Since it is not possible to invert the equations which calculate the three intensities as a function of n_3, k_3 and d a program was written for fitting the *measured* triplet $R_f(m)$, $R_v(m)$ and $T(m)$ to *calculated* triplets $R_f(c)$, $R_v(c)$ and $T(c)$ by minimizing the r.m.s. fluctuation about the theory:

$$\Delta_{rms}(n_3, k_3, d) = \left(\frac{1}{3} \left[\left(\frac{R_f(m)}{R_f(c)} - 1 \right)^2 + \left(\frac{R_v(m)}{R_v(c)} - 1 \right)^2 + \left(\frac{T(m)}{T(c)} - 1 \right)^2 \right] \right)^{1/2} \quad (4.22)$$

The program varied n_3 from 1.0 to 6.0 in steps of 0.05, k_3 from 0.0 to 5.0 in steps of 0.05 and d from 5.0 nm to 50.0 nm in steps of 1 nm (n_2 was fixed at 1.5, from [51]).

Each measurement was made twenty times over by Timan who observed an r.m.s. fluctuation of 5% about the mean of each measurement. The statistical fluctuation in the *mean* should therefore be of the order of 1%. However the systematic errors have not been estimated so we take a pessimistic view and search for fits with a Δ_{rms} of less than 4%.

For each measured triplet a vast number of such fits with $\Delta_{rms} < 4\%$ were found covering much of the three dimensional parameter space. These fits were arranged in lines across the 3D space which were characterised by approximately constant values of n_3/k_3 and $|\tilde{n}_3|^2 d$, just as was observed in fitting the angular dependence of reflectivity (Section 4.3), except that here Δ_{rms} changed very slowly along the lines. The measured triplets do not sufficiently constrain the photocathode parameters.

[1]There is a sign error in the equations quoted by Timan [51] from Heavens [57], but using either sign we calculate a different set of values for R_f, R_v and T than Timan quotes for the same set of parameters n_3, k_3 and d.

$R_f(c)$	$T(c)$	$R_v(c)$	d (nm)	n_3	k_3	n_3/k_3	$d\|\tilde{n}_3\|\lambda 2$	Δ_{rms} (%)
0.274	0.190	0.451	6	5.70	3.10	1.84	2520	0.6
0.275	0.188	0.449	10	4.50	2.45	1.84	2620	1.0
0.277	0.188	0.446	14	3.90	2.05	1.90	2710	1.3
0.281	0.191	0.442	18	3.55	1.75	2.03	2810	2.1
0.282	0.188	0.437	22	3.30	1.60	2.06	2950	2.9
0.281	0.191	0.431	24	3.20	1.50	2.13	2990	3.4
0.277	0.191	0.451	8	2.45	4.70	0.52	2240	0.7
0.280	0.189	0.451	12	1.95	3.80	0.51	2180	1.3
0.274	0.192	0.442	16	1.65	3.20	0.52	2070	1.9
0.284	0.190	0.444	20	1.40	2.85	0.49	2010	2.3
0.283	0.189	0.439	24	1.25	2.55	0.49	1930	2.7
0.278	0.189	0.429	28	1.15	2.30	0.50	1850	3.6
0.287	0.194	0.437	44	5.95	0.55	10.82	15710	3.6
0.284	0.185	0.433	50	5.35	0.55	9.73	14460	3.8

Table 4.1: Possible fits to the measured triplet of B1 at 453.5 nm. End points and selected intermediate points of the lines in the 3D parameter space which have a $\Delta_{rms} \leq 4\%$ for fitting the measured triplet: $R_f = 0.275, T = 0.190$ and $R_v = 0.455$.

Tables 4.1 and 4.2 show the end points and some intermediate points of these lines in the 3D parameter space for the two photocathodes B1 and B3 at 453 nm. The lines cover a broad range in the parameter space so that it is impossible to determine the photocathode parameters unambiguously from these measured triplets. Timan suggests that by measuring the triplets at many different wavelengths one can resolve this ambiguity since there should be only one value for d which is found at *every* wavelength amongst the many possible fits. However we find that there is a broad range of values of d which allow equally good fits at all the wavelengths and the ambiguity remains. Furthermore the *total* r.m.s. fluctuations about the theory of these fits across all wavelengths are all greater than 2% which retrospectively justifies the search for fits with $\Delta_{rms} < 4\%$ at individual wavelengths.

Nevertheless we can select, out of the many possible fits in Tables 4.1 and 4.2, the closest set of values of n_3 and k_3 to those of P1 (2.7,1.5). The values selected are $n_3 = 3.2$, $k_3 = 1.5$ for B1 and $n_3 = 3.25$, $k_3 = 1.5$ for B3 which fixes d at 24 nm for B1 and 29 nm for B3. Having fixed the thickness of each photocathode one can

$R_f(c)$	$T(c)$	$R_v(c)$	d (nm)	n_3	k_3	n_3/k_3	$d\|\tilde{n}_3\|\lambda 2$	Δ_{rms} (%)
0.307	0.156	0.484	6	5.95	3.60	1.65	2900	3.3
0.309	0.156	0.482	10	4.70	2.80	1.68	2990	2.9
0.308	0.157	0.477	14	4.05	2.35	1.72	3060	2.5
0.313	0.155	0.475	18	3.70	2.05	1.80	3220	1.8
0.312	0.157	0.466	22	3.45	1.80	1.92	3330	1.2
0.315	0.154	0.460	26	3.30	1.65	2.00	3530	0.5
0.319	0.156	0.455	29	3.25	1.50	2.17	3710	1.1
0.317	0.155	0.449	31	3.20	1.45	2.21	3820	1.4
0.327	0.155	0.446	35	3.25	1.30	2.50	4280	2.7
0.326	0.155	0.434	40	3.40	1.15	2.96	5150	3.9
0.307	0.155	0.483	8	2.90	4.95	0.59	2630	3.1
0.307	0.156	0.479	12	2.25	4.00	0.56	2520	2.8
0.313	0.155	0.479	16	1.85	3.45	0.54	2450	2.4
0.314	0.153	0.476	20	1.60	3.05	0.52	2370	2.1
0.317	0.152	0.473	24	1.40	2.75	0.51	2280	1.9
0.316	0.152	0.466	28	1.25	2.50	0.50	2180	1.3
0.321	0.154	0.463	32	1.10	2.30	0.48	2080	1.3
0.314	0.154	0.453	35	1.05	2.15	0.49	2000	1.0
0.318	0.154	0.456	33	5.85	1.05	5.57	11650	0.9
0.320	0.153	0.447	37	4.95	1.05	4.71	9470	2.1
0.323	0.155	0.435	41	4.00	1.05	3.81	7010	3.6
0.322	0.154	0.471	45	5.95	0.65	9.15	16120	1.9
0.318	0.160	0.464	50	5.45	0.60	9.08	15030	2.0

Table 4.2: Possible fits to the measured triplet of B3 at 453.5 nm. End points and selected intermediate points of the lines in the 3D parameter space which have a $\Delta_{rms} \leq 4\%$ for fitting the measured triplet: $R_f = 0.315$, $T = 0.155$ and $R_v = 0.460$.

then uniquely determine the values of n_3 and k_3 at the other wavelengths where the three intensities have been measured by searching only for fits with the given values of d. This extra constraint resolves the ambiguity at all the other wavelengths except for 390 nm where a certain ambiguity remains as many fits are possible even with the fixed thicknesses. However these numerous fits at 390 nm cover relatively well defined regions in the 2D space (n_3,k_3), as can be seen in Figure 4.8 where a strong anticorrelation is noted between n_3 and k_3.

The full sets of values for n_3 and k_3 as a function of wavelength obtained by fixing — somewhat artificially — the thicknesses of photocathodes B1 and B3 are shown in Figures

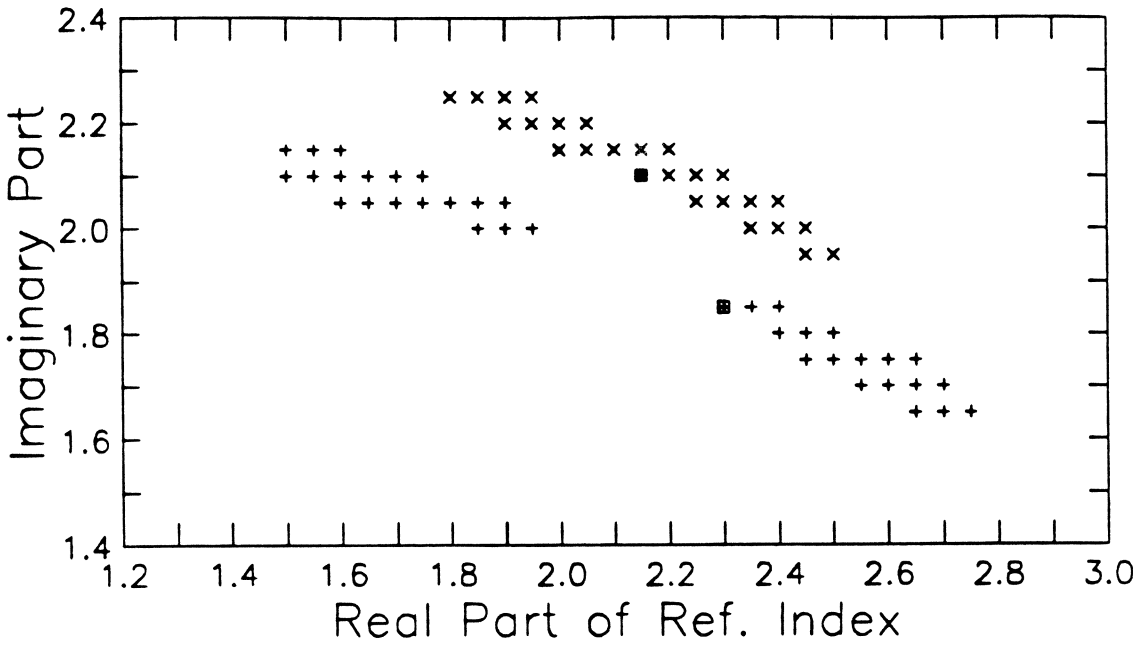

Figure 4.8: Allowed fits ($\Delta_{rms} < 4\%$) at 390 nm for photocathode B1 (crosses) with d fixed at 24 nm and for photocathode B3 (pluses) with d fixed at 29 nm. The boxed cross is P2 and the boxed plus is P3.

4.9 and 4.10. It is satisfying that one can obtain such good agreement between the refractive indices of the EMI photocathode and those of the B1 and B3 photocathodes. The magnitude and wavelength dependence of the real part of the refractive index shown in Figure 4.9 is very similar to that of the Cs_3Sb photocathode as measured by Wallis [58] and reported in [59]. The wavelength dependence of the imaginary part of the refractive index mirrors the wavelength dependence of the quantum efficiency of the bialkali photocathode (Figure 4.1) as one would expect.

Ghosh and Varma [52] have measured the complex refractive index of a bialkali photocathode as a function of wavelength. They report a value of $2.4 + i2.55$ at 442 nm, c.f. $2.7 + i1.5$ from P1. Their wavelength dependence of the real part of the refractive index is similar to that shown in Figure 4.9. However for the imaginary part of the refractive index the wavelength dependence is the same as in Figure 4.10 but shifted to longer wavelengths by about 100 nm. From the paper it would seem that the imaginary part of the refractive index is determined from a direct measurement of transmission at normal incidence. This method is highly dependent on an accurate knowledge of the

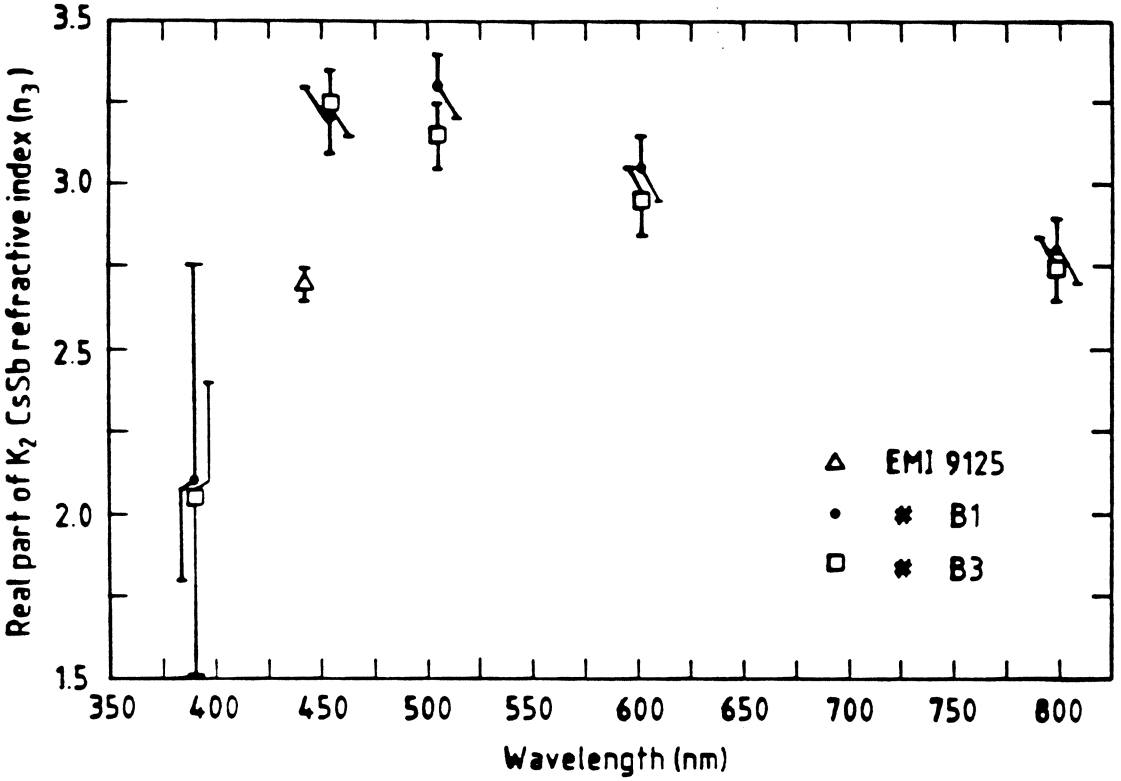

Figure 4.9: Wavelength dependence of the real part of the bialkali complex refractive index from the re-analysis of the measurements in [51] and the results of Section 4.3.

thickness of the photocathode. There is no mention of how the thickness was estimated nor are any of the reflectivity or transmissivity data presented.

The angular dependence of the quantum efficiency of a bialkali photocathode has been measured by Radcliffe and Leslie [60]. The result of this measurement is shown in Figure 4.11. It can be compared to the angular dependence of the absorptivity, A_3, which is inferred from the calculated reflectivity, R_3, and transmissivity, T_3, using the relation $A_3 + R_3 + T_3 = 1$. This calculation of A_3 as a function of the angle of incidence at the photocathode, θ_2, which assumes P1, i.e. $n_3 = 2.7$, $k_3 = 1.5$, $d = 23$ nm and $\lambda_0 = 442$ nm, is shown in Figure 4.12. It can be seen from the figure that the absorptivity exhibits qualitatively the same angular behaviour as the quantum efficiency. Unfortunately there are three significant differences between the experimental conditions of the quantum efficiency measurement and the assumptions of the absorptivity calculation which limit

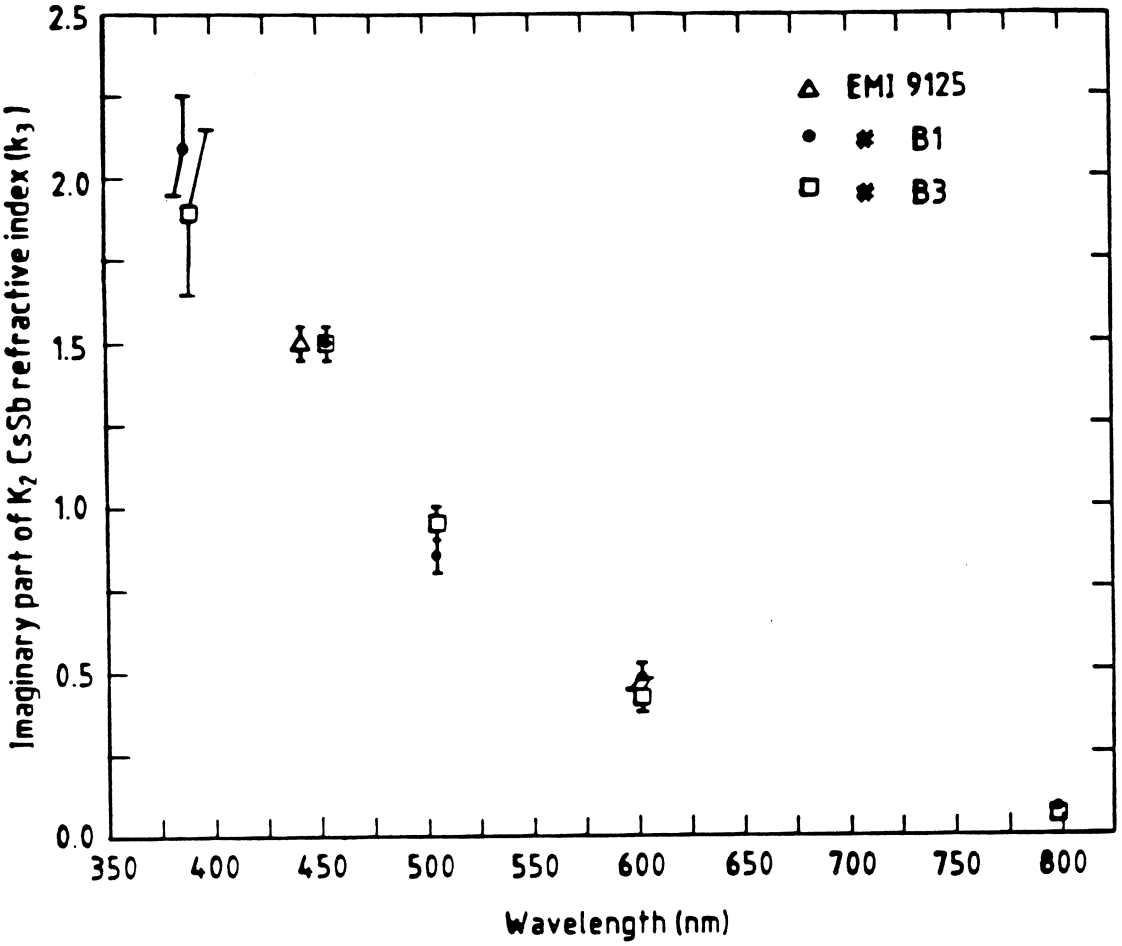

Figure 4.10: Wavelength dependence of the imaginary part of the bialkali complex refractive index from the re-analysis of the measurements in [51] and the results of Section 4.3.

a detailed comparison:

1. The absorptivity calculation assumes monochromatic illumination at 442 nm whereas the light source used in the quantum efficiency measurement was an optical pulser with a broad spectral distribution (250-450 nm) peaking at ~350 nm.

2. The photocathode parameters, in particular the thickness, which are used in the absorptivity calculation are derived from a different photocathode — even a different manufacturer — than the one which was used in the quantum efficiency measurement.

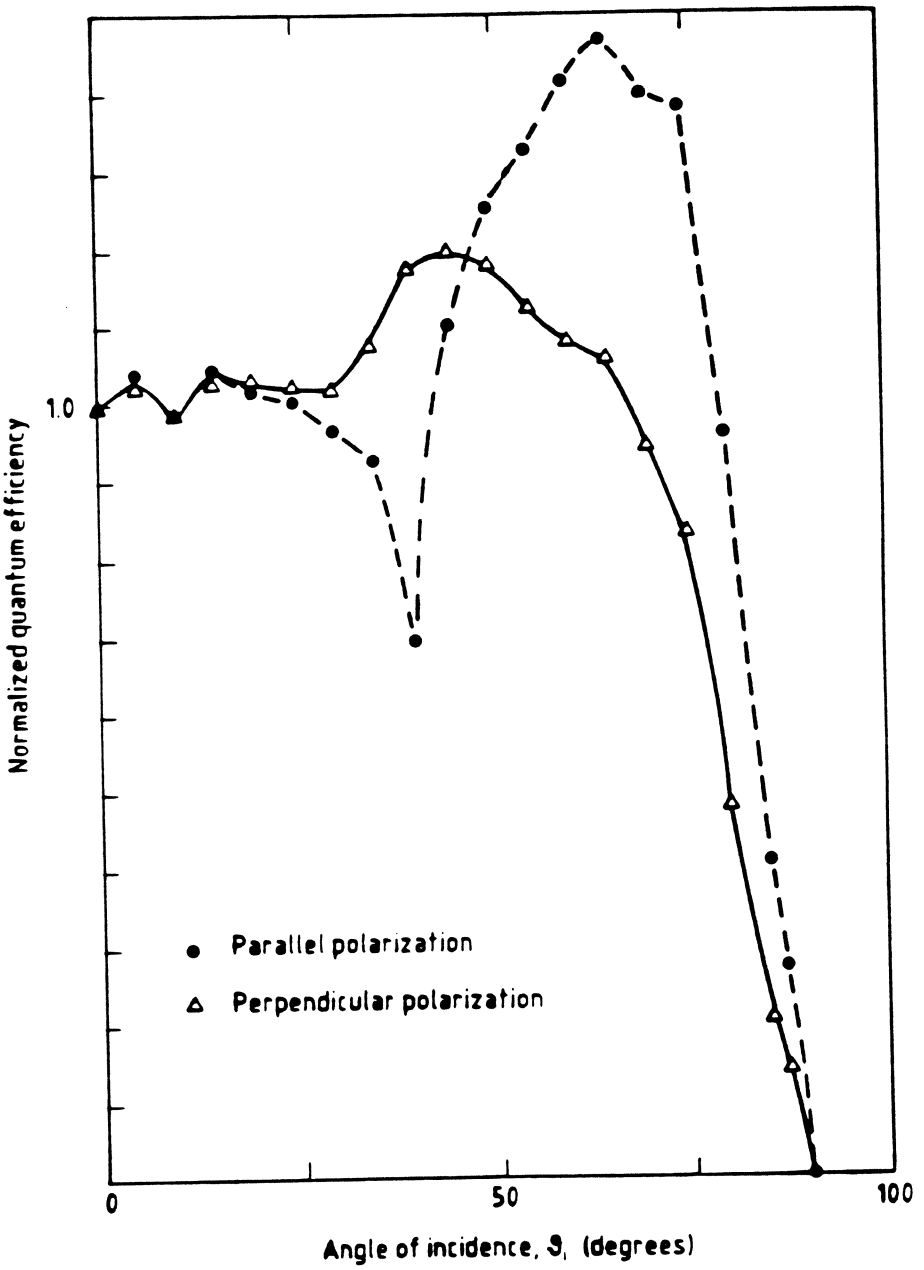

Figure 4.11: Measured angular dependence of the quantum efficiency of a bialkali photocathode from [60].

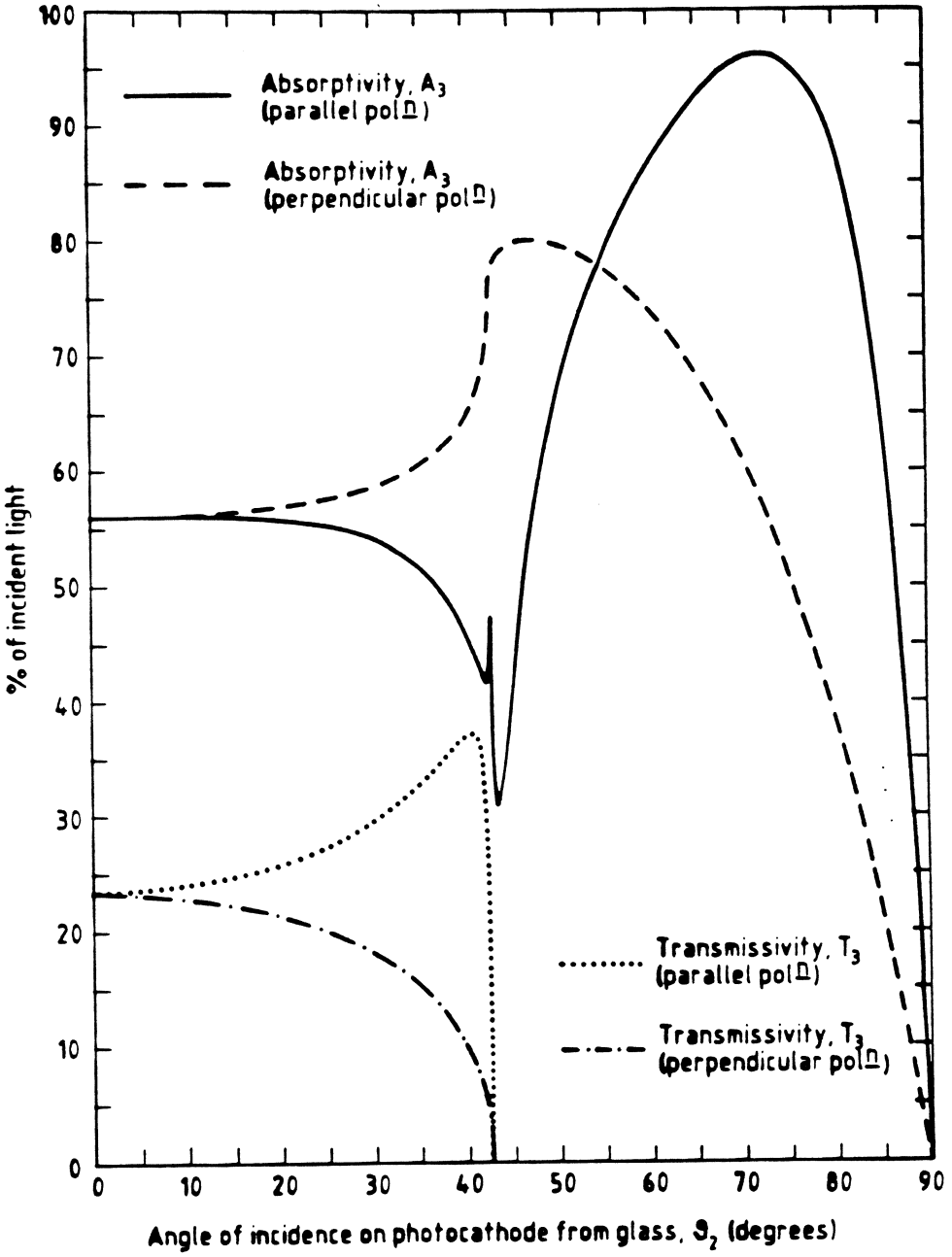

Figure 4.12: Calculated angular dependencies of the absorptivity and transmissivity of the bialkali photocathode assuming P1: $n_2 = 1.490$, $n_3 = 2.7$, $k_3 = 1.5$, $d = 23$ nm and $\lambda_0 = 442$ nm.

3. The photomultiplier used in the quantum efficiency measurement had a plano-concave window so that the measured angle of incidence, θ_i, does not correspond exactly to the angle of incidence at the photocathode, θ_2 — θ_i is slightly less than θ_2 but the exact relation between the two is not known because of uncertainties in the thickness of the glass window. This fact also precludes us from fitting the quantum efficiency data *directly* to the three parameter model.

Given these differences, the similarity in angular behaviour between the measured quantum efficiency and the calculated absorptivity is pleasing.

4.5 Inferred Optical Properties

From the theory presented in Section 4.3 and a given parametrization of the photocathode it is possible to calculate the optical properties of a photomultiplier with its window in contact with any medium of refractive index n_1. The optical properties we shall consider are the total reflectivity, R_t, total transmissivity, T_t, and total absorptivity, A_t, of the photomultiplier as a function of the angle of incidence at the PMT window, θ_1. These 'total' quantities are calculated by summing the geometrical series of the multiple reflections inside the photomultiplier window (Figure 4.4). With the aid of the usual combinatorial expansions they can be expressed as

$$R_t = R_{12} + \frac{R_3(T_{12})^2}{1 - R_{12}R_3} \tag{4.23}$$

$$T_t = \frac{T_{12}T_3}{1 - R_{12}R_3} \tag{4.24}$$

$$A_t = \frac{A_3T_{12}}{1 - R_{12}R_3} \tag{4.25}$$

where R_{12}, T_{12}, R_3, T_3 and A_3 are the same quantities as in Section 4.3.

Assuming P1 for the photocathode, i.e. the values $n_2 = 1.49$, $n_3 = 2.7$, $k_3 = 1.5$, $d = 23$ nm and $\lambda_0 = 442$ nm, these three total quantities have each been calculated for the three cases of the PMT window in contact with media of refractive indices 1.0 (gases), 1.34 (water) and 1.49 (scintillator, oil, glycerol etc.). The polarization averaged results are shown in Figures 4.13, 4.14 and 4.15.

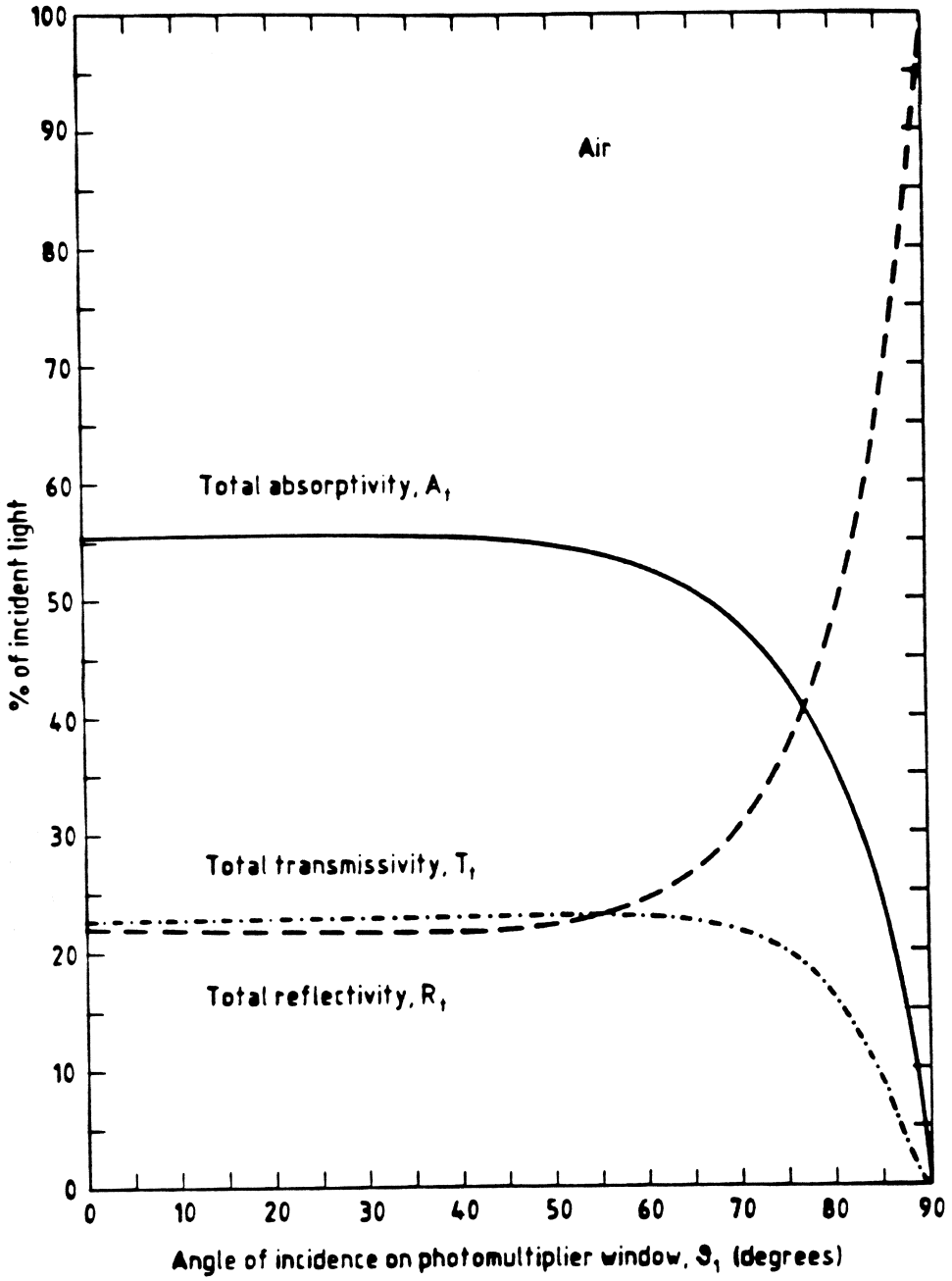

Figure 4.13: Calculated angular dependencies of the polarization averaged total absorptivity, reflectivity and transmissivity of a photomultiplier in *air* ($n_1 = 1.0$) assuming P1: $n_2 = 1.49$, $n_3 = 2.7$, $k_3 = 1.5$, $d = 23$ nm and $\lambda_0 = 442$ nm.

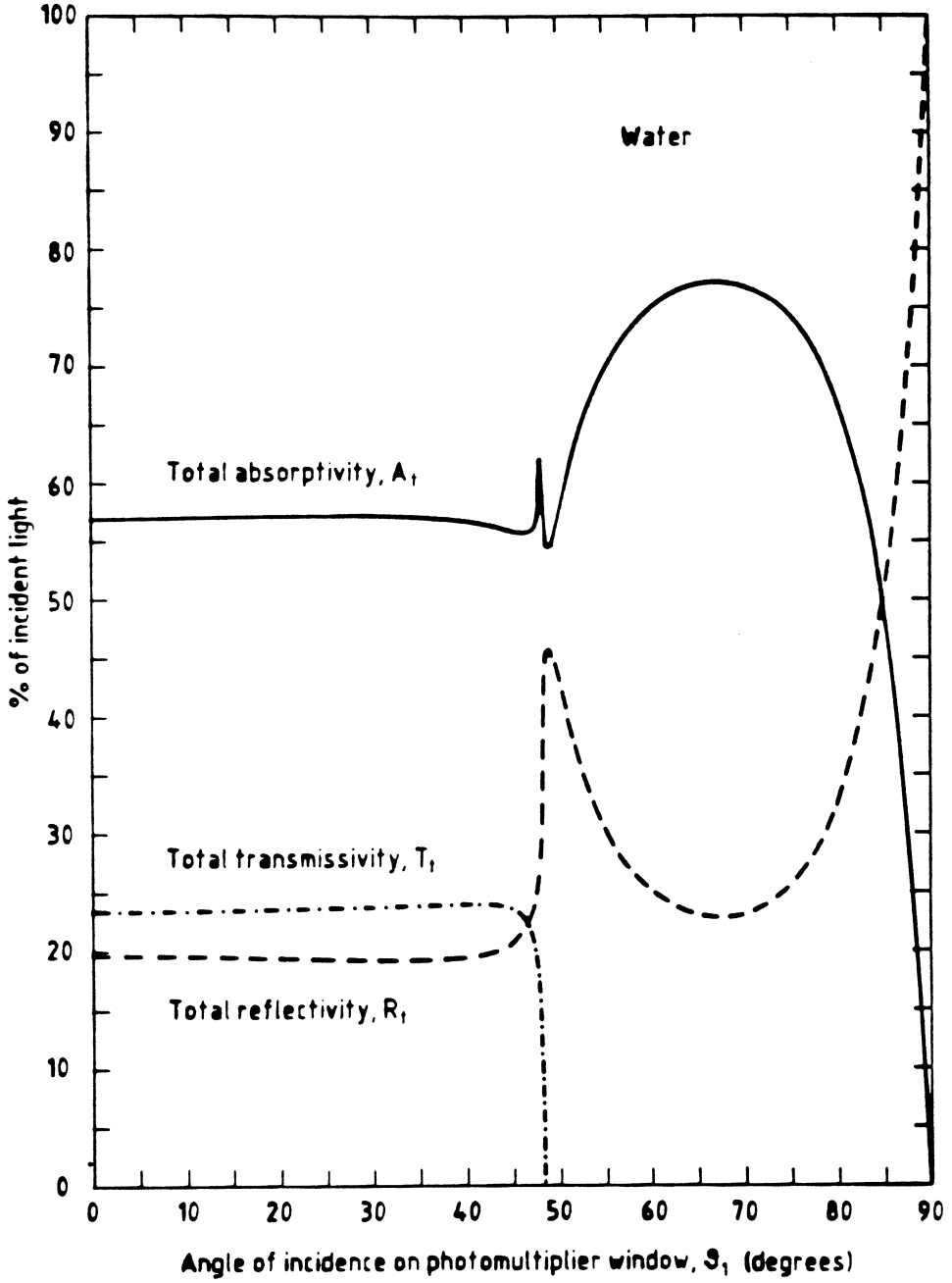

Figure 4.14: Calculated angular dependencies of the polarization averaged total absorptivity, reflectivity and transmissivity of a photomultiplier in *water* ($n_1 = 1.34$) assuming P1: $n_2 = 1.49$, $n_3 = 2.7$, $k_3 = 1.5$, $d = 23$ nm and $\lambda_0 = 442$ nm.

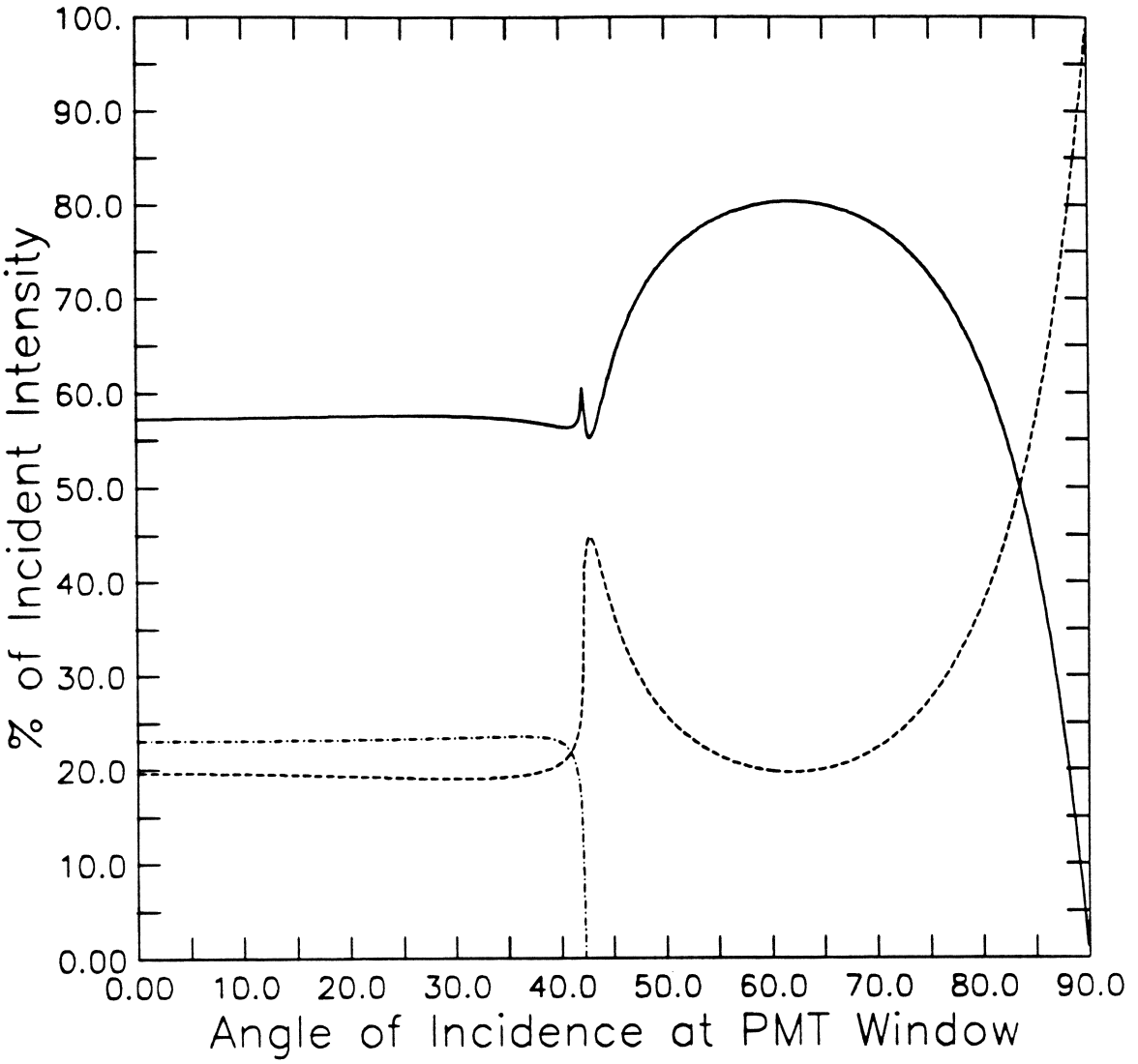

Figure 4.15: Calculated angular dependencies of the polarization averaged total absorptivity (——), reflectivity (– – –) and transmissivity (–·–·–) of a photomultiplier in *scintillator* ($n_1 = 1.49$) assuming P1: $n_2 = 1.49$, $n_3 = 2.7$, $k_3 = 1.5$, $d = 23$ nm and $\lambda_0 = 442$ nm.

For the photomultiplier in air the total reflectivity, transmissivity and absorptivity are constant at angles of incidence $\leq 50°$. Beyond 50° the reflectivity of the air/glass boundary begins to increase from its normal incidence 4%. At 75° it is already 25% and by 85° it has reached 61%. It is this sharp rise in reflectivity which dominates the cut-off in both absorptivity and transmissivity at large angles. The 54% absorptivity at near-normal incidence is consistent with the typical 24% quantum efficiency of bialkali photocathodes at this wavelength (see Figure 4.1) as roughly half the photo-electrons are

lost to the glass side of the photocathode and a few are trapped inside the photocathode.

When the photomultiplier is immersed in water the angular behaviour changes dramatically. Below the critical angle $\theta_{1,c}$ for total internal reflection (48.3°) the absorptivity, transmissivity and reflectivity are more or less constant. In the region of total internal reflection the absorptivity increases up to 80% as the transmissivity drops to zero and the reflectivity stays roughly the same apart from its narrow peak. The cut-off in absorptivity at large angles is dominated by the reflectivity of the water/glass boundary which is smaller than the reflectivity of the air/glass boundary, e.g. water/glass is 10% at 75° and 45% at 85°. Hence the photomultiplier is effective at larger angles of incidence in water than it is in air.

In scintillator ($n_1 = 1.49$) the behaviour of the photomultiplier is similar to its behaviour in water. The critical angle $\theta_{1,c}$ for total internal reflection is of course smaller (42.2°) and the reflectivity of the scintillator/glass boundary is clearly zero at all angles of incidence. Hence the total quantities R_t, T_t and A_t are simply given by R_3, T_3 and A_3. The cut-off in absorptivity at large angles is now caused by the rise in reflectivity of the glass/photocathode boundary which it is interesting to note is similar to that of the water/glass boundary, e.g. at 75° R_3 has increased by 9.5% from its normal incidence 19.5% and at 85° it has increased by 38%.

In SNO the effective wavelength spectrum of light which is detected by the photomultipliers peaks at about 380 nm with half maximum points at about 350 and 480 nm (Figure 2.4). Although P1 was measured at 442 nm, which is relatively well suited to the wavelength range of interest, and it is the most reliable parametrization obtained so far, it will be instructive to consider the parametrization which was obtained at 390 nm from the reanalysis of [51] in Section 4.4. Unfortunately the photocathode's complex refractive index is not uniquely determined from this measurement but is constrained to small regions of the 2D space (n_3, k_3) (see Figure 4.8). We shall consider two parametrizations which lie within the allowed regions of this 2D space: P2: $\tilde{n}_3 = 2.15 + i2.1$ with $d = 24$ nm for B1, and P3: $\tilde{n}_3 = 2.3 + i1.8$ with $d = 29$ nm for B3.

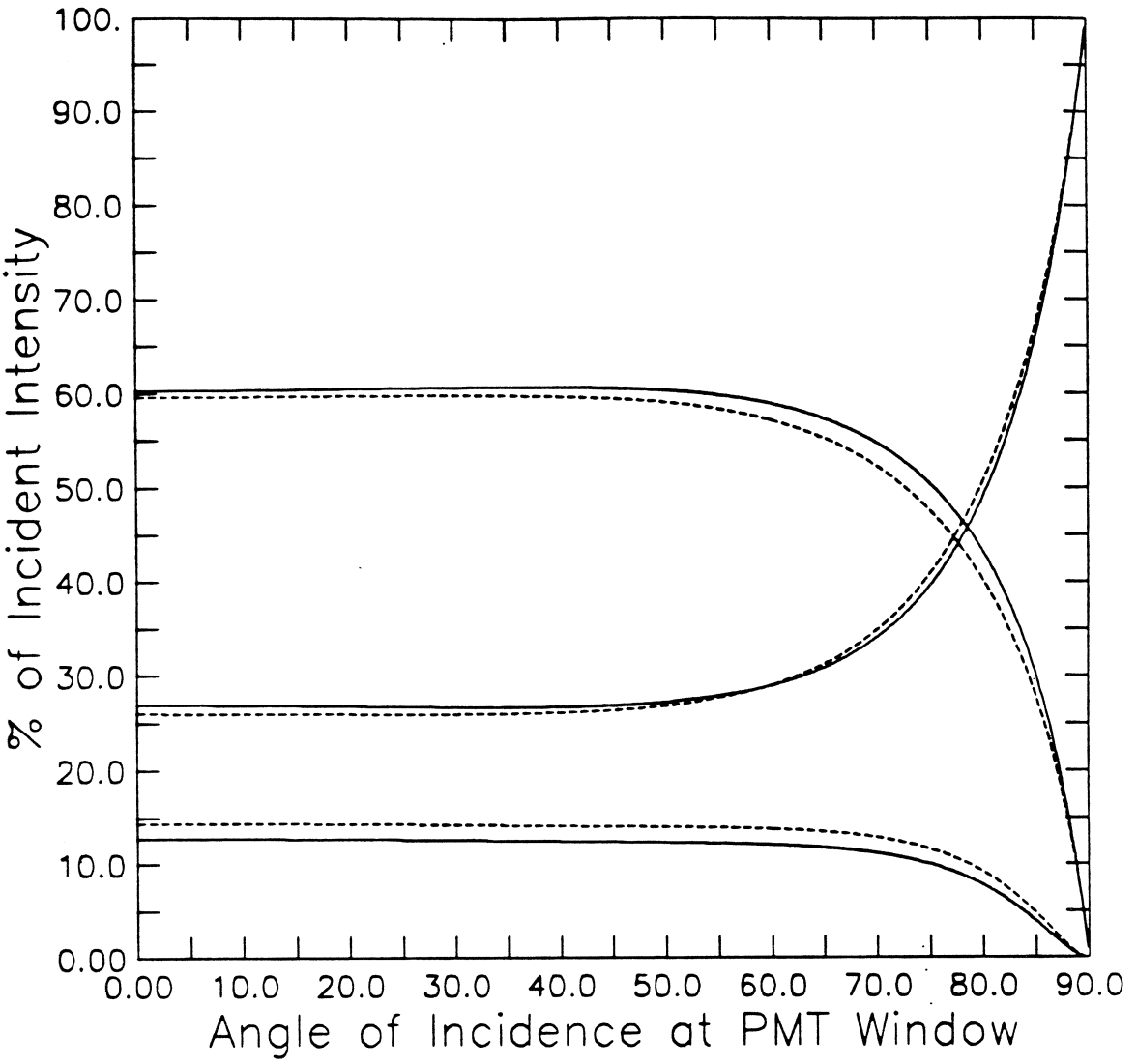

Figure 4.16: Calculated angular dependencies of the polarization averaged total absorptivity (begins at $\sim 60\%$), reflectivity (rises to 100% at 90°) and transmissivity of a photomultiplier in *air* ($n_1 = 1.0$) assuming P2 (– – –) and P3 (——), (see Table 4.3 for details).

Assuming these two parametrizations at 390 nm, the polarization averaged total absorptivity, reflectivity and transmissivity for the three cases $n_1 = 1.0$, $n_1 = 1.34$ and $n_1 = 1.49$ are shown in Figures 4.16, 4.17 and 4.18. The most striking feature of these three figures is how insensitive the optical properties are to the different parametrizations. The most significant difference between the three parametrizations considered so far is the increase (decrease) in the reflectivity (transmissivity) of the photocathode at 390 nm (P2 and P3) compared with 442 nm (P1).

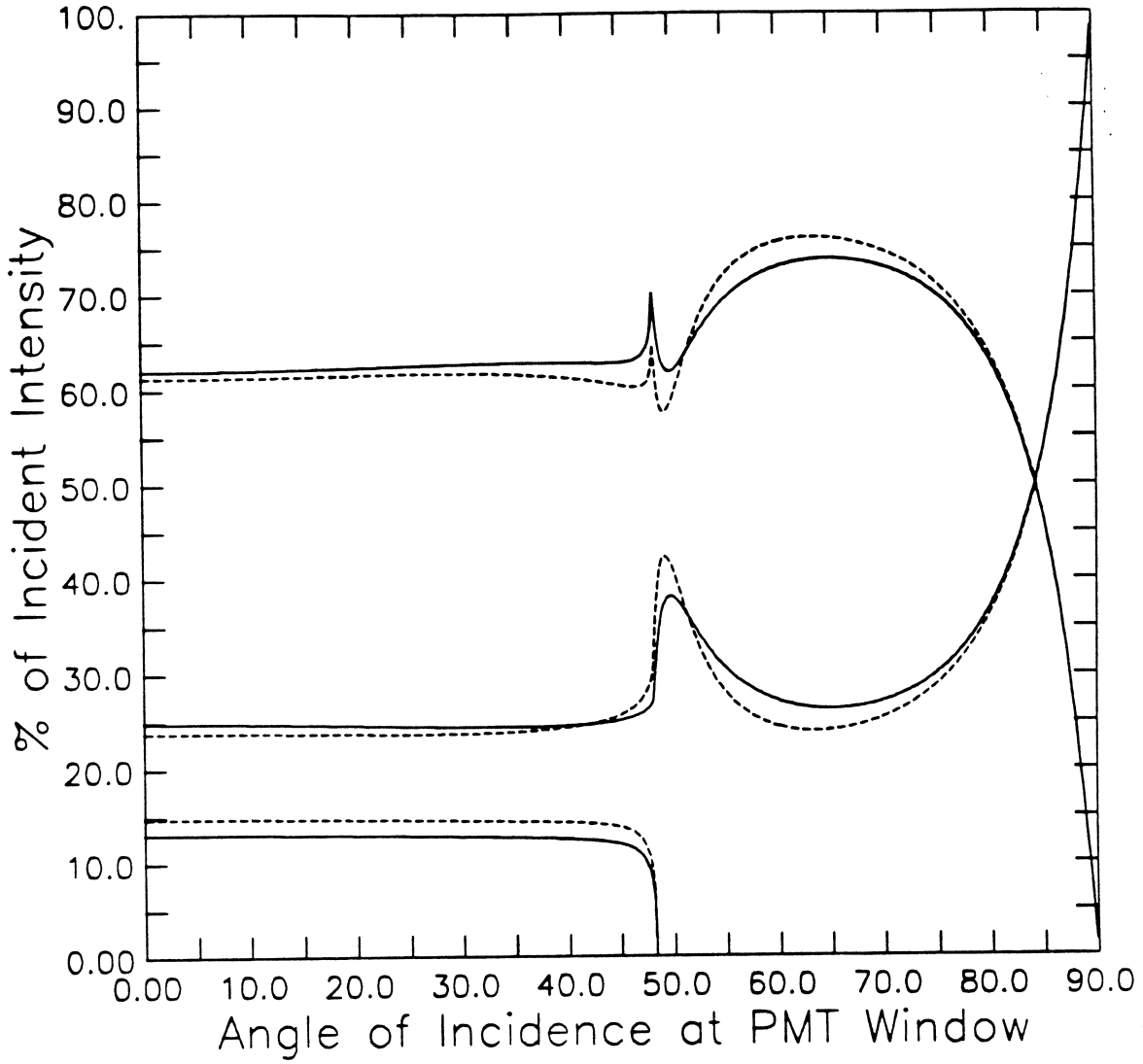

Figure 4.17: Calculated angular dependencies of the polarization averaged total absorptivity (begins at $\sim 62\%$), reflectivity (rises to 100% at 90°) and transmissivity of a photomultiplier in *water* ($n_1 = 1.34$) assuming P2 (– – –) and P3 (——), (see Table 4.3 for details).

In many PMTs, most of the light which is transmitted by the photocathode is reflected back onto the photocathode by an evaporated Al layer on the back hemisphere of the bulb (e.g. see Figure 6.1). Thus the transmitted light has a second chance of being absorbed. The net effect is to increase the overall efficiency of the PMT for angles of incidence $\theta_1 < \theta_{1,c}$. This makes the overall PMT efficiency a much more uniform function of the angle of incidence at the PMT window, even when the PMT window is in contact with media of refractive indices $n_1 = 1.34$ or 1.49 (see Figures 4.14–4.18).

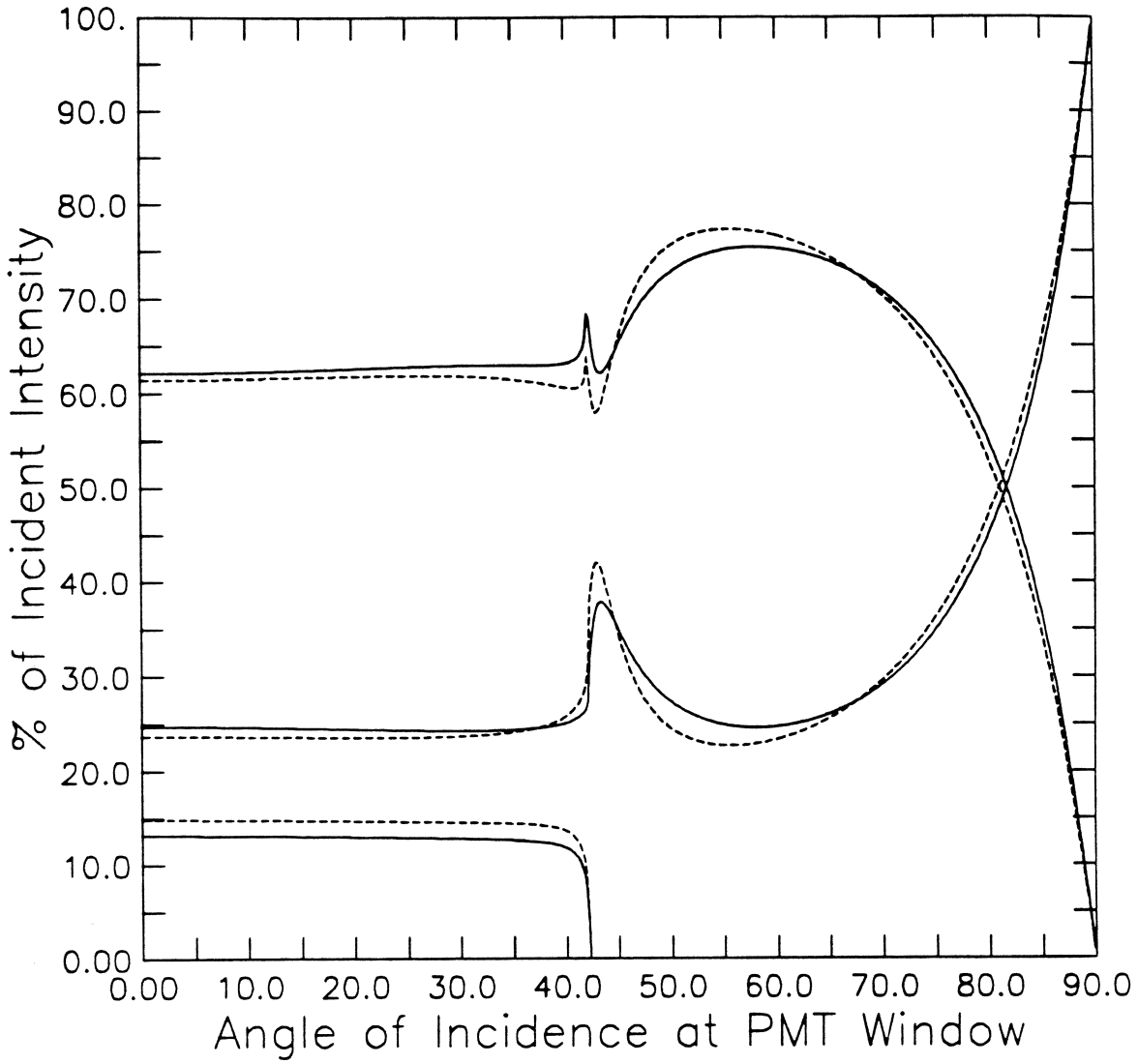

Figure 4.18: Calculated angular dependencies of the polarization averaged total absorptivity (begins at $\sim$ 62%), reflectivity (rises to 100% at 90°) and transmissivity of a photomultiplier in *scintillator* (n_1 = 1.49) assuming P2 (– – –) and P3 (——), (see Table 4.3 for details).

Let us quantify the cut-off in absorptivity of the PMT window/photocathode system at large angles that is observed in Figures 4.13 to 4.18, by defining θ_{cut} as the angle at which this absorptivity drops to 50% of its peak value. Table 4.3 shows the values of θ_{cut} for the three different photocathode parametrizations and the three different values of n_1 investigated. It is clear from this table that θ_{cut} does not depend significantly on the photocathode parametrization (at least for P1, P2 and P3) and depends only weakly on the value of n_1 (provided $n_1 \leq n_2$). If $n_1 > n_2$ then θ_{cut} is a few degrees less than

Param.	λ_0 (nm)	n_3	k_3	d (nm)	$\theta_{cut}(1.0)$	$\theta_{cut}(1.34)$	$\theta_{cut}(1.49)$
P1	442	2.7	1.5	23	84.0°	86.6°	85.4°
P2	390	2.15	2.1	24	84.4°	86.4°	84.1°
P3	390	2.3	1.85	29	85.0°	86.5°	84.7°
'average'	-	-	-	-	84.5°	86.5°	84.7°

Table 4.3: The angle θ_{cut} at which the absorptivity of the glass envelope/photocathode system drops to 50% of its peak value as a function of the refractive index (n_1) of the medium in contact with the window (1.0, 1.34 and 1.49) for P1, P2 and P3.

the critical angle for total internal reflection at the n_1/n_2 boundary which is given by $\sin^{-1}(n_2/n_1)$.

4.6 Conclusion

The detailed measurement of the angular dependence of the reflectivity in water of the bialkali photocathode, in particular the magnitude of the peak in the parallel polarization, allows an *unambiguous* determination of the photocathode's optical parameters. This measurement is able to avoid the ambiguities which are inherent in the interpretation of other measurements such as the three intensities. Thus the thickness and complex refractive index of the particular photocathode investigated have been reliably and accurately determined (P1).

A possible departure of $3.6 \pm 1.5\%$ from the three parameter model is observed in this measurement. It is much smaller than the departure reported for the multialkali photocathode under similar circumstances [56].

The results are consistent with a re-interpretation of the measurements of [51] from which the wavelength dependence of the real and imaginary parts of the refractive index, and two parametrizations at 390 nm (P2 and P3), have been obtained.

For the purposes of SNO, or any other Cherenkov detector, it would be very valuable to obtain more parametrizations of the bialkali photocathode across the wavelength range of interest and, in particular, for the actual PMTs used in the detector. The

method of determining photocathode parameters developed in Sections 4.2 and 4.3 is ideal for this purpose. It does not rely on photocathode *transmission* measurements, which are notoriously difficult and require the fabrication of special PMTs, but only on the measurement of the angular dependence of the PMT's *front reflectivity* in water, which can be measured relatively easily by laser with standard production PMTs.

The comparison of the angular dependences of the calculated absorptivity (for P1) and measured quantum efficiency [60] of a bialkali photocathode shows qualitative agreement. Unfortunately the comparison is limited by the differences between the assumptions of the absorptivity calculation and the experimental conditions of the quantum efficiency measurement. It would be most interesting to measure the angular dependences of the quantum efficiency and reflectivity of the *same* bialkali photocathode. The absorptivity could be deduced from the parametrization obtained from the reflectivity measurement. It could then be *directly* compared to the quantum efficiency to establish whether they both have the same angular dependences.

For the three photocathode parametrizations obtained here one can calculate the optical properties of a photomultiplier placed in any medium of given refractive index n_1. Three cases have been studied in detail ($n_1 = 1.0$, $n_1 = 1.34$ and $n_1 = 1.49$) from which it is concluded that the optical properties are relatively insensitive to the differences in the three photocathode parametrizations, apart from an overall change in the magnitude of the photocathode reflectivity and transmissivity between the parametrization at 442 nm wavelength (P1) and the parametrizations at 390 nm (P2 and P3). The overall efficiency of the PMT is approximately uniform with respect to the angle of incidence at the PMT window out to an angle $\theta_{\rm cut}$ which is largely insensitive to the different parametrizations and only weakly dependent on the value of n_1, as long as it does not exceed n_2, the refractive index of the PMT window (see Table 4.3).

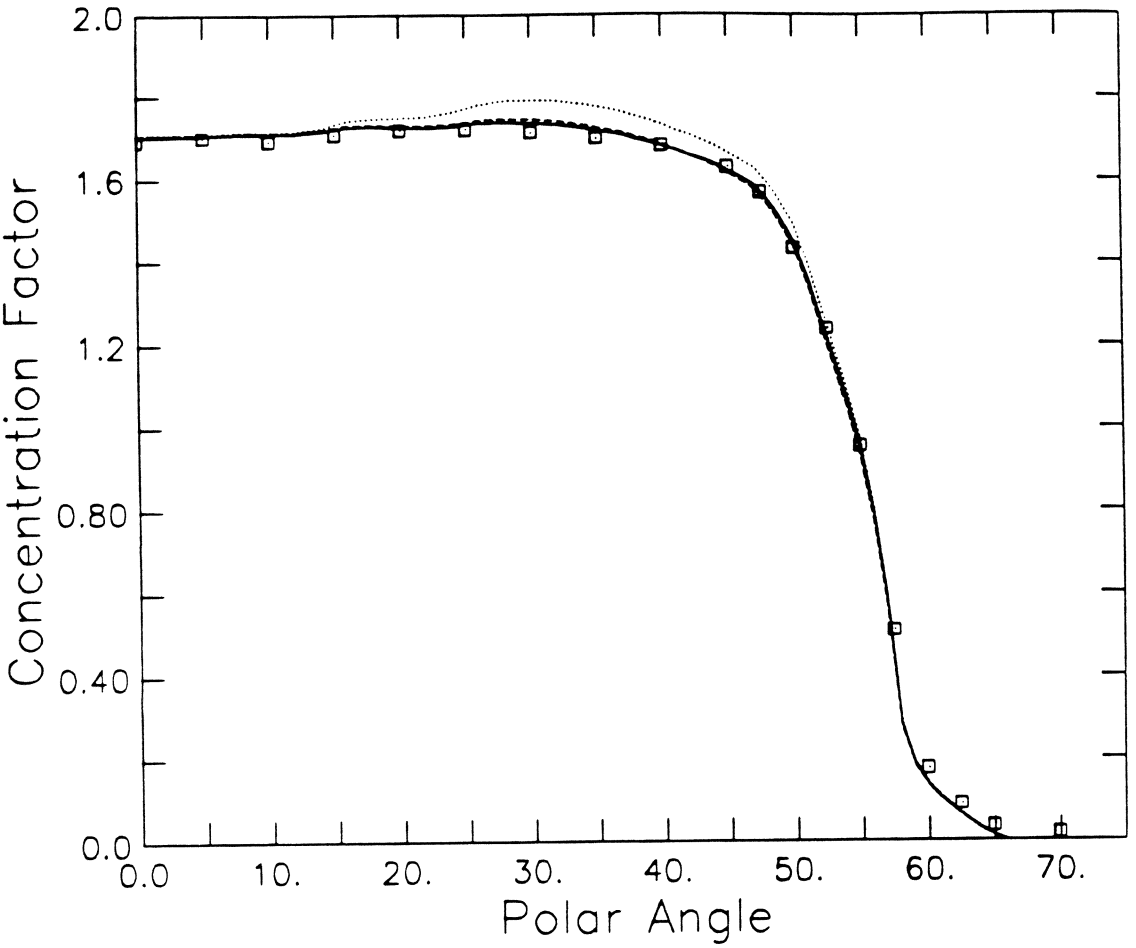

Figure 6.19: Measured concentration factor in *air* for the front surface glass/Al/MgF_2 concentrator. The three simulations assume P1 (·····), P2 (– – –) and P3 (——), and 84% reflectivity.

of the CTC and PMT are completely understood at the 1% level. However the global properties are clearly well understood and there are no significant errors in the ray-tracing simulation.

When the concentration factor of this front surface glass/Al/MgF_2 CTC was measured in water, the Al layer gradually lost its reflectivity, as it dissolved in the water! This behaviour of the Al/MgF_2 layer was not entirely unexpected (see Chapter 7) but the time scale of the corrosion was indeed surprising. Further measurements of glass/Al/SiO concentrators are planned, in which this effect should not recur.

The measurements of the concentration factors of the Omega prototype CTC in air and in water are shown in Figures 6.21 and 6.22. In both cases, the data below 20° has

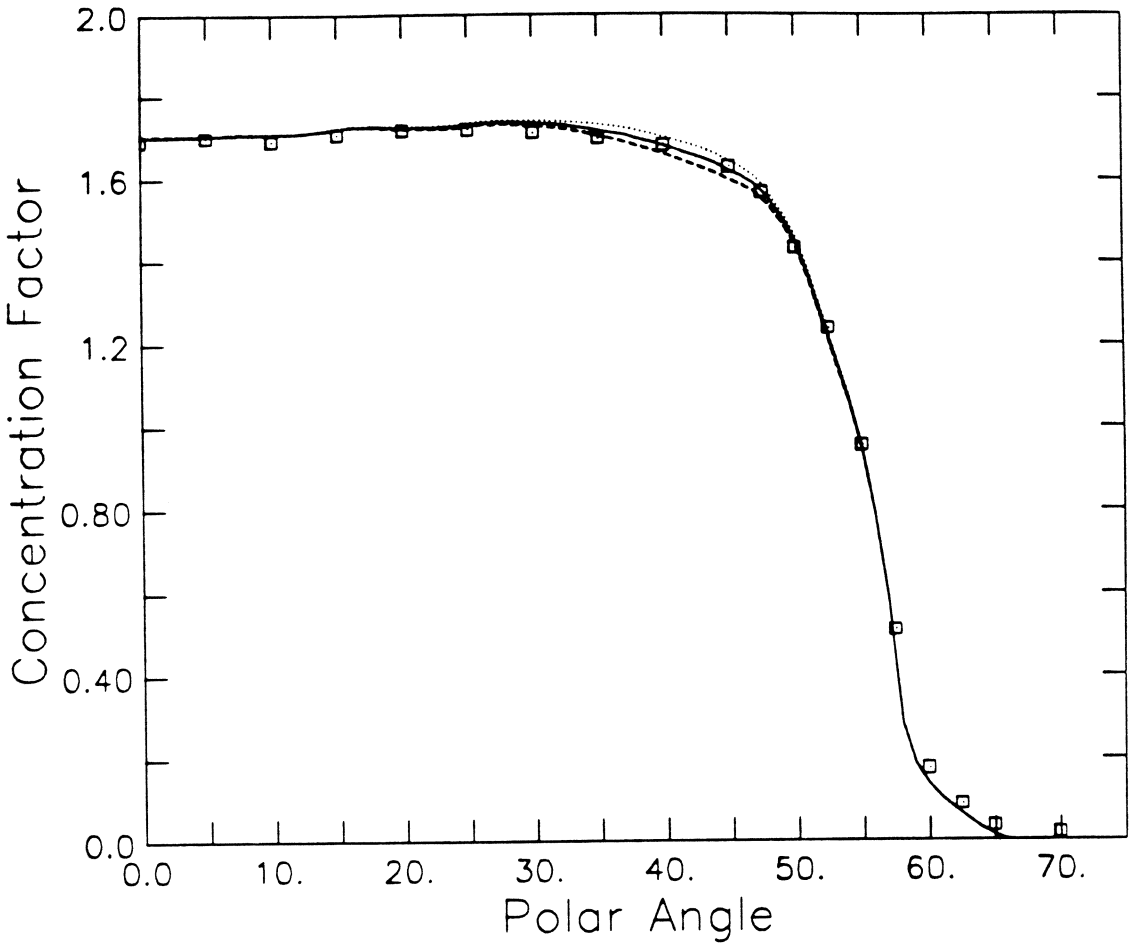

Figure 6.20: Measured concentration factor in *air* for the front surface glass/Al/MgF_2 concentrator. The three simulations assume 84% reflectivity, P3 and the following relative efficiencies for the band of photocathode below the equator: 0.25 (– – –), 0.5 (———) and 0.75 (· · · · ·).

been fitted, by eye, to simulated concentration factors in which the effective reflectivity of Omega is the only free parameter. For all three parametrizations the best fit values for this reflectivity are 85 ± 1% in air, which is consistent with the direct measurements of Omega reflectivity shown in Figure 6.11, and 80 ± 1% in water which is perhaps a little lower than expected, although the computer prediction of Figure 6.11 has recently come into question.

These effective reflectivities should be slightly higher for D_2O events in SNO where they will be averaged over the wavelength range 340–460 nm instead of the range 320–460 nm of this measurement. The theoretical concentration factors shown in Figures 6.21

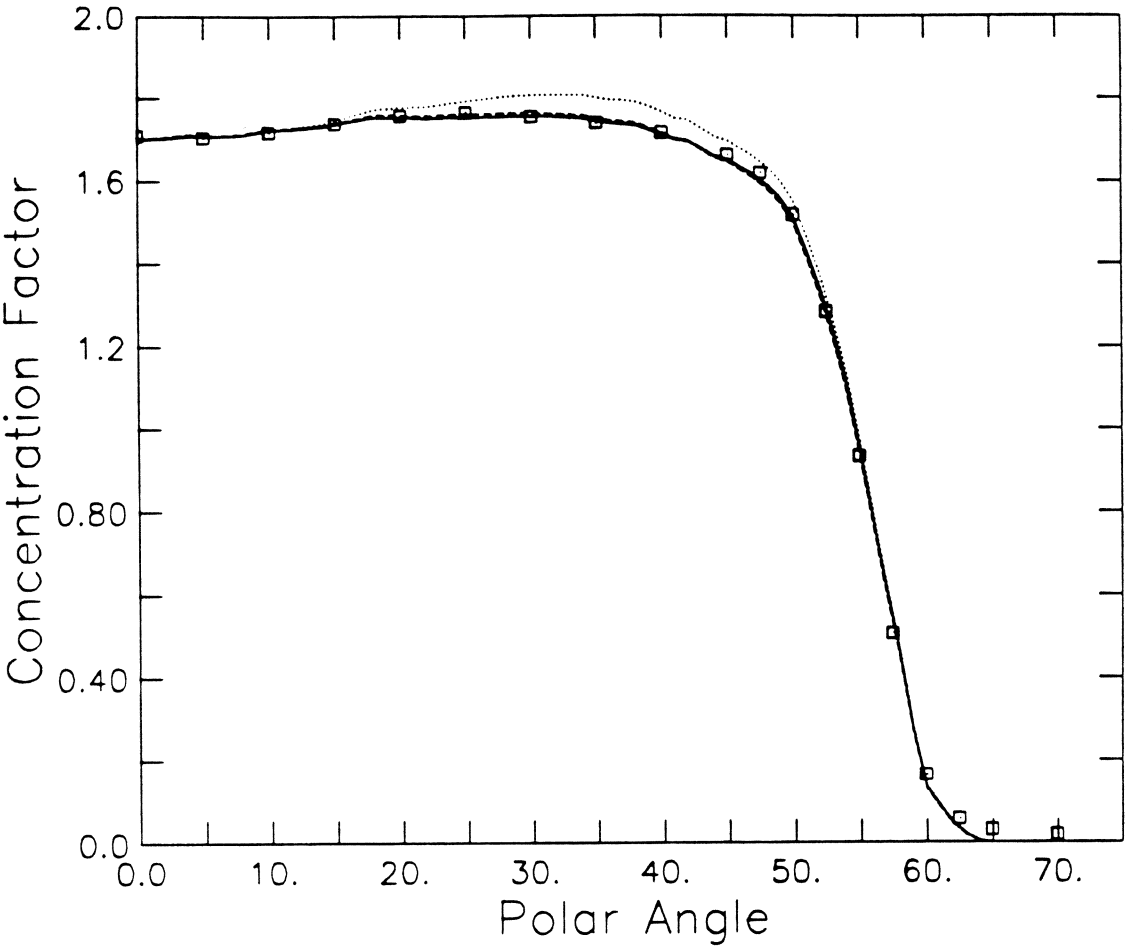

Figure 6.21: Measured concentration factor in *air* for the prototype Omega concentrator. The three simulations assume a (constant) effective reflectivity of 85%, and P1 (·····), P2 (– – –) and P3 (——).

and 6.22, for the three parametrizations, are simulated assuming that the above effective reflectivities do not depend on polar angle. From the excellent agreement between the data and the simulations with both P2 and especially P3, it is concluded that the effective reflectivities of Omega in air and in water do not vary significantly with polar angle. This result simplifies the simulation task enormously.

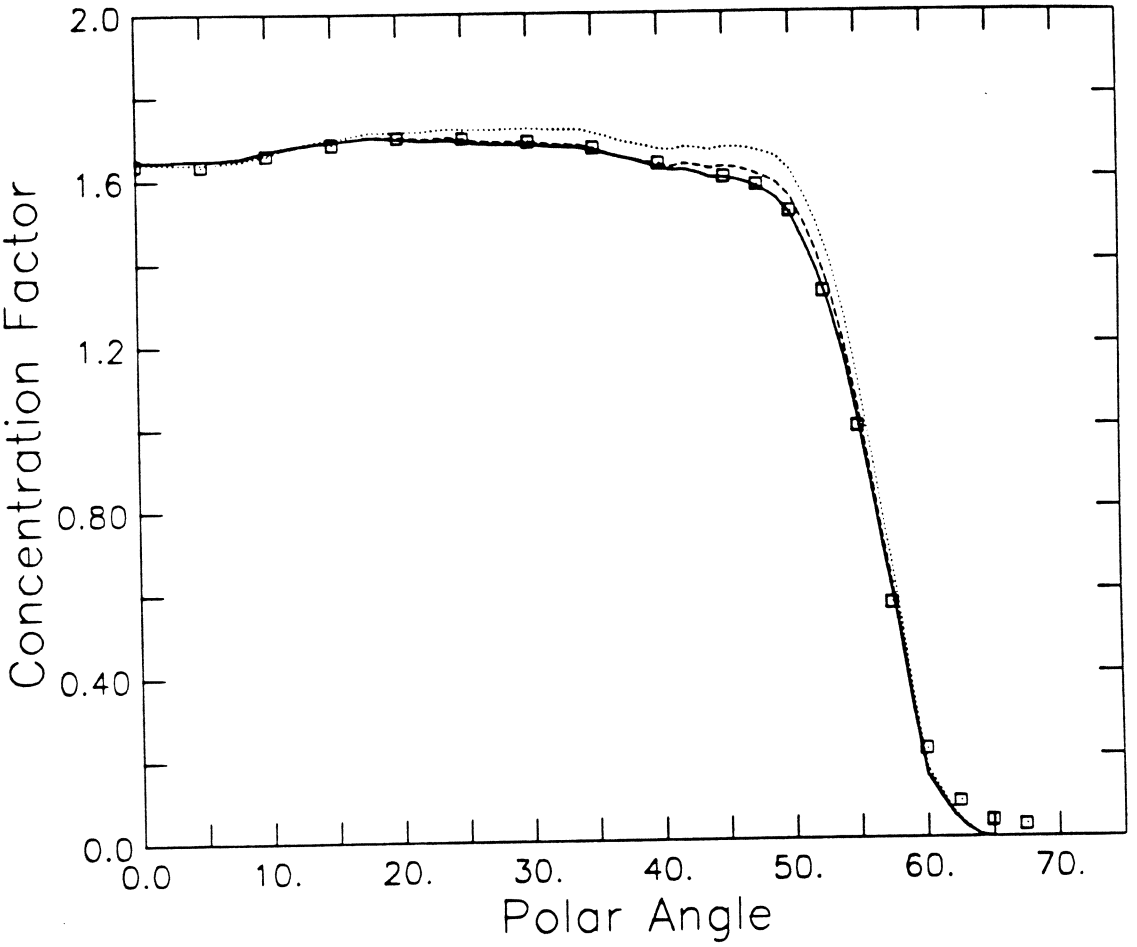

Figure 6.22: Measured concentration factor in *water* for the prototype Omega concentrator. The three simulations assume a (constant) effective reflectivity of 80%, and P1 (·····), P2 (– – –) and P3 (——).

6.5 Conclusion

The measurement of the front surface glass/Al/MgF_2 CTC's concentration factor in air demonstrates that the ray-tracing programme accurately simulates the behaviour of both the concentrator and the photomultiplier. Furthermore, this data favours P2 and P3.

The measured concentration factors in air and in water of the prototype Omega CTC can be reproduced by a simulation in which the effective reflectivity is $85 \pm 1\%$ in air and $80 \pm 1\%$ in water and in both cases, independent of polar angle. In SNO, one can expect these values to increase slightly for events in the D_2O and decrease for events in the H_2O.

Unfortunately the concentration factors of back surface glass/Al/TiO CTCs made with good quality U.V.transmitting glass have not been measured. However it is estimated that the edge-effect caused by the ground glass rims in these CTCs would be of the same order of magnitude as the edge-effect caused by the black lips in the Omega CTCs. In theory the reflectivity of these CTCs would be 89% in both air and water (Figure 6.8). In practice it tends to be about 87%, as measured by laser (442 nm) on samples of evaporated glass/Al/TiO.

Thus the concentration factors of the two prototype SNO concentrators are most likely to be very similar with the glass/Al CTC probably a few percent higher than the Omega CTC. Therefore the decision between the two was made on the basis of practical considerations such as water survival, robustness and cost (see Chapter 7); the Omega design being finally adopted.

At present, the design phase of the Omega SNO concentrator is coming to a close. Drawings for injection moulded plastic holders will soon be sent to potential manufacturers. The parameters of the final design are as follows: (i) an exit aperture of polar radius 98 mm; (ii) a Liouville cut-off angle of 56.4°; (iii) a skew parameter of $h_{rel} = 0.6$ (see Section 5.6); (iv) a 24% truncation in axial length corresponding to a 2% decrease in entrance aperture area; and (v) a 24-sided polygonal holder with 2 mm lips at either

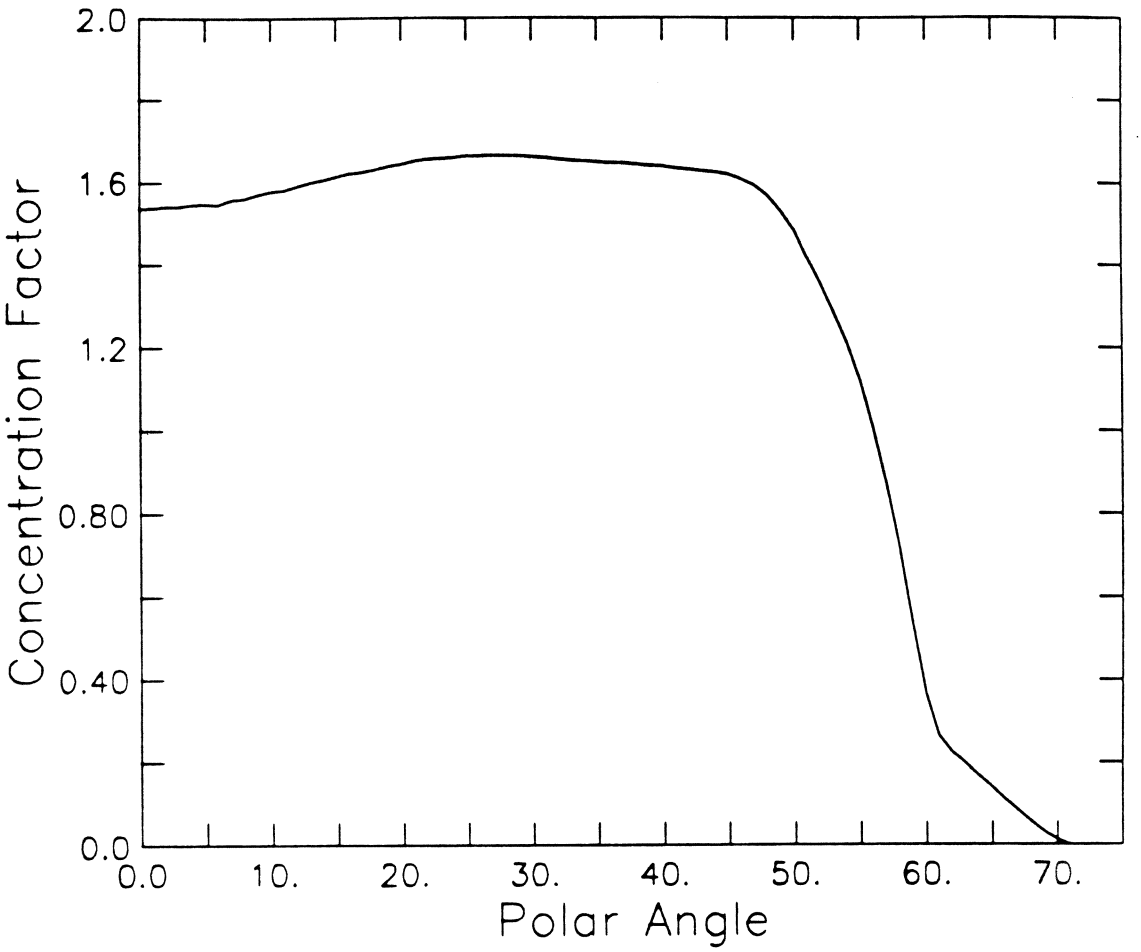

Figure 6.23: Simulated concentration factor in water of the SNO Omega concentrator (see text for details) assuming a constant effective reflectivity of 80% and P3.

end to hold in the petals with a compressive stress of 0.8 N/mm (see Figure 6.15 for the resulting profile of the petals).

The concentration factor of this CTC in water has been simulated assuming P3, the radial dependence of the photocathode efficiency shown in Figure 6.3, a constant effective reflectivity of 80% and a bare PMT which is *not* masked off beyond r_{polar} = 98 mm in the normalisation of the concentration factor. The resulting angular response is shown in Figure 6.23 where the 8% dip in concentration factor at small polar angles is caused by light being funneled, at these polar angles, onto the lower lip of the black plastic holder and the edge of the photocathode where the efficiency is lower.

The corresponding radial response for this angular response, ignoring absorption in the acrylic, H_2O and D_2O, is shown in Figure 6.24. The 7% non-uniformity inside

Chapter 5

Theoretical Performance of CTCs

5.1 Introduction

The concentration of light onto photomultipliers is an important consideration for all scintillation and Cherenkov counters, particularly the latter as the light intensities are about two orders of magnitude lower, and concentration becomes a major concern for large volume detectors (up to the order of 10^3 m^3) employing large numbers of photomultipliers. It should be pointed out that the use of concentrators is not restricted to the geometry of Figure 3.1. They are equally efficient in any situation where the source fills a cone of half angle θ_i. Another example of such a geometry is a cylindrical light guide which relies on total internal reflection, see Figure 5.1. In this case θ_i is given by $\frac{\pi}{2} - \theta_c$ where θ_c, the critical angle for total internal reflection, is given by $\sin^{-1}(n_0/n_1)$. Typical values of θ_i for commonly occurring ratios n_0/n_1 are

n_0/n_1	θ_c	θ_i
1.0/1.49	42.2°	47.8°
1.0/1.34	48.3°	41.5°
1.34/1.49	64.1°	25.9°

All of the bigger photomultipliers, and some as small as 50 mm diameter, have convex photocathodes due to the practical necessity to provide mechanical strength for the glass

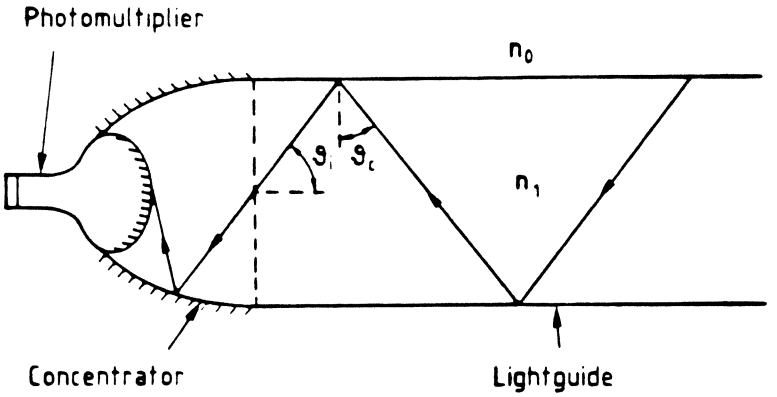

Figure 5.1: Geometry of photomultiplier/concentrator with totally internally reflecting light guide.

entrance window and to optimize the collection of photo-electrons by the first dynode and the transit time spread. The curvature of the photocathode is not always spherical and is dictated by the requirements of the electron optics of the photomultiplier and the minimisation of stresses in the glass bulb.

The most general photocathode shape that will be considered here is an axisymmetric *convex* photocathode of which the 2D profile can be defined in terms of the polar coordinates (r, θ) where r is a known function of θ and where θ is restricted to the range $-\theta_{cath} \rightarrow \theta_{cath}$ (see Figure 5.2). In 3D, the shape of this photocathode can be defined in terms of the spherical coordinates (r, θ, ϕ) where r is the same function of θ as for the 2D profile and where θ is restricted to the range $0 \rightarrow \theta_{cath}$ and ϕ to the range $0 \rightarrow 2\pi$. The angle between the normal to the photocathode at the photocathode edge (where $\theta = \theta_{cath}$) and the vertical ($\hat{\mathbf{z}}$) is called α_{cath} and the polar radius (in 3D) of the edge of photocathode is called r_{polar}.

It has been established in Chapter 4 that the overall efficiency of a PMT with a K_2CsSb bialkali photocathode is approximately uniform with respect to angle of incidence at the PMT window out to an angle θ_{cut} which is respectively 84.5°, 86.5° and 84.7° when the PMT window is immersed in media of refractive indices 1.0, 1.34 and 1.49, (see Table 4.3). Compared with an 'ideal' photocathode (uniformly efficient out to 90° incidence) this represents a decrease in the phase space acceptance ($\sin^2 \theta_{max}$) of

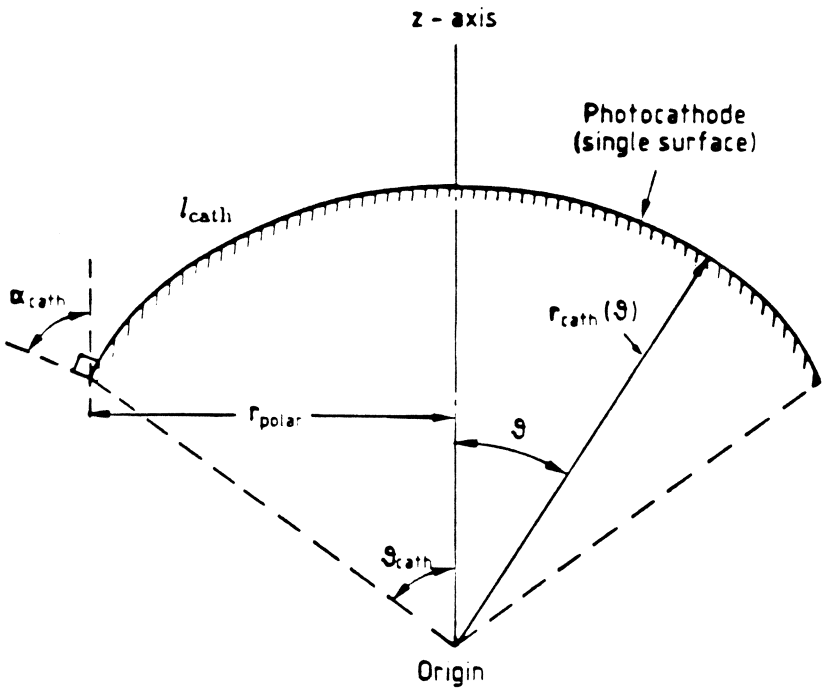

Figure 5.2: Cross-section of a generic convex photocathode. Notice that α_{cath} does not necessarily equal θ_{cath} unless the photocathode is spherical.

about 1%, 0.5% and 1%, respectively. These are very small corrections which in this chapter will be disregarded and the PMT window/photocathode system will be approximated by a (single surface) ideal photocathode. Thus the profile of the concentrator can be generated by applying the tangent-ray principle and the $\sin^2\theta_{max}$ factor in the Liouville limit on concentration, (3.5) and (3.8), can be ignored.

Furthermore it will be assumed throughout this chapter that all concentrators are made with 'ideal' reflective surfaces (100% reflectivity). Thus the discussion in this chapter will aim to establish the *theoretical* performance of CTCs and how these depend on the *shapes* of the CTC and of the photocathode. The effect of real reflective surfaces and the complicated angular behaviour of the K_2CsSb photocathode on the performance of CTCs will be investigated in Chapter 6.

It will also be assumed, until Section 5.7, that the refractive index is constant throughout the optical system so that the $(n_2/n_0)^2$ factor in the Liouville limit on concentration, (3.5) and (3.8), can also be disregarded.

5.2 Application of the Tangent-Ray Principle

Strictly the tangent-ray principle described in Section 3.4 which operates on the 2D cross-section of the photocathode is sufficient for the design of a CTC only in the cases where (i) $\theta_i + \alpha_{cath} = \frac{\pi}{2}$, where the entire profile is generated by the stated tangent-ray principle; and (ii) $\theta_i + \alpha_{cath} > \frac{\pi}{2}$, where the lower section of the profile is an involute of the photocathode and the upper section is generated by the tangent-ray principle (Figure 3.11). The third case where $\theta_i + \alpha_{cath} < \frac{\pi}{2}$ can also be solved in terms of the tangent-ray principle by the device of providing the edge of the photocathode with an extension of small meridional radius of curvature ϵ out to the angle $\alpha_{cath} = \frac{\pi}{2} - \theta_i$ (see Figure 5.3). The concentrator can then be designed for arbitrarily small ϵ. In the limit of $\epsilon \rightarrow 0$ the uppermost section of the CTC profile becomes an off-axis parabola identical to the off-axis parabola from which the entire profile of the Winston cone is constructed (Figure 3.5).

The first order linear differential equations for generating the CTC profile from the tangent-ray principle have been derived in Appendix H of [49]. These equations are valid for the general convex photocathode considered here (Figure 5.2) but have only been specifically formulated for the case $\theta_i + \alpha_{cath} > \frac{\pi}{2}$ as it is assumed that the 2D profile of the absorber (photocathode) is a closed loop, i.e. $\alpha_{cath} = \pi$. In Appendix A of this thesis the derivation of these differential equations is reproduced and the resulting equations are adapted so that the 2D profiles of CTCs can be constructed for all three of the above cases ($\theta_i + \alpha_{cath} >, =, < \frac{\pi}{2}$).

Thus the profile of a 2D CTC can be constructed for *any* combination of limiting angle and convex photocathode shape. The resulting Liouville-exact 2D CTC will have both the ideal transmission-angle characteristic and the maximum concentration ratio in 2D, i.e.

$$\frac{l_{conc}}{l_{cath}} = \frac{1}{\sin \theta_i} \tag{5.1}$$

where l_{conc} is *half* the entrance aperture length of the CTC, l_{cath} is *half* the *arc-length* of the 2D cross-section of the photocathode and θ_i is the limiting angle defining the angular

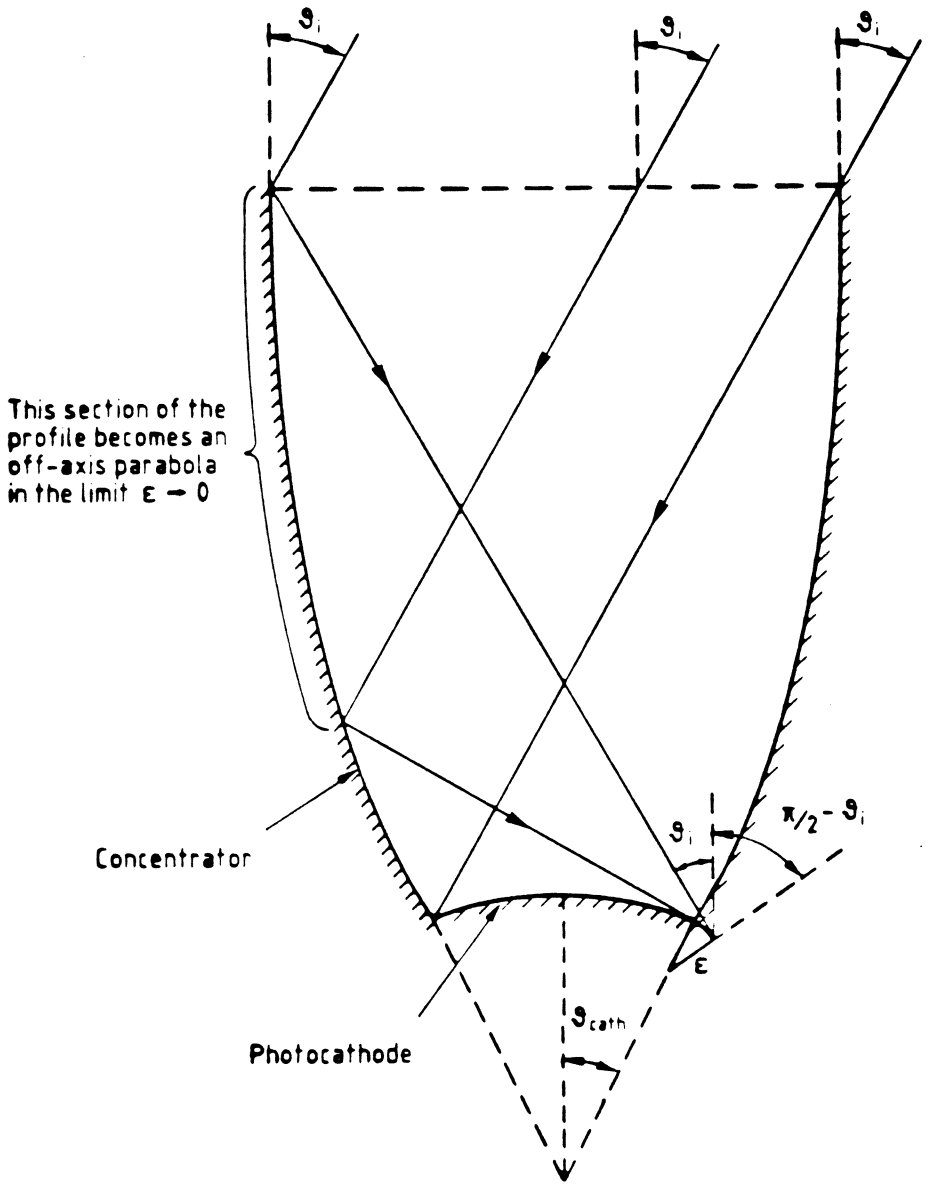

Figure 5.3: Construction of the CTC profile by the tangent-ray principle for the case $\theta_i + \alpha_{cath} < \frac{\pi}{2}$. An extension of small meridional radius of curvature ϵ out to the angle $\alpha_{cath} = \frac{\pi}{2} - \theta_i$ is added to the edge of the photocathode. In the limit of $\epsilon \rightarrow 0$ the upper portion of the profile becomes an off-axis parabola.

acceptance of the CTC.

A 3D CTC for a convex photocathode is simply the surface of revolution of the corresponding 2D CTC constructed with reference to the 2D cross-section of the photocathode and with the appropriate limiting angle θ_i. The transmission-angle curves of these 3D CTCs have been investigated by computer simulation using a ray tracing method. At each polar angle (θ), 9,600 rays starting on a square grid across the CTC entrance aperture were traced until they were either transmitted to the photocathode or rejected by the CTC (assuming 100% reflectivity). The transmission-angle curves of the corresponding 2D CTCs were also simulated by tracing, at each polar angle (θ), 9,600 rays equally spaced on the meridional diameter of the concentrator entrance aperture. Typical results of the ray tracing simulation are shown in Figure 5.4. In the simulation the 2D profile of the concentrator was approximated by about 400 straight line segments which joined points on the true profile; and the 3D shape of the concentrator was represented by the corresponding 400 conical segments. If the number of straight line segments (and hence also conical segments) was increased the 2D transmission-angle curves moved even closer to the perfect cut-off at θ_i but the 3D transmission-angle curves did not change.

5.3 The Liouville Theorem Revisited

At first it might seem from the transmission-angle curves in Figure 5.4 that the 3D CTCs are not conserving the phase space acceptance of the photocathode since their transmission cut-offs are not spread symmetrically about θ_i as in the case of Winston cones (Figure 3.7). In fact the 3D transmission-angle curves in Figure 5.4 conserve phase space exactly and the Liouville theorem itself implies that the 3D cut-off should occur at a smaller angle than θ_i.

The 3D CTC has a *flat* entrance aperture and so its area A_{conc} is related to the half-length of its 2D entrance aperture, l_{conc}, by the simple relation

$$A_{conc} = \pi l_{conc}^2. \tag{5.2}$$

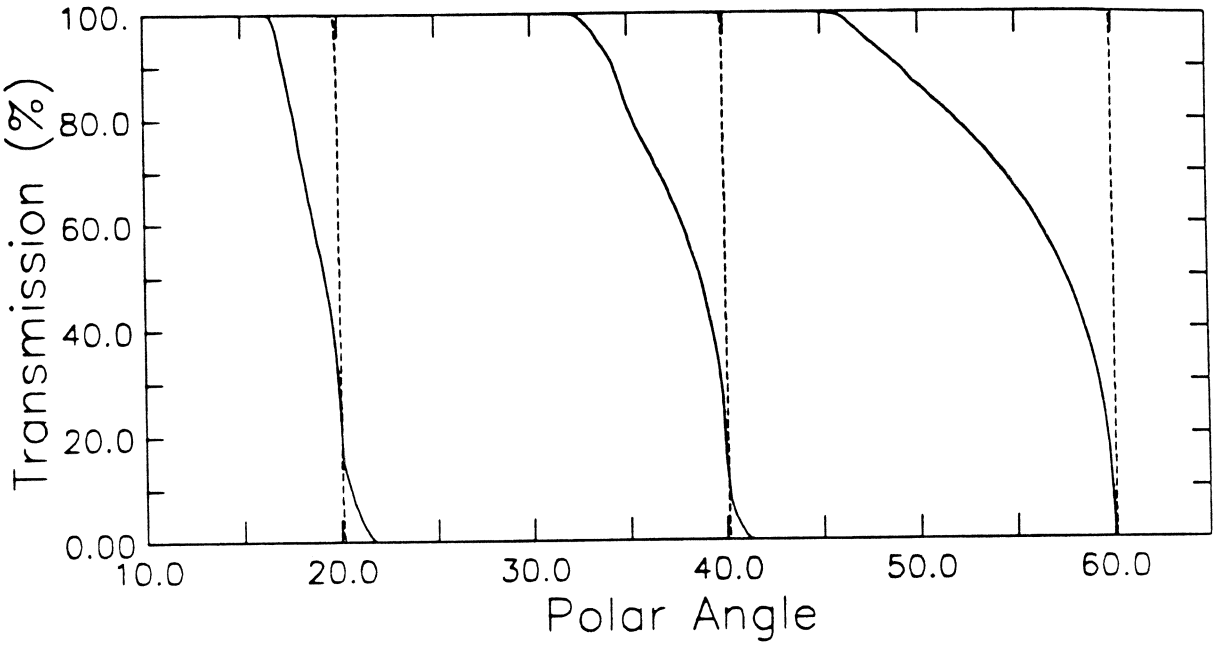

Figure 5.4: Computed transmission-angle curves for 2D (– – –) and 3D (——) CTCs with limiting angles θ_i = 20°, 40° and 60° and which have all been constructed with reference to the same photocathode shape (a spherical photocathode of half angle θ_{cath} = 60°).

In contrast the relation between the area of the photocathode A_{cath} and its half-arc-length in 2D, l_{cath}, is more complicated but it can be shown for any *convex* photocathode that

$$A_{cath} < \pi l_{cath}^2. \tag{5.3}$$

Dividing (5.2) by (5.3) one obtains the following inequality which can be related to the limiting angle θ_i through (5.1):

$$\frac{A_{conc}}{A_{cath}} > \frac{l_{conc}^2}{l_{cath}^2} = \frac{1}{\sin^2 \theta_i}. \tag{5.4}$$

This inequality implies that the 3D CTC has a greater concentration ratio than is allowed by the Liouville theorem, i.e. (3.5) assuming $\sin^2 \theta_{max} = 1$ and $n_2/n_0 = 1$. The entrance area A_{conc} of the 3D CTC is too great for it to collect all the light within the angle θ_i (that it was designed for in 2D) without violating the conservation of phase space.

Let us define θ_{ps} as the limiting angle of a Liouville-exact concentrator with the same

entrance aperture area as the given 3D CTC, i.e.

$$\frac{A_{\text{conc}}}{A_{\text{cath}}} = \frac{1}{\sin^2 \theta_{\text{ps}}} \tag{5.5}$$

By substituting A_{conc} in this equation with l_{cath} from (5.2) and (5.1) one finds that

$$\sin \theta_{\text{ps}} = \sqrt{\frac{A_{\text{cath}}}{\pi l_{\text{cath}}^2}} \sin \theta_{\text{i}} \tag{5.6}$$

where the factor in the square root depends only on the shape of the photocathode and is necessarily less than 1 for all convex photocathodes (see (5.3)). In Figure 5.5 the 3D CTC transmission-angle curves of Figure 5.4 are compared to the ideal transmission-angle curves of the corresponding Liouville-exact concentrators with limiting angles θ_{ps} given by (5.6). It is clear from the figure that the 3D CTCs have the same phase space acceptance as the Liouville-exact concentrators which by definition conserve the phase space acceptance of the photocathode.

This can be confirmed numerically by calculating the phase space acceptances of the Liouville-exact concentrators and the 3D CTCs which are both given by

$$\Psi_{\text{conc}} = \pi A_{\text{conc}} E_{\text{cath}} \int_0^{\frac{\pi}{2}} T(\theta) \sin 2\theta \, d\theta \tag{5.7}$$

where E_{cath} is the (constant) efficiency of the photocathode and $T(\theta)$ is the probability of transmission to the photocathode as a function of polar angle θ averaged over the concentrator's entrance aperture, i.e. the transmission-angle curve. Evaluating these integrals numerically it is found that the 3D CTCs in Figure 5.5 conserve the phase space acceptance of the photocathode to better than 1 part in 10,000.

However it is also clear from Figure 5.5 that the 3D CTCs do not have the desired ideal transmission-angle characteristic. This departure from the ideal can be quantified by calculating the fraction $\Delta\Psi$ of the photocathode's available phase space which is *not* accepted by the concentrator *inside* the angle θ_{ps}, i.e.

$$\Delta\Psi = \left[\pi A_{\text{conc}} E_{\text{cath}} \int_0^{\theta_{\text{ps}}} (1 - T(\theta)) \sin 2\theta \, d\theta\right] / \Psi_{\text{cath}} \tag{5.8}$$

For the three CTCs in Figure 5.5, $\Delta\Psi$ is respectively 5.5%, 4.5% and 4.2%, starting with the CTC of smallest limiting angle.

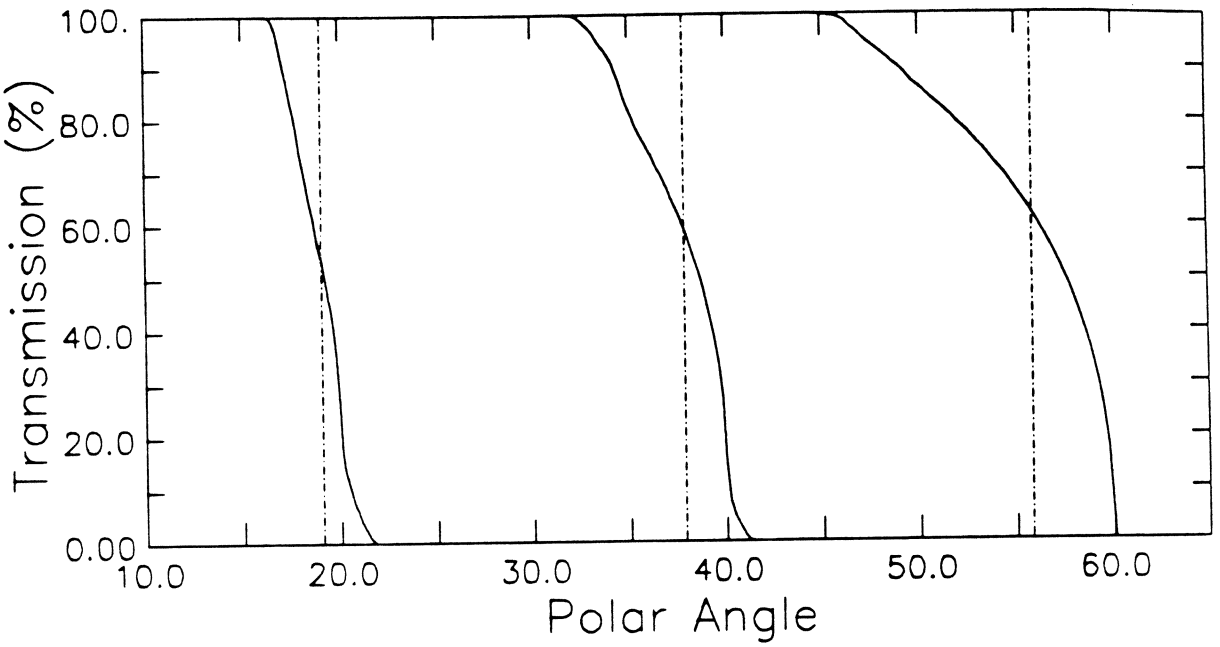

Figure 5.5: Comparison of computed transmission-angle curves for 3D CTCs (——) with limiting angles θ_i = 20°, 40° and 60° and ideal transmission-angle curves (–·–·–) of the corresponding Liouville-exact concentrators with limiting angles θ_{ps} calculated from (5.6).

We have shown that any 3D CTC will have an overall 3D transmission cut-off at a smaller angle (θ_{ps}) than the 2D cut-off of its meridional rays (θ_i). Hence by conservation of phase space all 3D CTCs must reject some off-axis rays at smaller angles than θ_{ps} because they will necessarily collect some meridional rays at larger angles than θ_{ps}. To derive this result we have assumed only that the 3D CTC has a flat entrance aperture and is cylindrically symmetric and that the photocathode is convex. Therefore it is impossible to construct, for any convex photocathode, a 3D Liouville-exact concentrator of cylindrical symmetry and flat entrance aperture. If the photocathode is *flat* then the inequality in (5.3) becomes an equality, (5.6) can be rewritten $\theta_{ps} = \theta_i$ and the arguments discussed above become irrelevant.

For 3D CTCs (constructed with ideal reflective surfaces and for ideal photocathodes)

the concentration *factor* defined by (3.7) reduces simply to

$$C(\theta) = \frac{A_{\text{conc}}\, T(\theta)}{A_{\text{proj}}(0)} = \frac{A_{\text{cath}}\, T(\theta)}{A_{\text{proj}}(0)\, \sin^2 \theta_{\text{ps}}} \tag{5.9}$$

where $T(\theta)$ is the usual transmission-angle curve and where (5.5) has been used to substitute for A_{conc}.

5.4 The Angular Momentum Limit

The transmission-angle curves of 3D CTCs are constrained by another limitation which is in some sense more stringent than the Liouville theorem. This limitation is a direct consequence of the conservation of the axial component of angular momentum or skew invariance in an axisymmetric optical system.

Assuming for the moment that the refractive index is constant throughout the optical system and can therefore be ignored, the maximum skewness (see (3.13) for the definition of skewness) that a ray can have at the photocathode is $h_{\text{max}} = r_{\text{polar}}$ which occurs when the ray is tangent to the photocathode edge with its direction of propagation perpendicular to $\hat{\mathbf{z}}$. Now, for a given polar angle θ the most extreme (off-axis) ray at the concentrator entrance aperture has a skewness $l_{\text{conc}} \sin\theta$. Hence there is a polar angle θ_{am} at which this most extreme ray has the maximum skewness allowed at the photocathode, i.e.

$$l_{\text{conc}} \sin\theta_{\text{am}} = r_{\text{polar}} \tag{5.10}$$

At polar angles $> \theta_{\text{am}}$ the extreme rays at the concentrator entrance aperture will have greater values of skewness than is allowed at the photocathode and so they cannot be concentrated onto the photocathode without violating skew invariance. Thus θ_{am} is the maximum angle at which the 3D CTC can transmit 100% of the incident light. In Figure 5.6 it can be seen that the the transmission-angle curves of 3D CTCs begin to cut-off at precisely this angle. However the percentage of rays which are rejected by the concentrator at polar angles $> \theta_{\text{am}}$ is greater than the percentage of rays which are necessarily rejected by skew invariance. Hence skew invariance is not the only cause of rejected rays.

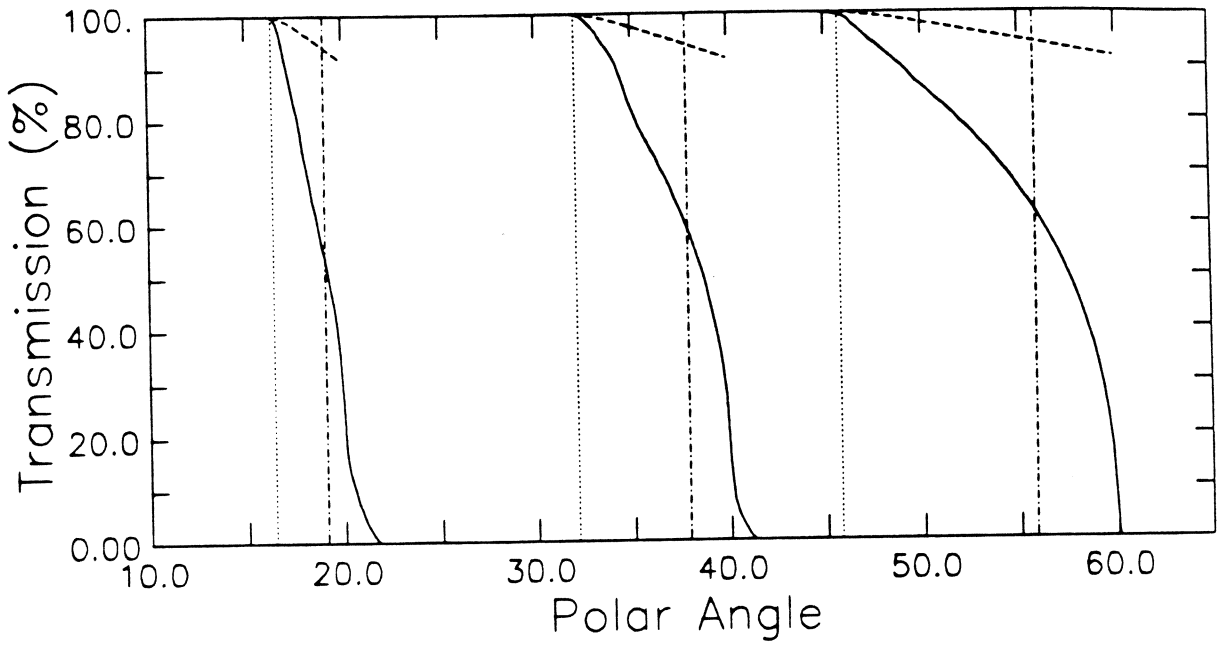

Figure 5.6: The computed transmission-angle curves for 3D CTCs (——) begin to cut-off at the angle θ_{am} (·····) given by (5.9). The – – – curves represent the percentage of rays incident at the concentrator entrance aperture with skewness $h > h_{max}$ and therefore necessarily rejected by the concentrator (skew invariance). The –·–·– line is the Liouville-exact cut-off at θ_{ps}.

The angular momentum condition (5.10) can be rewritten

$$\frac{\pi\, l_{conc}^2}{\pi\, r_{polar}^2} = \frac{A_{conc}}{A_{proj}(0)} = \frac{1}{\sin^2\theta_{am}}. \tag{5.11}$$

This equation represents a much more stringent limitation on the concentration ratio than the Liouville theorem imposes (5.5) since the maximum aperture area of the concentrator is decreased by a factor A_{cath}/A_{proj} which can be quite substantial for photocathodes of large curvature (for flat photocathodes it reduces to 1 and the angular momentum and Liouville limits are identical). In essence, conservation of angular momentum is not allowing us to make full use of the extra phase space acceptance of a convex photocathode with respect to a flat photocathode of equal projected area.

Let us now consider two different concentrators, one a CTC with a given limiting angle θ_i for a given convex photocathode, the other a Winston cone constructed according to the edge-ray principle with reference to a flat photocathode with the same area as

the projected area of the given convex photocathode. If the limiting angle in the edge-ray construction is equal to the angle θ_{am} given by (5.11) then these two concentrators will have identical entrance aperture areas. One might then ask how they compare in their ability to transmit light to the given convex photocathode. This question has been investigated assuming a spherical photocathode of half angle $\theta_{cath} = 60°$ and limiting angles $\theta_i = 20°$, 40° and 60°. The results are shown in Figure 5.7 where it can be seen that the Winston cones are able to transmit slightly more light at angles just beyond θ_{am} but much less light at angles near the Liouville cut-off angle θ_{ps}, especially when θ_i is greater. Starting with the concentrators of smallest limiting angle the integrated phase space acceptances Ψ_{conc} of the three Winston cones are respectively 98.4%, 96.1% and 92.5% (c.f. 100% for the CTCs) and the fractions $\Delta\Psi$ of the photocathode's phase space acceptance which are not accepted inside θ_{ps} are 4.9%, 5.8% and 7.2% respectively (c.f. 5.5%, 4.5% and 4.2% for the CTCs). So there is perhaps an argument for preferring the Winston cone in the case of limiting angle $\theta_i = 20°$ but not in the other two cases. It should also be pointed out that the ratio of the axial length (along $\hat{\mathbf{z}}$) of the Winston cone to that of the CTC is given by $\tan\theta_i / \tan\theta_{am}$ which is respectively 1.23, 1.33 and 1.69 for the three cases considered here, starting with the concentrators of smallest limiting angle.

Substituting l_{conc} in (5.10) with l_{cath} from (5.1) the angular momentum condition can be rewritten

$$\sin\theta_{am} = \left[\frac{r_{polar}}{l_{cath}}\right] \sin\theta_i \tag{5.12}$$

where the factor in the square brackets depends only on the shape of the photocathode and is necessarily less than 1 for all convex photocathodes. Furthermore it can be shown for any convex photocathode that

$$\frac{r_{polar}}{l_{cath}} < \sqrt{\frac{A_{cath}}{\pi l_{cath}^2}} < 1 \tag{5.13}$$

hence it follows from (5.6) and (5.12) that $\theta_{am} < \theta_{ps} < \theta_i$. The transmission-angle curves of most 3D CTCs are dominated by the respective values of these three angles and especially the differences between them. The more 'curved' a photocathode the greater

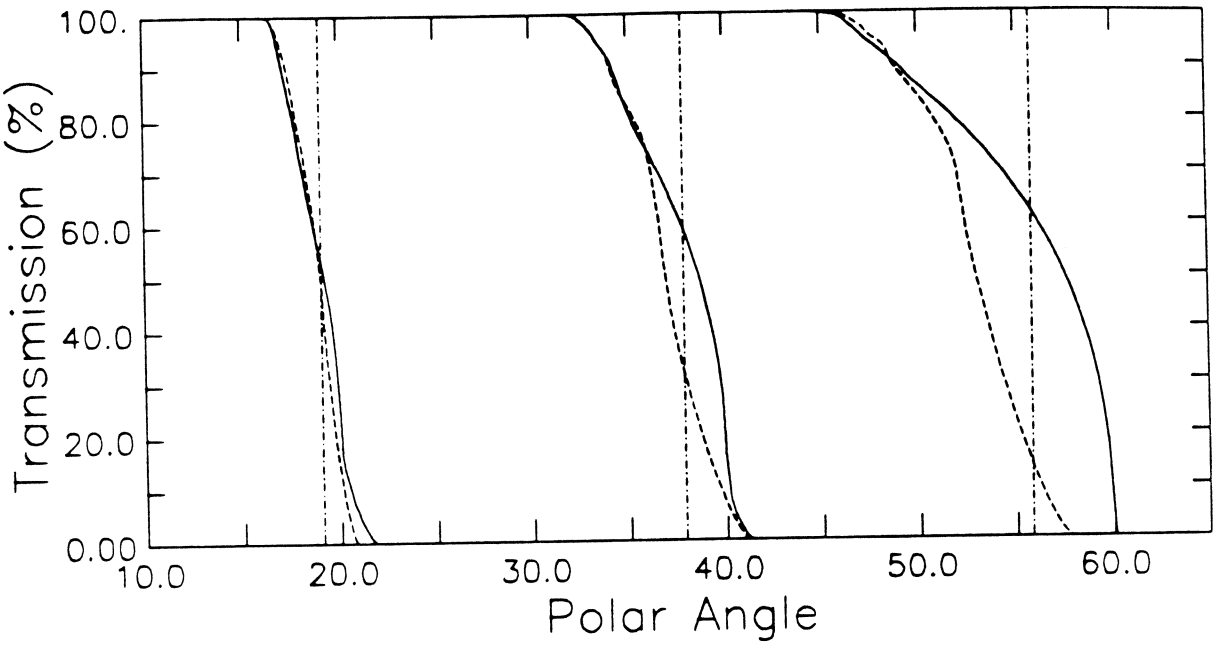

Figure 5.7: Comparison of the 3D transmission-angle curves of CTCs (——) with limiting angles, θ_i, of 20°, 40° and 60° and Winston cones (– – –) where the limiting angle is the angle θ_{am} given by (5.10) so that both sets of concentrators have equal entrance aperture areas. For both sets of concentrators the transmission onto the spherical photocathode of half angle $\theta_{cath} = 60°$ is computed. The –·–·– line is the Liouville-exact cut-off at θ_{ps}.

the difference between the three angles. Conversely if the photocathode is almost flat the three angles converge and the transmission-angle curve is then very similar to that of the Winston cone.

5.5 Spherical Photocathodes

The dependence of the transmission-angle curve of CTCs on the amount of curvature in the photocathode is more easily quantified for the special, but not unusual, case of a spherical photocathode of *constant* radius of curvature r_{cath} and of half angle θ_{cath}. For this photocathode it can be shown that $A_{cath} = 4\pi r_{cath}^2 \sin^2(\theta_{cath}/2)$, $l_{cath} = r_{cath}\theta_{cath}$ and $r_{polar} = r_{cath} \sin\theta_{cath}$. Hence (5.6) and (5.12) can be rewritten

$$\sin\theta_{ps} = \left[\frac{\sin(\theta_{cath}/2)}{\theta_{cath}/2}\right] \sin\theta_i \tag{5.14}$$

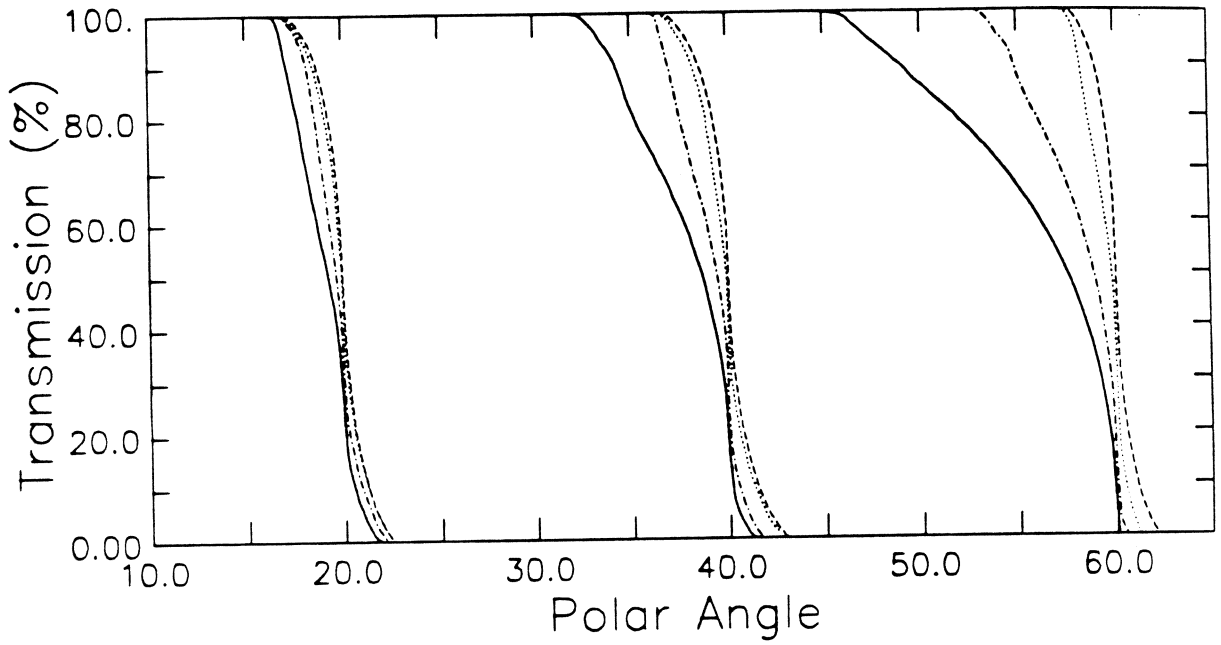

Figure 5.8: Computed transmission-angle curves for 3D CTCs with limiting angles θ_i = 20°, 40° and 60° for spherical photocathodes with half angles θ_{cath} = 60° (——), 40° (– · – · –) and 20° (· · · · ·); and for Winston cones (– – –) with the same limiting angles.

and

$$\sin\theta_{am} = \left[\frac{\sin\theta_{cath}}{\theta_{cath}}\right] \sin\theta_i \tag{5.15}$$

where it is now much clearer that the factors in the square brackets depend purely on the amount of curvature in the photocathode. In the limit where $\theta_{cath} \rightarrow 0$ the photocathode becomes flat and $\theta_{am} = \theta_{ps} = \theta_i$.

Figure 5.8 shows the transmission-angle curves of nine 3D CTCs constructed with limiting angles 20°, 40° and 60° and for spherical photocathodes of half angles 20°, 40° and 60°. Also shown in this figure are the transmission-angle curves of three Winston cones constructed with the same limiting angles. This figure illustrates the dependence of the transmission-angle curve on both the curvature of the photocathode and the value of the limiting angle itself. This dependence can be further quantified by calculating for each of the above concentrators the percentage $\Delta\Psi$ of the photocathode's phase space acceptance which is not accepted within the Liouville-exact cut-off angle (see Table 5.1).

θ_i	Flat	$\theta_{cath} = 20°$	$\theta_{cath} = 40°$	$\theta_{cath} = 60°$
20°	3.3%	3.6%	4.0%	5.5%
40°	1.6%	1.8%	2.4%	4.5%
60°	0.6%	0.7%	1.9%	4.2%

Table 5.1: The parameter $\Delta\Psi$ as a function of θ_i and θ_{cath} for CTCs constructed for spherical photocathodes; and as a function of θ_i for Winston cones constructed for flat photocathodes.

In terms of this parameter the performance of a 3D CTC improves as θ_i increases and θ_{cath} decreases.

For spherical photocathodes, the concentration factor of 3D CTCs, given by (5.9), can be rewritten

$$C(\theta) = \frac{T(\theta)}{\cos^2(\theta_{cath}/2)\sin^2\theta_{ps}} \tag{5.16}$$

from which it is clear that the deterioration in the transmission-angle curve as θ_{cath} increases is somewhat compensated by an increase in the overall concentration factor.

5.6 Skew CTCs

Although we have shown how the transmission-angle curves of CTCs for convex photocathodes are characterised by three angles: θ_i, θ_{ps} and θ_{am}, there is still room for approaching closer to the ideal transmission-angle curve without violating the fundamental constraints of conservation of phase space and z-component of angular momentum (see Figure 5.6). However, having specified the 2D profile of the CTC by applying the tangent-ray principle no further optimisation of the 3D CTC is possible without destroying the CTC's ideal transmission of meridional (2D) rays. Nevertheless, it is the off-axis rays (of large skewness) which are first rejected by the 3D CTC and so it might be possible to improve the CTC by optimising the transmission of these rays.

The CPC design for skew rays which is found in [49] (see Section 3.3) has been extended to accommodate non-plane (convex) photocathodes by replacing the edge-ray

principle with the tangent-ray principle. This development is described in Appendix B of this thesis where the differential equations are derived for generating the 2D profiles of 'skew' CTCs optimised for the transmission of rays given skewness h.

The profile of a skew CTC for a particular convex photocathode is determined by the choice of 2 parameters: the usual limiting angle θ_i and the skewness h which is allowed to assume any value between 0 and $r_{\text{polar}} \sin\theta_i$. If h exceeds this range then a continuous profile starting at the photocathode edge cannot be generated (see Appendix B). Let us hence define a relative scale of skewness

$$h_{\text{rel}} = \frac{h}{r_{\text{polar}} \sin\theta_i} \tag{5.17}$$

in which h_{rel} is constrained to the range $0 \rightarrow 1$.

The greater the value of h_{rel} (keeping θ_i constant) that the profile is constructed for, the *smaller* the aperture area A_{conc} of the resulting skew CTC. This phenomenon is a consequence of the complicated relationship between the 2D and 3D phase space transformations of a convex photocathode onto a concentrator of flat entrance aperture. It is not observed for flat photocathodes (see Appendix H of [49]). It is to some extent compensated by the transmission-angle curve of the skew CTC cutting off at larger angles as h_{rel} increases, so that the phase space acceptance is conserved (to first order). Figure 5.9 shows the transmission-angle curves of 8 CTCs constructed for a spherical photocathode of half angle $\theta_{\text{cath}} = 60°$ and with $\theta_i = 40°$ or $60°$ and $h_{\text{rel}} = 0.0$, 0.4, 0.6 or 0.8. The case of $\theta_i = 20°$ has not been shown because there is so little difference between the transmission-angle curves (or aperture areas) for different values of h_{rel}. This is largely due to the fact that when θ_i is small the maximum *design* value of skewness ($r_{\text{polar}} \sin\theta_i$) is small compared with the maximum skewness allowed at the photocathode ($h_{\text{max}} = r_{\text{polar}}$).

In order to compare the transmission-angle curves of skew CTCs designed with different h_{rel} values it is useful to adjust their respective values of θ_i accordingly so that the aperture areas of the CTCs are all the same. A comparison of such transmission-angles curves is shown in Figures 5.10 and 5.11 for the CTCs considered in Figure 5.9. Clearly,

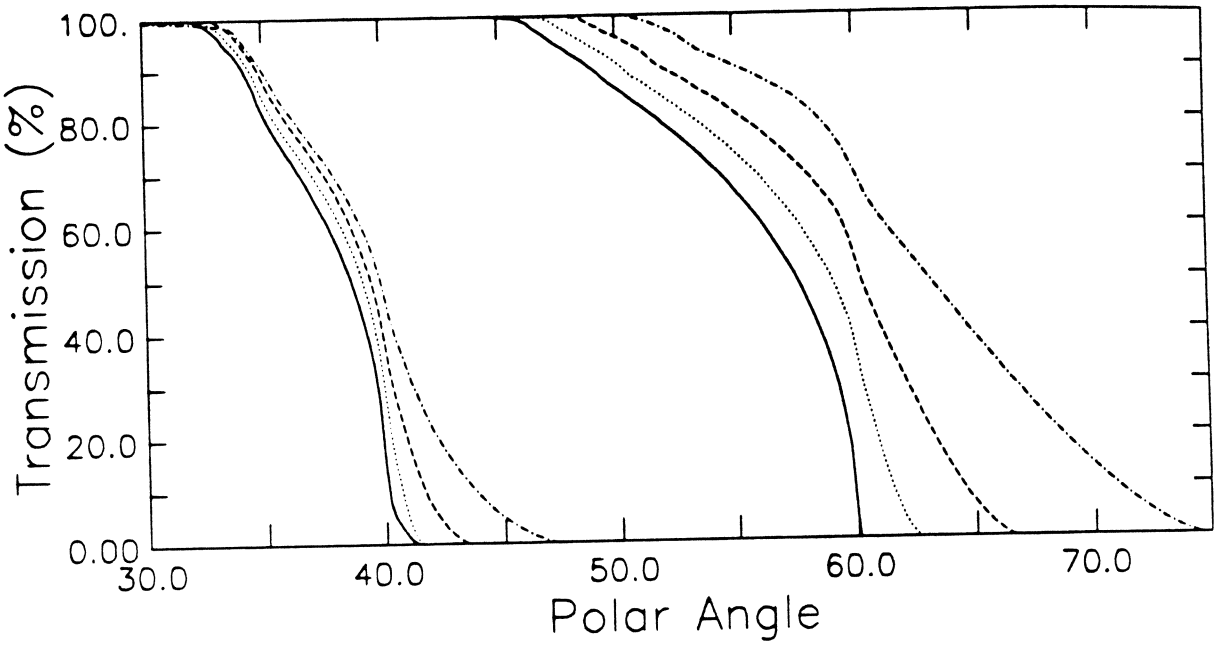

Figure 5.9: Computed transmission-angle curves for skew CTCs with limiting angles $\theta_i = 40°$ and 60° and optimised for the following values of relative skewness: $h_{rel} = 0.0$ (——), $h_{rel} = 0.4$ (·····), $h_{rel} = 0.6$ (– – –) and $h_{rel} = 0.8$ (–·–·–). In all cases the photocathode is spherical with a half angle $\theta_{cath} = 60°$.

there is very little advantage, if any, in the skew design. In Figure 5.11 the $h_{rel} = 0.4$ and $h_{rel} = 0.6$ CPCs are slightly more efficient in the sense that they transmit slightly more light inside the Liouville cut-off angle, but this is not the case in Figure 5.10. One marginal advantage of the skew design is that the axial length of the CPC is slightly reduced which might decrease manufacturing costs or simplify mounting by saving space. A summary of the relative merits of the 8 CTCs of Figures 5.10 and 5.11 is given in Table 5.2

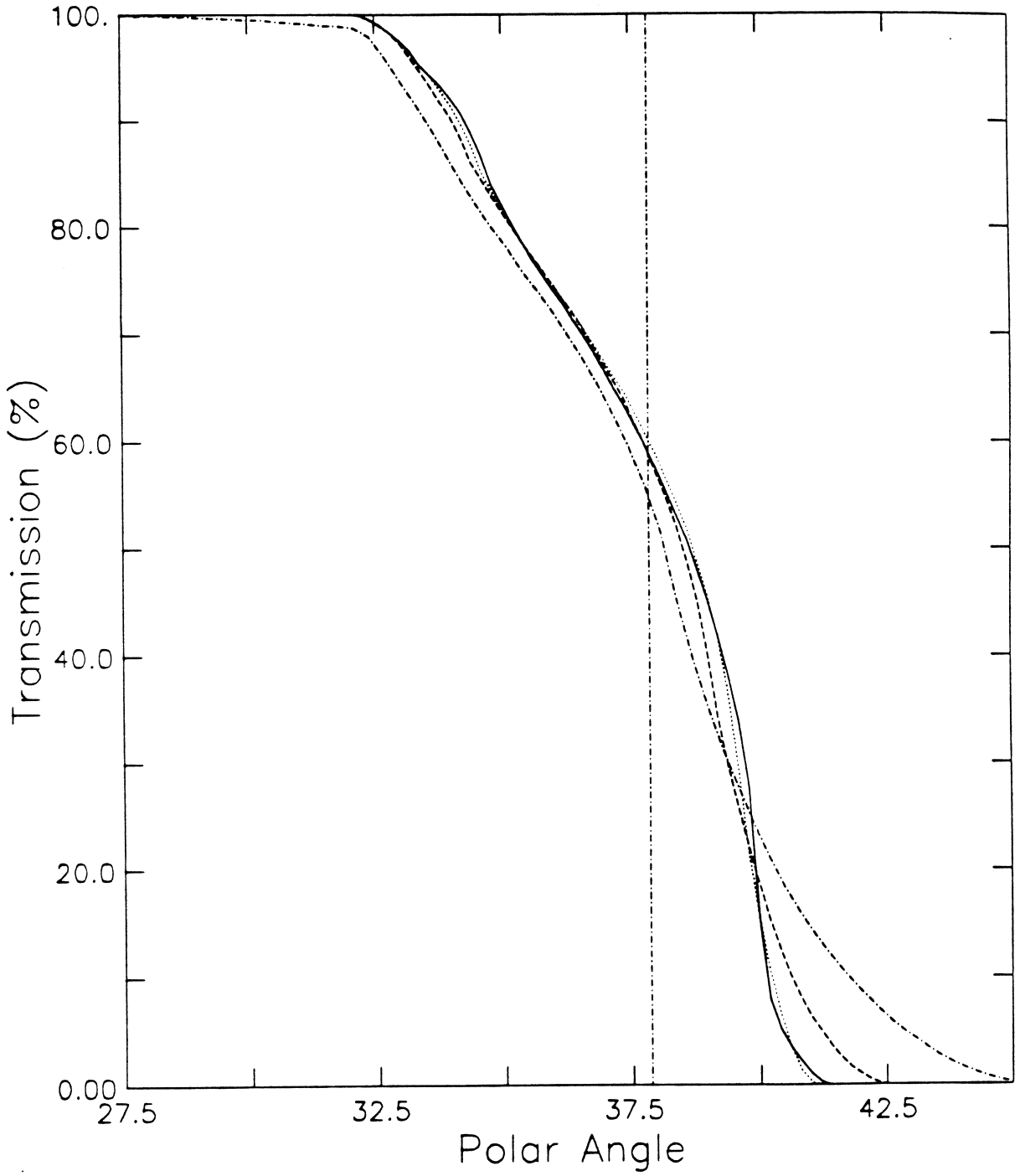

Figure 5.10: Computed transmission-angle curves of skew CTCs constructed to have the same entrance aperture areas. The values of θ_i and h_{rel} are as follows: $\theta_i = 40°$ and $h_{rel} = 0.0$ (——), $\theta_i = 39.57°$ and $h_{rel} = 0.4$ (·····), $\theta_i = 39.05°$ and $h_{rel} = 0.6$ (– – –) and $\theta_i = 38.35°$ and $h_{rel} = 0.8$ (–·–·–). In all cases the photocathode is spherical with a half angle $\theta_{cath} = 60°$.

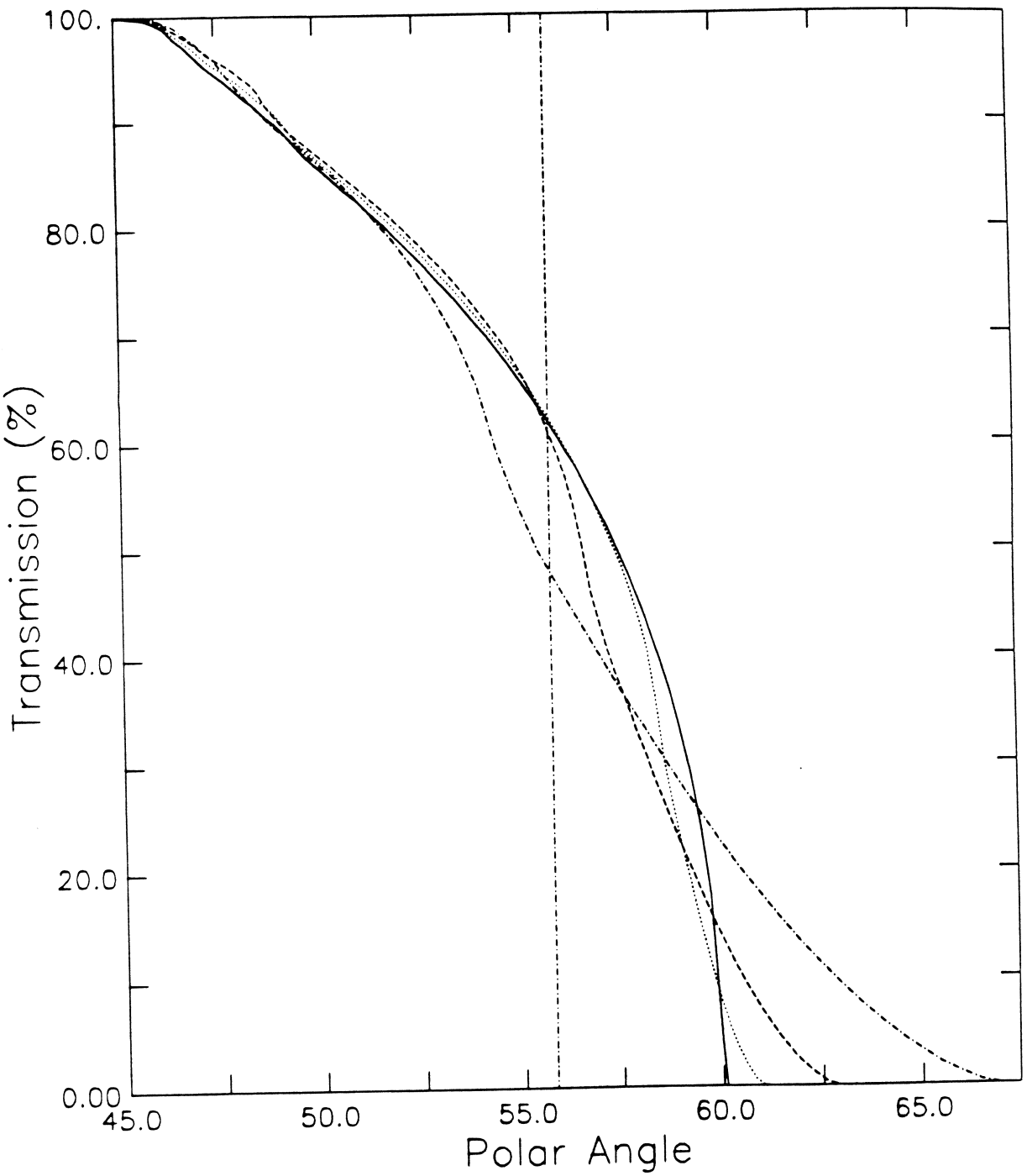

Figure 5.11: Computed transmission-angle curves of skew CTCs constructed to have the same entrance aperture areas. The values of θ_i and h_{rel} are as follows: $\theta_i = 60°$ and $h_{rel} = 0.0$ (——), $\theta_i = 58.45°$ and $h_{rel} = 0.4$ (·····), $\theta_i = 56.64°$ and $h_{rel} = 0.6$ (– – –) and $\theta_i = 54.33°$ and $h_{rel} = 0.8$ (–·–·–). In all cases the photocathode is spherical with a half angle $\theta_{cath} = 60°$.

θ_t	h_{rel}	L/L_0	$\Delta\Psi$	Ψ_{conc}/Ψ_{cath}
40.0°	0.0	1.0	4.5%	100.0%
39.57°	0.4	0.97	4.5%	100.0%
39.05°	0.6	0.92	4.6%	100.0%
38.35°	0.8	0.84	5.5%	100.0%
60.0°	0.0	1.0	4.2%	100.0%
58.45°	0.4	0.97	4.1%	99.9%
56.64°	0.6	0.92	3.9%	99.8%
54.33°	0.8	0.81	4.8%	99.9%

Table 5.2: Relative merits of the various skew CTCs of Figures 5.10 and 5.11. The limiting angles θ_t are chosen so that the entrance aperture areas of the two sets of four CTCs are the same. L/L_0 is the ratio of the axial length of the CTC to the axial length of the corresponding CTC with $h_{rel} = 0.0$. In all cases the photocathode is spherical with a half angle $\theta_{cath} = 60°$.

5.7 Refractive Indices: The Dielectric-filled CTC

Let us now consider the effect of allowing the refractive index to vary in the optical system, e.g. as in the dielectric-filled CPC of [49] (Figure 3.8). In many of the applications of the tangent-ray principle to *convex* photocathodes there will be an involute section in the profile of the CTC ($\theta_t + \alpha_{cath} > \frac{\pi}{2}$). Now the light which is transmitted to the photocathode by the CTC is incident at the involute at all angles from 0° to 90°. Hence total internal reflection is not suitable as a reflection mechanism, at least not for the lower section of the CTC. However one can still consider a dielectric-filled CTC which relies on specular reflection from a metallic surface, e.g. a solid acrylic CTC coated with aluminium or silver, or a hollow aluminium CTC filled with water or any other transparent liquid of high refractive index.

Such a CTC filled with a dielectric of refractive index n_1 and in contact at the entrance aperture with a medium of refractive index n_0 is shown in Figure 5.12. All the rays incident with polar angle θ at the entrance aperture are transmitted into the dielectric with a polar angle θ' where

$$\sin\theta' = \frac{n_0}{n_1}\sin\theta. \tag{5.18}$$

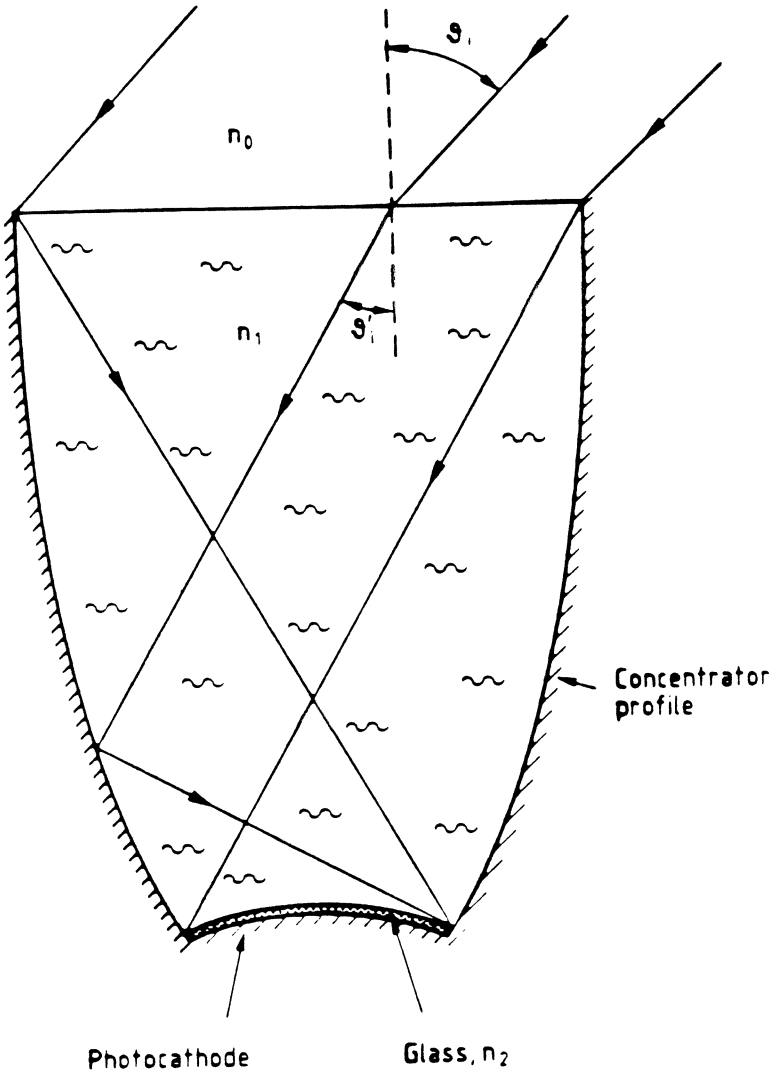

Figure 5.12: A CTC filled with a dielectric of refractive index n_1 and in contact at its entrance aperture with a medium of refractive index n_0. The rays which are incident at the entrance aperture at the limiting angle θ_i are transmitted into the dielectric with polar angle θ_i' given by (5.18).

The other boundary where refraction takes place is the boundary between the dielectric and the photomultiplier window of refractive index n_2. There are three separate cases to be considered here. Firstly, if $n_1 = n_2$ then there is no refraction and this boundary can be altogether ignored. Moreover, in Chapter 4 it was established that the photocathode is (more-or-less) uniformly efficient out to an angle of incidence of about 84.7° which to a good approximation can be treated as 90°. Secondly, there is the case where $n_1 < n_2$. In this case light is refracted *towards* the photocathode and the maximum

angle of incidence which can occur at the photocathode is given by $\sin^{-1}(n_1/n_2)$. This means that only a fraction $(n_1/n_2)^2$ of the photocathode's total phase space acceptance $\sin^2\theta_{max}$ is being exploited. There is also a reflection loss at the n_1/n_2 boundary which increases dramatically with angle, but even if $n_1 = 1.0$ the PMT window/photocathode system is efficient out to an angle of incidence of about 84.5° at the PMT window. Thus the outer surface of the photomultiplier window effectively acts as a photocathode which to a good approximation is uniformly efficient out to 90° incidence. Lastly, there is the case where $n_1 > n_2$ and the light is refracted *away* from the photocathode. At the critical angle $\theta_c = \sin^{-1}(n_2/n_1)$ total internal internal reflection begins to take place at the n_1/n_2 boundary. Thus the PMT window/photocathode system cannot be approximated by a single surface absorber which is efficient out to 90° incidence.

Let us start by considering the first two cases together ($n_1 \leq n_2$) in which the PMT window/photocathode system can be approximated by a single surface ideal photocathode (uniformly efficient out to 90° incidence) in direct contact with the medium n_1 (we will return to the case $n_1 > n_2$ later). The effective phase space acceptance of this ideal photocathode is given by the double integral

$$\Psi_{cath}(n_1 \leq n_2) = \int\int_0^{\frac{\pi}{2}} \pi\, n_1^2\, E_{cath}(\theta_1, \mathbf{r}_{cath}) \sin 2\theta_1\, d\theta_1\, dA_{cath} \qquad (5.19)$$

where the surface of integration is the n_1/n_2 boundary in the case $n_1 < n_2$ and the photocathode itself in the case $n_1 = n_2$ and where θ_1 and $\mathbf{r}_{cath}$ are respectively the angle of incidence and point of incidence at the surface of integration. This integral reduces to

$$\Psi_{cath}(n_1 \leq n_2) = \pi\, n_1^2\, E_{cath}\, A_{cath} \qquad (5.20)$$

assuming that the photocathode is uniformly efficient over its useful surface area A_{cath}.

Let us now define, as before, θ_{ps} as the polar angle at which the transmission of a Liouville-exact concentrator cuts-off sharply in the unprimed coordinate frame. Let us also define θ'_{ps} as the corresponding angle in the primed coordinate frame. The phase space acceptance of this Liouville-exact concentrator in both the primed and unprimed

coordinate frames is given by the double integrals

$$\Psi_{\text{conc}} = \int\int_0^{\theta_{\text{ps}}} \pi\, n_0^2\, E_{\text{cath}} \sin 2\theta\, d\theta\, dA = \int\int_0^{\theta'_{\text{ps}}} \pi\, n_1^2\, E_{\text{cath}} \sin 2\theta'\, d\theta'\, dA \qquad (5.21)$$

where the surface of integration is the n_0/n_1 boundary (the entrance aperture of the concentrator) and where θ and θ' are respectively the angles of incidence and transmission at this boundary. These integrals reduce simply to

$$\Psi_{\text{conc}} = \pi n_0^2\, E_{\text{cath}}\, A_{\text{conc}} \sin^2 \theta_{\text{ps}} = \pi n_1^2\, E_{\text{cath}}\, A_{\text{conc}} \sin^2 \theta'_{\text{ps}}. \qquad (5.22)$$

Equating this Ψ_{conc} with $\Psi_{\text{cath}}(n_1 \leq n_2)$ one obtains the following equation

$$\frac{A_{\text{conc}}}{A_{\text{cath}}} = \frac{1}{\sin^2 \theta'_{\text{ps}}} = \frac{n_1^2}{n_0^2 \sin^2 \theta_{\text{ps}}} \qquad (5.23)$$

which represent the maximum concentration ratio allowed by the Liouville theorem for the case $n_1 \leq n_2$, c.f. (5.5) where the effect of refractive indices is ignored. Notice that if $n_1 = n_2$ then (5.23) is identical to the 'ultimate' Liouville limit given by (3.5) with $\theta_{\text{max}} = \pi/2$ and $\theta_{\text{i}} = \theta_{\text{ps}}$.

Any dielectric-filled 2D CTC constructed with a limiting angle θ'_{i} will have a limiting angle θ_{i} in the unprimed coordinate frame where the transformation from primed to unprimed coordinate frame is given by (5.16). The concentration ratio of this 2D CTC is therefore given by

$$\frac{l_{\text{conc}}}{l_{\text{cath}}} = \frac{1}{\sin \theta'_{\text{i}}} = \frac{n_1}{n_0 \sin \theta_{\text{i}}} \qquad (5.24)$$

Now relation (5.2) between A_{conc} and l_{conc} is obviously still valid so that substituting A_{conc} in (5.23) with l_{cath} through (5.2) and (5.24) one obtains the following relations between θ_{ps} and θ_{i} and between θ'_{ps} and θ'_{i}:

$$\sin \theta_{\text{ps}} = \sqrt{\frac{A_{\text{cath}}}{\pi l_{\text{cath}}^2}}\, \sin \theta_{\text{i}} \qquad (5.25)$$

and

$$\sin \theta'_{\text{ps}} = \sqrt{\frac{A_{\text{cath}}}{\pi l_{\text{cath}}^2}}\, \sin \theta'_{\text{i}} \qquad (5.26)$$

which are identical to each other and to the relation (5.6) between θ_{ps} and θ_{i} when refractive indices are ignored.

The maximum skewness allowed at our ideal photocathode (for the case $n_1 \leq n_2$) is $n_1 r_{\text{polar}}$ (see (3.11) for the definition of skewness including the effect of refractive index). At the same time the skewness of the most extreme ray at the concentrator aperture is now given by $n_0 l_{\text{conc}} \sin\theta = n_1 l_{\text{conc}} \sin\theta'$. Let us define θ'_{am} and θ_{am} as the polar angles in the primed and unprimed coordinate frames at which this most extreme ray has the maximum skewness allowed at the photocathode, i.e.

$$n_0 l_{\text{conc}} \sin\theta_{\text{am}} = n_1 l_{\text{conc}} \sin\theta'_{\text{am}} = n_1 r_{\text{polar}} \tag{5.27}$$

This equation can be rewritten

$$\frac{\pi l_{\text{conc}}^2}{\pi r_{\text{polar}}^2} = \frac{A_{\text{conc}}}{A_{\text{proj}}(0)} = \frac{1}{\sin^2\theta'_{\text{am}}} = \frac{n_1^2}{n_0^2 \sin^2\theta_{\text{am}}} \tag{5.28}$$

which shows how the angular momentum limit on concentration also scales by a factor $(n_1/n_0)^2$ from its value (5.11) when refractive indices are ignored. Substituting l_{conc} in (5.27) with l_{cath} from (5.24) one obtains the following relations between θ_{am} and θ_i and between θ'_{am} and θ'_i:

$$\sin\theta_{\text{am}} = \left[\frac{r_{\text{polar}}}{l_{\text{cath}}}\right] \sin\theta_i \tag{5.29}$$

$$\sin\theta'_{\text{am}} = \left[\frac{r_{\text{polar}}}{l_{\text{cath}}}\right] \sin'\theta_i \tag{5.30}$$

which are identical to each other and to the relation (5.12) between θ_{am} and θ_i when refractive indices are ignored.

So the properties of dielectric-filled CTCs (with $n_1 \leq n_2$) are very similar to those of 'normal CTCs' (constant refractive index) apart from the $(n_1/n_0)^2$ factor which appears in both the Liouville and angular momentum limits on concentration. This factor can be quite appreciable, especially for gas Cherenkov detectors where n_0 is practically unity.

The transmission-angle curve of a dielectric-filled CTC in the unprimed coordinate θ will be very similar to that of a normal CTC with the same θ_i value and designed for the same photocathode shape as they will both have exactly the same θ_{ps} and θ_{am} values. A comparison between the transmission-angle curves of two such CTCs is shown in Figure 5.13.

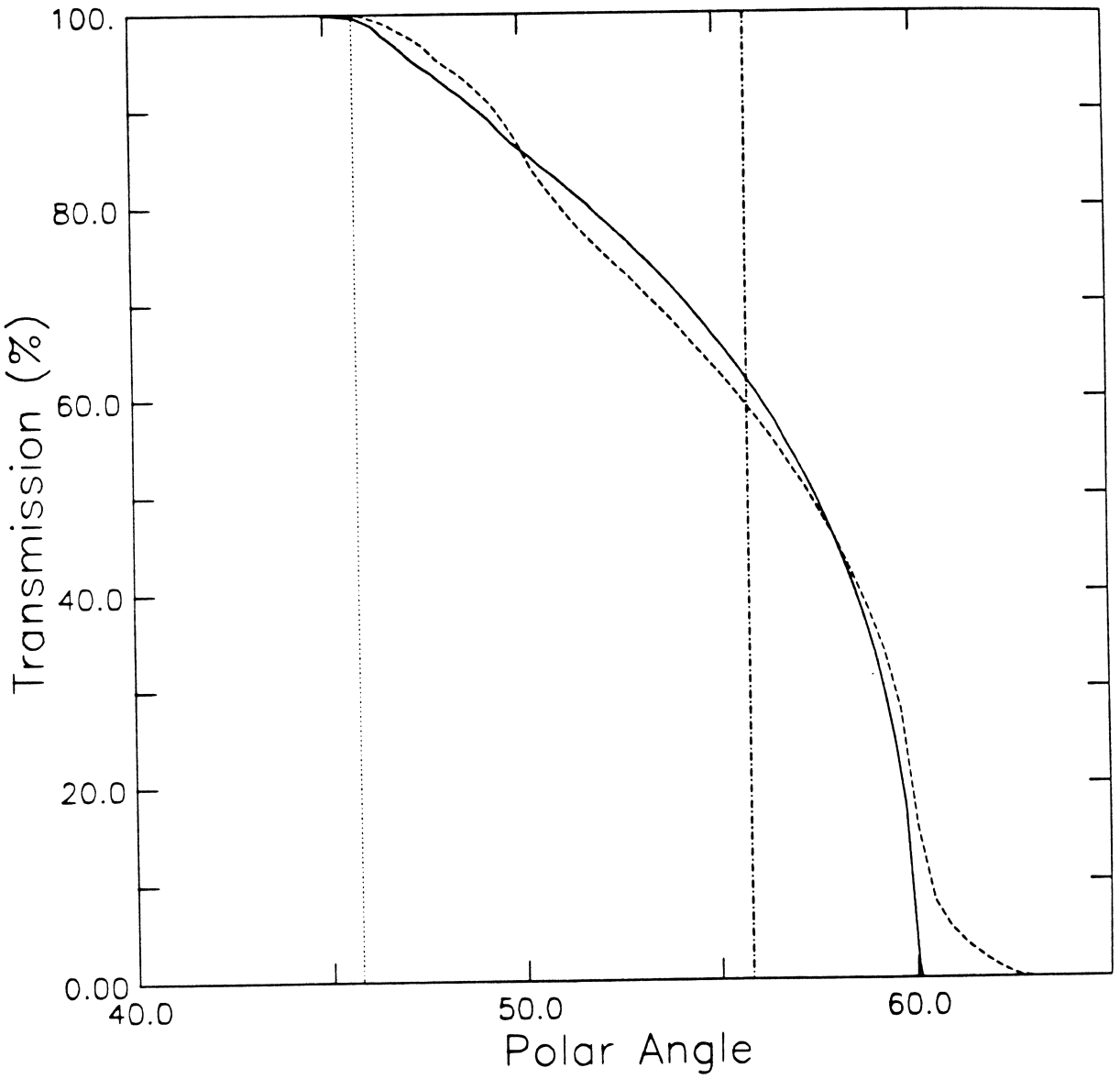

Figure 5.13: Comparison of 3D transmission-angle curves of a normal CTC (——) and a dielectric-filled CTC with $n_1/n_0 = 1.347$ (– – –). Both CTCs are constructed for a limiting angle $\theta_t = 60°$ and a spherical photocathode of half angle $\theta_{cath} = 60°$. The –·–·– line is the Liouville-exact cut-off at θ_{ps} and the ····· line is the angle θ_{am}.

Let us now return to the case $n_1 > n_2$. In this case the n_1/n_2 boundary effectively acts as a photocathode which is uniformly efficient out to an angle of incidence $\theta_c = \sin^{-1}(n_2/n_1)$. Hence the effective phase space acceptance of this photocathode is given by

$$\Psi_{\text{cath}}(n_1 > n_2) = \pi n_1^2 E_{\text{cath}} A_{\text{cath}} \sin^2 \theta_c \tag{5.31}$$

which is equal to the Ψ_{cath} given by (5.20) with $n_1 = n_2$. Equating $\Psi_{\text{cath}}(n_1 > n_2)$ (5.31) with the phase space acceptance Ψ_{conc} (5.22) of a Liouville-exact concentrator one obtains the following limit on the concentration ratio

$$\frac{A_{\text{conc}}}{A_{\text{cath}}} = \frac{n_1^2 \sin^2 \theta_c}{n_0^2 \sin^2 \theta_{\text{ps}}} = \frac{n_2^2}{n_0^2 \sin^2 \theta_{\text{ps}}} \tag{5.32}$$

which is the same limit as in the case where $n_1 = n_2$.

Similarly, when $n_1 > n_2$ the maximum skewness at the photocathode is given by $n_1 r_{\text{polar}} \sin \theta_c$ so that the angular momentum limit can be written

$$\frac{A_{\text{conc}}}{A_{\text{proj}}} = \frac{n_1^2 \sin^2 \theta_c}{n_0^2 \sin^2 \theta_{\text{am}}} = \frac{n_2^2}{n_0^2 \sin^2 \theta_{\text{am}}} \tag{5.33}$$

which is also the same limit as when $n_1 = n_2$. So there is no advantage in choosing $n_1 > n_2$. There are, however, many disadvantages such as the increased reflection losses at both the n_0/n_1 and n_1/n_2 boundaries and the fact that the CTC can no longer be constructed by the tangent-ray principle. The optimum concentrator design is therefore a CTC filled with a dielectric of refractive index n_1 equal to the refractive index n_2 of the PMT window. This concentrator has the ultimate concentration ratio allowed by the Liouville theorem and the usual transmission-angle curve characterised by the three angles: θ_i, θ_{ps} and θ_{am}.

A note of warning should however be added to the dielectric-filled CTC. If the medium of refractive index n_0 is allowed to permeate between the dielectric and the PMT window then total internal reflection will occur at the boundary between the dielectric, n_1, and the permeate, n_0. This boundary will effectively act as a photocathode which is efficient out to an angle $\theta_c = \sin^{-1}(n_0/n_1)$. In this case the Liouville and

angular momentum limits reduce to

$$\frac{A_{\text{conc}}}{A_{\text{cath}}} = \frac{n_1^2 \sin^2\theta_c}{n_0^2 \sin^2\theta_{\text{ps}}} = \frac{1}{\sin^2\theta_{\text{ps}}} \tag{5.34}$$

and

$$\frac{A_{\text{conc}}}{A_{\text{proj}}} = \frac{n_1^2 \sin^2\theta_c}{n_0^2 \sin^2\theta_{\text{am}}} = \frac{1}{\sin^2\theta_{\text{am}}} \tag{5.35}$$

which are identical to the limits of a normal CTC which is *not* filled with a dielectric. It is therefore essential that the dielectric, n_1, is in direct optical contact with the PMT window, n_2, and that the medium of refractive index n_0 is not allowed to permeate between the two.

5.8 CTCs in the SNO Detector

In SNO, the maximum increase in light concentration that can be achieved with dielectric-filled CTCs compared with normal CTCs is given by $(n_2/n_0)^2 = (1.49/1.34)^2 = 1.24$, where 1.49 is the refractive index of the PMT windows and 1.34 is the refractive index of water. This represents a 24% increase in light collection efficiency. However, there are many practical difficulties associated with dielectric-filled CTCs. The weight of the 10,000 concentrators would increase from about 3 tons to about 50 tons which is a substantial load for the support structure. More importantly, the dielectric medium would have to be *sealed* to the PMTs so that water could not permeate between the dielectric and the PMT windows over the 10 year life time of the detector. This sealing requirement raises serious technical difficulties which make the potential gain of 24% in light collection much less attractive. Thus dielectric-filled CTCs have not been pursued for SNO. From now on in this thesis the discussion will be restricted to CTCs where the refractive index on either side of the CTC's entrance aperture is the same and never greater than the refractive index of the PMT window, i.e. $n_1 = n_0 \leq n_2$.

The photomultipliers in SNO have to be mounted 2.5 m away from the D_2O volume in order to reduce their contribution to the β-γ background. Thus the fiducial volume subtends a cone of half angle 56.4° at the entrance aperture of the CTCs; and the D_2O volume a cone of half angle 45.6° (see figure 2.2).

Let us consider the most curved of the candidate PMTs for SNO: the EMI 9351 20 cm PMT which has a spherical photocathode with $\theta_{cath} = 60°$ and which would induce the least favourable CTC transmission-angle curve. A CTC designed for this PMT with a Liouville cut-off angle, θ_{ps}, equal to the fiducial volume cone angle, 56.4°, will have an angular momentum cut-off angle $\theta_{am} = 46.2°$ and a 2D limiting angle $\theta_i = 60.7°$ (see (5.14) and (5.15)). As the angular momentum cut-off angle, 46.2°, is greater than the D_2O cone angle, 45.6°, one can expect this CTC to collect light *uniformly* from the entire volume of D_2O. The transmission-angle curve of this CTC will be very similar to that of the $\theta_i = 60°$, $\theta_{cath} = 60°$ CTC shown in Figure 5.4.

The response of the SNO detector as a function of radius has been simulated by Monte-Carlo for three different cases: (i) CTCs as discussed above ($\theta_{ps} = 56.4°$) on EMI 9351 PMTs ($\theta_{cath} = 60°$); (ii) Liouville-exact concentrators with the same entrance aperture area as the CTCs and hence an ideal transmission-angle cut-off at $\theta_{ps} = 56.4°$; and (iii) bare EMI 9351 photomultipliers without concentrators. In all three cases, ideal reflective surfaces and ideal photocathodes were assumed, and the number of PMTs was 9,500. The simulation calculates the average number of photons detected per 7 MeV electron, N_{pe}, as a function of radius R in the detector by tracking 200 electrons with random initial directions at each R. The results are shown in Figure 5.14 where the x-axis is linear in R^3 since equal increments in R^3 represent equal volume steps.

The concentration *factor* of the CTCs is given by (5.16) which reduces to $C(\theta) = 1.92 \times T(\theta)$ for the given values $\theta_{ps} = 56.4°$ and $\theta_{cath} = 60°$. This concentration factor is reflected in the ratio of N_{pe} with and without the CTCs. Inside the D_2O, where $T(\theta) = 1$ as θ is always less than θ_{am}, this ratio is 1.92. Outside the D_2O it decreases slightly as a consequence of the non-ideal transmission-angle curve of the CTCs. At the edge of the fiducial volume (7 m) it is has dropped by 10%. By comparison, the Liouville-exact concentrator exhibits a concentration factor of 1.92 throughout the fiducial volume (within statistics), as expected. This difference in radial response between the CTC and the Liouville-exact concentrator is, however, not as marked as the difference between their angular responses (see Figure 5.5). The reason for this is that light from an isotropic

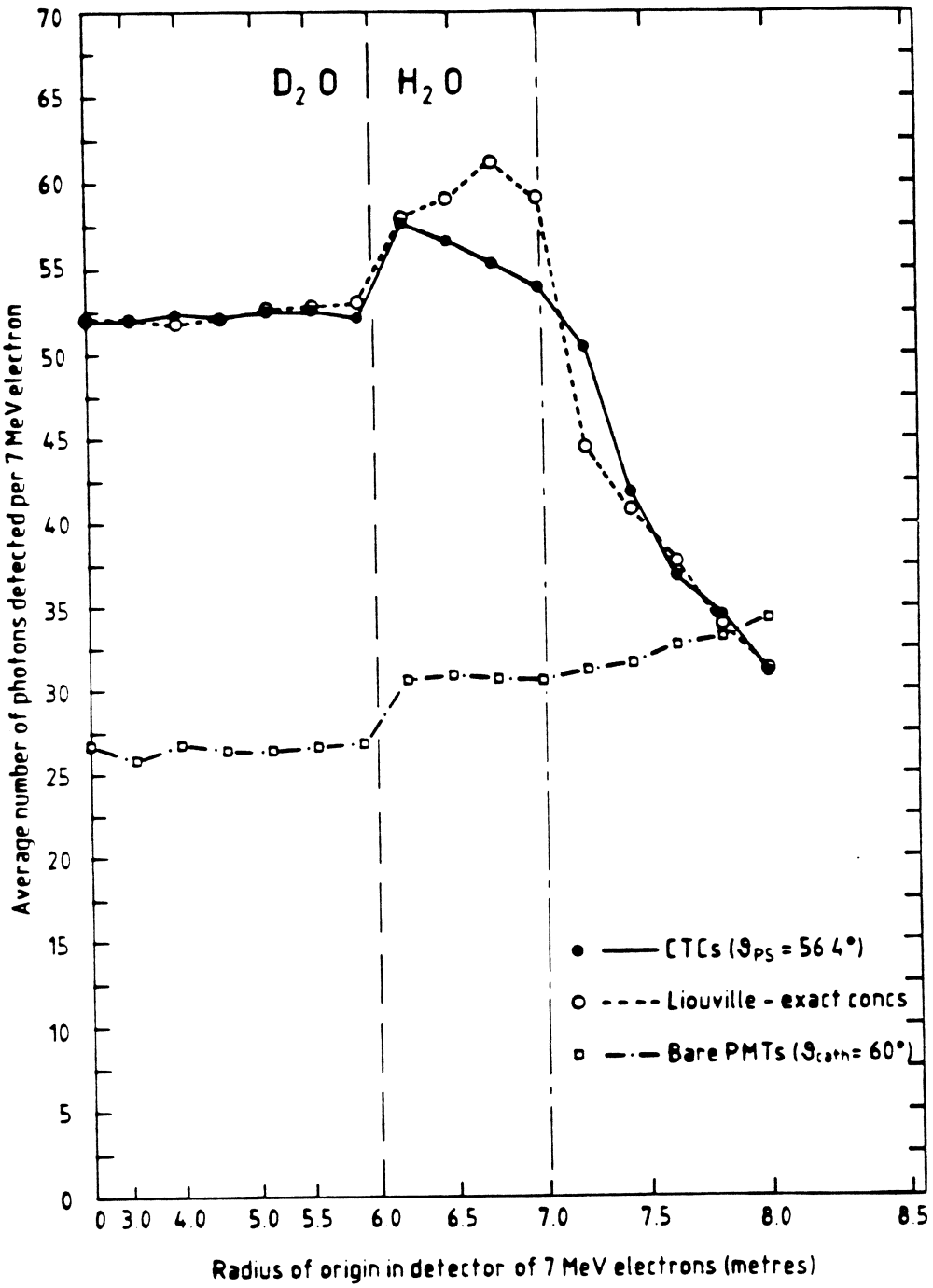

Figure 5.14: Monte-Carlo simulation of the radial response of the SNO detector, assuming, in all cases 9,500 EMI 9351 PMTs with ideal photocathodes, and for both the CTCs and the Liouville-exact concentrators ideal reflective surfaces.

event at a given radius R in the detector (see Figure 2.2) is incident at the PMT sphere at all polar angles between 0° and $\sin^{-1}(R/8.4\,\mathrm{m})$. Thus the average detector response as a function of R is a convolution of the concentrator's angular response with the distribution in polar angle at the PMT sphere from an event at radius R. The net effect is to 'soften' even the sharpest angular cut-off of a Liouville-exact concentrator.

The β-γ background in SNO increases exponentially with R in the vicinity of the photomultipliers (R approaching 8.5 m). Beyond 7.5 m the CTC and the Liouville-exact concentrator provide the same pulse height reduction which decreases the number of PMT β-γ events reconstructed in the D_2O by more than an order of magnitude. The slight rise in N_{pe} at very large radii, for the simulation with bare PMTs, is a consequence of the curved shape of the photocathode which results in A_{proj} increasing at large polar angles.

In passing from the heavy water to the light water there is a discontinuity in the response because there is less absorption in the acrylic vessel. This 10% discontinuity in N_{pe} at 6 m has been re-evaluated to a 30% discontinuity in a recent simulation [39] with more up to date values for acrylic absorption and PMT quantum efficiencies[1]. It is also apparent from this simulation that for events in the light water N_{pe} will be a strong function of direction, varying by up to a factor of 4 according to whether the electron starts off in the direction of the nearest PMT or in the opposite direction. Compared with these systematic effects, the 10% drop in N_{pe} at 7 m from the CTC's imperfect transmission-angle curve is negligeable. Therefore it is concluded that fixing the Liouville cut-off angle, θ_{ps}, at the half angle of the cone subtended by the fiducial volume, 55.6°, is the optimum choice for the design of CTCs for SNO. However, it is implicitly assumed in this conclusion that the real properties of photocathodes and reflective surfaces do not have a significant effect on the angular response of CTCs. The validity of this assumption will be investigated in Chapter 6.

[1]This simulation does not include the wavelength dependence of the reflectivity of the SNO CTC which should decrease the discontinuity to perhaps 20%.

Chapter 6

Simulated and Measured Performances of Prototype CTCs

6.1 Introduction

In real CTCs, the reflectivity (R_{conc}) is a function of wavelength (λ), polarization[1] at the reflective surface (ε_0), refractive index of the medium in contact with the reflective surface (n_1), point of incidence on the reflective surface ($\mathbf{r}_{\text{ref}}$) and angle of incidence at the reflective surface (θ_0 — not to be confused with θ, the polar angle at the CTC entrance aperture, and θ_1, the angle of incidence at the photomultiplier window). Similarly, in real PMTs the efficiency of the photocathode (E_{cath}) is a function of wavelength, polarization at the photomultiplier window (ε_1), refractive index of the medium in contact with the photomultiplier window (n_1), point of incidence on the photomultiplier window ($\mathbf{r}_{\text{cath}}$) and angle of incidence at the photomultiplier window (θ_1). Thus the concentration factor, defined by (3.7), can be rewritten

$$C(\theta) = \frac{\int\int T(\theta, \mathbf{r}_{\text{conc}})\, R^{\beta}_{\text{conc}}(\lambda, \varepsilon_0, n_1, \mathbf{r}_{\text{ref}}, \theta_0)\, E_{\text{cath}}(\lambda, \varepsilon_1, n_1, \mathbf{r}_{\text{cath}}, \theta_1)\, dA_{\text{conc}}\, d\lambda}{\int\int E_{\text{cath}}(\lambda, \varepsilon_1, n_1, \mathbf{r}_{\text{cath}}, \theta_1)\, dA_{\text{surf}}\, d\lambda} \qquad (6.1)$$

where dA_{conc} is an area element of the entrance aperture of the CTC; dA_{surf} is an area element of a *flat* surface directly in front of the bare photomultiplier (see Figure

[1]The polarization at any surface is given by $\epsilon = (I_{TE} - I_{TM})/(I_{TE} + I_{TM})$ where I_{TE} and I_{TM} are the intensities of the TE and TM waves, respectively.

3.1); $T(\theta, r_{conc})$ is a geometrical factor expressing the probability of transmission to the photocathode for a CTC with the same *shape* as the real CTC but with ideal reflective surfaces (see below); and $\beta = 0,1,2,3,...$ is a function of θ and r_{conc} expressing the number of times a photon is reflected by the CTC before reaching the photomultiplier. The variables ε_0, ε_1, r_{ref}, r_{cath}, θ_0 and θ_1 in the numerator on the r.h.s. of this equation are functions of the variables ε, θ and r_{conc} which are the polarization, angle of incidence and point of incidence of a photon at the CTC entrance aperture. Similarly, the variables ε_1, r_{cath}, and θ_1 in the denominator are functions of the variables ε, $\theta = 0$ and r_{surf} which are the polarization, angle of incidence and point of incidence of a photon at the flat surface in front of the bare PMT. For CTCs with ideal reflective surfaces (100% reflectivity for all λ, ε_0, n_1, r_{ref} and θ_0) and PMTs with ideal photocathodes (uniform efficiency for all λ, ε_1, n_1, r_{cath} and θ_1) (6.1) reduces to (5.9).

The question, then, is what are the effects of realistic functions for $R_{conc}(\lambda, \varepsilon_0, n_1, r_{ref}, \theta_0)$ and $E_{cath}(\lambda, \varepsilon_1, n_1, r_{cath}, \theta_1)$ on the concentration factor, $C(\theta)$? The discussion here will be restricted to prototype CTCs for the SNO detector. However, many of the conclusions reached will be generally applicable to most CTCs and Winston Cones.

All of the simulations and measurements in this chapter are based on, or made with, the R1408 Hamamatsu photomultiplier which will be used in SNO. The shape of the glass envelope of this PMT is shown in Figure 6.1. It is spherical over most of the front face with a toroidal section around the equator.

As discussed in Section 5.8, the optimum design constraint for SNO CTCs is to fix the Liouville cut-off angle, θ_{ps}, at 56.4°. This constraint will be assumed throughout this chapter. Another property of all CTCs in this chapter is that their axial lengths are truncated by an amount such that their entrance aperture areas, A_{conc}, are reduced by 2%. This results in a $\simeq$ 25% reduction in the axial length of the CTCs which makes both manufacture and mounting cheaper and easier. A comparison of the concentration factors of a truncated CTC and a full-length CTC, assuming ideal reflective surfaces and ideal photocathodes, is shown in Figure 6.2. The truncated CTC shows a 2% drop in concentration factor, with respect to the full-length CTC, from the 2% drop in its

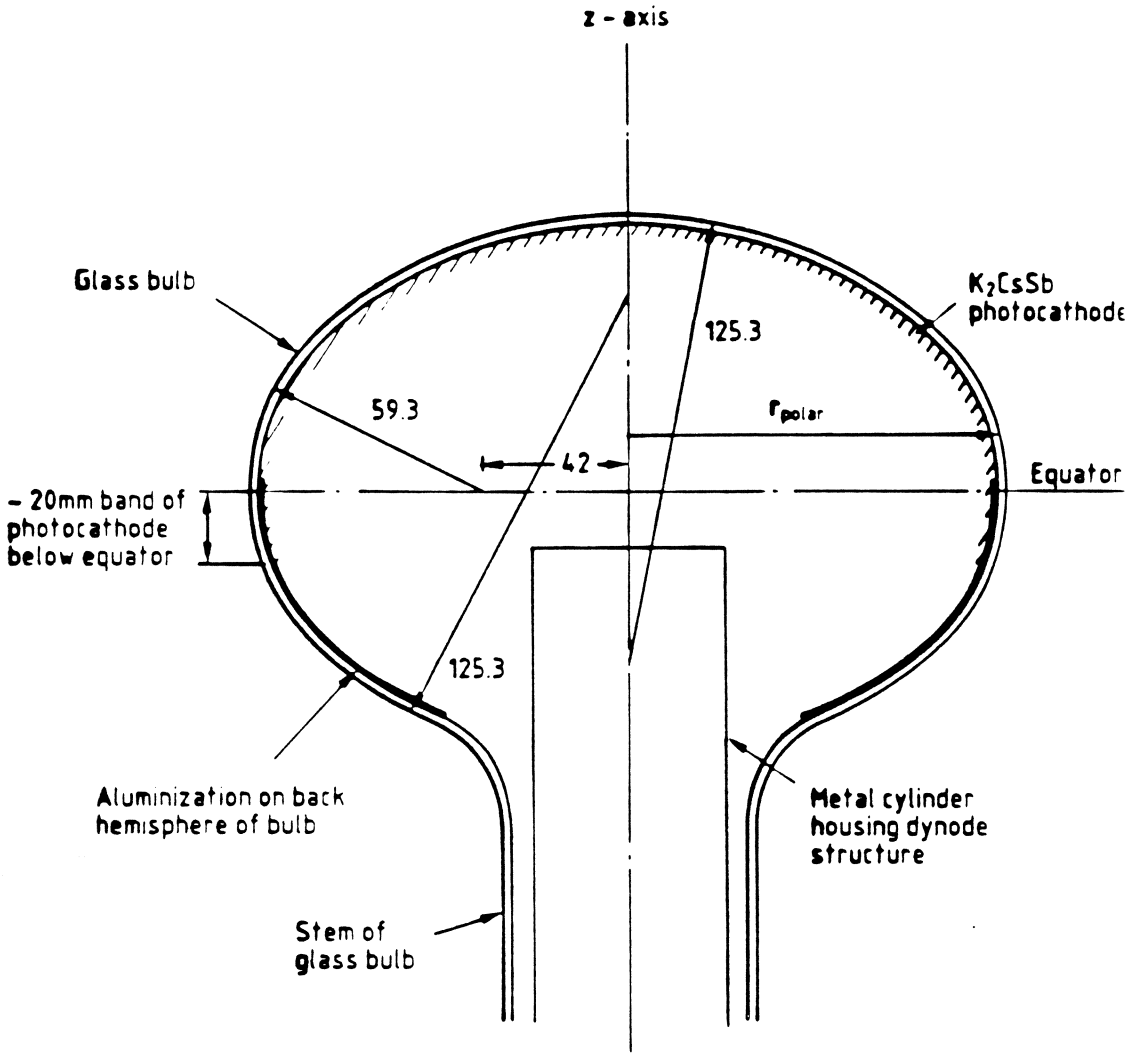

Figure 6.1: Shape of the glass bulb of the Hamamatsu R1408 photomultiplier. At the equator $r_{polar} = 101.3$ (all dimensions are in mm).

entrance aperture area. However, at large polar angles the truncated CTC has a slightly larger concentration factor from light which is able to reach the photocathode directly, without being reflected by the CTC. This light would be blocked by the uppermost section of a full-length CTC (the extra 25% axial length).

In the ray-tracing simulations of concentrator performance presented here the effect of polarization will be ignored. It will be assumed that $\varepsilon = \varepsilon_0 = \varepsilon_1 = 0$ (unpolarised light). Although this procedure is not physically correct, it is expected to be a fair approximation for calculating concentration factors for unpolarised light at the concen-

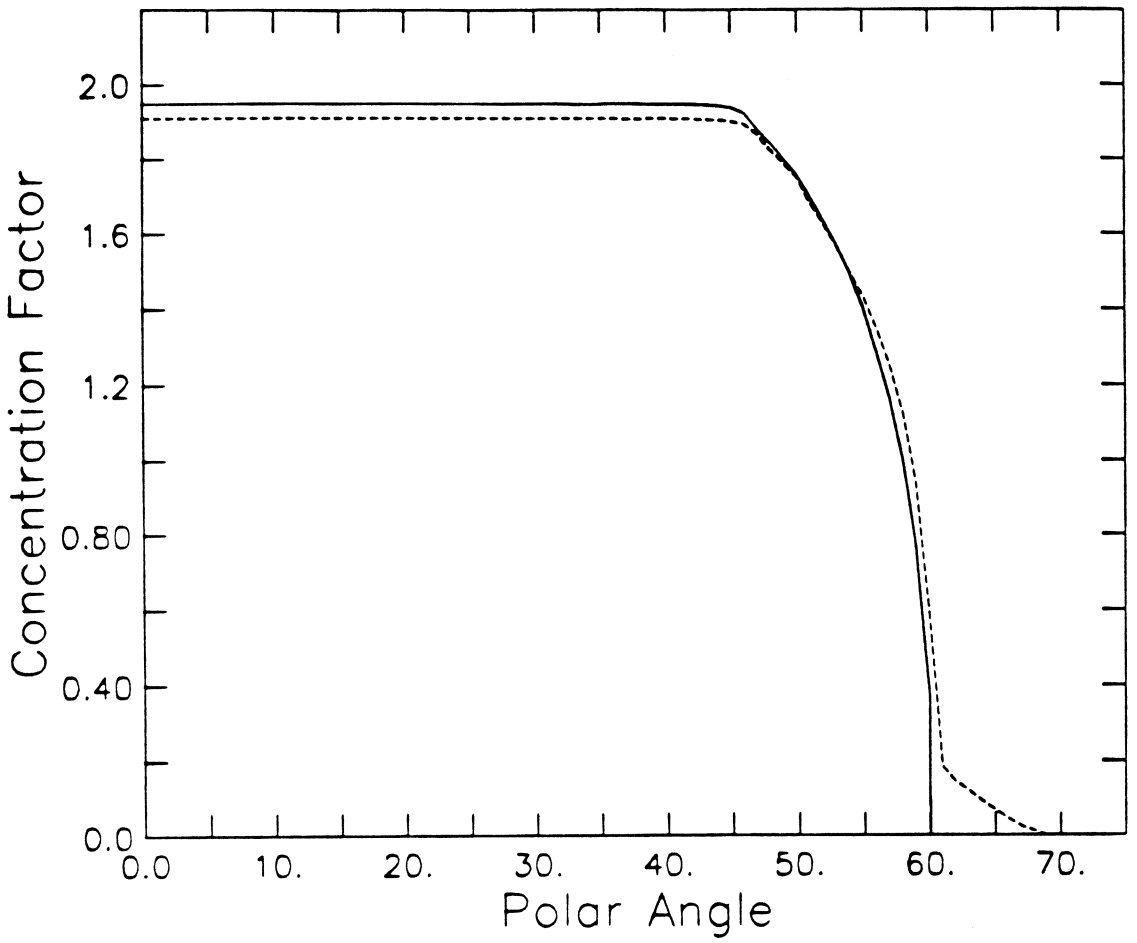

Figure 6.2: Comparison of the concentration factors of a full-length CTC (——) and a truncated CTC (– – –) in which the entrance aperture area has been decreased by 2%. The simulation assumes ideal reflective surfaces and ideal photocathodes.

trator aperture ($\varepsilon = 0$). Nevertheless, since Cherenkov photons are polarized (ϵ-vector perpendicular to Cherenkov cone surface), a correct treatment of polarization will have to be included in the full Monte-Carlo simulation of the SNO detector.

6.2 Realistic Photocathodes

In this section, the effect of realistic functions for the (unpolarised) photocathode efficiency, $E_{\mathrm{cath}}(\lambda, \varepsilon_1 = 0, n_1, r_{\mathrm{cath}}, \theta_1)$, on the concentration factor will be investigated by ray-tracing, assuming CTCs with ideal reflective surfaces.

The relative efficiency of the R1408 PMT as a function of polar radius, r_{polar}, has been measured with a collimated ($\simeq$ 2 mm) ^{90}Sr Cherenkov light source [61]. The results,

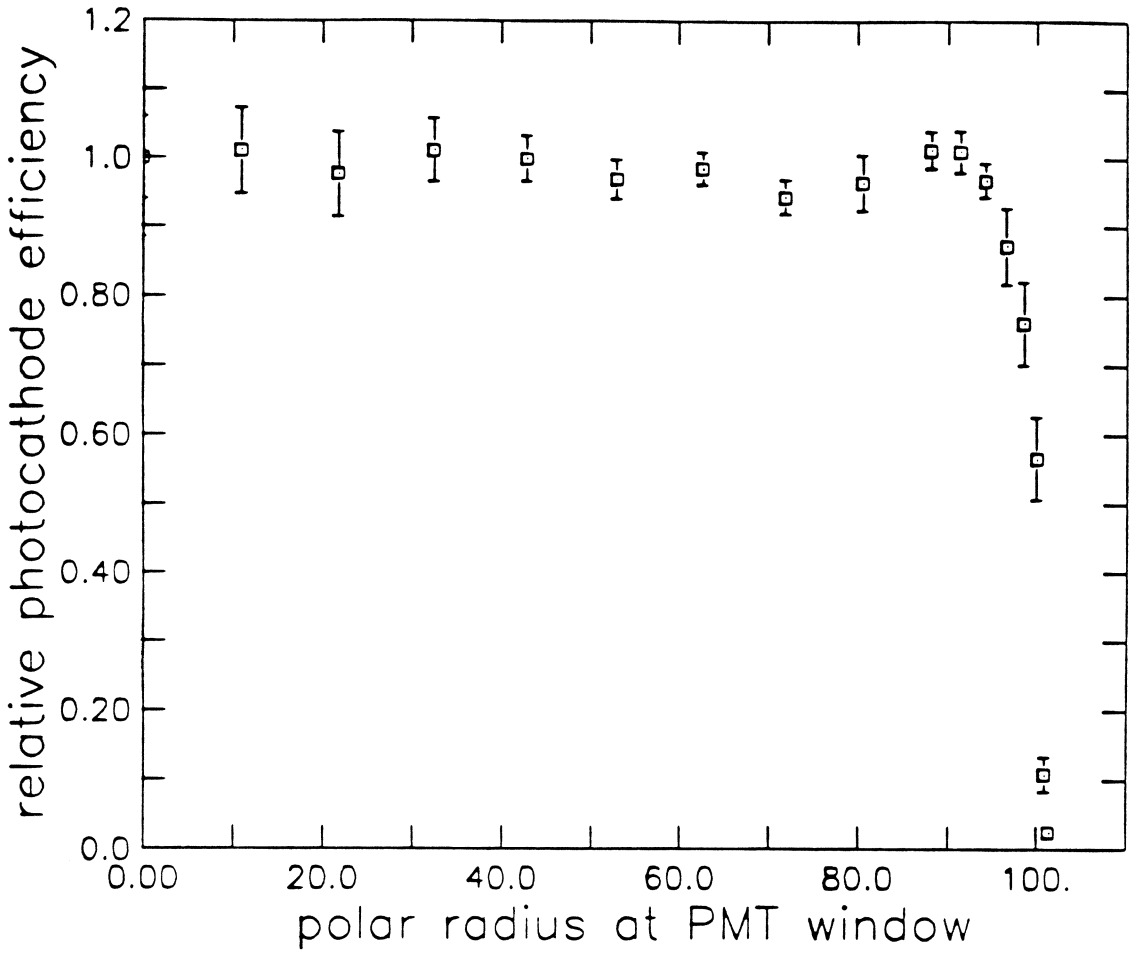

Figure 6.3: Measurement of the relative photocathode efficiency, averaged over five R1408 PMTs, as a function of r_{polar} [61].

averaged over 5 PMTs, are shown in Figure 6.3 where the cut-off in efficiency at the edge of the photocathode is probably caused by both poor electron collection efficiency at the first dynode for electron trajectories beginning near the equator of the bulb, and the presence of an opaque aluminium layer which is deposited on the inside of the glass bulb *before* the photocathode and which extends a few millimetres above the equator (see Figure 6.1).

The concentration factors of four different CTCs have been computed, assuming the above radial dependence of the photocathode efficiency (no ϕ dependence) and ignoring the dependence on λ, n_1 and θ_1. The four CTCs were simulated with the same Liouville cut-off angle (θ_{ps} = 56.4°) and photocathode shape (R1408 PMT bulb) but assuming that the photocathode extended to four different polar radii: 97, 98, 99 and 100 mm.

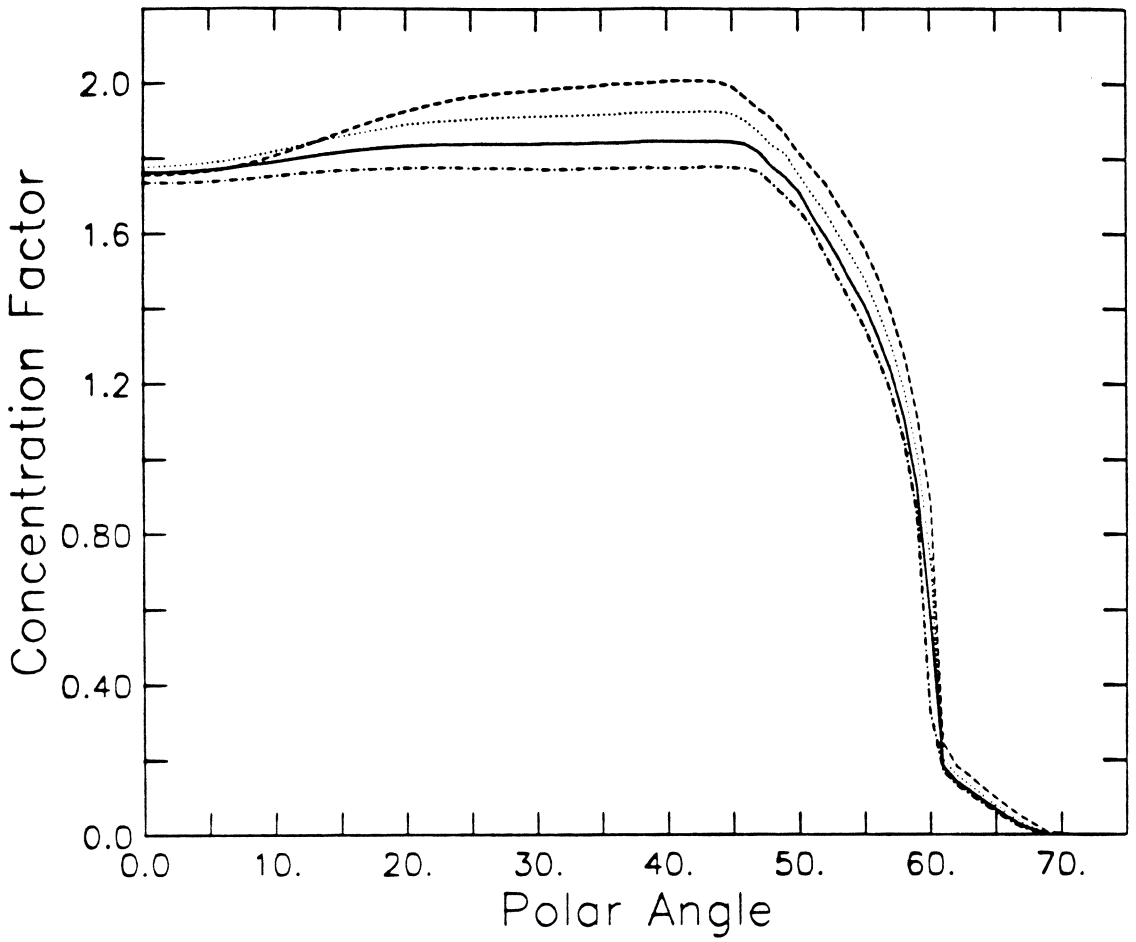

Figure 6.4: Concentration factor for four CTCs of exit aperture polar radii: 97 mm (– · – · –), 98 mm (——), 99 mm (· · · · ·) and 100 mm (– – –). The simulation assumes ideal reflective surfaces and an R1408 photocathode with an efficiency that depends on r_{polar} (see Figure 6.3) but *not* on ϕ, λ, n_1, or θ_1.

Thus the exit and entrance aperture areas of the CTCs were all different but their ratios $A_{\text{conc}}/A_{\text{cath}}$ were all the same, (5.5). As expected, the CTC constructed for the largest polar radius (100 mm), which uses the most of the photocathode area and consequently has the largest entrance aperture area, achieves the largest overall concentration factor (see Figure 6.4). However, at small polar angles the CTCs funnel light onto the outer edge of their exit apertures. The larger the polar radius of construction, the poorer the photocathode efficiency at the outer edge of the exit aperture and hence the greater the depression in concentration factor at small polar angles. Clearly, there is a compromise between *maximum* and *uniform* concentration. For the SNO detector, where uniformity

in the D_2O is critical, the CTC of polar radius 98 mm has been chosen.

Let us now assume an R1408 photocathode with an efficiency that does *not* depend on r_{polar} (for $r_{polar} \leq 98$ mm) or ϕ but *does* depend on wavelength, angle of incidence at the PMT window and refractive index, n_1, of the medium in contact with the PMT window. Unfortunately, there is not sufficient data (Figures 4.9 and 4.10) to prescribe in detail the wavelength dependence of the real and imaginary parts of the K_2CsSb photocathode over the wavelength range of interest to SNO (Figure 2.4). Nevertheless, three relevant parametrizations of the K_2CsSb photocathode (P1, P2 and P3) have been obtained in Chapter 4 (see Table 4.3).

A technical problem in simulating concentration factors with these parametrizations comes from the difficulty in treating the small (but significant) fraction of light which is *transmitted* by the photocathode. In the R1408 photomultiplier this light can be reflected back onto the photocathode by the evaporated layer of aluminium on the back hemisphere of the bulb (see Figure 6.1). The difficulty in simulating this effect is caused by the poor knowledge of the reflectivity of the metal cylinder which houses the dynode structure and of the relative efficiency of a $\simeq$ 2 cm band of photocathode below the equator which is deposited on top of the aluminium layer (to ensure good electrical contact). The reflectivity of the metal cylinder was estimated by passing a 442 nm wavelength laser beam through the glass stem of the PMT bulb, onto the metal cylinder, back through the glass stem and onto a photodiode. After correcting for reflection losses at the glass stem, the specular component of the metal cylinder reflectivity was about 30%. The diffuse component could not be accurately measured but was estimated at about 10% giving a total reflectivity of about 40%. The relative efficiency of the equatorial band of photocathode was fixed at the plausible value of 50% in the absence of any direct evidence. This estimate was guided by the *measurements* of concentration factors in Section 6.4.

Having established these parameters, the effect on the concentration factor of the angular behaviour of the K_2CsSb photocathode can be simulated by ray-tracing. For each of the three parametrizations in Table 4.3 the concentration factor has been computed

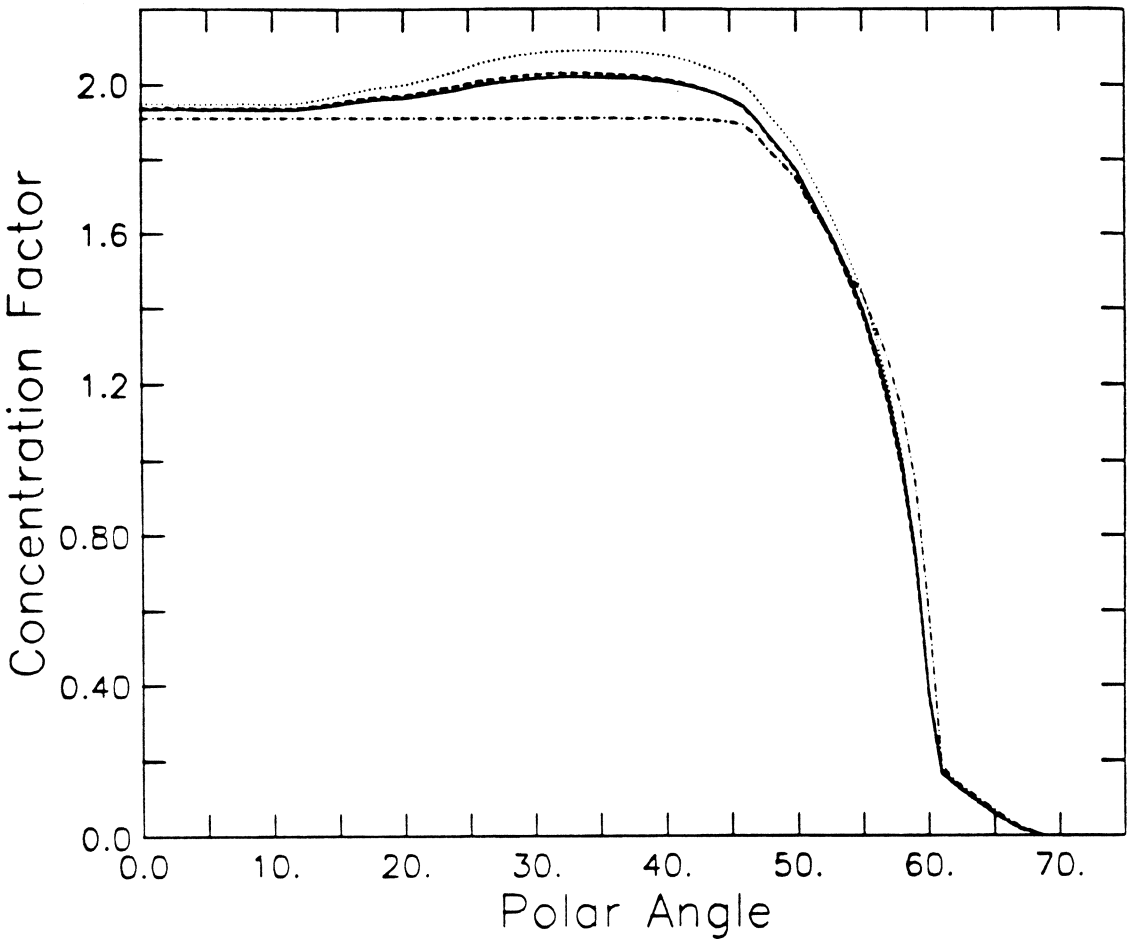

Figure 6.5: Concentration factors in *air* assuming P1 (····), P2 (– – –) and P3 (——); and an ideal photocathode (–·–·–). The simulation assumes no radial or ϕ dependence for the efficiency of the photocathode; and ideal reflective surfaces for the CTC.

assuming three different values for the refractive index, n_1, of the medium in contact with the PMT window. The results for n_1 = 1.0 (air), n_1 = 1.34 (water) and n_1 = 1.49 (scintillator) are shown in Figures 6.5, 6.6 and 6.7 together with the concentration factor simulated for an ideal photocathode.

In all three figures, the slight increase in concentration factor, at polar angles of 20°–50°, for all three parametrizations with respect to the ideal photocathode, is caused by the behaviour of the rays which are transmitted by the photocathode into the bulb. At small polar angles, 0°–20°, most of these rays are reflected by the back hemisphere of Al (90% reflectivity) on to the metal cylinder (40% reflectivity). Then they are mostly reflected onto the equatorial band of photocathode (50% relative efficiency) and so do

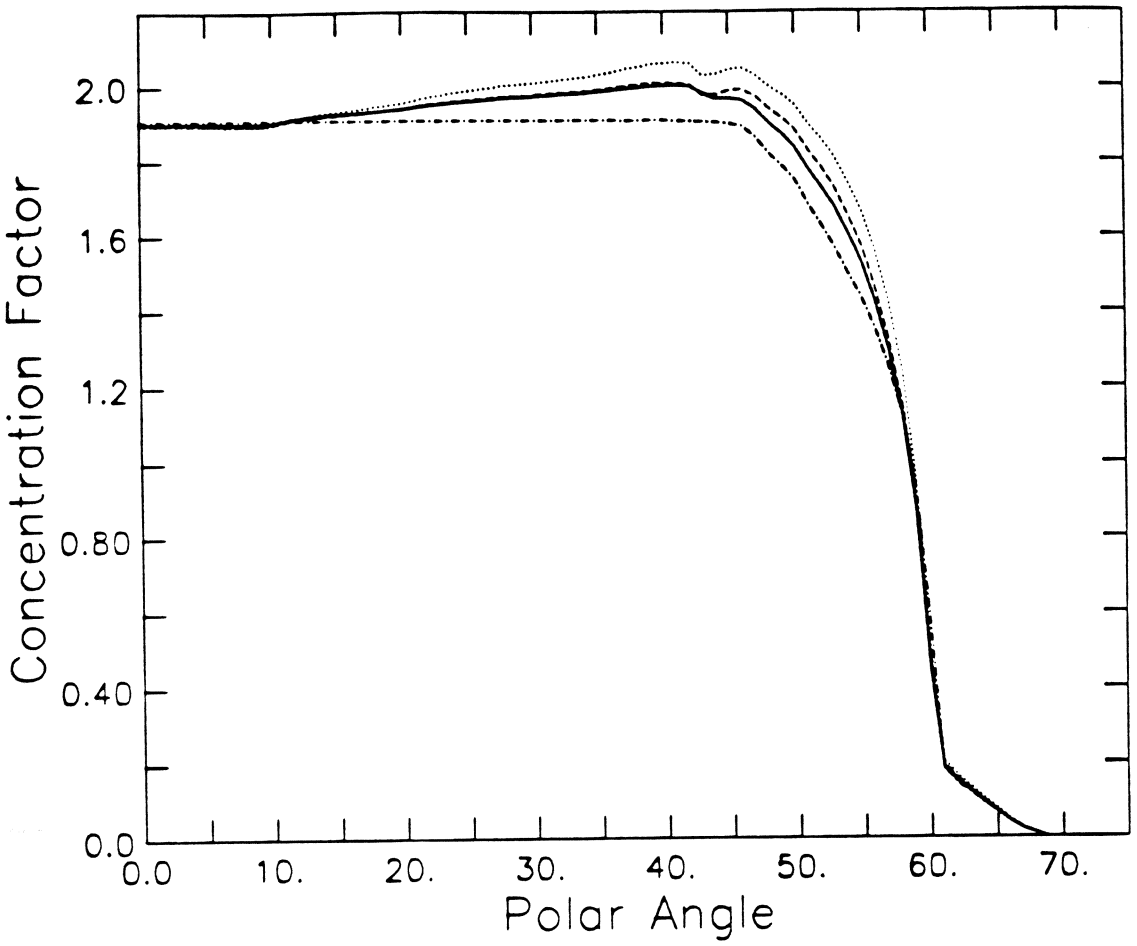

Figure 6.6: Concentration factors in *water* assuming P1 (·····), P2 (– – –) and P3 (——); and an ideal photocathode (– · – · –). The simulation assumes no radial or ϕ dependence for the efficiency of the photocathode; and ideal reflective surfaces for the CTC.

not contribute very much to the overall efficiency of the PMT. As the polar angle at the concentrator aperture increases beyond 20°, a greater fraction of the transmitted rays is reflected by the Al directly onto 'good' photocathode (above the equator). Thus the contribution to the overall efficiency of the PMT from the transmitted rays increases with polar angle. This effect is about twice as pronounced for P1 as it is for P2 and P3 in which the transmission coefficient of the photocathode is about half that for P1, (see Chapter 4).

In air, the cut-off in concentration factor occurs at a slightly smaller polar angle ($\sim 1°$ less) for the three parametrizations than for the ideal photocathode (see Figure 6.5). This effect is caused by the cut-off in photocathode absorptivity at about 84.5° incidence at

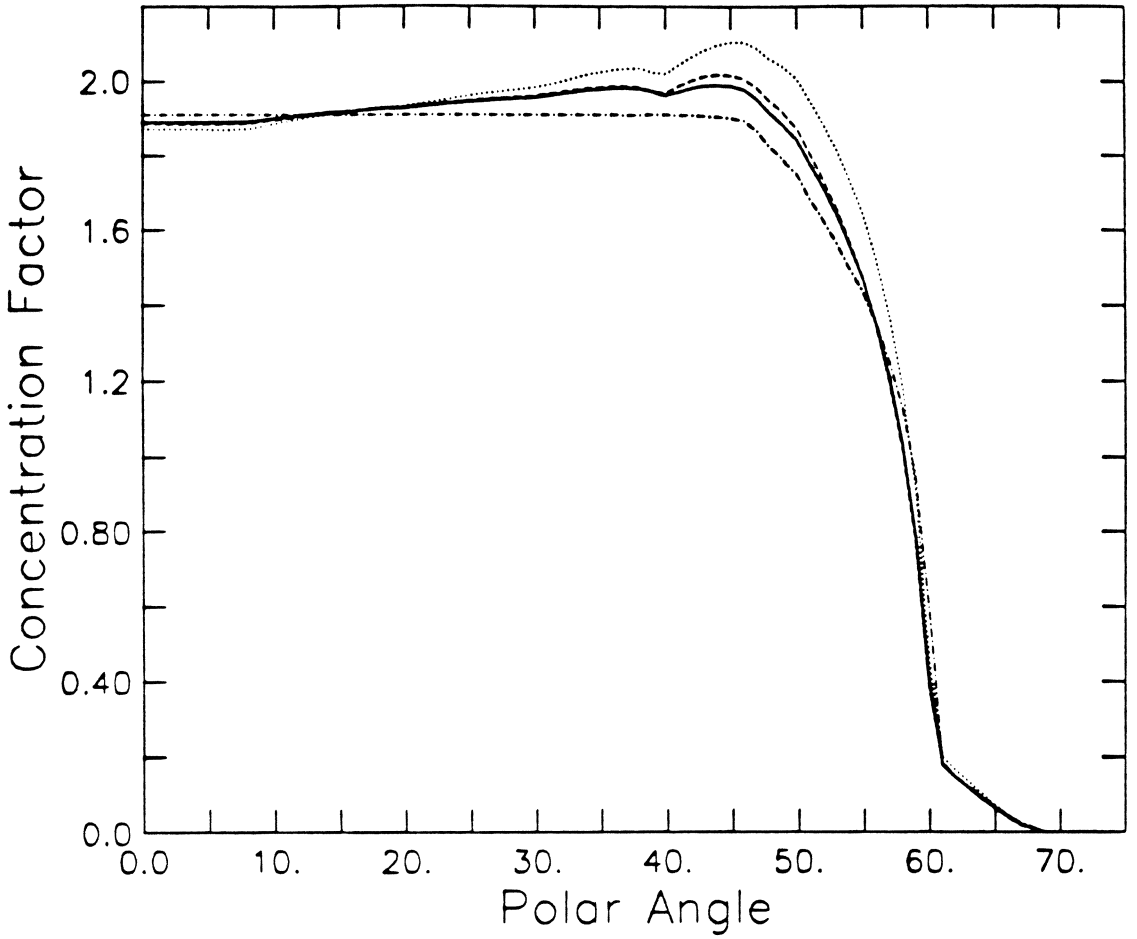

Figure 6.7: Concentration factors in *scintillator* assuming P1 (·····), P2 (– – –) and P3 (——); and an ideal photocathode (–·–·–). The simulation assumes no radial or ϕ dependence for the efficiency of the photocathode; and ideal reflective surfaces for the CTC.

the PMT window for the three parametrizations, (see Table 4.3 and Figures 4.13 and 4.16). In water, the case relevant to SNO, this effect is much smaller ($\sim 0.1°$) because the photocathode absorptivity for the three parametrizations cuts-off at a greater angle ($\sim 86.5°$) at the PMT window and also peaks at about 70° incidence (see Figures 4.14 and 4.17). This peak in absorptivity at about 70° incidence at the PMT window causes a slight increase in the concentration factor at polar angles beyond 45°. The small 'dip' in the concentration factor at a polar angle of about 43° is caused by the peak in reflectivity of the photocathode at 50° incidence at the PMT window. In scintillator the shift in the cut-off angle of the concentration factor is about 0.5°. The photocathode absorptivity cuts-off at about 84.5° and peaks at about 60° incidence at the PMT window (see Figures

4.15 and 4.17). This produces a marked increase in the concentration factor at polar angles beyond 40°. The slight dip in concentration factor at 40° is caused by the peak in photocathode reflectivity at 45° incidence at the PMT window.

6.3 Realistic Reflective Surfaces

In this section the effect of realistic reflective surfaces on the concentration factor will be investigated with ray-tracing simulations in which the photocathode is assumed to be ideal.

In the application of the CTC design to SNO the reflective surface is required to have a high (and reasonably uniform) reflectivity for all angles of incidence, over the wavelength range given in Figure 2.4. This requirement eliminates the possibility of relying on total internal reflection or multi-layer dielectric stacks which are both known for their extremely high reflectivity in limited angular ranges. On the other hand, the specular reflectivity of metallic films is known to be very uniform with respect to angle of incidence (see Figure 6.8). Of these metallic films the two most suited to the wavelength range of scintillation or Cherenkov counters are aluminium and silver. Aluminium has an approximately constant reflectivity of 90% across the whole wavelength range 250–600 nm, whereas the reflectivity of silver is 95% at 620 nm and 90% at 500 nm dropping to 80% at 380 nm and 50% at 335 nm. Hence in most circumstances aluminium is favoured since the bialkali photocathode is efficient down to a wavelength of 300 nm defined by the transmission cut-off of its glass envelope (see figure 4.1). However there might be circumstances (e.g. a scintillator with poor U.V.-transmission) in which silver is preferred by virtue of its higher reflectivity above 500 nm wavelength. In SNO, silver is ruled out for practical reasons (see Chapter 7).

Two prototype aluminium CTCs have been developed for SNO. Their manufacturing methods are described in detail in Chapter 7. The first is a glass CTC (Figure 6.9) in which Al is evaporated on the outer surface of the glass dish and hence the CTC acts as a 'back surface reflector' since light is incident on the Al film after passing through the glass

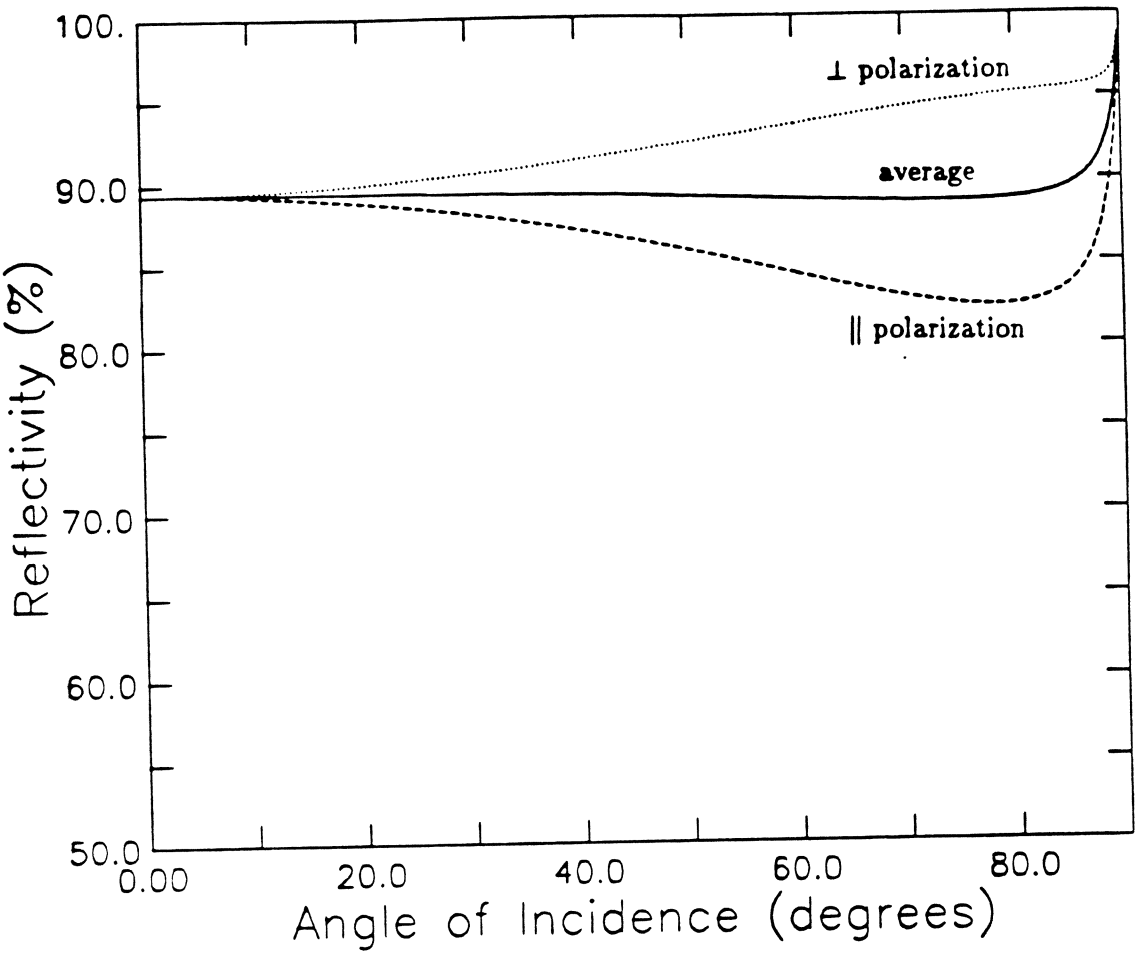

Figure 6.8: Total reflectivity of a back surface glass/Al CTC in water as a function of angle of incidence at the water/glass boundary. The calculation is at 410 nm wavelength (where $n = 0.523$ and $k = 5.024$ for Al [62]) but does not change significantly over the wavelength range 250–500 nm.

substrate. The total reflectivity (water/glass + glass/Al) of this CTC is approximately constant ($\simeq 89\%$) with respect to angle of incidence at the water/glass boundary (see Figure 6.8) and across the wavelength range of interest to SNO. The second prototype CTC is a polygonal concentrator (Figure 6.10) in which an evaporated multi-layer film, $SiO_2/Al/MgF_2/Pr_2O_3{+}TiO_2$, is deposited on anodised Al sheet. This coated sheet, called 'Omega', acts as a 'front surface reflector' since light is directly incident on the evaporated film (in which the Al layer provides the reflectivity). The reflectivity of Omega has been measured in air, as a function of wavelength, at 0° and 45° incidence. The results of this measurement are shown in Figure 6.11 together with a computer simulation of the reflectivity in water at 47° incidence [63].

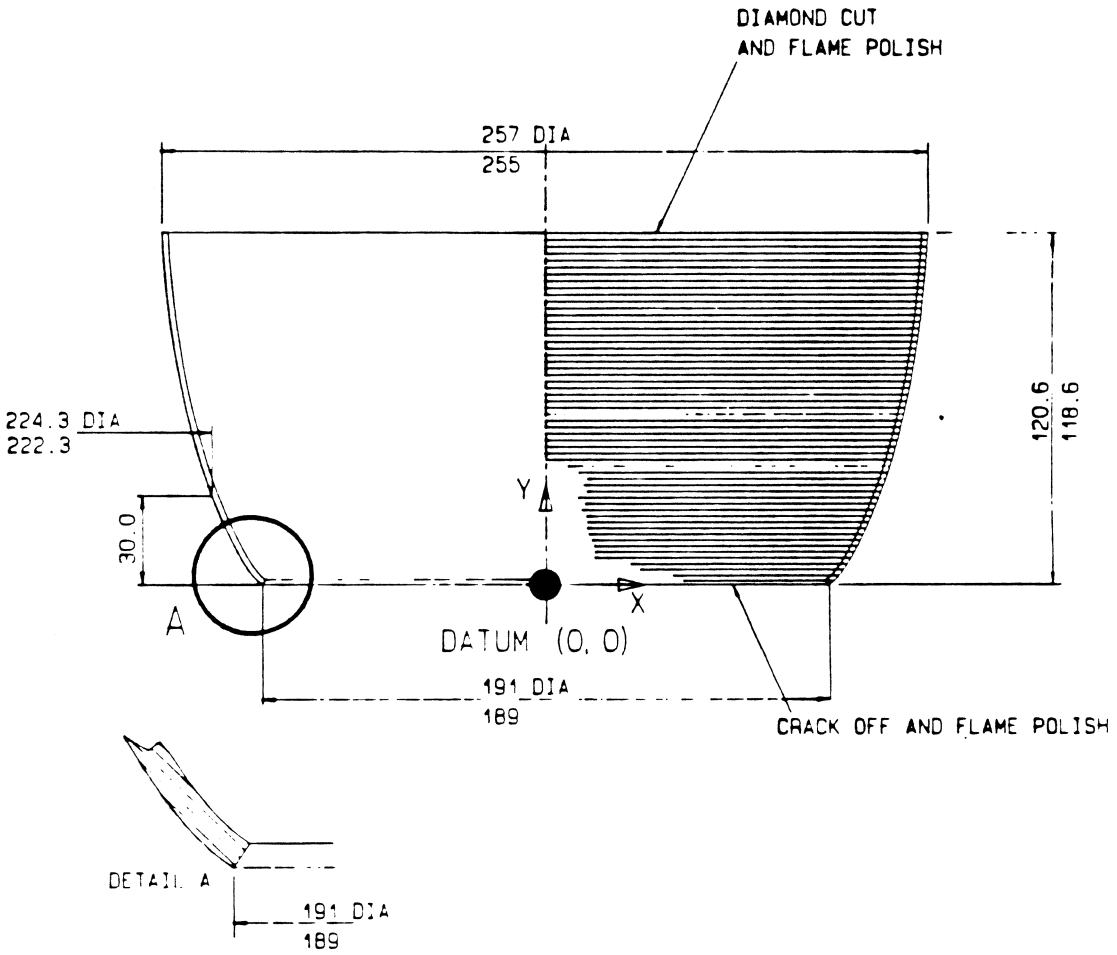

Figure 6.9: Prototype glass CTC which can be evaporated with Al on the outer surface to form a back surface reflector, or on the inner surface to form a front surface reflector.

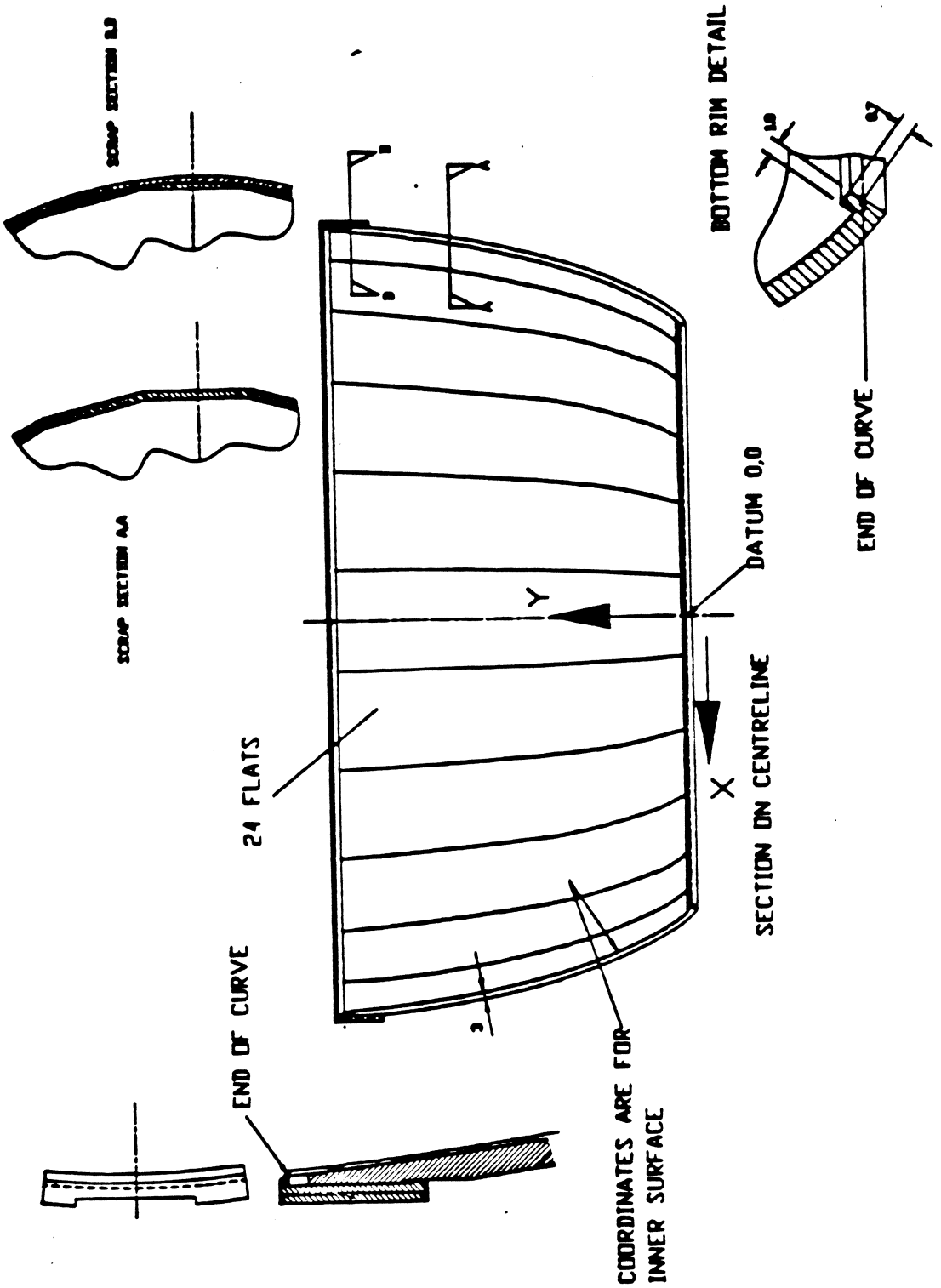

Figure 6.10: Prototype plastic holder for making a polygonal Omega CTC. The shaped petals of Omega sheet are located on the inner surfaces of the holder and are held in place by the lips at either extremity.

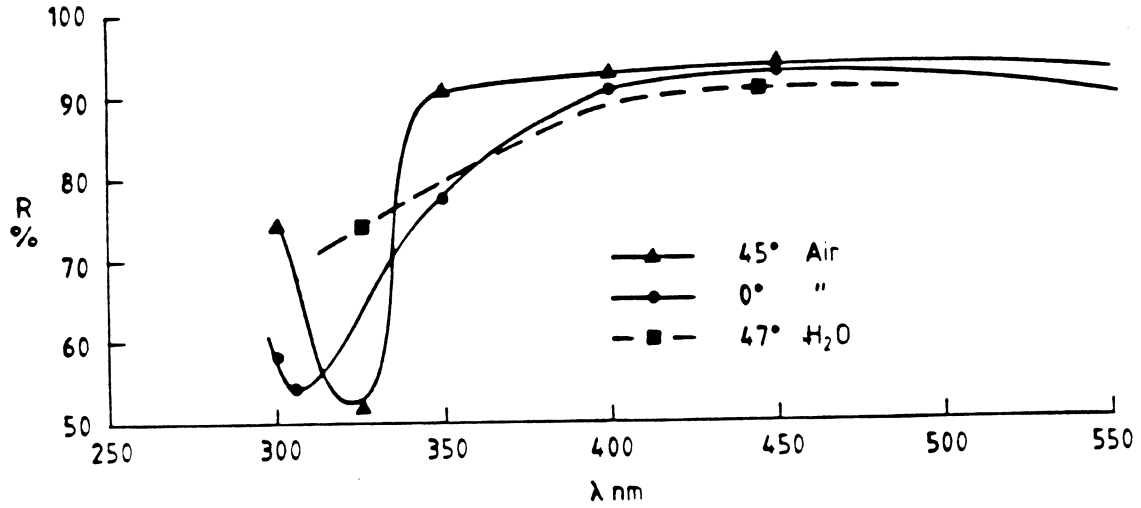

Figure 6.11: Wavelength dependence of the reflectivity of Omega *measured* in air and *calculated* in water.

Recently, the validity of this computer simulation, which does not include absorption in the Pr_2O_3+TiO_2 layer, has come into question. Hence it has not been used to model the complicated angular and wavelength dependence of Omega reflectivity in air and in water. Instead, an 'effective' reflectivity (a weighted average over wavelength, angle of incidence and polarization) has been included as a single parameter in the ray-tracing simulation programme. At different polar angles at the concentrator entrance aperture, this effective reflectivity is averaged over a different distribution in angle of incidence at the reflective surface. Hence it is not necessarily constant with polar angle. Its value, as a function of polar angle, can be deduced from the *measured* concentration factors in air and in water of prototype Omega CTCs (see Section 6.4). It is expected to be between 80% and 90% both in air and in water and perhaps slightly higher in air than in water.

Figure 6.12 shows the expected concentration factor for four CTCs with constant reflectivities (for all λ, ε_0, n_1, r_{ref}, and θ_0) of 100%, 90%, 80% and 70%. The decrease in concentration factor of the 90%, 80% and 70% reflective CTCs with respect to the 100% reflective CTC is significantly less than the corresponding decrease in reflectivity. This is because up to half of the concentrated light at a given polar angle is *directly* incident on the photocathode without being reflected by the CTC (i.e. the average value

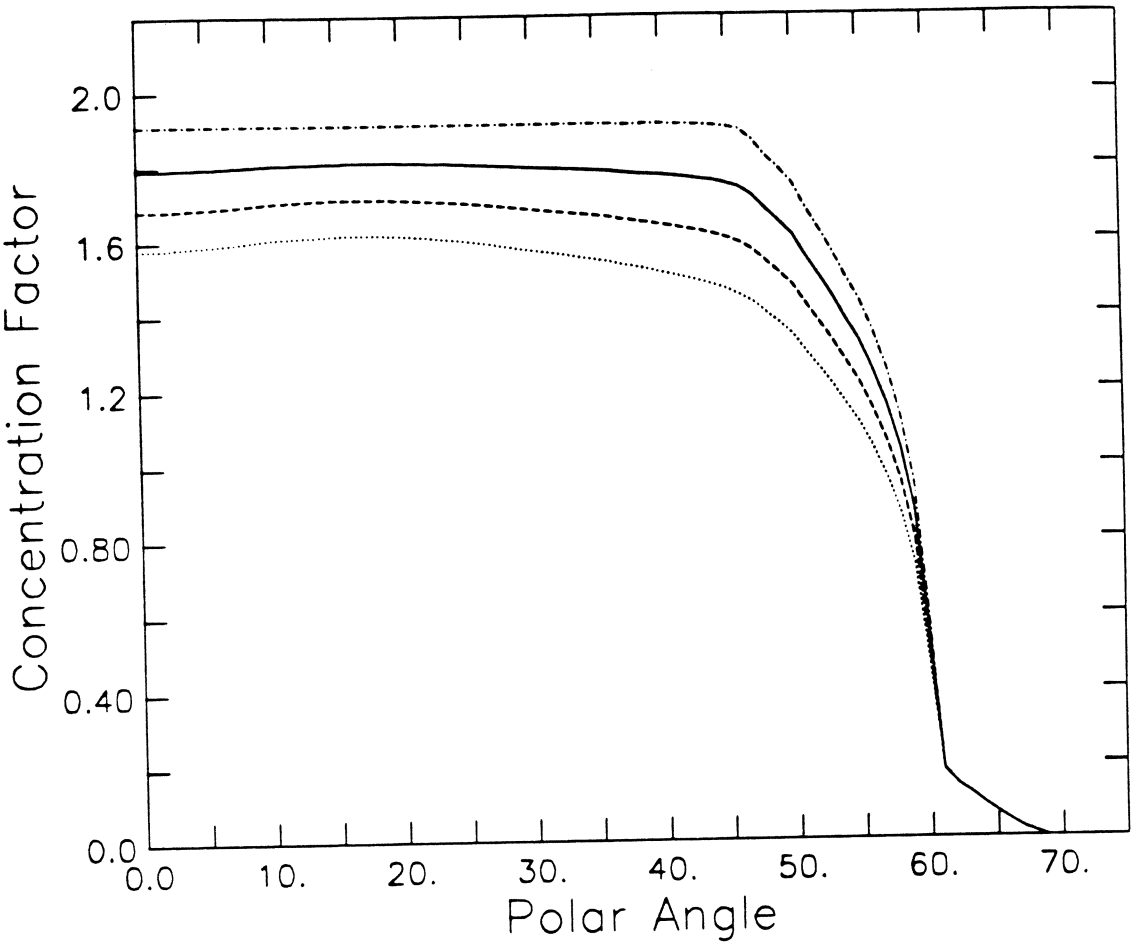

Figure 6.12: Concentration factor for four CTCs with different reflectivities: 100% (–·–·–), 90% (——), 80% (– – –) and 70% (·····). The simulation assumes an ideal photocathode.

of β in (6.1) is less than 1). At large polar angles (40°–60°) the proportion of this direct light decreases (β increases) and hence the concentration factor decreases slightly. At small polar angles (0°–10°) much of the light which is incident on the CTC is *multiply-reflected* before reaching the photocathode (causing β to increase slightly) and hence the concentration factor shows a slight dip at 0°.

The Omega concentrator is not a perfect CTC in that it is made from a number of shaped strips which fit together like the petals of a flower but *without* overlapping (see Figure 6.10). The 2D profile of the centerline of each 'petal' is constrained to the 2D profile from which the usual figure-of-revolution 3D CTC is constructed. The concentration factors of such polygonal CTCs have been simulated by ray-tracing. Figure 6.13

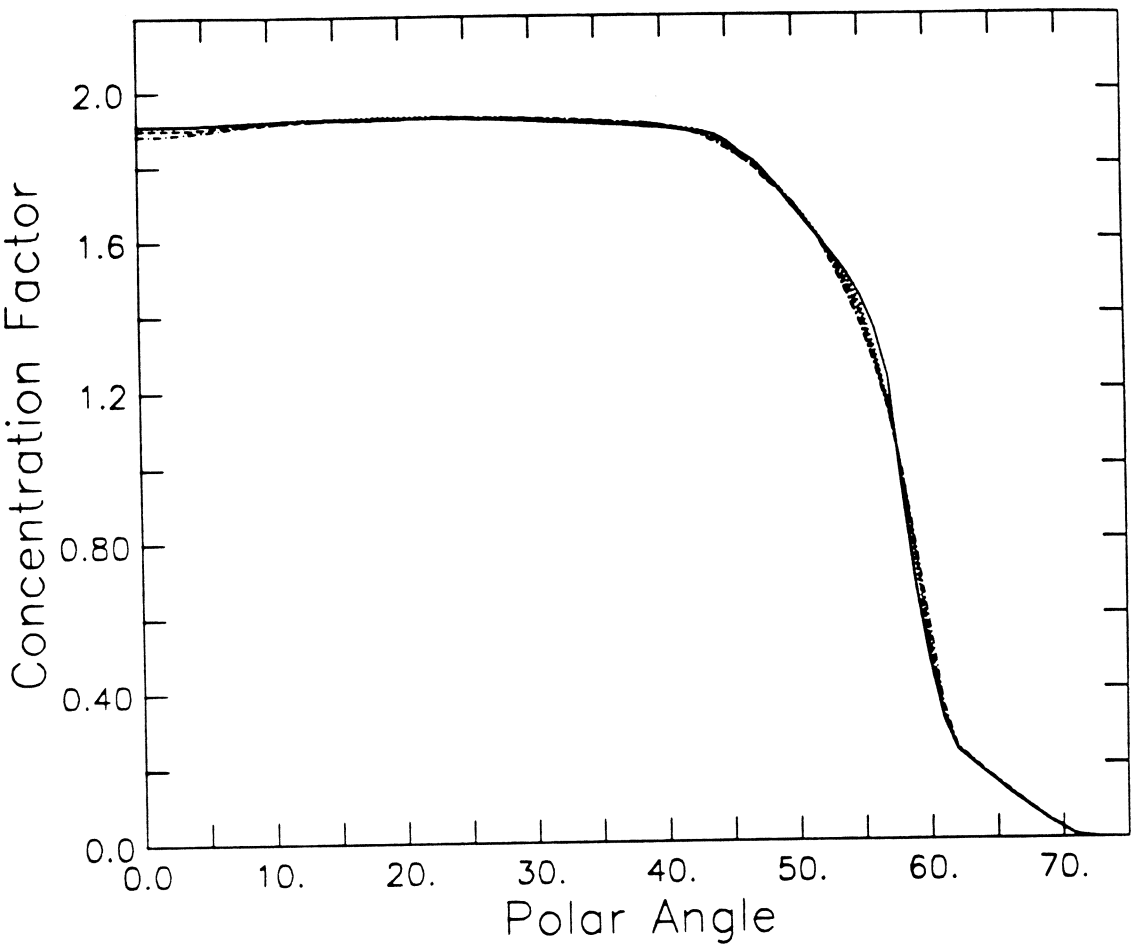

Figure 6.13: Concentration factor for three polygonal CTCs with different numbers of petals: 18 (– · – · –), 24 (– – –) and 30 (· · · · ·) and the corresponding figure-of-revolution CTC (——). The simulation assumes a constant reflectivity of 90% and an ideal photocathode.

shows the results of these simulations for 18, 24, and 30-sided polygonal CTCs compared with the concentration factor of the usual figure-of-revolution CTC. The differences are very small which is not surprising, given the uncritical nature of a non-imaging device such as the CTC. For SNO the 24-sided case has been chosen. In the limit where the number of sides of the polygon goes to infinity the concentration factor approaches that of the figure-of-revolution CTC. This provides a useful check on the simulation.

A plastic polygonal holder is used to constrain the petals, which are cut from flat sheet, into the required 2D profile. This holder is made slightly larger than the desired polygonal CTC by an amount equal to the thickness of the petals (0.3 mm). The petals

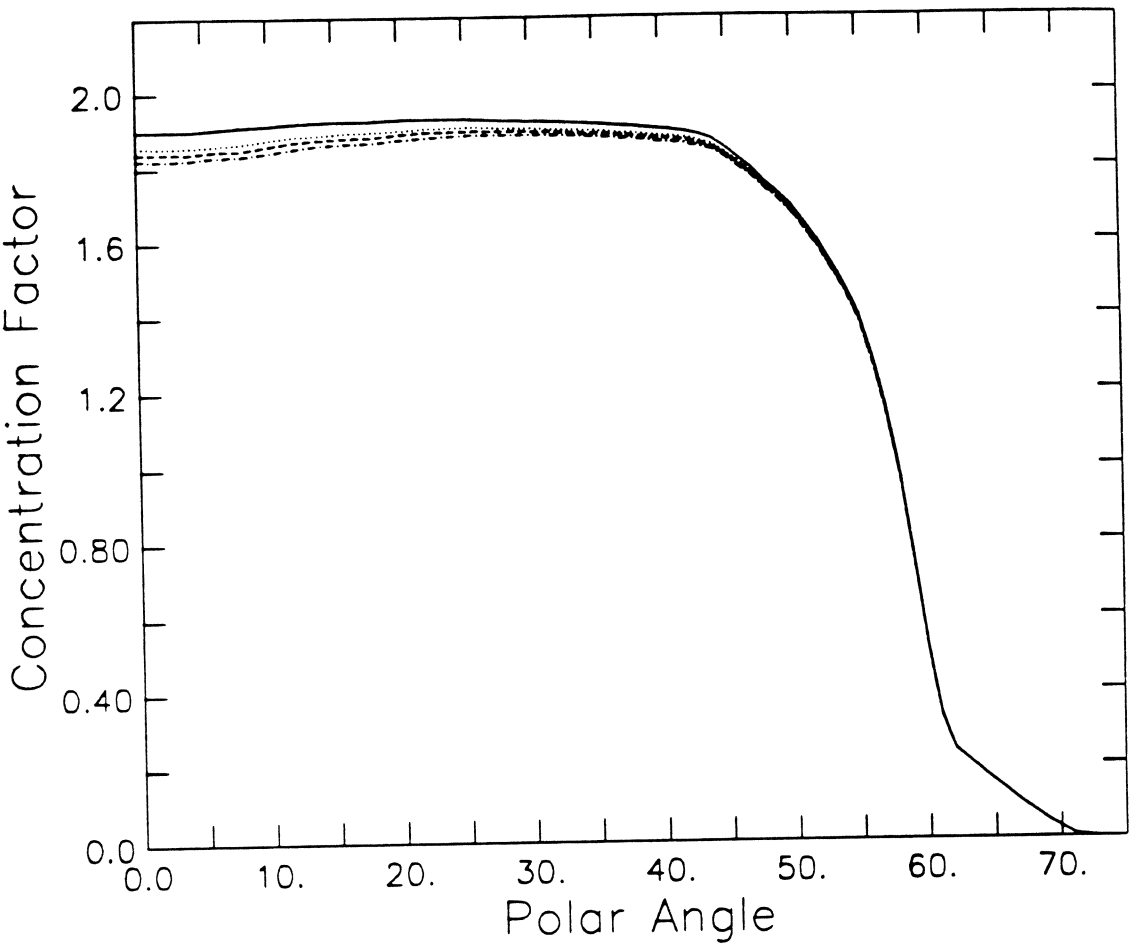

Figure 6.14: Concentration factor for four 24-sided polygonal CTCs with different longitudinal (black) lip thicknesses: 0 mm (——), 1.0 mm (·····), 1.5 mm (– – –) and 2 mm (– · – · –). The simulation assumes a constant reflectivity of 90% and an ideal photocathode.

are held against the plastic holder by the compressive force exerted by plastic lips at either end of the holder (see Figure 6.10). The effect of these black lips (ABS plastic) on the concentration factor has been simulated for different lip thicknesses (in the direction of the petal surface): 1, 1.5 and 2 mm. The results are shown in Figure 6.14 where the decrease in concentration factor is strongest at small polar angles when light is funneled onto the lower lip.

The conformation of the petals to the required profile of the plastic holder is not absolutely perfect. At the bottom end of the CTC (near the exit aperture), where the curvature of the profile is greatest, the petals do not rest on the plastic backing but

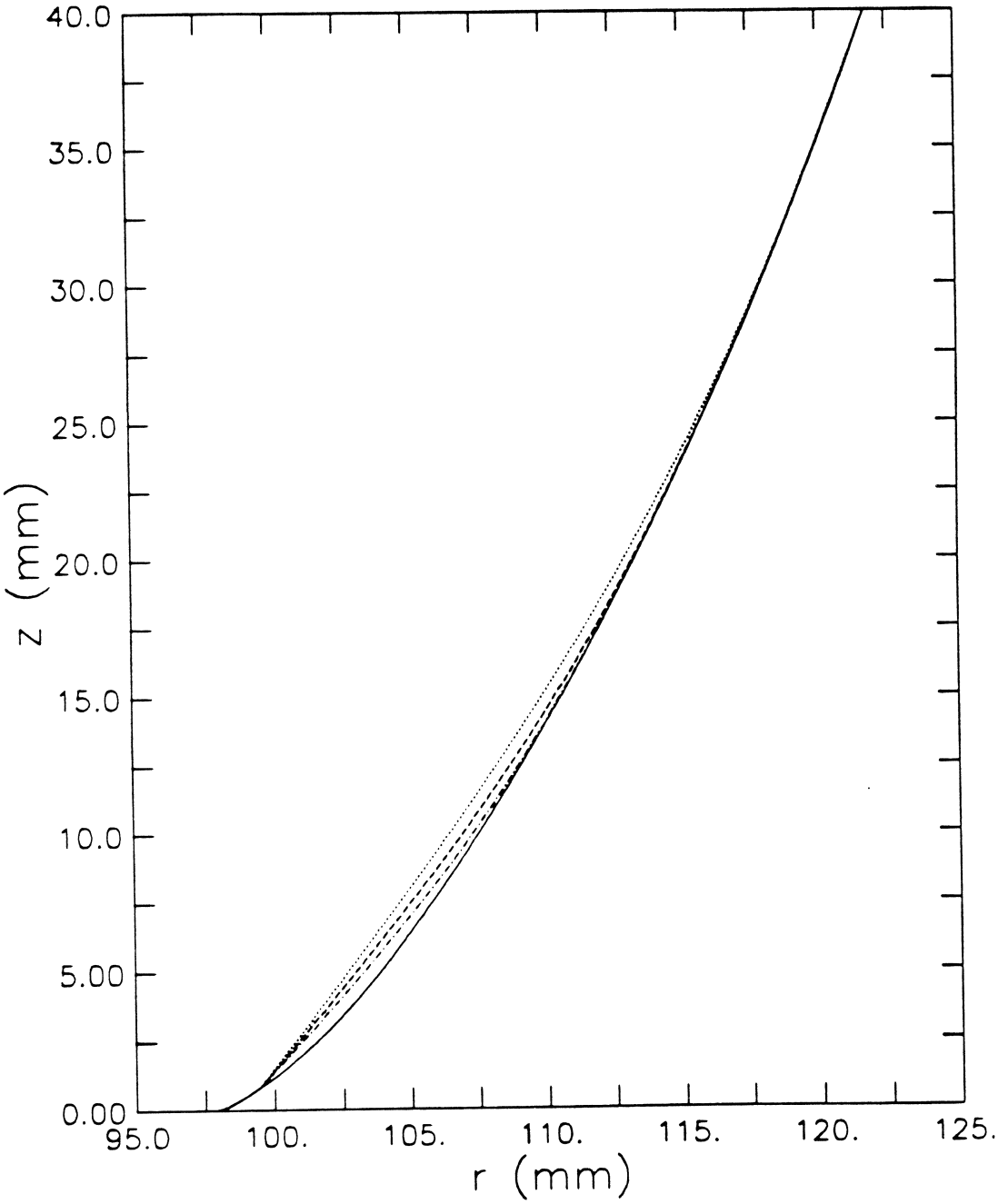

Figure 6.15: Conformation of the midsection profile of a petal to the required 2D CTC profile (——) assuming the following compressive stresses: 0.4 N/mm (·····), 0.8 N/mm (– – –) and 1.6 N/mm (·····). The first 1.5 mm at the lower extremity of the profile is the plastic lip which holds the petals. The other extremity of the profile is at coordinate (r = 135.5 mm, and z = 107.7 mm).

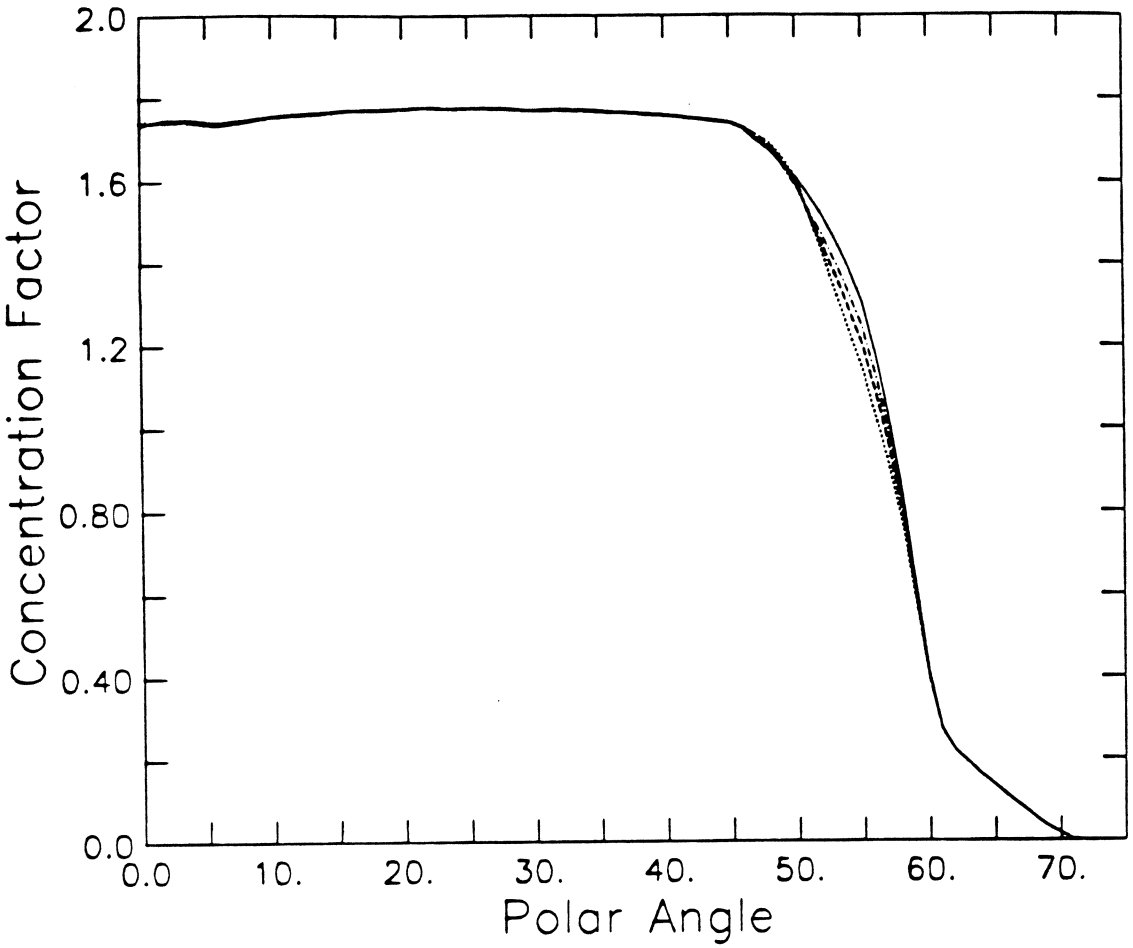

Figure 6.16: Concentration factor of four 24-sided polygonal CTCs assuming the petal 2D midsection profiles of Figure 6.15: ideal profile (——), 0.4 N/mm (·····), 0.8 N/mm (– – –) and 1.6 N/mm (·····). The simulation assumes 90% reflective CTCs with 1.5 mm (black) lips and ideal photocathodes.

are suspended from the plastic in the shape of an Euler strut. The resulting profile of the midsection of a petal has been calculated [64] for various stresses at either end of the petal: 0.4, 0.8 and 1.6 N/mm (see Figure 6.15). From an analysis of the breaking stress of the plastic lips which hold the petal and of the creep in length of the plastic holder under a given stress, it is estimated that a stress of 0.8 N/mm is acceptable [64]. The concentration factors for 24-sided CTCs of 90% reflectivity with the four petal midsection profiles given in Figure 6.15 and with 1.5 mm lips, are shown in Figure 6.16. As expected, the change in shape has a small effect on the CTC's angular cut-off. The effect of this small change in angular response on the radial response of the SNO

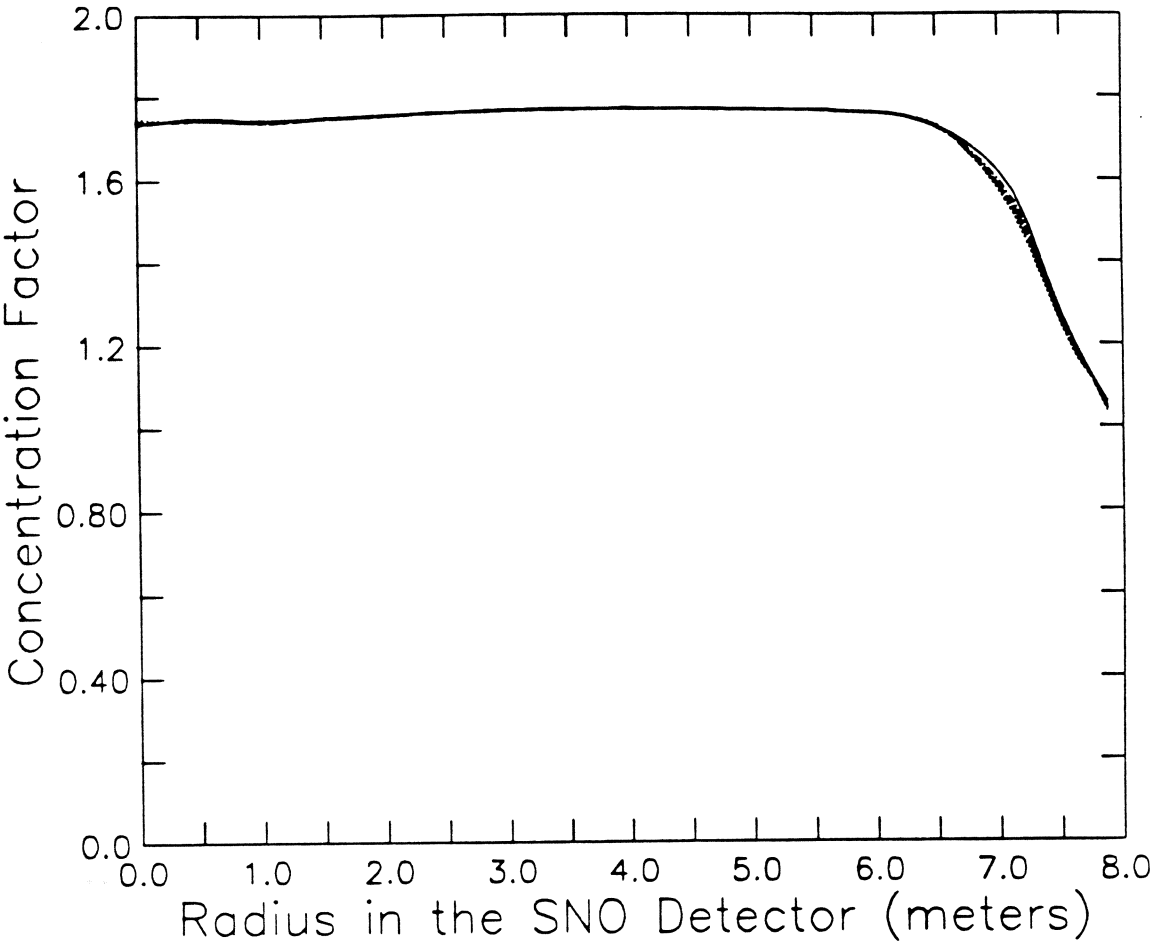

Figure 6.17: Radial dependence of the concentration factor calculated from the four angular responses shown in Figure 6.16: ideal profile (——), 0.4 N/mm (·····), 0.8 N/mm (– – –) and 1.6 N/mm (·····). The calculation does not take into account any absorption in the acrylic vessel, D_2O or H_2O.

detector can be calculated by convolving the four angular responses in Figure 6.16 with the distribution in polar angle at the photomultiplier sphere of isotropic light from an event at radius R (Figure 2.2). This calculation does not include absorption in the D_2O, H_2O or acrylic sphere. The results are shown in Figure 6.17 where it is clear that the change in shape has a marginal effect on the radial response.

The concentration factor of the *back surface* glass/Al CTC will be slightly reduced by imperfect transmission through the ground glass rims at the top and bottom of the CTC. This edge-effect is very difficult to simulate accurately and no attempt has been made here as it should be much easier to assess this edge-effect from direct measurements

of the concentration factors of prototype glass/Al CTCs.

6.4 Measurement of CTC Concentration Factors

An experiment was carried out to verify that the concentration factors of CTCs are indeed as predicted by the ray-tracing simulation and also to measure the concentration factors of prototype CTCs for SNO. To carry out the former, a front surface glass/Al concentrator was made by evaporating Al/MgF_2 on the *inner* surface of a glass CTC. This concentrator suffers no edge-effects and its reflectivity is independent of angle of incidence and wavelength (MgF_2 transmits well below 300 nm). Its reflectivity was measured at four separate locations with a 442 nm wavelength laser beam. At every location a reflectivity of $84 \pm 1\%$ was recorded. This slightly low reflectivity was caused by non-ideal evaporation conditions and is well understood (poor collimation of the evaporation sources, see Chapter 7). The polar radius of the exit aperture of this CTC was 93.5 mm which avoids the region of poor photocathode efficiency at large polar radii (see Figure 6.3).

A prototype 24-sided Omega CTC was made with a vacuum formed ABS plastic holder with 1.5 mm lips. This CTC had an exit aperture of polar radius 94.5 mm and hence also avoids the region of poor photocathode efficiency (see Figure 6.3). Prototype back surface glass/Al CTCs were made by evaporating Al/TiO on the outer surface of glass CTCs. Unfortunately, the glass in these CTCs had poor U.V. transmission[1] and so the measured concentration factors could not be reliably interpreted and the magnitude of the edge-effect from the ground glass rims could not be deduced.

The apparatus for measuring concentration factors in air and in water is shown in Figure 6.18. The source of light was the Cherenkov radiation from ^{90}Sr (a pure beta-

[1]The walls of the high-purity silica pot in which U.V.-transmitting glass was originally melted were not sufficiently rigid to sustain a large enough gob of glass being extracted from the pot. For the purpose of obtaining glass CTCs for accelerated ageing tests, a stronger 'dirty' pot was used in which low quality sand was melted, resulting in glass with poor U.V. transmission. When this was realised, there was not sufficient time to make U.V. transmitting glass CTCs before having to decide between the two prototype CTCs for SNO.

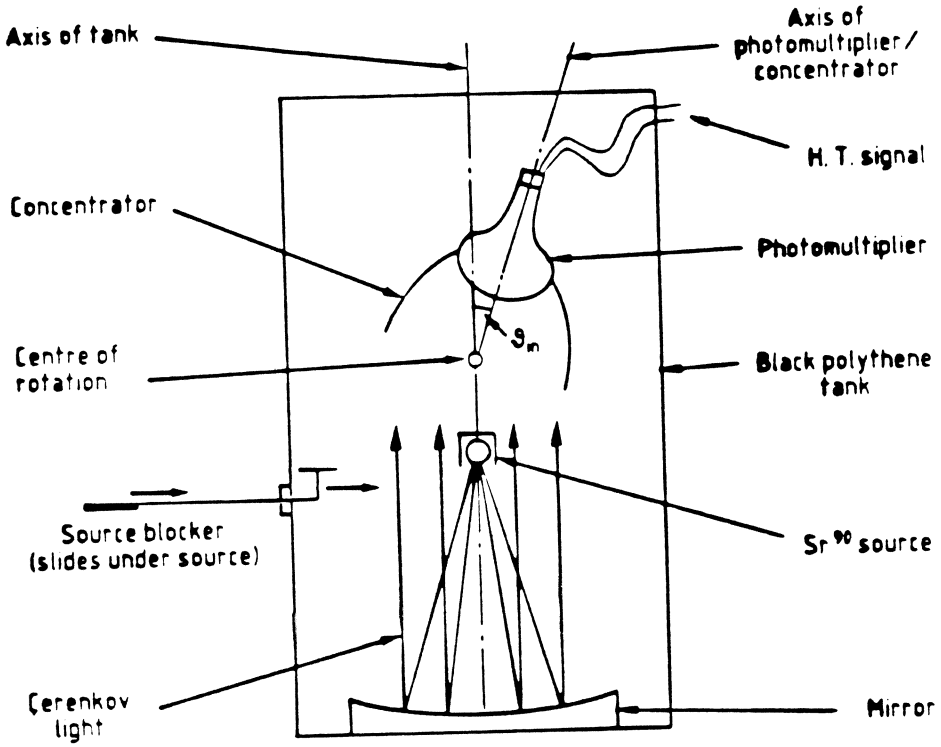

Figure 6.18: Apparatus for measuring concentration factors in air and in water.

emitter) deposited at the centre of a 30 mm diameter acrylic sphere. The acrylic used to make this source was the same U.V.-transmitting acrylic that will be used in SNO. Hence the wavelength spectrum of the detected light from this source was very similar to that in SNO (Figure 2.4) although the U.V. cut-off occurred at a slightly shorter wavelength ($\simeq$ 320 nm) than in SNO ($\simeq$ 340 nm) since the mean distance travelled in acrylic was much less here than it will be in SNO. The light from the source can be considered unpolarised and isotropic since each data point was averaged over about 10^6 decays. The acrylic sphere was housed in a 50 mm diameter brass cylinder which was closed at the top end so that the light only shone downwards in a 45° cone. A source blocker could slide under the cylinder and block the source off completely. The source centre was located 560 mm above a concave mirror of 1130 mm radius in order to produce an upwards beam of parallel light with minimal spherical aberration. An R1408 PMT was mounted (with and without a concentrator attached) on a rotating shaft above the source, looking down at the beam of parallel light. Even though the source blocked

the very central portion of the upwards beam its area was so small compared with the photocathode area that the effect was minimal, and was included in the ray-tracing program. A pair of Helmholtz coils were fitted to the outside of the light-tight polythene tank in which the experiment was contained, in order to cancel the earth's magnetic field within the region of movement of the photomultiplier. Plumbing was provided for filling the polythene tank with high-purity (18 MΩ) deionised water so that concentration factors could be measured in water as well as in air.

The photoelectron count rate was measured as a function of the angle of incidence of the upward beam at the concentrator aperture (the polar angle θ) with both the source on and off in order to subtract the noise rate — the signal to noise ratio being about 20:1. This procedure was carried out for the photomultiplier with and without the concentrator. In both circumstances the photocathode area outside the concentrator exit aperture was masked off to avoid any effects from the edge of the photocathode. The net count rate of the PMT/concentrator as a function of θ was divided by $\cos\theta$ and normalized to the net count rate of the bare photomultiplier at 0° incidence. Thus the concentration factor for unpolarised light was measured as a function of θ.

The measured concentration factor in air for the front surface glass/Al CTC is shown in Figure 6.19 together with three simulated concentration factors assuming P1, P2 and P3, and a constant reflectivity of 84%. The measurement clearly favours P2 and P3 which is not surprising as they were obtained at 390 nm which is very close to the peak in the wavelength spectrum of the detected light (Figure 2.4). P1 was obtained at 442 nm which is on the shoulder of this wavelength distribution. There is no significant disagreement between the measurement and the ray-tracing simulation; the agreement in the concentration factor cut-off at large polar angles is especially pleasing.

The same data is shown in Figure 6.20 plotted against three simulations assuming P3 and three different values for the relative efficiency of the band of photocathode below the equator: 0.75, 0.5 and 0.25. The value 0.5 is favoured although this conclusion is strongly dependent on the assumptions of the simulation, e.g. photocathode parametrization. In a sense there are too many free parameters in this fit to determine whether the behaviours

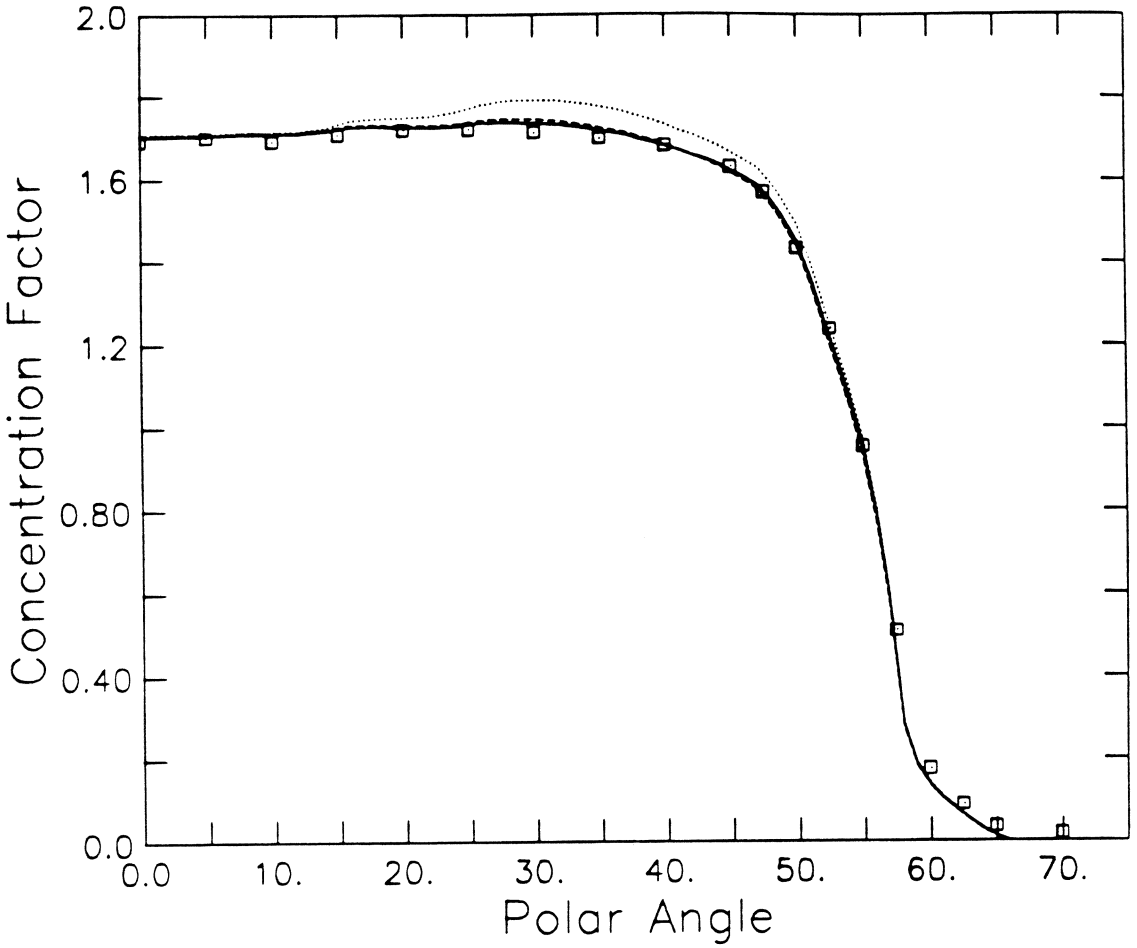

Figure 6.19: Measured concentration factor in *air* for the front surface glass/Al/MgF_2 concentrator. The three simulations assume P1 (·····), P2 (– – –) and P3 (——), and 84% reflectivity.

of the CTC and PMT are completely understood at the 1% level. However the global properties are clearly well understood and there are no significant errors in the ray-tracing simulation.

When the concentration factor of this front surface glass/Al/MgF_2 CTC was measured in water, the Al layer gradually lost its reflectivity, as it dissolved in the water! This behaviour of the Al/MgF_2 layer was not entirely unexpected (see Chapter 7) but the time scale of the corrosion was indeed surprising. Further measurements of glass/Al/SiO concentrators are planned, in which this effect should not recur.

The measurements of the concentration factors of the Omega prototype CTC in air and in water are shown in Figures 6.21 and 6.22. In both cases, the data below 20° has

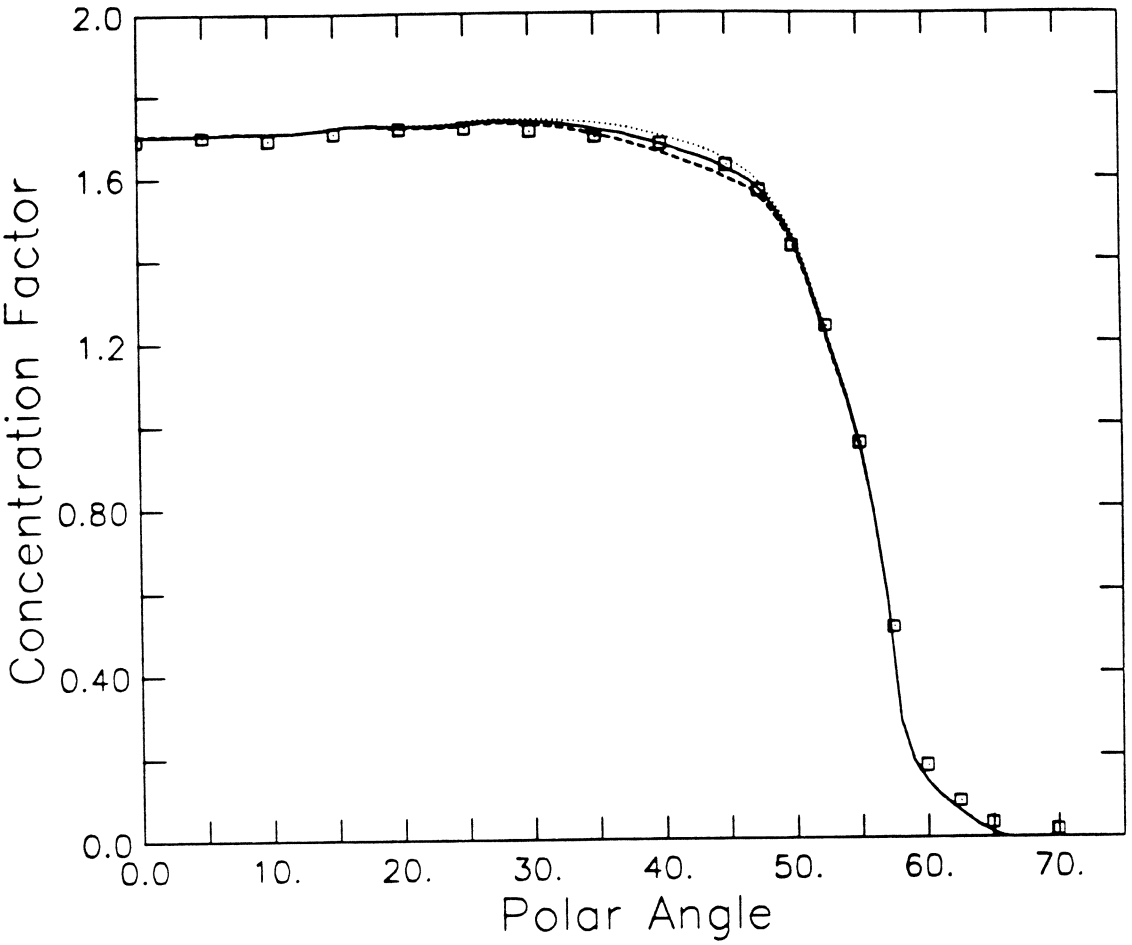

Figure 6.20: Measured concentration factor in *air* for the front surface glass/Al/MgF_2 concentrator. The three simulations assume 84% reflectivity, P3 and the following relative efficiencies for the band of photocathode below the equator: 0.25 (– – –), 0.5 (———) and 0.75 (· · · · ·).

been fitted, by eye, to simulated concentration factors in which the effective reflectivity of Omega is the only free parameter. For all three parametrizations the best fit values for this reflectivity are 85 ± 1% in air, which is consistent with the direct measurements of Omega reflectivity shown in Figure 6.11, and 80 ± 1% in water which is perhaps a little lower than expected, although the computer prediction of Figure 6.11 has recently come into question.

These effective reflectivities should be slightly higher for D_2O events in SNO where they will be averaged over the wavelength range 340–460 nm instead of the range 320–460 nm of this measurement. The theoretical concentration factors shown in Figures 6.21

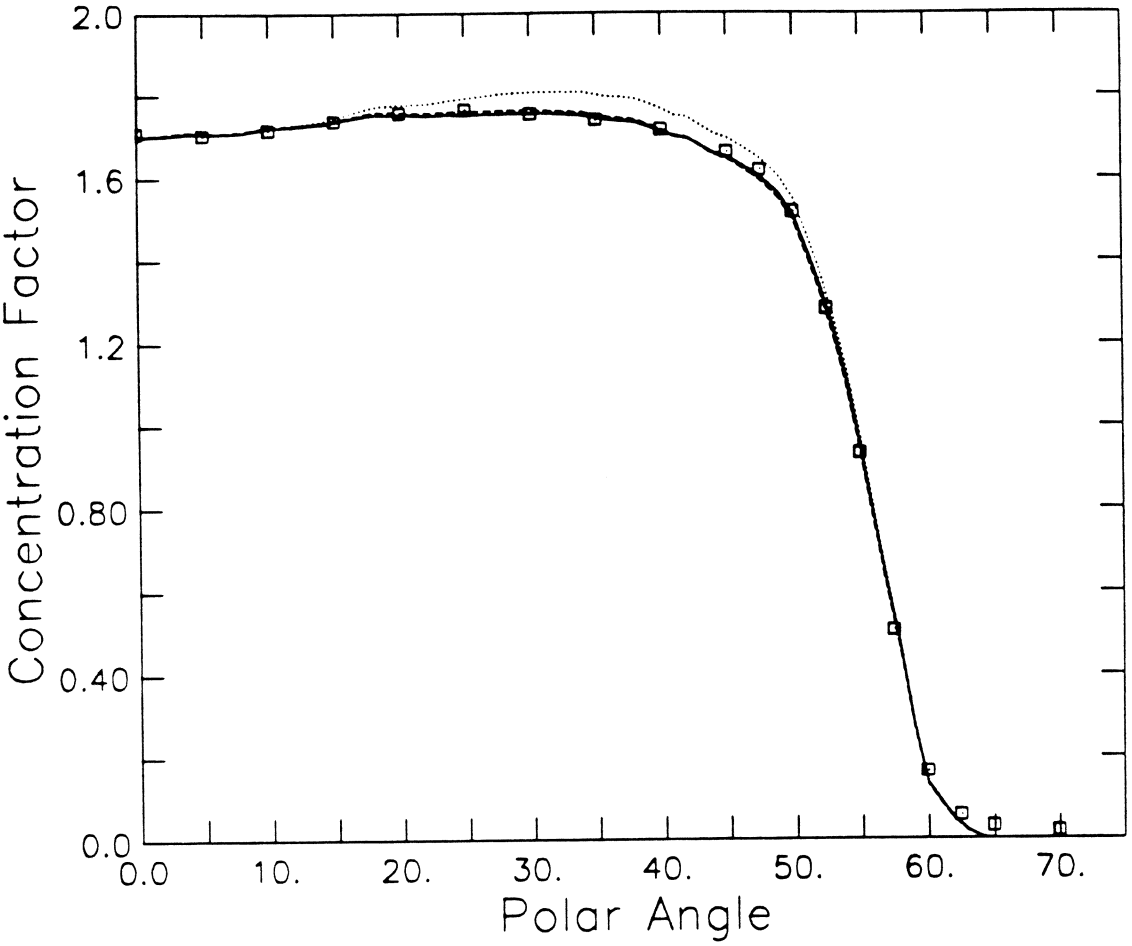

Figure 6.21: Measured concentration factor in *air* for the prototype Omega concentrator. The three simulations assume a (constant) effective reflectivity of 85%, and P1 (·····), P2 (– – –) and P3 (——).

and 6.22, for the three parametrizations, are simulated assuming that the above effective reflectivities do not depend on polar angle. From the excellent agreement between the data and the simulations with both P2 and especially P3, it is concluded that the effective reflectivities of Omega in air and in water do not vary significantly with polar angle. This result simplifies the simulation task enormously.

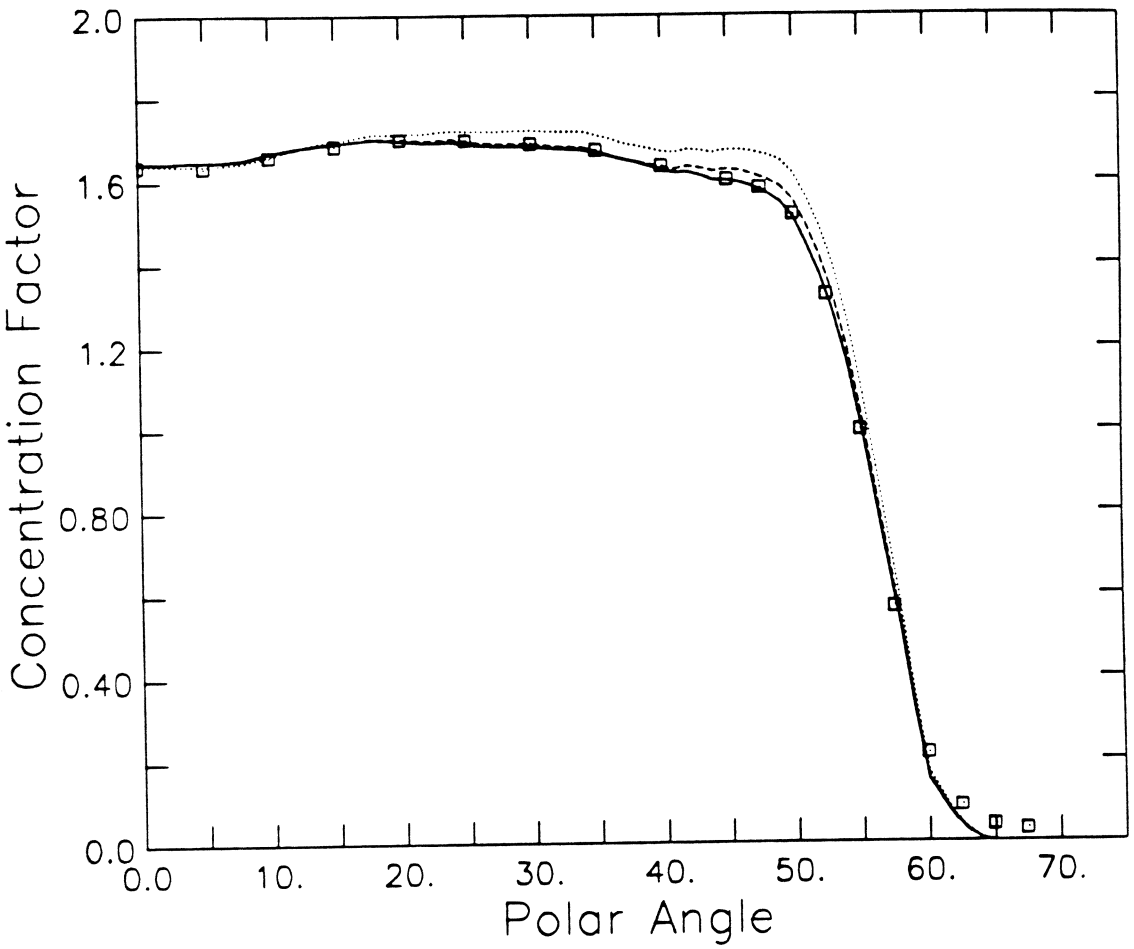

Figure 6.22: Measured concentration factor in *water* for the prototype Omega concentrator. The three simulations assume a (constant) effective reflectivity of 80%, and P1 (·····), P2 (– – –) and P3 (——).

6.5 Conclusion

The measurement of the front surface glass/Al/MgF_2 CTC's concentration factor in air demonstrates that the ray-tracing programme accurately simulates the behaviour of both the concentrator and the photomultiplier. Furthermore, this data favours P2 and P3.

The measured concentration factors in air and in water of the prototype Omega CTC can be reproduced by a simulation in which the effective reflectivity is 85 ± 1% in air and 80 ± 1% in water and in both cases, independent of polar angle. In SNO, one can expect these values to increase slightly for events in the D_2O and decrease for events in the H_2O.

Unfortunately the concentration factors of back surface glass/Al/TiO CTCs made with good quality U.V.transmitting glass have not been measured. However it is estimated that the edge-effect caused by the ground glass rims in these CTCs would be of the same order of magnitude as the edge-effect caused by the black lips in the Omega CTCs. In theory the reflectivity of these CTCs would be 89% in both air and water (Figure 6.8). In practice it tends to be about 87%, as measured by laser (442 nm) on samples of evaporated glass/Al/TiO.

Thus the concentration factors of the two prototype SNO concentrators are most likely to be very similar with the glass/Al CTC probably a few percent higher than the Omega CTC. Therefore the decision between the two was made on the basis of practical considerations such as water survival, robustness and cost (see Chapter 7); the Omega design being finally adopted.

At present, the design phase of the Omega SNO concentrator is coming to a close. Drawings for injection moulded plastic holders will soon be sent to potential manufacturers. The parameters of the final design are as follows: (i) an exit aperture of polar radius 98 mm; (ii) a Liouville cut-off angle of 56.4°; (iii) a skew parameter of $h_{rel} = 0.6$ (see Section 5.6); (iv) a 24% truncation in axial length corresponding to a 2% decrease in entrance aperture area; and (v) a 24-sided polygonal holder with 2 mm lips at either

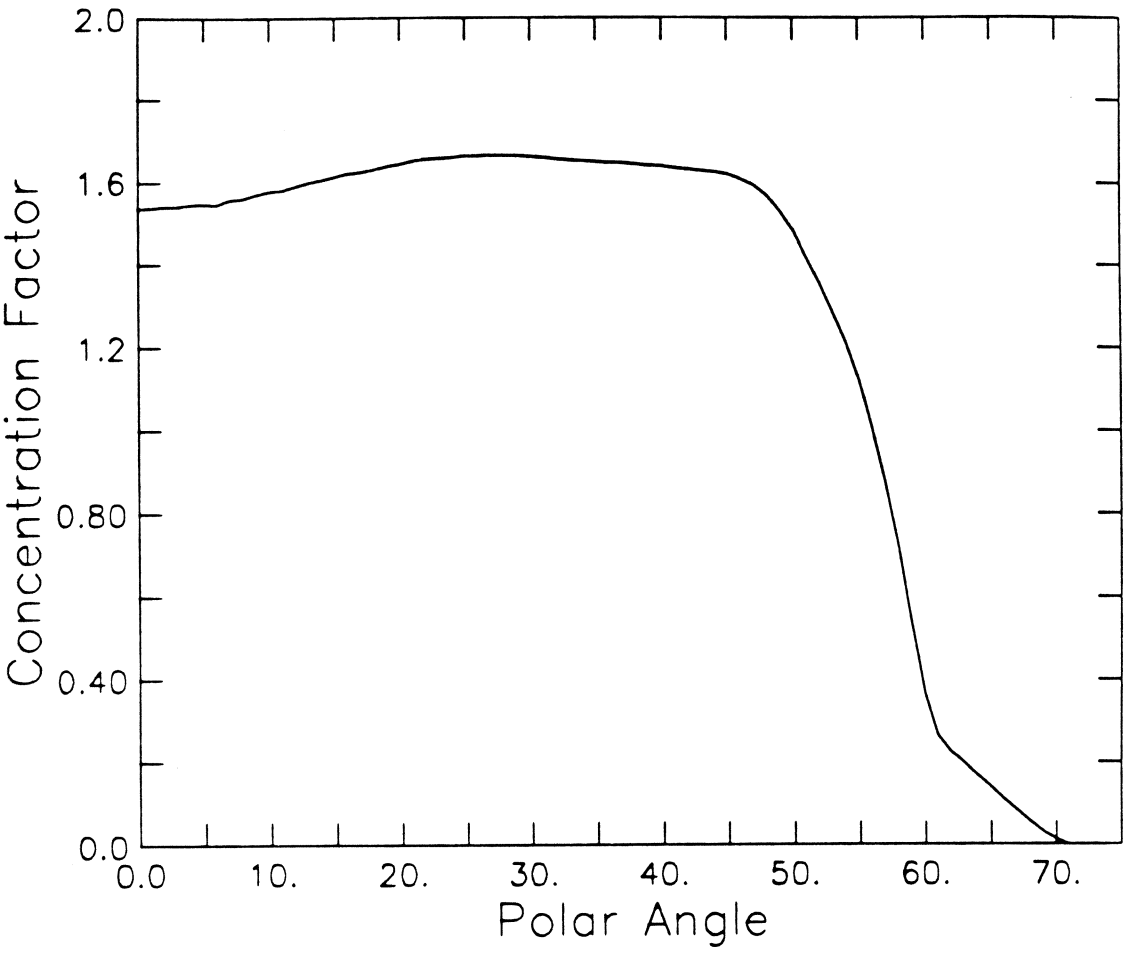

Figure 6.23: Simulated concentration factor in water of the SNO Omega concentrator (see text for details) assuming a constant effective reflectivity of 80% and P3.

end to hold in the petals with a compressive stress of 0.8 N/mm (see Figure 6.15 for the resulting profile of the petals).

The concentration factor of this CTC in water has been simulated assuming P3, the radial dependence of the photocathode efficiency shown in Figure 6.3, a constant effective reflectivity of 80% and a bare PMT which is *not* masked off beyond $r_{polar} = 98$ mm in the normalisation of the concentration factor. The resulting angular response is shown in Figure 6.23 where the 8% dip in concentration factor at small polar angles is caused by light being funneled, at these polar angles, onto the lower lip of the black plastic holder and the edge of the photocathode where the efficiency is lower.

The corresponding radial response for this angular response, ignoring absorption in the acrylic, H_2O and D_2O, is shown in Figure 6.24. The 7% non-uniformity inside

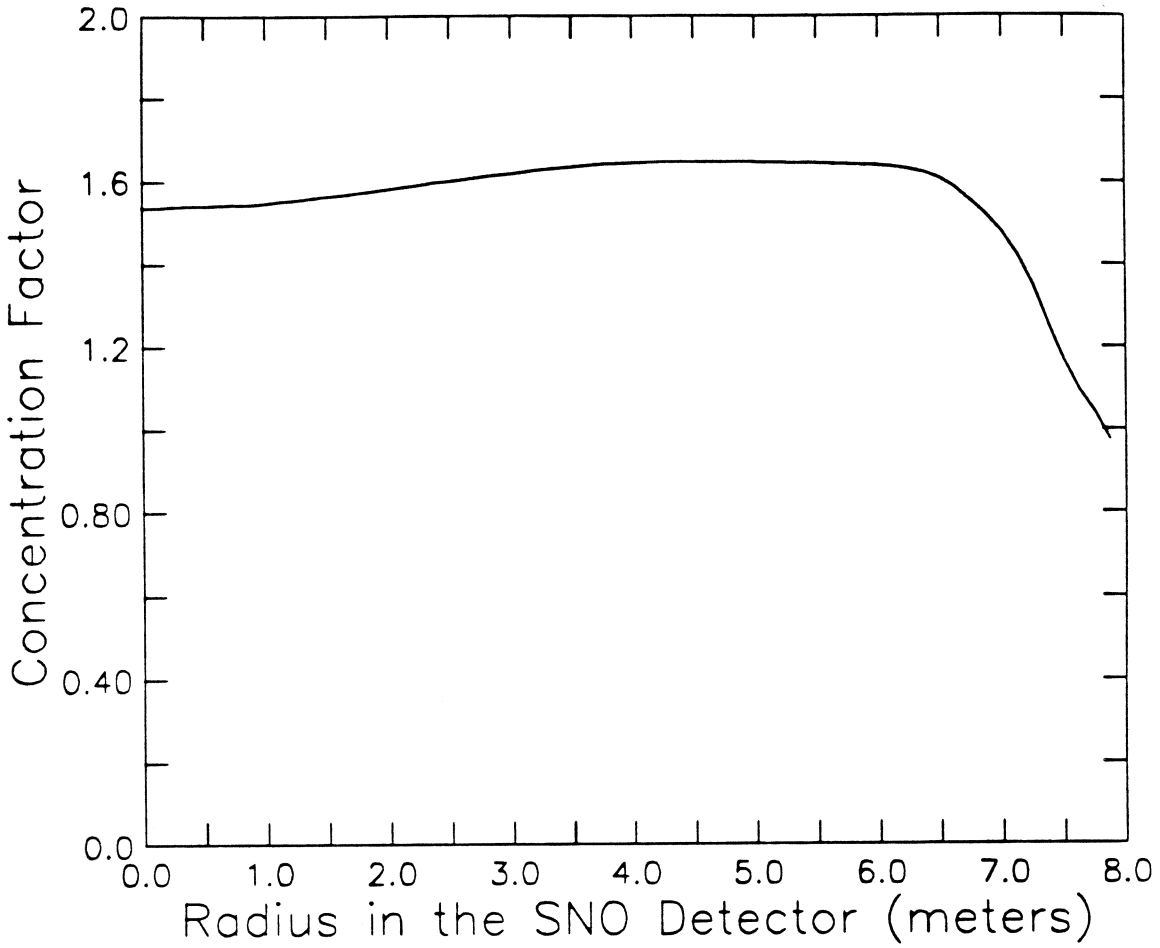

Figure 6.24: Radial dependence of the concentration factor in water of the SNO Omega concentrator (see text for details) calculated from the angular response shown in Figure 6.23 and ignoring absorption in the acrylic vessel, D_2O and H_2O.

the D_2O is caused by the dip in the angular response at small polar angles. This non-uniformity will be measured in SNO with small ($\simeq$ 5 cm) ^{90}Sr Cherenkov sources which can be moved around inside the D_2O. It will then be possible to correct for this non-uniformity since it will be a slow function of radius and the vertex reconstruction accuracy is expected to be about 30 cm. The 10% drop in concentration factor at the edge of the fiducial volume (7 m) will be swamped by systematic effects from absorption in the acrylic vessel and is thus of no great concern.

Chapter 7

Manufacturing Methods

7.1 Introduction

There are four major criteria which a potential concentrator for SNO must satisfy. These are *sine qua non* conditions and only if several designs are able to reach these criteria does cost become a relevant consideration (within reason). They can be summarised as follows:

1. **Reflectivity**: High reflectivity (80–90%) over the wavelength range of interest to SNO (Figure 2.2) and at all angles of incidence is required.

2. **Corrosion Resistance**: The 10,000 concentrators in SNO will be fully immersed in high purity water for the life-time of the detector, 10–15 years. During this time they will be completely inaccessible for any maintenance or repair barring a major catastrophe. Hence it is vital that their optical performance does not deteriorate over a 15 year period.

3. **Radioactivity**: A low concentration of ^{238}U, ^{232}Th and their daughters is necessary to limit the contribution of the concentrators to the β-γ background from the PMT region. For a 1 kg concentrator this concentration level is $\leq 10^{-7}$ g/g ^{238}U and ^{232}Th or equivalent for the daughters, if the chain is in disequilibrium. The flux of high energy (> 5 MeV) γ's reaching the D_2O, from $(\alpha, p\gamma)$ and (n, γ)

reactions in the concentrators should not be any higher than the present flux of these γ's from the walls of the cavity.

4. **Leaching**: The permissible concentration levels of ^{238}U and ^{232}Th in the light water are very much smaller ($\leq 10^{-14}$ g/g) than in the concentrators. Hence there is a possibility that ^{238}U or ^{232}Th or their longer-lived daughters could leach out from the concentrators into the light water at a rate which would increase the β-γ background from the light water to unacceptable levels. This puts constraints on the permissible leaching rates of Th, U or Ra from concentrators.

As far as the radioactivity and leaching criteria are concerned the three significant materials (glass, ABS plastic and Omega sheet) in terms of mass and surface area, which are contemplated for concentrators are known to be acceptable. This conclusion has been reached after numerous painstaking measurements and calculations and by controlling and monitoring the activities of the raw materials used in the production of glass and Omega. The work involved is beyond the scope of this thesis and the reader is referred to the following reports: [65], [66], [67], [68] and [69].

In this chapter four potential manufacturing techniques will be reviewed with emphasis on their ability to meet the reflectance and corrosion resistance criteria. There is a fair amount of information in the literature about the survival of many different reflectors for long periods of time in various environments. Unfortunately, the vast majority of these tests were performed in an atmosphere of air which had been contaminated in some manner, e.g. sulphur dioxide or high humidity content. The few tests in which the reflecting surface was totally immersed in water (or sea water) have not been carried out over sufficiently long periods of time to be relevant to SNO. There is no experience in industry or research of making reflecting surfaces capable of withstanding 10 years' immersion in high purity water.

Consequently, it is has been necessary to rely on the results of accelerated ageing tests in order to ascertain the viability of potential manufacturing techniques. The chemists' rule of thumb states that the rate of corrosion is accelerated by a factor of 2 for every 10°C

increase in temperature. This exponential behaviour of corrosion rate with temperature is supported by an extensive body of empirical evidence. However, the precise value of the exponential factor is not *a priori* known and does vary slightly according to the exact chemical process of corrosion. It is the poor knowledge of this exponential factor (and the possibility of phase changes in the materials) which underlies the difficulty of extrapolating the results of accelerated ageing tests over large temperature ranges. At best, these tests can be used on a 'go, no-go' basis for acceptance purposes.

Assuming the canonical exponential factor of 2 per 10°C, one day at 95°C corresponds to one year at 10°C, the operating temperature of the SNO detector. Hence, the concentrators are required to exhibit a $< 2\%$ change in reflectivity after 10–15 days' immersion in high purity ($18M\Omega$) water at 95°C.

It is also possible to accelerate the corrosion rate in water by changing the pH. However, since the factor by which this accelerates corrosion are much less well known such tests are even more difficult to interpret.

7.2 Evaporated Aluminium on Glass Substrate

The vacuum deposition of thin aluminium films on glass substrates is a well known technique for achieving high reflectivity ($\sim 90\%$) throughout the wavelengths of interest to SNO. It is common practice to protect the soft and reactive Al film from abrasion and corrosion by depositing a $\frac{1}{4}$ wavelength[1] layer of silicon monoxide directly onto the Al film in the same evaporation sequence. At this thickness the SiO is transparent and so the glass/Al/SiO can be used as a front surface reflector, i.e. light incident through the SiO layer. The SiO layer is very hard and provides adequate corrosion resistance

[1] In the vacuum deposition trade the thickness of 'dielectric' films (TiO, SiO etc.) is measured in terms of wavelengths. This scale is calibrated with respect to a measurement of a reflection minimum (destructive interference) made with a monochromatic light source of usually 550nm wavelength. The true thickness of the film, τ, can be derived from the expression

$$\tau = \frac{\#\text{ of wavelengths } \times \lambda_0}{n(\lambda_0)}$$

where λ_0 is the wavelength of the light source and $n(\lambda_0)$ is the refractive index of the dielectric at $\lambda_0 = 550$ nm and is approximately 1.5 for both TiO and SiO at 550nm.

for most applications. However accelerated ageing tests in high purity water at 95°C showed that after about one day of immersion the Al film began to deteriorate rapidly until it was completely dissolved in less than two days.

If the Al film is evaporated onto the *outside* of a glass concentrator then it will act as a back surface reflector, i.e. light incident through the glass substrate which can be made transparent in the wavelengths of interest to SNO. Now the Al film can be overcoated with any number of protective layers which are not restricted by the very limiting requirement of transparency. It would be very attractive to find two mutually compatible coatings which provide *independent* water protection to the Al film, but this may not be possible.

7.2.1 Evaporated Protective Coatings

The main cost in the evaporation of Al is the time required to pull the necessary vacuum for deposition and the labour of cleaning the glass substrate and mounting and dismounting the glass dishes from their jigging. Hence a second evaporated coating on top of the Al can be obtained at relatively low cost provided its deposition time is not excessive. In any case, a minimal $\lambda/4$ coating of SiO is necessary for handling purposes. Perhaps an evaporated coating can be found which provides water resistance for 10–15 days' immersion at 95°C.

All the vacuum chambers large enough to handle 10,000 off production on a reasonable timescale are equipped with thermal evaporators. These evaporators are simple and economical but have a maximum temperature of $\sim$ 1900°C. Hence the choice of protective overcoats which can be evaporated is limited to SiO, TiO and MgF_2.

It was soon discovered, from tests on 50 mm square samples of float glass, that an approximately 2 wavelength layer of SiO or TiO protects the Al film from corrosion for 35 days' immersion at 95°C. During these tests a few pinholes developed quite soon in the Al film but they only increased very slowly in number and in size and did not affect the overall reflectivity (<1% change in reflectivity measured by laser at 442 nm). MgF_2 did not perform as well. After 3–4 days' immersion at 95°C the Al film had completely

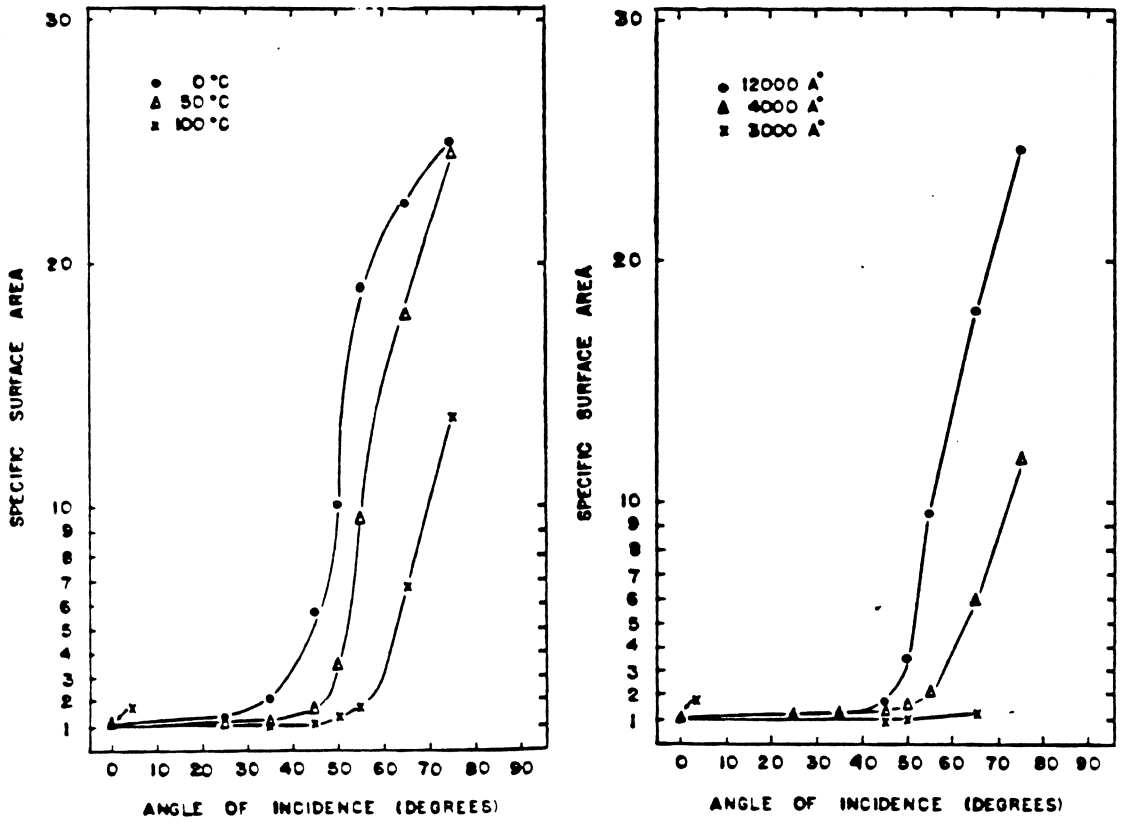

Figure 7.1: Specific surface area of aluminium films as a function of angle of incidence of the evaporated aluminium at the glass substrate, for (a) different substrate temperatures and a film thickness of 12,000 Å; and (b) different film thicknesses and a substrate temperature of 50°C, [71]. The specific surface area is defined as the ratio of the area of the film to the area of the substrate and is a measure of the 'roughness' of the film.

dissolved.

In all of these initial tests the geometry of evaporation was such that the deposition of material, which travels in straight lines from the evaporation source, was always normal or near-normal to the substrate. In order to vacuum deposit Al and TiO or SiO from a limited number of evaporation sources onto the whole *outer* surface of a glass concentrator it is necessary to continuously rotate the concentrator about its axis during evaporation. Consequently, some of the deposition of material will occur at oblique angles with respect to the glass substrate.

It has been established [71] that above a certain critical angle of deposition Al films have very large surface areas in comparison with the area of the substrate. This is clearly

shown in Figure 7.1 where it is noted that the critical angle depends somewhat on the thickness of the Al film and the temperature of the glass substrate. The large relative surface areas are believed to be caused by 'shadowing' from 'islands' which are formed in the early stages of deposition. The resultant Al film has a rough surface with tall columns and deep gulleys and can be full of voids.

This dependence of the quality of Al films on angle of deposition is also known to affect the reflectivity of the film [70]. When Al is deposited onto the outside of a cylinder through a baffle which restricts the angles of deposition (see, for example, Figure 7.4) the typical 90% specular reflectivity is obtained, whereas if a baffle is not used a more diffuse reflectivity is observed.

Thus it is expected that the water protection afforded by evaporated layers of SiO or TiO on Al will be strongly dependent on the angles of incidence of material during deposition. This was verified by depositing Al/SiO and Al/TiO on horizontal glass plates from an evaporation source directly below one of the ends of the plate (see Figure 7.2).

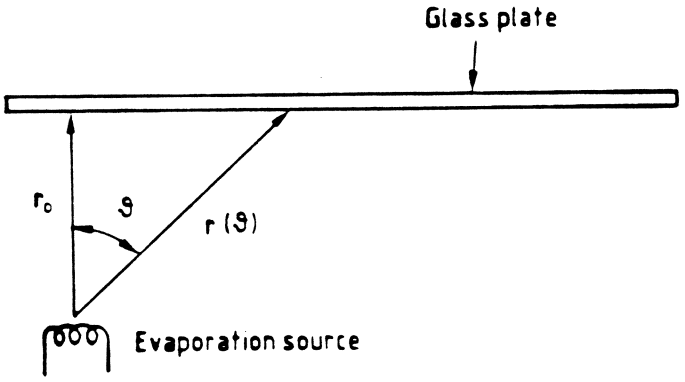

Figure 7.2: Geometry of test evaporations of aluminium + dielectric on glass plates.

The angle of deposition, θ, varied continuously along the length of the plate as did the thickness of deposits, τ, given by

$$\tau(\theta) = \frac{\tau_{cal}\, r_{cal}^2 \cos^2\theta}{r(\theta)^2 \cos^2\theta_{cal}} \tag{7.1}$$

where $r(\theta)$ is the distance from the source to the point along the plate where the deposition occurs at angle θ with respect to the normal of the glass substrate; and where τ_{cal}

is the thickness of the dielectric layer measured on a calibrated film thickness monitor located at a distance r_{cal} from the source and at an angle $\theta_{cal} = 39°$ with respect to the source.

Substituting $r(\theta)$ in (7.1) with $r_0/\cos\theta$ where r_0 is the height of the plate above the source, one finds that the thickness of deposit varies as $\cos^4\theta$ along the plate. This very strong dependence of thickness with angle is a nuisance for interpreting the results of ageing tests as the water protection afforded by a dielectric layer will depend on both thickness and angle of deposition. To remove this ambiguity several evaporation runs for each dielectric were made in which the dielectric thickness was varied whilst keeping the Al thickness constant ($\sim$ 100nm at 39° incidence). Four plates were prepared of Al/TiO in which the dielectric thicknesses, measured at $\theta = 39°$, were respectively $1/4\lambda$, $1/2\lambda$, 1λ and 2λ. Three plates of Al/SiO were prepared with thicknesses of $1/2\lambda$, 1λ and 2λ.

It is possible to partially oxidize the SiO or TiO 'in flight' by evaporating in an atmosphere of air or O_2 in which the partial pressure of O_2 is $\sim 10^{-4}$ bar. The resulting film is denoted SiOx or TiOx where x lies somewhere between 1 and 2. The dioxides of silicon and titanium are known for their extreme 'hardness' (very high evaporation or sublimation temperature) and cannot be evaporated directly in thermal evaporators, as they can in electron bombardment evaporators (c.f. Omega coating, see Section 7.3). A further three plates of Al/SiOx were prepared with dielectric thickness of $1/2\lambda$, 1λ and 2λ.

In the first day of immersion at 95° the Al film in the $1/4\lambda$ Al/TiO plate had completely dissolved. On all the other plates the Al film had also completely dissolved beyond a critical angle, θ_c, of deposition which varied according to the thickness and type of dielectric. Below this critical angle the Al film was intact apart from a few pinholes which did not affect the overall reflectivity (checked by laser at 442 nm). During the rest of the 10 day immersion period very little change was observed in the Al/SiO and Al/TiO plates. However in the Al/SiOx plates the pinholes continued to grow in number and in size and the region of unaffected Al gradually decreased in size. The final values of θ_c, together with the thickness of the dielectric at θ_c are shown in Table 7.1 for each

Plate	θ_c	$\tau(\theta_c)$	Observation
1/4λ TiO	-	-	Al completely dissolved
1/2λ TiO	9°	1.3λ	Al film slightly hazy in parts
1λ TiO	35°	1.2λ	Very few pinholes
2λ TiO	35°	2.4λ	Very few pinholes
1/2λ SiO	30°	0.8λ	Some minute pinholes
1λ SiO	35°	1.2λ	Some minute pinholes
2λ SiO	38°	2.4λ	Few minute pinholes
1/2λ SiOx	-	-	Excessive pinholing
1λ SiOx	18°	2.2λ	Very many pinholes
2λ SiOx	32°	2.8λ	Very many pinholes

Table 7.1: Results of 10 day immersion test at 95°C of plates of Al/TiO, Al/SiO and Al/SiOx.

of the plates tested.

The TiO gives slightly better protection than SiO in that there are fewer pinholes in the Al film (although both show less than 1% change in Al reflectivity). However SiO can give adequate protection at slightly larger angles and slightly smaller thicknesses than TiO.

The transition at the critical angle of deposition between a region where the Al survives intact and a region where it dissolves completely is very sharp indeed. This behaviour is consistent with the results of [71], (see Figure 7.1). Hence it is postulated that beyond the critical angle the Al film becomes so rough and filled with voids that the dielectric overcoat cannot form an impermeable barrier on the uneven Al surface. Further evidence to bolster this hypothesis was obtained with test evaporations of Al/TiO and Al/SiO on *unbaffled* revolving concentrators in which the Al dissolved completely in less than 1 day at 95°C even though the thickness of the dielectric was between 1 and 2λ.

A scheme for limiting the angles of deposition from a single source onto a glass concentrator is shown in Figures 7.3 and 7.4. During the evaporation process the concentrator revolves hundreds of times about its axis. Hence the coating is identical along any circumference of the dish and only varies along the length of the dish. At any point along this length the Al + dielectric coating can be characterized by three parameters:

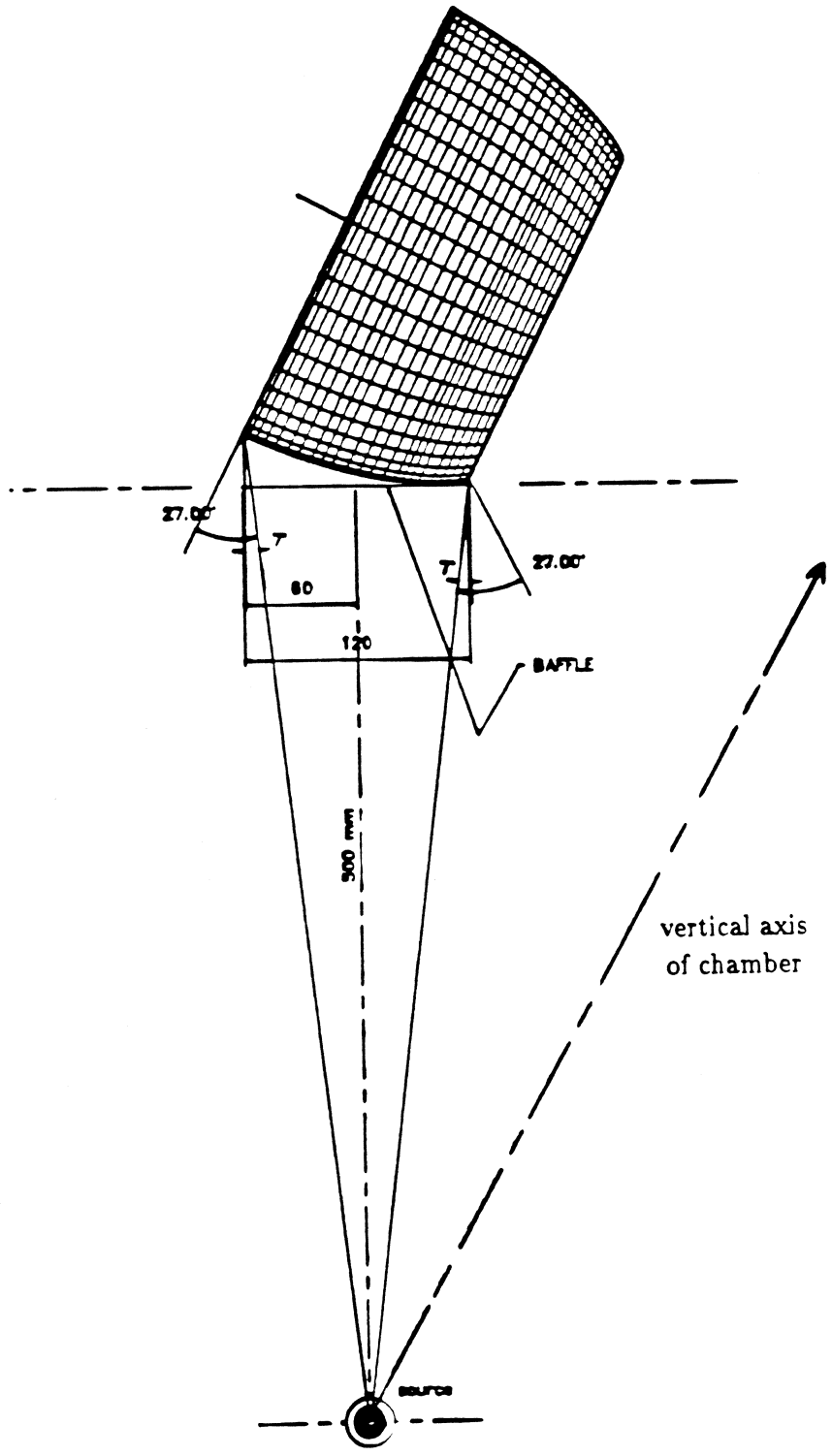

Figure 7.3: Scheme for limiting the angles of deposition onto the proposed SNO concentrator from a single evaporation source. The diagram is drawn in the meridional plane through the axis of the concentrator and the source. At either extremity of the dish, the *minimum* angle of deposition is 27°.

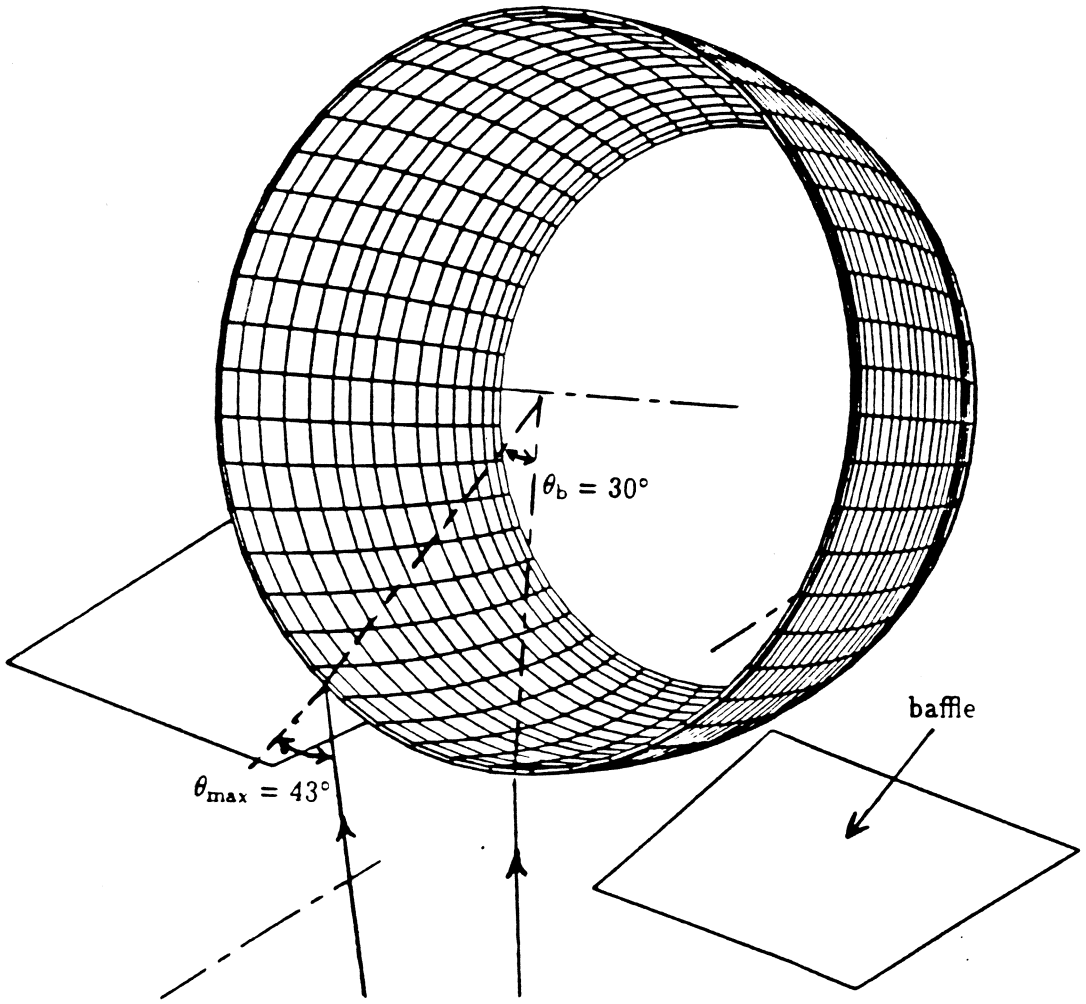

Figure 7.4: Projected view of the scheme for limiting the angles of deposition onto the proposed SNO concentrator from a single evaporation source. For the baffle angle $\theta_b = 30°$, the *maximum* angle of deposition at the wide end of the dish is 43°.

(i) the *minimum* angle of deposition along the relevant circumference (θ_{min}), i.e. in the plane of the source and concentrator axis (see Figure 7.3); (ii) the *maximum* angle of deposition along the relevant circumference (θ_{max}), i.e. at the point where the evaporated material which passes *just inside* the baffle is incident on the relevant circumference (see Figure 7.4); and (iii) the thickness τ of the dielectric which can be approximated by

$$\tau \cong \frac{\tau_{cal}\, r_{cal}^2 \sin\theta_b \cos\theta_s \cos\theta_{min}}{\pi\, r_b^2} \tag{7.2}$$

where τ_{cal} is the thickness measured on a calibrated monitor at fixed distance r_{cal} directly above and normal to the source, r_b is the distance from the source to the point of

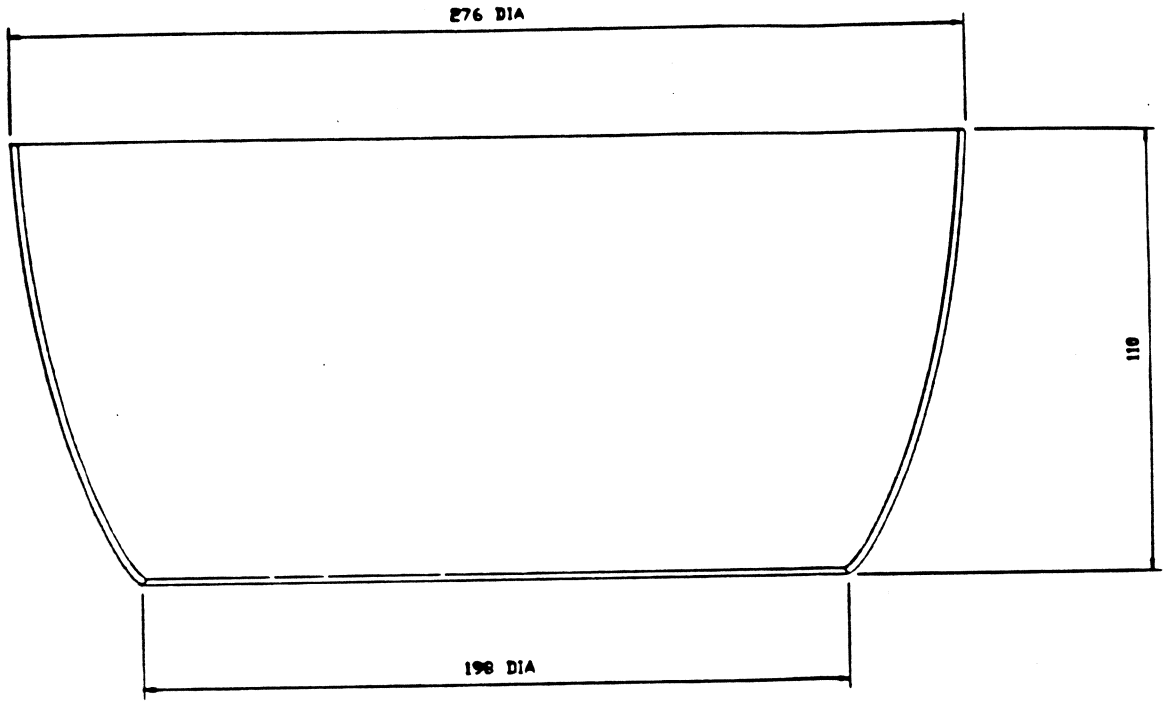

Figure 7.5: Dimensions of proposed glass concentrator for SNO.

maximum angle of deposition, θ_b is the opening angle of the baffle and θ_s is the angle between the axis of the chamber and the vector from the source to the point of minimum angle of deposition.

For the proposed SNO concentrator (Figure 7.5) the geometry of evaporation from a single source can be optimized so that θ_{min} is 27° at either extremity of the dish (see Figure 7.3). With a baffle opening angle θ_b = 30°, θ_{max} will be 43° at the wide end of the dish and 41° at the narrow end (see Figure 7.4). These latter angles are slightly greater than the critical angle of deposition for achieving water protection (see Table 7.1). If the opening angle of the baffle is decreased then θ_{max} will decrease at either end of the dish but this will also decrease the thickness, τ, of the dielectric coating (proportional to $\sin\theta_b$) which is also a critical parameter for achieving water protection. There is clearly a trade-off between θ_{max} and thickness,τ, for a given mass of dielectric evaporated. It turns out that the mass of dielectric which must be evaporated to achieve a coating of sufficient thickness (for water protection), without exceeding the critical angle of deposition, is just beyond the capabilities of conventional large-scale thermal

evaporation plants.

The technique of evaporating through a baffle has been investigated in two vacuum chambers of somewhat different characteristics. The Kendal Hyde chamber is a large cylinder of 1 metre radius and 3.5 metre length, with its axis horizontal. There is a rectangular grid of ($3 \times 5 = 15$) evaporation sources along the bottom of the chamber. Each source can coat at least four and possibly 8 SNO concentrators in the optimum geometry. The other chamber, belonging to Omitec OEC, is a more conventional bell-jar of 0.7m height and 0.46m radius. It has a single source at the centre which can coat at least 9 and possibly 12 dishes in the optimum geometry. It compensates for its smaller capacity compared with the Kendal Hyde chamber by its quicker turn-over time as it has a smaller volume to evacuate.

For the test runs in both these chambers, prototype glass concentrators were used (Figure 6.9) which have slightly different dimensions to those of the proposed SNO concentrator (Figure 7.5). The geometry of evaporation was hence slightly different to the optimum geometry for the SNO concentrator. In the Omitec runs θ_{min} was 31° at both extremities of the dish[2] For the first Kendal Hyde run θ_{min} was 32.5° at the wide end of the dish and 27.5° and the narrow end. For the second Kendal Hyde run these angles were respectively 32° and 30.5°.

Four dielectrics — SiO, SiOx, TiO and TiOx — were tested with baffle angles ranging from 23.5° to 40° and dielectric thicknesses from $1/4\lambda$ to $3/2\lambda$ as measured by a film thickness monitor directly above the sources at a distance of 500 mm in the Omitec chamber and 560 mm in the Kendal Hyde chamber.

When the concentrators from these test runs were then immersed in water at 95° for 10 days a very similar behaviour was observed as in the tests with flat plates. In the first few days the Al film dissolved completely at the extremities of the dishes. In between two well defined critical circumferences of the dish, which depended on the type and thickness of the dielectric, the Al survived intact apart from a few pinholes.

[2]The sum of the θ_{min} angles at either end of the prototype concentrator is about 10° more than for the proposed SNO concentrator in which the 10° curvature in the first 1 mm of the profile (at the narrow end) has been removed.

If the dielectric coating was thick enough and it was evaporated in high vacuum, i.e. it was TiO or SiO and *not* TiOx or SiOx, then this band of intact Al inside the critical circumferences remained unaffected for the rest of the immersion period. Otherwise it was attacked and eventually the Al film was either excessively pinholed or completely dissolved.

Run	Dielectric	τ_{cal}	θ_b	$\theta_{min}(c)$	$\theta_{max}(c)$	$\tau(c)$	Observation
OM5	TiO	3λ	23.5°	9°	30°	0.4λ	extreme pinholing
OM5	TiO	3λ	30.0°	9°	35°	0.5λ	extreme pinholing
OM5	TiO	3λ	37.5°	7°	42°	0.6λ	extreme pinholing
OM6	TiOx	3λ	30.0°	16°	40°	0.45λ	extreme pinholing
OM6	TiOx	3λ	37.5°	9°	44°	0.55λ	extreme pinholing
OM7	SiOx	3λ	23.5°	–	–	–	nothing left
OM7	SiOx	3λ	30.0°	–	–	–	nothing left
OM7	SiOx	3λ	37.5°	–	–	–	nothing left
OM8	SiO	3λ	23.5°	5°	28°	0.4λ	extreme pinholing
OM8	SiO	3λ	30.0°	10°	37°	0.5λ	extreme pinholing
OM8	SiO	3λ	37.5°	5°	43°	0.6λ	extreme pinholing
OM10	TiOx	4λ	23.5°	13°	31°	0.5λ	extreme pinholing
OM10	TiOx	4λ	30.0°	9°	37°	0.7λ	extreme pinholing
OM11	SiOx	4λ	23.5°	–	–	–	nothing left
OM11	SiOx	4λ	30.0°	–	–	–	nothing left
OM12	SiO	4λ	23.5°	24°	37°	0.45λ	few pinholes
OM12	SiO	4λ	30.0°	26°	44°	0.55λ	few pinholes
OM13	TiO	5λ	23.5°	16°	32°	0.65λ	very few pinholes
OM13	TiO	5λ	30.0°	19°	40°	0.75λ	very few pinholes
KH1	SiOx	5.3λ	30.0°	7°	35°	0.85λ	extreme pinholing
KH1	SiOx	5.3λ	40.0°	10°	46°	1.05λ	extreme pinholing
KH2	SiO	5.3λ	40.0°	23°	52°	1.2λ	few pinholes

Table 7.2: Results of 10 days' immersion at 95°C of test evaporation runs on prototype glass concentrators. OM refers to Omitec OEC, KH to Kendal Hyde; τ_{cal} is the thickness of dielectric measured on a monitor directly above the source at r_{cal} = 500 mm for the OM runs and 560 mm for the KH runs; $\theta_{min}(c)$, $\theta_{max}(c)$ and $\tau(c)$ are the minimum angle of deposition, maximum angle of deposition and thickness of dielectric on the critical circumference of the concentrator which separates the region where the Al film has been totally dissolved and the region where it remains after 10 days' immersion at 95°C; and the observation refers to the remaining Al film.

The detailed results of these initial tests are shown in Table 7.2. Once more it is

noted that SiO provides adequate water protection at slightly smaller thicknesses and larger angles of deposition than TiO, but that there is less pinholing with TiO than with SiO although in neither case does the pinholing affect the overall reflectivity. The most promising runs were OM11, OM12 and KH2 where the dielectric protected the Al over most ($\simeq$ 5/6) of the surface area of the dishes. At the extremities of the dish the maximum angle of deposition was greater than the critical angle for achieving water protection and the Al dissolved completely within 5 days' immersion.

The best paint-like overcoating for spraying onto the evaporated layers is a photoresist which adheres extremely well to TiO but poorly to SiO, (see Section 7.2.2). Kendal Hyde are not able to evaporate thick layers of TiO but are capable of evaporating a thick layer of SiO for water protection, followed by a thin layer of TiO for adhesion to the photoresist. Tests of these Al/SiO/TiO coatings were not very encouraging in that the dielectric protected the Al over only 2/3 of the dish and even this 'protected' Al was quite seriously pinholed. Thus Al/TiO was found to be the leading evaporated coating for glass CTCs. Although it is by no means a fully independent water protective coating, it does provide adequate protection over about 5/6 of the dish and some protection (5 days at 95°C) at the extremities.

7.2.2 Other Protective Coatings

To protect the Al layer over the entire surface of a glass/Al/dielectric concentrator a further coating is necessary. A very sensitive test of the water protection afforded by any such coating is to apply it directly onto a layer of evaporated bare Al (no dielectric) which, without the coating, would dissolve completely within hours of being immersed in water at 95°C. If the coating protects the Al film for 10 days at 95°C then it can be considered a fully independent water protection. This coating will also have to be compatible with and provide good adhesion to an evaporated layer of Al/TiO or Al/SiO. Its usefulness as a water barrier can also be tested by applying it onto evaporated films of Al/TiO or Al/SiO in which the angles of deposition and dielectric film thickness are such that the dielectric coating would provide very little water resistance on its own,

i.e. there would be no Al film left after 1–2 days immersion at 95° without the extra protection afforded by the coating.

The potential coatings can be divided into two categories according to their method of application. The first category is the thin (10–200 μm) paint-like coatings which can either be sprayed or dipped. The second category is the encapsulants which are thicker (1–3 mm) and can be used to pot the glass dish into an ABS plastic shell of similar shape to the glass dish but 1–3 mm larger in size. Note that these two categories are not mutually exclusive. A glass dish on which an Al + dielectric layer has been evaporated could be sprayed or dipped and then encapsulated to give it triple protection (although this might seem excessive).

Sprayed or Dipped Coatings

The techniques of spraying or dipping are well established and readily available at an approximate cost of £3 per dish.

In the first instance potential coatings were tested on 50 mm square samples of evaporated Al on glass. Most of the coatings failed to provide any substantial water protection to the Al film which still dissolved completely within the first 24 hours of immersion at 95°C. The list of such failures includes Araldite PZ820, stove araldite, water standard epoxy, hempel polyurethane and acrylic paint all of which were recommended for their water resistance. This result is not surprising, though, given the fact that all plastics are known to be permeable to water at a level which is significant over a timescale of years. Bitumastic (tar loaded) epoxy fared slightly better in that the Al film was still present after 4 days' immersion at 95° although its reflectivity had deteriorated (~50%).

Only two coatings protected the Al film from 10 days' immersion at 95°C: Finnigan's Smoothrite (or Hammerite) and the photoresist CM8000 from Brent Chemicals. Both Smoothrite and Hammerite are based on an alkyd resin which is loaded with tiny glass flakes. When the resin sets the glass flakes intertwine and greatly increase the path length of water diffusing through the resin. Unfortunately the resin takes a long time to cure completely (~3 months) and when immersed in water it continuously leaches

organic compounds. Hence there is a concern that with 1,000 m^2 of exposed surface in SNO the light water purification system might have difficulty in coping with the amount of leached material. Furthermore, since the glass flakes are not made from low-activity glass there is a danger of leaching significant quantities of Th, Ra or U into the light water.

The best paint-like coating from the point of view of both water protection and leaching is the photoresist CM8000 which can be either sprayed or dipped to a thickness of $\sim$ 30 μm. It dries in 24 hours (or it can be pre-baked for 1 hour at 80°C) and then is U.V. polymerized. It can then, if required, be post-baked for an hour at 80°C, which increases its 'resilience'. It was developed for the chemical etching industry and can withstand immersion in strong acids when U.V. polymerized, but is not recommended for use in alkali solutions.

Its water resistance was tested on ten 50 mm square glass samples which had been evaporated as follows: (i) samples 1–4: bare Al (normal incidence geometry); (ii) samples 5–6: Al/TiO evaporated on a rotating mandril with no baffling and hence angles of deposition up to 90°, and (iii) samples 7–10: Al/SiO also evaporated with no baffling. All samples were dipped in CM8000 to a thickness of about 30 μm. Samples 1–8 were pre-baked for 1 hour at 80°C and samples 9–10 were left to dry for 24 hours. Samples 3–4 and 6–10 were polymerized, 1, 2 and 5 were not. None of the samples were post-baked. The results of the accelerated ageing tests of these samples are shown in Table 7.3, in terms of the number of days' immersion at 95°C before the Al film became pinholed to an extent that the reflectivity began to be slightly affected.

Samples 1–6 show that CM8000 provides significant water resistance and that this resistance is increased when the CM8000 is U.V. polymerized. It is clear from samples 7–9 that the adhesion of CM8000 to SiO is very poor which is not surprising as CM8000 is known to bond weakly to glass. The adhesion to TiO is satisfactory, as demonstrated by the 35 days' immersion of sample 6 without any damage apart from some pinholing of the Al film.

After this encouraging performance CM8000 was tested on actual glass concentrators

Sample #	Substrate	Pre-baked	Polymerized	Result
1	Glass/Al	Yes	No	pinholing after 10 days
2	Glass/Al	Yes	No	pinholing after 10 days
3	Glass/Al	Yes	Yes	pinholing after 20 days
4	Glass/Al	Yes	Yes	pinholing after 20 days
5	Glass/Al/TiO	Yes	No	pinholing after 15 days
6	Glass/Al/TiO	Yes	Yes	pinholing after 35 days
7	Glass/Al/SiO	Yes*	Yes	CM8000 peeled off after 6 days
8	Glass/Al/SiO	Yes*	Yes	CM8000 peeled off after 7 days
9	Glass/Al/SiO	No	Yes	CM8000 peeled off after 3 days
10	Glass/Al/SiO	No	Yes	pinholing after 10 days

Table 7.3: Results of 10 days' immersion at 95°C of samples 1–10: Glass/Al/CM8000, Glass/Al/TiO/CM8000 and Glass/Al/SiO/CM8000. The glass/Al/dielectric samples were evaporated on a rotating mandril with no baffling. Hence, the angles of deposition extended up to 90° and the Al film would dissolve completely in less than 24 hours' immersion at 95°C without the protection afforded by the CM8000.
* During baking the oven temperature rose up to 150°C for 20 minutes from the usual 1 hour at 80°C.

which had been evaporated as follows: (i) one bare Al with a baffle angle of 37° and with the same geometry of evaporation as runs OM11–14; (ii) one Al/TiO with baffle angle $\theta_b = 37°$ from run OM11; and (iii) one Al/SiO with $\theta_b = 37°$ from run OM12. All three dishes were sprayed with a full coat of ~ 30 μm of CM8000 and a second coat of ~ 30 μm on half the dish. The CM8000 was then pre-baked for 30 minutes at 80°, U.V. polymerized and post-baked for 30 minutes at 80°C.

Within 2 days' immersion at 95°C the CM8000 was peeling off the Al/SiO, especially where a double coating had been applied. Two days later most of the CM8000 had peeled off the Al/SiO concentrator. On the bare Al and Al/TiO concentrators the CM8000 stayed intact for 10 days before cracking slightly where the double thickness layer had been applied. The Al film was attacked in the vicinity of these cracks on the bare Al concentrator but not on the Al/TiO concentrator, except at the extremities of the dish where the angle and thickness of the TiO deposition were such that it did not provide protection (see Table 7.2). Very little change was noticed in the next 35

days' immersion. Under the single layer of CM8000 both the bare Al and Al/TiO were completely unaffected after 45 days' immersion at 95°C. This was an even better performance than expected from the results of the small sample tests (see Table 7.3). The reason for this improvement in behaviour could be attributed to either the method of application (spraying as opposed to dipping) and/or the use of a post-bake stage which is recommended by the manufacturer.

The questions which remain regarding the use of CM8000 are as follows:

1. What are the maximum and minimum thicknesses of coat which can be applied before the CM8000 cracks or is not effective?
2. Is a single coat necessarily preferable to a double coat?
3. Is it preferable to pre-bake for 30 minutes at 80°C or leave to dry overnight?
4. What are the optimum conditions for U.V. polymerizing? (Exposure time and distance).
5. Is it preferable to post-bake for 30 minutes at 80–100°C?
6. Does it adhere well to Al/SiO/TiO which is a possible evaporated coating?

It has also been observed that spraying produces a much better finish quality than dipping. With dipping it is difficult to avoid a thick layer of CM8000 where a meniscus forms between the edges of the concentrator and the jigging used to hold the concentrator and keep the CM8000 from coating the inner surface of the glass. Spraying produces an even distribution of material and can be controlled so that the edges of the concentrator are not coated and hence the light transmission of the edges is unaffected.

It is concluded that a glass/Al/TiO/CM8000 concentrator satisfies the requirement of no change in reflectivity after 15 days' immersion at 95°. The two protective layers do not quite provide *independent* water protection: the TiO layer is not fully effective at the extremities of the glass dish and the CM8000 has a potential weakness from cracking. However, the combination of these layers provides sufficient water protection for the purposes of SNO.

Encapsulants

In general terms these coatings are more expensive than the very cheap sprayed or dipped coatings and since CM8000 has proven to be an excellent protective layer there is little case for the use of encapsulants. However encapsulation has other benefits such as increasing the mechanical robustness of the glass concentrator and aiding the mounting of the 10,000 concentrators onto the photomultiplier support structure, making it worthwhile to consider.

Two methods of encapsulation have been identified. Method A involves two separate curing stages. First, a quick curing high viscosity encapsulant is used to seal the glass concentrator at both ends into an ABS plastic dish of similar shape but with a 1–2 mm larger diameter. The ABS dish is made in two pieces which are glued together with a solvent glue after the glass dish has been inserted and sealed within. This glueing step enables the ABS dish to accommodate the ± 1 mm variability in length of the glass dish. Next, the low viscosity encapsulant is injected via a hole in the top rim of the ABS dish into the gap between the ABS and glass dishes. This requires a further hole on the top rim of the ABS dish for letting the air escape. After the gap has been completely filled a small reservoir of encapsulant is attached to one of the holes (the other hole is taped up) as there will inevitably be some shrinkage during curing. The reservoir could be a very cheap disposable ABS injection moulded piece. The overall cost of this method is approximately £10–15 per concentrator.

Method B is much less labour intensive and requires only one quick curing stage. The encapsulant is applied in a 1–2 mm layer on the under side of a 2 mm sheet of ABS, which is then vacuum formed onto the glass dish. During the vacuum forming process the ABS is heated to $\sim 150°$ in order to be sufficiently ductile. As it cools down to room temperature it will contract by an amount of order 1 mm in radius which can generate a significant compressive stress on the glass dish. The viscosity and curing time of the encapsulant are suitably chosen so that the encapsulant is able to take up most of this ABS strain without being completely squeezed out from between the ABS and the glass.

After vacuum forming, the ABS + encapsulant is cut off at either end of the glass dish. The estimated cost of this method is £5 per dish.

The main advantage of Method A over Method B is that the ABS dish which is injection moulded to a precision of 0.2 mm takes up the ±1 mm variability in the dimensions of the glass dish and can also be moulded with spigots making the mounting of the concentrators in SNO relatively easy. In Method B the dimensional variability of the glass dish is *not* taken up by the ABS.

Both methods will greatly increase the robustness of the glass concentrator which is extremely fragile with respect to relatively modest impacts across its diameter. Encapsulating the glass dish minimizes the repercussions of a dish cracking as it will remain fixed to the encapsulant. Furthermore since the encapsulants are cured at an elevated temperature they will impart a small compressive stress on the dish which will not allow the CM8000 to peel off. It is also possible that the encapsulants eliminate the slight risk of the CM8000 cracking, but this has not been investigated.

The general properties of the encapsulants are dictated by the need to avoid contaminating the light water in any way which will either affect its light transmission or put an excessive load on the water purification system. Thus it is essential to use a two-part fully curing encapsulant which contains no solvents (nor does it release any during curing). Furthermore, it must be self-curing (requiring no oxygen or moisture to cure) as it is fully enclosed between the ABS and glass.

Two silicon rubber encapsulants have been identified which are suitable for Method A: Dow Corning 3-6512 and Sylgard (Dow Corning) 170. Sylgard 182 is a possible sealant for the first stage of Method A. It has been tested on bare Al samples of glass and found to give 2–3 days' protection at 95°C before serious pitting develops. No accelerated ageing tests have been made with full glass CTCs, evaporated with bare Al and then encapsulated in ABS dishes. Neither 3-6512 nor Sylgard 170 have been tested on bare Al samples, but 3-6512 has been found to give some water protection in that a sample of Al/TiO where the evaporation conditions (angle of deposition and thickness) were unfavourable for water protection was protected with 3-6512 for 10 days' immersion

at 95°C. Similarly Al/TiO/Sylgard 182 has proved an effective water protection even though the conditions of the Al/TiO evaporation were unfavourable.

Apparently Aylesbury Polymer Products have identified a suitable encapsulant for Method B and performed some tests on 'pudding bowls' but no samples have been received nor details of the encapsulants given. In the final analysis, encapsulation is too expensive to be worthwhile.

7.3 Omega

Omega mirror is a commercially available evaporated Al front surface reflecting sheet of which the principal supplier is O.C.L.I. a company based in California. The substrate is 1 m × 400 mm sheets of highly polished anodized aluminium. These are continuously fed into a high vacuum chamber equipped with electron beam evaporators which are capable of evaporating high temperature dielectrics such as TiO_2. The continuous feed mechanism effectively eliminates the down time for pulling the vacuum (necessary in conventional plants). Hence the production rate is vastly increased and the finished product is available at relatively low cost, £35 per square meter.

The composition of Omega mirror was analysed by Auger spectrometry at NRC, Ottawa, with the following result, reading downwards from the outer evaporated layer to the aluminium substrate:

Pr_2O_3+TiO_2	65 nm
MgF_2+oxygen	82 nm
Al	56 nm
SiO_2	29 nm
Al_2O_3	2000 nm
Al	substrate

The Pr_2O_3+TiO_2 layer is a well known mixture for achieving outstanding durability. The reflectivity of the Al layer is enhanced above 400 nm wavelength by the low refractive index MgF_2 layer but is also reduced below 350 nm from absorption in the Pr_2O_3+TiO_2 layer (see Figure 6.11). The SiO_2 layer acts as a key for bonding the Al layer onto the anodised Al substrate and also prevents the Al_2O_3 from oxidizing the Al layer.

In order to manufacture a concentrator out of Omega, the finished sheet is CNC machined into petals which are assembled into a 24-sided polygonal plastic holder (see Figure 6.10).

Initial accelerated ageing tests of 50 mm^2 off-cuts of Omega sheet immersed in high purity water at 95°C were very encouraging. No change in reflectivity was detected at 442 nm (laser beam measurement) after up to 35 days' immersion. However, some subsequent tests showed two kinds of corrosion on the front surface of Omega sheet. One was a yellowish staining that occurred when iron was present in the water [63]. This corrosion can be avoided by ensuring that free iron is not present in the water in SNO (stainless steel is acceptable). The other type of corrosion was a white cloudiness that could sometimes be removed by rubbing vigorously. It was hypothesized that this corrosion was associated with the unprotected bare aluminium surface on the back of the Omega sheet. This aluminium surface was slowly dissolving in the water and was either depositing on the front surface or inducing corrosion in the front surface by raising the conductivity of the water.

In either case the remedy is to protect the back surface of Omega sheet so that aluminium cannot dissolve in the water. Many different methods of back protection were investigated, all of which proved successful in avoiding any corrosion in the front surface. The most practical of these is simply to coat *both* sides of the anodised sheet with the evaporated Omega mirror coating.

The water protection afforded by the Pr_2O_3+TiO_2 dielectric layer in Omega presumably depends on the angle of deposition of the Al layer in the same way that the water protection afforded by SiO and TiO layers on glass/Al reflectors depends on angle of deposition (Section 7.2.1). However in the evaporation geometry for coating *flat* sheets it is much easier to limit the angles of deposition than in the geometry for coating curved domes. In fact, for the purpose of achieving a uniform thickness of coating across the entire sheet, the evaporation sources in the O.C.L.I. plant are backed-off from the sheet by a distance such that the maximum angle of deposition at the edges of the sheet is about 15°. Hence one can expect uniform water protection across the entire surface of

the Omega sheet. This was verified by cutting a whole 1 m × 400 mm sheet (both sides coated) into 20 pieces which were immersed in water at 95°C for 20 days. No corrosion was observed on any of the pieces except in small areas which were exposed to steam above the water level during the immersion period. On these small areas a cloudy deposit was visible which could be removed by rubbing vigorously with a cloth, revealing an intact Omega front surface below. Although the back surface of this sheet was coated with Omega the edges of the 20 pieces were unprotected bare aluminium.

With 240,000 petals (10,000 concentrators) each of ~ 300 mm edge length and 0.3 mm thickness there will be 21 square meters of bare aluminium in SNO, just from the edges of these petals! Apart from the question of whether this could cause corrosion or give rise to deposition on the front surface of the Omega concentrators, there is a possibility that the leaching of radioactive contaminants from this exposed aluminium surface could increase the background contribution from the light water.

Several techniques for protecting the edges of the petals have been investigated. The only successful technique, so far, is the thermal evaporation of SiO or TiO onto stacks of petals resembling decks of playing cards. The surfaces of these stacks are almost flat and can thus be coated with 1.5 λ of SiO or TiO at angles of deposition not exceeding 20°. These evaporation conditions should ensure good water protection (Section 7.2.1). Several tests have been performed in which the coated edges of Omega petals show no visible signs of corrosion, under a microscope, after 20 days immersion at 95°. The TiO coating is favoured because it forms a black layer at these thicknesses and consequently its presence can be easily checked in a quality control visual inspection.

It is concluded that the Omega CTC satisfies the SNO design criteria provided that *both* sides of the anodised sheet are coated with the Omega mirror coating and that the edges of the petals are coated with 1.5 λ of TiO at angles of deposition not exceeding 20°.

7.4 Silver on Glass Substrate

Although silver is not as reflective in the U.V. as aluminium, its effective reflectance, averaged over the wavelength spectrum of interest to SNO, is expected to be between 80% and 85% which is similar to that of Omega and only a few percent less than aluminium on glass. The major advantage of silver over aluminium is that it does not dissolve in water. Silver is well known for its corrosive reaction with sulphur, but there will be negligeable quantities of sulphur in the high purity water of SNO. Another advantage of silver is that it can be *chemically* deposited onto glass by precipitation from a silver nitrate solution. This quick and simple method would cost between £3 to £5 per glass dish for a 10,000 off production — the 1 μm layer of silver does not represent a significant material cost.

Initial accelerated ageing tests of bare silver on glass concentrators immersed in high purity water at 95°C showed that after 3 days the silver began to peel off the glass. The adhesion to the glass had become so poor that the silver could be wiped off with minimal pressure. An adhesion test which is commonly used in the evaporation industry is to check whether a coating remains firmly attached to its substrate after an adhesive tape is applied and removed. Silver on glass failed this test *before* being aged.

To try and minimise this adhesion problem several different overcoats were applied onto the silver: chemically deposited copper, CM8000, redox paint and copper/CM8000. None of these were successful in preventing the silver from peeling off after 3 days in water at 95°. The adhesion problem of chemically deposited silver on glass is well known in the silvering trade. It can be solved by previously evaporating CrO onto the glass substrate *before* depositing the silver. Unfortunately this extra evaporation step in the production of silver concentrators makes them too expensive for SNO.

7.5 Anodized Aluminium

This is by far the cheapest method of producing 10,000 concentrators that was investigated. An aluminium dish is spun to the required profile, polished and anodized at a

total cost of about £5 per dish.

It is known that the reflectivity of anodized aluminium has a significant diffuse component as well as a dominant specular component. The concentrators are designed for specularly reflecting surfaces and so this is the relevant component for SNO. This component was measured by laser with a silicon diode detector which covered a solid angle $2\pi(1-\cos 4.5°)$ which is the widest possible interpretation of specular reflectivity that can be adopted without significantly affecting the performance of the concentrator. Samples of anodised aluminium, with anodic film thicknesses from 0.5 μm to 2 μm, were obtained and their specular reflectances measured before and after 10 days immersion in high purity water at 95°C. In every sample the reflectivity dropped from about 80% before the immersion to about 60% afterwards. It has been suggested that this drop in specular reflectivity (called 'smutting') is caused by the excessive temperature of the ageing tests which should not be carried out at temperatures greater than 65°. Unfortunately we have no option but to make a decision based on the results of these tests.

7.6 Conclusion

Two manufacturing methods have been found which satisfy the four major design criteria in SNO: glass/Al/TiO/CM8000 and ABS/Omega. In order to decide between the two it is necessary to open up the discussion and consider the following secondary criteria:

1. **Alkali resistance**: So far, the water resistance of concentrators has been investigated at neutral pH. There is a possibility that the pH in SNO might swing in either direction from the leaching of acids or alkalis into the water (the pH of ultra-pure water is not at all buffered). Moreover, it may be necessary to introduce biocides into the water and most of these biocides (but not all) are mild alkalis. The corrosion resistance of both concentrators to acids is excellent. However, at pH 12 at room temperature, CM8000 dissolves slowly and TiO provides about 1 days' protection before the Al is severely pitted. In contrast Omega mirror is unaffected after 25 days' immersion.

2. **Robustness**: All the equipment in SNO will be transported down to the 6800 ft level of the Creighton mine by a free-fall elevator which suffers severe lateral accelerations as it hits the walls of the shaft. Furthermore the equipment will be installed by miners (union regulations) who are not known for their delicate handling of equipment. In terms of ease of handling the Omega design is vastly superior to the glass concentrator. A significant percentage ($\simeq$ 10%) of prototype glass concentrators have been broken by every company that has handled them: the glass blowers, the two evaporation plants, the chemical silvering outfit and the spraying company. The robustness of the glass dish can be greatly improved by encapsulating in an ABS shell but this is too expensive. In comparison, the Omega concentrator can be dropped without any adverse effect (experimental observation).

3. **Cost**: Firm quotations for every manufacturing process in each design have not been obtained. In some cases it is necessary to use cost estimates which are notoriously unreliable. Nevertheless it would seem that the Omega design is cheaper than the glass design. The total costs for producing 10,000 concentrators are estimated at £265,000 for Omega and £390,000 for glass.

After taking these secondary considerations into account it was decided to adopt the Omega design for SNO. The expected optical performance of this design is described in detail in Section 6.5. Overall, a 60% percent increase in the light collection from the fiducial volume is expected. This represents real 'value for money' when one considers that the cost of the 10,000 PMTs in SNO is about £3 million and approaches £5 million if one includes the cost of the electronics and the PMT support structure. Moreover, the concentrators also reduce the sensitivity of the experiment to the β-γ background from the PMT region by an order of magnitude which means that the detector threshold is unlikely to be determined by this background. Thus the concentrators are even more useful than an extra £2 million worth of photomultipliers.

Appendix A

Differential Equations for the Profile of 2D CTCs

In this appendix a general method for constructing the profile of 2D CTCs is obtained by application of the tangent-ray principle of [49] to the 2D cross-section of the photocathode. In section A.1 the differential equations governing this construction are derived for the general case of a convex photocathode specified by its polar coordinates (r, θ) where r is a known function of θ (see Figure 5.2). In section A.2 the solutions to these differential equations are presented for the special case of a spherical photocathode of fixed radius of curvature and polar half angle θ_{cath}. For both the general and the spherical photocathodes there are three separate cases to be considered: (i) $\alpha_{cath} + \theta_i = \pi/2$, (ii) $\alpha_{cath} + \theta_i > \pi/2$ and (iii) $\alpha_{cath} + \theta_i < \pi/2$, where θ_i is the limiting angle of the 2D angular acceptance of the CTC and α_{cath} is the angle between the z-axis and the normal to the photocathode at the edge of the photocathode (see Figure 5.2). Only case (ii) has been specifically considered in [49] in which the 2D profile of the absorber (photocathode) is assumed to be a closed loop, i.e. $\alpha_{cath} = \pi$.

A.1 General Convex Photocathode

Let us introduce the coordinate system of [49], (r, θ') where $\theta' = \pi - \theta$ and in which the 2D profile of the photocathode extends from $\theta' = \pi - \theta_{cath}$ to $\theta' = \pi + \theta_{cath}$ (see Figure A.1). In this figure the point S (of polar angle θ_S) has been drawn at which a ray of polar angle θ_i is *directly* tangent to the photocathode. The location of point S can also be used to determine which of the three above cases ($\alpha_{cath} + \theta_i =, >, < \pi/2$) is relevant. If S is at the edge of the photocathode ($\theta_S = \theta_{cath}$) then it is case (i); if S is *inside* the edge of the photocathode ($\theta_S < \theta_{cath}$) then it is case (ii); and if S lies *outside* the photocathode ($\theta_S > \theta_{cath}$) then it is case (iii).

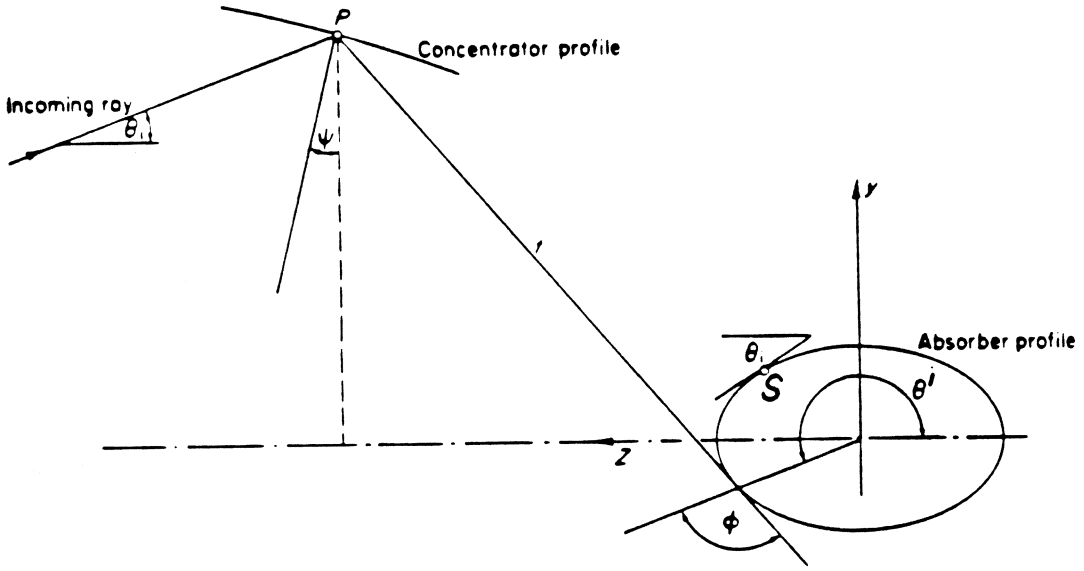

Figure A.1: Construction of the 2D profile of a CTC from the 2D cross-section of the photocathode by application of the tangent-ray principle [49].

Let us consider case (i) first, in which all rays which are tangent to the photocathode are reflected by the CTC to have polar angle θ_i. One such ray, incident at point P on the CTC profile, is shown in Figure A.1. The condition for reflection (Snell's law) at P can be written

$$\theta_i + \theta' + \phi + 2\psi = 2\pi \qquad \text{(A.1)}$$

where ϕ is the angle between the vector from the origin to the tangent at the photocath-

ode and the tangent itself and ψ is the angle between the normal to the concentrator profile at P and the y-axis. Thus

$$\frac{dy}{dz} = \tan\psi = -\tan\frac{1}{2}(\theta_i + \theta' + \phi) \tag{A.2}$$

and the coordinates of point P are

$$\begin{aligned} y &= r\sin\theta' - t\sin(\theta' + \phi) \\ z &= -r\cos\theta' + t\cos(\theta' + \phi) \end{aligned} \tag{A.3}$$

where t is the length from P to the tangent at the photocathode. Differentiating (A.3) and using (A.2) one obtains

$$\frac{\dot{r}\sin\theta' + r\cos\theta' - \dot{t}\sin(\theta' + \phi) - t\cos(\theta' + \phi)(1 + \dot{\phi})}{-\dot{r}\cos\theta' + r\sin\theta' + \dot{t}\cos(\theta' + \phi) - t\sin(\theta' + \phi)(1 + \dot{\phi})} + \tan\frac{1}{2}(\theta_i + \theta' + \phi) = 0. \tag{A.4}$$

In this first-order linear differential equation t is the dependent variable, θ' is the independent variable and r and ϕ are both known functions of θ'. Hence this equation can be solved (numerically) for $\dot{t}$ as a function of t and θ' which can then be integrated from the beginning of the profile, where $\theta' = \pi - \theta_{cath}$ and $t = 0$, to the end of the profile, where $\theta' = \pi + \theta_{cath}$. Thus t is a calculable function of θ' and the full profile for case (i) is given by (A.3) where θ' is restricted to the range $\pi - \theta_{cath} \leq \theta' \leq \pi + \theta_{cath}$.

If case (ii) is relevant, then there is a section of the photocathode profile ($\theta > \theta_S$) which is shadowed from *direct* rays at polar angle θ_i. The corresponding section of the concentrator profile is an involute of this shadowed section of the photocathode (see Figure 3.11). For the involute we have the classical result

$$\dot{t} = (r^2 + \dot{r}^2)^{\frac{1}{2}} \tag{A.5}$$

for a point P given by (A.3). Thus the full profile of the CTC can be obtained by integrating (A.5) from $\theta' = \pi - \theta_{cath}$ (where $t = 0$) to $\theta' = \pi - \theta_S$, which completes the involute section, and then integrating (A.4) from $\theta' = \pi - \theta_S$ to $\theta' = \pi + \theta_S$.

If case (iii) applies, then an extension of small radius of curvature ϵ is provided to the photocathode out to the angle $\alpha_{cath} = \pi/2 - \theta_i$ (see Figure 5.3). The CTC can then be designed for arbitrarily small ϵ and the problem is reduced to case (i). In the limit

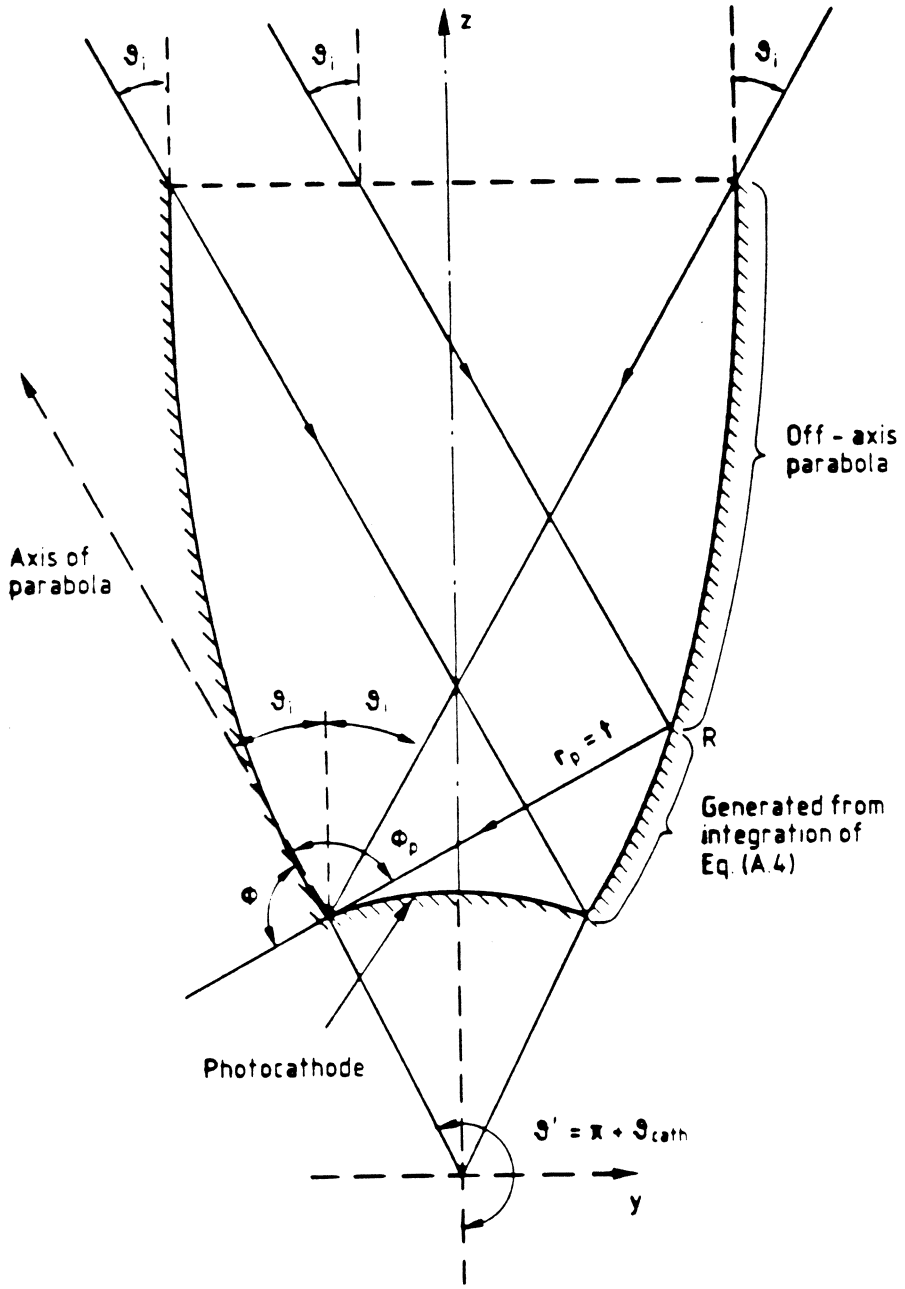

Figure A.2: Construction of the 2D profile of a CTC for case (iii), $\alpha_{cath} + \theta_i < \pi/2$.

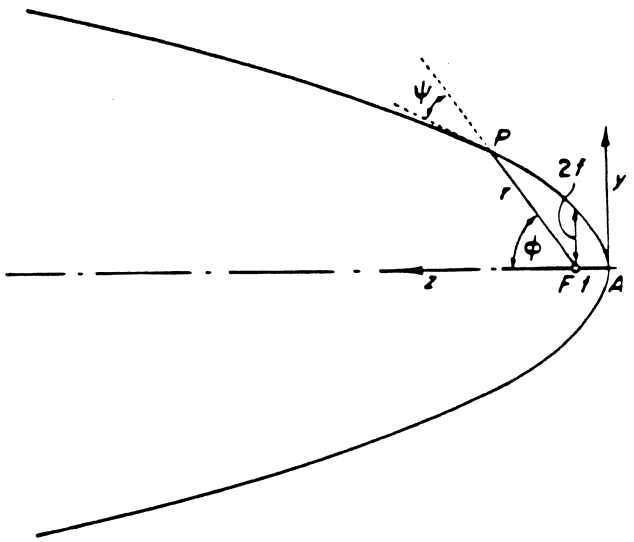

Figure A.3: The parabola in polar coordinates with origin at the focus [49].

$\epsilon \rightarrow 0$ the upper (greatest in z) section of the CTC profile becomes an off-axis parabola with focus at the edge of the photocathode, just as in the edge-ray construction of the Winston cone (see Figure 3.5). To generate the *lower* section of the CTC profile, (A.4) is integrated from $\theta' = \pi - \theta_{cath}$ to $\theta' = \pi + \theta_{cath}$. At this point on the CTC profile (point R in Figure A.2) the off-axis parabola begins.

The general equation of a parabola in polar coordinates, with focus at the origin, is given by

$$r_p = f \sin^2(\phi_p/2) \tag{A.6}$$

where r_p and ϕ_p are the polar radius and polar angle of a point P on the parabola and f is a constant which determines the scale of the parabola (see Figure A.3).

At the starting point R of the off-axis parabola drawn in Figure A.2 it is easily shown that $\phi_p = \pi + \theta_i - \theta_{cath} - \phi$ and that r_p is given by the final value of t (at $\theta' = \pi + \theta_{cath}$) from the construction of the lower section of the profile. Hence the constant f for this off-axis parabola is given by

$$f = \frac{t(\theta' = \pi + \theta_{cath})}{\sin^2[(\pi + \theta_i - \theta_{cath} - \phi)/2]} \tag{A.7}$$

and the coordinates of any point P on this off-axis parabola with focus at the edge of

the photocathode are given by

$$\begin{aligned} y &= -r\sin\theta_{cath} + r_p\sin(\phi_p - \theta_i) \\ z &= r\cos\theta_{cath} + r_p\cos(\phi_p - \theta_i) \end{aligned} \tag{A.8}$$

where r is evaluated at the edge of the photocathode ($\theta' = \pi + \theta_{cath}$), r_p is given by (A.6) in which the constant f is determined by (A.7), and where ϕ_p lies in the range $\pi + \theta_i - \theta_{cath} - \phi \geq \phi_p \geq 2\theta_i$.

A.2 Spherical Photocathode

For spherical photocathodes; where $\phi = \pi/2$, $\alpha_{cath} = \theta_{cath}$, $\theta_S = \pi/2 - \theta_i$ and $r(\theta)$ is constant; the solution to (A.5) is trivially

$$t = r\theta' + \text{const}, \tag{A.9}$$

the solution to (A.4) is

$$t = \frac{r[\theta' - \theta_i - \pi/2 - \cos(\theta' - \theta_i) + \text{const}]}{1 + \sin(\theta' - \theta_i)}, \tag{A.10}$$

as shown by Rabl [72], and the coordinates of the point P on the CTC profile are given by

$$\begin{aligned} y &= r\sin\theta' - t\cos\theta' \\ z &= -r\cos\theta' - t\sin\theta'. \end{aligned} \tag{A.11}$$

For case (i), t is given by (A.10), where the constant of integration is fixed by requiring t at $\theta' = \pi - \theta_{cath}$ to be zero and where θ' is restricted to the range $\pi - \theta_{cath} \leq \theta' \leq \pi + \theta_{cath}$. For case (ii), t is given by (A.9), when θ' lies in the range $\pi - \theta_{cath} \leq \theta' \leq \pi/2 + \theta_i$ and where the constant of integration is fixed by requiring $t(\theta' = \pi - \theta_{cath}) = 0$, and by (A.10) when θ' lies in the range $\pi/2 + \theta_i \leq \theta' \leq 3\pi/2 - \theta_i$ and where the constant of integration is fixed by matching the two solutions at $\theta' = \pi - \theta_i$. For case (iii), the lower section of the CTC profile is obtained in exactly the same manner as the entire profile for case (i) is obtained. Then, the upper section (the off-axis parabola) is given by (A.8), in which ϕ_p is restricted to the range $\pi/2 + \theta_i - \theta_{cath} \geq \phi_p \geq 2\theta_i$.

Appendix B

Differential Equations for the 2D Profile of 3D Skew CTCs

In this appendix the 2D profiles of 3D skew CTCs are obtained from a construction in which the tangent-ray principle is applied to a set of *non-meridional* rays of given skewness $h \neq 0$. In Section B.1 the form of the differential equations governing this construction will be derived for the general convex photocathode shown in Figure 5.2 and in Section B.2 these differential equations are explicitly derived for the special case of a spherical photocathode.

In analogy with the application of the tangent-ray principle to *meridional* rays presented in appendix A there are three separate cases to be considered here (for both the general photocathode and the spherical photocathode): (i) rays of polar angle θ_t and skewness h are tangent to the photocathode at the *edge* of the photocathode, (ii) a section of the photocathode is shadowed from rays of polar angle θ_t and skewness h and (iii) the rays of polar angle θ_t and skewness h which are directly incident at the photocathode edge are *not* tangent to the photocathode.

B.1 General Convex Photocathode

The vector from the origin to any point Q on the general convex photocathode shown in Figure 5.2 can be written $\mathbf{r}_Q = r_Q(\sin\theta_Q\cos\phi_Q, \sin\theta_Q\sin\phi_Q, \cos\theta_Q)$ where r_Q is a known function of the polar angle θ_Q which is restricted to the range $0 \leq \theta_Q \leq \theta_{cath}$ and where ϕ_Q lies in the range $0 \leq \phi_Q < 2\pi$. The unit vector normal to the photocathode at point Q can be written $\hat{\mathbf{n}}_Q = (\sin\theta_n\cos\phi_Q, \sin\theta_n\sin\phi_Q, \cos\theta_n)$ where θ_n is a known function of θ_Q (for spherical photocathodes $\theta_n = \theta_Q$).

To generate the profile of a skew CTC for a given limiting angle θ_i and skewness h one must first determine which of the three above cases is relevant. For this purpose let us consider the ray with direction cosines $\hat{\mathbf{s}} = (\sin\theta_i, 0, \cos\theta_i)$ which is tangent to the photocathode at a point S and which has the required skewness h. The angles θ_S and ϕ_S defining the point S can be found by solving the two simultaneous equations pertaining to this ray: $\hat{\mathbf{s}}.\hat{\mathbf{n}}_S = 0$ and $h = (\mathbf{r}_S \times \hat{\mathbf{s}}).\hat{\mathbf{z}}$. The value of θ_S determines which case is relevant. If $\theta_S = \theta_{cath}$ then it is case (i), if $\theta_S < \theta_{cath}$ (point S *inside* the edge of the photocathode) then it is case (ii) and if $\theta_S > \theta_{cath}$ (point S *outside* the photocathode) then it is case (iii).

Let us first consider case (i) in which there is no shadowed portion of the photocathode nor any need to extend the photocathode. All rays of skewness h which are tangent to the photocathode are reflected by the CTC to have polar angle θ_i. One such ray, which is tangent to the photocathode at point Q and incident at a point R on the CTC profile is shown in Figure B.1. In this figure the following vectors have been included: $\mathbf{r}_Q$, the vector to point Q; $\hat{\mathbf{n}}_Q$, the normal to the photocathode at point Q; $\mathbf{r} = (0, y, z)$, the vector from the origin to R; $\mathbf{t} = \mathbf{r} - \mathbf{r}_Q$, the vector from Q to R; $\hat{\mathbf{n}} = (0, -\cos\psi, \sin\psi)$, the unit vector normal to the concentrator profile at point R, and $\hat{\mathbf{t}}'$, the unit vector of the outgoing ray. Four conditions are imposed on these vectors:

$$\text{tangent at point Q,} \qquad \hat{\mathbf{n}}_Q.\hat{\mathbf{t}} = 0, \tag{B.1}$$

$$\text{skew invariant,} \qquad h = (\mathbf{r}_Q \times \hat{\mathbf{t}}).\hat{\mathbf{z}}, \tag{B.2}$$

$$\text{law of reflection,} \qquad \hat{\mathbf{t}}' = \hat{\mathbf{t}} - 2(\hat{\mathbf{n}}.\hat{\mathbf{t}})\hat{\mathbf{n}} \tag{B.3}$$

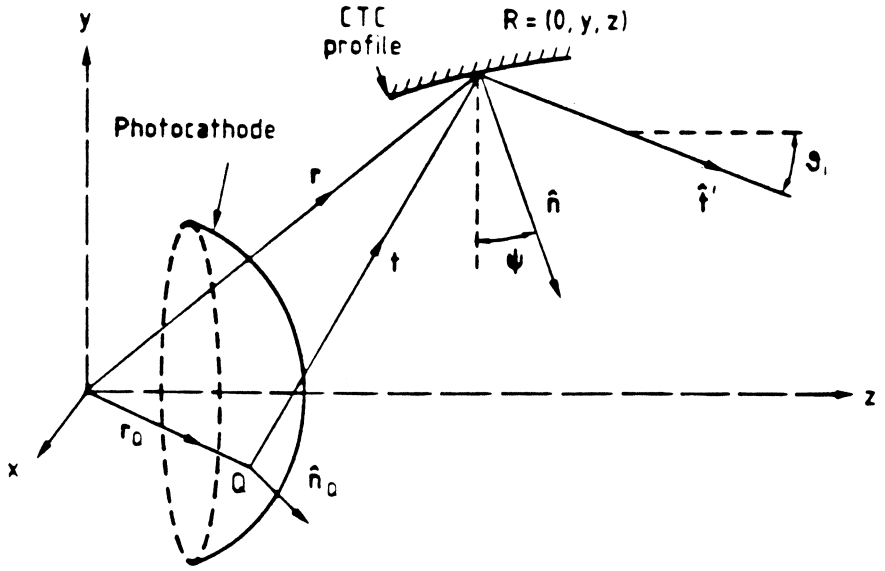

Figure B.1: Construction of the 2D profile of a skew CTC from the 3D shape of the photocathode by application of the tangent-ray principle to rays of skewness h.

$$\text{and polar angle of } \hat{\mathbf{t}}', \qquad \hat{\mathbf{t}}'.\hat{\mathbf{z}} = \cos\theta_1. \tag{B.4}$$

The vector $\hat{\mathbf{t}}'$ can be eliminated from (B.3) and (B.4) to give

$$\hat{\mathbf{t}}.\hat{\mathbf{z}} - 2(\hat{\mathbf{n}}.\hat{\mathbf{t}})(\hat{\mathbf{n}}.\hat{\mathbf{z}}) = \cos\theta_1. \tag{B.5}$$

This equation can be written as a first-order non-linear differential equation of the form

$$F\left[\frac{dy}{dz}, \left(\frac{dy}{dz}\right)^2, y, z, \theta_Q, \phi_Q\right] = 0 \tag{B.6}$$

by making the substitutions $\sin\psi = \frac{dy}{dz}\left[1 + \left(\frac{dy}{dz}\right)^2\right]^{-\frac{1}{2}}$ and $\cos\psi = \left[1 + \left(\frac{dy}{dz}\right)^2\right]^{-\frac{1}{2}}$. In this differential equation y is the dependent variable, z is the independent variable and θ_Q and ϕ_Q are functions of y and z through (B.1) and (B.2). Thus (B.6) can be solved for $\frac{dy}{dz}$ as a function of y and z and the profile can be generated by integrating $\frac{dy}{dz}$, providing that the starting conditions of the integration are known.

The starting point of the integration is at the edge of the photocathode where $\mathbf{r} = \mathbf{r}_Q(\theta_Q = \theta_{cath}, \phi_Q = \pi/2)$. However at this point, (B.5) and hence (B.6) are undefined since $\mathbf{t} = 0$. To find $\frac{dy}{dz}$ at this point, consider the ray of skewness h and polar angle θ_1 which is tangent to the photocathode at this point. We require that this ray be

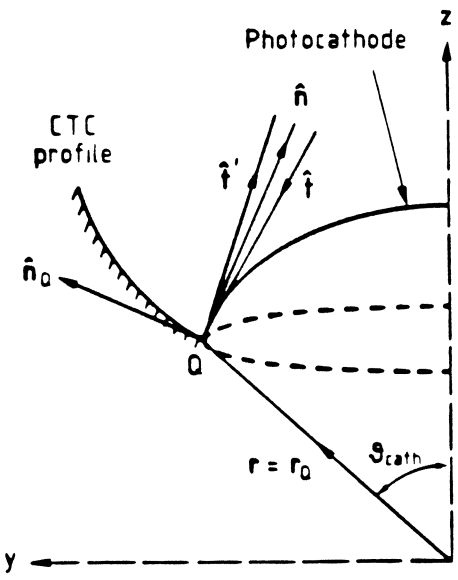

Figure B.2: The ray $\hat{\mathbf{t}}$ of skewness h and polar angle $\leq \theta_t$ which is tangent at the edge of the photocathode ($\theta_Q = \theta_{cath}$, $\phi_Q = \pi/2$), in cases (i) and (ii), is reflected ($\hat{\mathbf{t}}'$) so as to remain tangent to the photocathode.

reflected to remain tangent to the photocathode (tangent-ray principle). Such a ray is drawn, with unit vector $\hat{\mathbf{t}}$, in Figure B.2 with the usual vectors $\hat{\mathbf{t}}'$, $\hat{\mathbf{n}}$, $\mathbf{r}_Q$, $\hat{\mathbf{n}}_Q$ and $\mathbf{r}$. The conditions (B.1)-(B.3) apply to these vectors and a new condition is imposed onto the outgoing ray which is now required to be tangent to the photocathode:

$$\hat{\mathbf{t}}'.\hat{\mathbf{n}}_Q = 0 \tag{B.7}$$

Eliminating $\hat{\mathbf{t}}'$ from (B.3) and (B.7) and using (B.1) one finds that

$$(\hat{\mathbf{n}}.\hat{\mathbf{t}})(\hat{\mathbf{n}}.\hat{\mathbf{n}}_Q) = 0. \tag{B.8}$$

Since $\hat{\mathbf{n}}$ and $\hat{\mathbf{t}}$ are clearly not orthogonal (see Figure B.2) the conclusion is that $\hat{\mathbf{n}}$ and $\hat{\mathbf{n}}_Q$ are required to be orthogonal at the edge of the photocathode. Hence at the starting point of the integration the differential equation is simply

$$\frac{dy}{dz}(t = 0) = \frac{\hat{\mathbf{n}}_Q(\theta_Q = \theta_{cath},\, \phi_Q = \pi/2).\hat{\mathbf{y}}}{\hat{\mathbf{n}}_Q(\theta_Q = \theta_{cath},\, \phi_Q = \pi/2).\hat{\mathbf{z}}}. \tag{B.9}$$

Now we can integrate $\frac{dy}{dz}$ from the start point all the way to the end of the CTC profile where $\frac{dy}{dz} = 0$ and the parameter $\theta_Q(y, z)$ returns, from its minimum, to θ_{cath}.

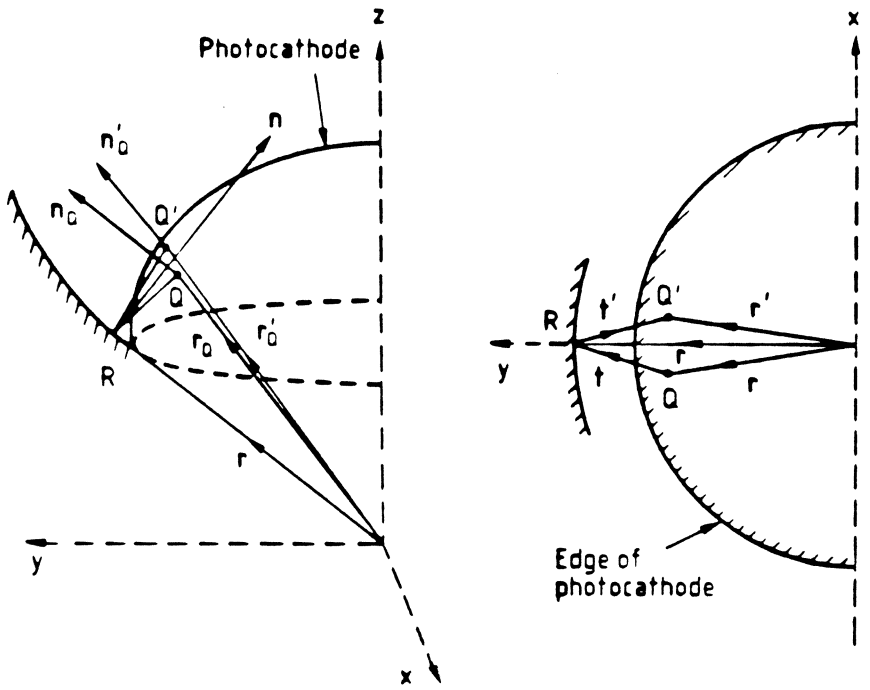

Figure B.3: Construction of the involute section of a skew CTC for case (ii). The ray **t** of skewness h and polar angle $< \theta_t$ which is tangent to the photocathode at Q is reflected (**t**′) to be tangent at Q′.

Let us now consider case (ii), i.e. when $\theta_S < \theta_{cath}$ and a section of the photocathode is shadowed from rays of polar angle θ_t and skewness h. This corresponds to case (ii) in appendix A where the lower section of the CTC profile is an involute of the shadowed section of the photocathode and the upper section is derived from the usual tangent-ray condition. The corresponding 'involute' section of the skew CTC being considered here, is generated by requiring all rays of skewness h and polar angle $\theta < \theta_t$ which are tangent to the shadowed section of photocathode to be reflected tangentially back onto the photocathode. One such ray which is tangent to the photocathode at point Q, reflected by the CTC at point R and tangent once more at point Q′ is shown in Figure B.3. The usual vectors **t**, $\hat{\mathbf{n}}$, **t**′, $\mathbf{r}_Q$, $\hat{\mathbf{n}}_Q$ and **r** have been drawn in this figure together with the vector $\mathbf{r}'_Q$ from the origin to Q′ and the vector $\hat{\mathbf{n}}'_Q$, the normal to the photocathode at Q′. The three conditions (B.1)-(B.3) are imposed on these vectors and the constraint on the outgoing ray is changed to

$$\hat{\mathbf{t}}'.\hat{\mathbf{z}} = -\hat{\mathbf{t}}.\hat{\mathbf{z}} \qquad \text{(B.10)}$$

Eliminating $\hat{\mathbf{t}}'$ from (B.3) and (B.10) one obtains the following equation

$$\hat{\mathbf{t}}.\hat{\mathbf{z}} = (\hat{\mathbf{n}}.\hat{\mathbf{t}})(\hat{\mathbf{n}}.\hat{\mathbf{z}}) \tag{B.11}$$

which can be transformed into a first-order second-degree differential equation

$$G\left[\frac{dy}{dz}, \left(\frac{dy}{dz}\right)^2, y, z, \theta_Q, \phi_Q\right] = 0 \tag{B.12}$$

by making the usual substitutions for $\cos\psi$ and $\sin\psi$. Since (B.1) and (B.2) are still valid, θ_Q and ϕ_Q are the same functions of y and z as in the previous differential equation. Thus (B.12) can be solved numerically for $\frac{dy}{dz}$ as a function of y and z and the profile can be generated by integrating $\frac{dy}{dz}$.

However, once again, at the start point of the integration $\mathbf{t} = 0$ and (B.11) and (B.12) are undefined. To find $\frac{dy}{dz}$ at this point consider the ray of skewness h and polar angle $\theta < \theta_t$ which is tangent to the photocathode at this point and which is reflected to remain tangent to the photocathode (see Figure B.2). The conditions (B.1)–(B.3) and (B.7) which are imposed on this ray are the same conditions which were imposed on the ray of polar angle θ_t and skewness h which was tangent at the start point when case (i) was being considered. Thus the value of $\frac{dy}{dz}$ at the start point of the integration is given by (B.9) for both cases (i) and (ii).

Hence the involute section of the profile for case (ii) can be generated by (numerically) integrating $\frac{dy}{dz}$, derived from (B.9) and (B.12), from $\mathbf{r} = \mathbf{r}_Q(\theta_Q = \theta_{\text{cath}}, \phi_Q = \pi/2)$ until $\theta_Q(y,z)$ reaches θ_S, the point at which the photocathode is no longer shadowed from direct rays of polar angle θ_t and skewness h. The rest of the profile is generated by integrating $\frac{dy}{dz}$, derived from (B.6), from the last point $\mathbf{r}$ of the involute section until $\frac{dy}{dz} = 0$ and $\theta_Q(y,z)$ has returned to θ_S.

Let us now consider how to generate the CTC profile for case (iii), where $\theta_S > \theta_{\text{cath}}$. This case is analogous to case (iii) of appendix A where the CTC profile was generated in two sections: the lower section by applying the tangent ray principle across photocathode and the upper section by applying the tangent-ray principle to the edge of the photocathode (the edge-ray principle). Similarly here, the lower section of the

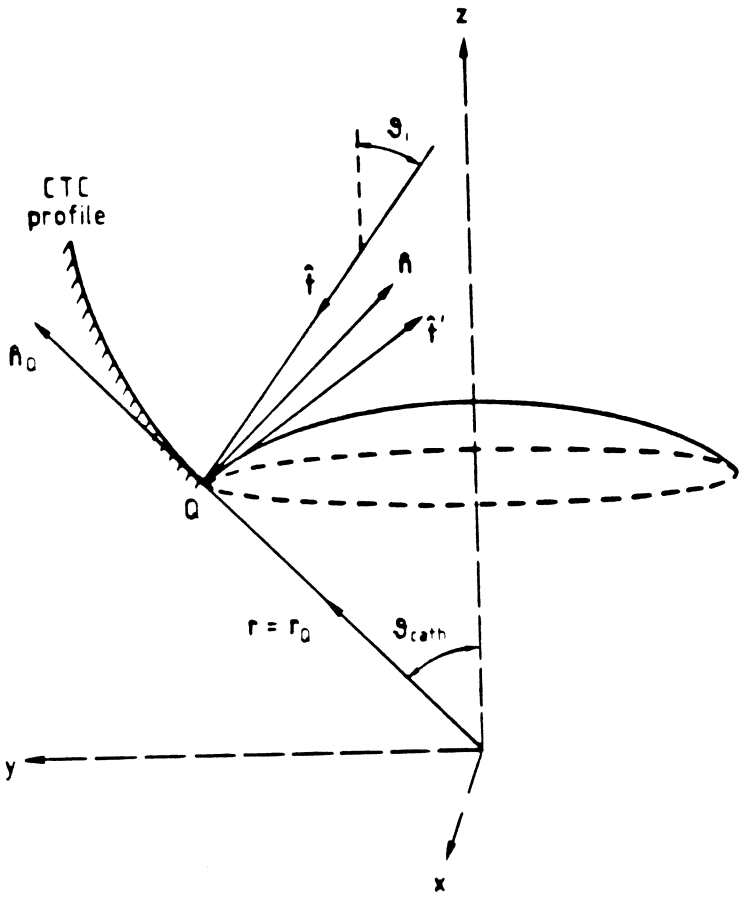

Figure B.4: The ray $\hat{\mathbf{t}}$ of skewness h and polar angle θ_1 which is *not* tangent at the edge of the photocathode ($\theta_Q = \theta_{cath}$, $\phi_Q = \pi/2$), in case (iii), is reflected ($\hat{\mathbf{t}}'$) so as to be tangent to the photocathode.

profile is generated by applying the tangent-ray principle across the photocathode and the upper section of the profile is generated by applying the edge-ray principle. The differential equation for the edge-ray construction with skew rays is given in appendix F of [49]. Before reproducing this derivation let us first consider the starting value of $\frac{dy}{dz}$ for the *lower* section of the profile which in case (iii) is *not* given by (B.9).

In this case, the ray of polar angle θ_1 and skewness h which is incident at the start point of the integration ($\mathbf{r} = \mathbf{r}_Q(\theta_Q = \theta_{cath}, \phi_Q = \pi/2)$ is *not* tangent to the photocathode. The tangent-ray principle requires the reflection of this ray ($\hat{\mathbf{t}}'$) to be normal to the photocathode (see Figure B.4). Hence the conditions (B.2),(B.3) and (B.7) which are imposed on this ray are the same conditions as for cases (i) and (iii) with the exception

of the tangent condition (B.1) which is replaced by the constraint on the polar angle of $\hat{\mathbf{t}}$:

$$\hat{\mathbf{t}}.\hat{\mathbf{z}} = -\cos\theta_i \tag{B.13}$$

Thus we can write $\hat{\mathbf{t}}$ as $(\cos\phi_i \sin\theta_i, \sin\phi_i \sin\theta_i, -\cos\theta_i)$ where θ_i is the given polar angle and ϕ_i is an unknown angle which can be found by solving (B.2) since h and $\mathbf{r}_Q$ are given. This solution can be written

$$\cos\phi_i = \frac{-h}{r_{\text{polar}} \sin\theta_i} \tag{B.14}$$

where $r_{\text{polar}} = \mathbf{r}_Q(\theta_Q = \theta_{\text{cath}}, \pi/2).\hat{\mathbf{y}}$ is the polar radius of the photocathode edge. It is clear from (B.14) that there is a maximum value of skewness, $h_{\text{max}} = r_{\text{polar}} \sin\theta_i$, for which a CTC profile can be constructed since if h exceeds this value then no ray of skewness h and polar angle θ_i can be incident at the photocathode edge and hence the profile cannot be generated from the photocathode edge. Eliminating $\hat{\mathbf{t}}'$ from (B.3) and (B.7) one obtains the following equation

$$\hat{\mathbf{t}}.\hat{\mathbf{n}}_Q - 2(\hat{\mathbf{n}}.\hat{\mathbf{t}})(\hat{\mathbf{n}}.\hat{\mathbf{n}}_Q) = 0 \tag{B.15}$$

which can be written as a quadratic in $\frac{dy}{dz}$ by making the usual substitutions for $\cos\psi$ and $\sin\psi$. The coefficients of this quadratic equation are functions of θ_{cath}, θ_i and ϕ_i which are all known. Thus the initial value of $\frac{dy}{dz}$ can be specified and $\frac{dy}{dz}$, derived from (B.6), can be integrated from the edge of the photocathode until $\theta_Q(y,z)$ returns to θ_{cath} and the lower section of the CTC profile for case (iii) is complete.

The upper section begins at the point $\mathbf{r} = (0, y, z)$ where $\theta_Q(y,z)$ has returned to θ_{cath}. It is generated according to the edge-ray principle whereby the rays of skewness h which originate from the edge of the photocathode are reflected to have polar angle θ_i, (see Figure 3.9). The same conditions (B.2)-(B.4) as before are imposed. Only the tangent condition (B.1) is replaced by the condition of originating from the edge of the photocathode. This is tantamount to setting $\theta_Q = \theta_{\text{cath}}$ which removes one variable to make up for the lost equation.

Let us adopt a slightly modified form of the notation of [49] in which $\mathbf{r}_Q$ is denoted by (x_0, y_0, z_0), where $\sqrt{x_0^2 + y_0^2} = r_{\text{polar}}$ and $z_0 = \mathbf{r}_Q(\theta_Q = \theta_{\text{cath}}).\hat{\mathbf{z}}$ (the axial distance to

the edge of the photocathode). In this coordinate frame $\hat{\mathbf{t}}$ can be written

$$\hat{\mathbf{t}} = (\alpha, \beta, \gamma) = \frac{(-x_0, y - y_0, z - z_0)}{[x_o^2 + (y - y_o)^2 + (z - z_0)^2]^{\frac{1}{2}}}, \tag{B.16}$$

the skew invariant condition becomes

$$h = \frac{x_0 y}{[x_o^2 + (y - y_o)^2 + (z - z_0)^2]^{\frac{1}{2}}} \tag{B.17}$$

and (B.5) can be written

$$\gamma \left[1 - \left(\frac{dy}{dz}\right)^2\right] + 2\beta \frac{dy}{dz} = \cos\theta_i \left[1 - \left(\frac{dy}{dz}\right)^2\right] \tag{B.18}$$

after making the usual substitutions for $\sin\psi$ and $\cos\psi$. The relevant root of this quadratic equation in $\frac{dy}{dz}$ is

$$\frac{dy}{dz} = \frac{\beta - \sqrt{\beta^2 + \gamma^2 - \cos^2\theta_i}}{\gamma + \cos\theta_i} \tag{B.19}$$

where the negative sign has been chosen for the square root so that $\frac{dy}{dz}$ can be zero at the end of the CTC profile, as required. In this equation, the variables β and γ are functions of y and z through (B.16) and (B.17). Hence $\frac{dy}{dz}$ can be integrated until it reaches 0 and the CTC profile for case (iii) is completed.

B.2 Spherical Photocathode

The vector $\mathbf{r}_Q$ from the origin to a point Q on a *spherical* photocathode can be written $r_Q(\sin\theta_Q\cos\phi_Q, \sin\theta_Q\sin\phi_Q, \cos\theta_Q)$ where r_Q is the constant radius of curvature of the photocathode. Moreover, the normal to the photocathode at point Q is simply $\hat{\mathbf{n}}_Q = \hat{\mathbf{r}}_Q = (\sin\theta_Q\cos\phi_Q, \sin\theta_Q\sin\phi_Q, \cos\theta_Q)$. Thus the tangent condition (B.1) can be rewritten $\hat{\mathbf{r}}_Q.\hat{\mathbf{t}} = 0$ and the magnitude of $\mathbf{t}$ is $|\mathbf{t}| = \sqrt{r^2 - r_Q^2}$ where $r^2 = y^2 + z^2$.

To generate the CTC profile for a given limiting angle θ_i, skewness h and spherical photocathode of polar half angle θ_{cath} and radius of curvature r_Q, one must first establish which of the three cases discussed in the previous section is relevant. This is easily done by evaluating the angle θ_S given by the following equation

$$\cos\theta_S = \sqrt{\sin^2\theta_i - (h/r_Q)^2} \tag{B.20}$$

which is obtained by eliminating ψ_S from the two simultaneous equations for θ_S and ϕ_S discussed in Section B.1. If $\theta_S = \theta_{\text{cath}}$ then case (i) applies; if $\theta_S < \theta_{\text{cath}}$ then case (ii); if $\theta_S > \theta_{\text{cath}}$ then case (iii).

Let us consider case (i) first. Eliminating ϕ_Q from (B.1) and (B.2) one can derive the following equation for $z_Q = r_Q \cos\theta_Q$ as a function of y and z:

$$z_Q = \frac{r_Q^2 z \pm r_Q\sqrt{y^2(r^2 - r_Q^2) - r^2(h/r_Q)^2(r^2 - r_Q^2)}}{r^2} \tag{B.21}$$

where the positive sign for the square root is identified by considering the solution for $z = r_Q$ and $h = 0$. By combining (B.1) and (B.2) with (B.5) and by making the usual substitutions for $\cos\psi$ and $\sin\psi$ one can derive a quadratic equation for $\frac{dy}{dz}$ which depends on y, z and z_Q, but *not* on ϕ_Q. The relevant root of this quadratic equation is

$$\frac{dy}{dz} = \frac{\left(y - \frac{r_Q^2}{y} + \frac{z}{y}z_Q\right) - \sqrt{\left(y - \frac{r_Q^2}{y} + \frac{z}{y}z_Q\right)^2 + (z - z_Q)^2 - (r^2 - r_Q^2)\cos^2\theta_i}}{(z - z_Q) + \sqrt{r^2 + r_Q^2}\cos\theta_i} \tag{B.22}$$

where the negative sign of the square root has been chosen so that at some point where $|\mathbf{r}| > r_Q$ the slope $\frac{dy}{dz}$ can be zero, as required. By combining (B.21) and (B.22) one can calculate $\frac{dy}{dz}$ as a function of y and z and thus, by numerical integration, generate the CTC profile, except that at the starting point of the integration, $\mathbf{r} = \mathbf{r}_Q(\theta_Q = \theta_{\text{cath}}, \phi_Q = \pi/2)$, (B.22) is undefined. However, the value for $\frac{dy}{dz}$ at this point is simply $\tan\theta_{\text{cath}}$ from (B.9). Thus the profile of the CTC can be generated by integrating $\frac{dy}{dz}$ until it equals 0 at which point the profile is complete.

When $\theta_S < \theta_{\text{cath}}$, case (ii), the lower section of the CTC profile is an involute of the shadowed portion of the photocathode. The conditions (B.1)–(B.3) and (B.10) apply in this case, so that z_Q is still given by (B.21) but the differential equation is now derived from (B.11). By combining (B.1), (B.2) and (B.11) one can eliminate ϕ_Q and obtain, after making the usual substitutions for $\cos\psi$ and $\sin\psi$, a quadratic equation for $\frac{dy}{dz}$ in which the second degree term vanishes and one is left with

$$\frac{dy}{dz} = \frac{y(z_Q - z)}{y^2 - r_Q^2 + zz_Q}. \tag{B.23}$$

As z_Q is a known function of y and z through (B.21), one can calculate $\frac{dy}{dz}$ as a function of y and z from this equation, except at the start point of the integration where (B.9) applies and $\frac{dy}{dz}$ is $\tan\theta_{\text{cath}}$. Hence the involute section of the profile can be generated by numerically integrating $\frac{dy}{dz}$ until the parameter $\theta_Q(y,z)$ reaches θ_S. At this point we switch over to using (B.21) and (B.22) to calculate $\frac{dy}{dz}$ and proceed with the integration until $\frac{dy}{dz} = 0$ and $\theta_Q(y,z)$ returns, from its minimum, to θ_S.

Let us now consider case (iii) where the lower section of the profile is generated by integrating (B.21) from $\mathbf{r} = \mathbf{r}_Q(\theta_Q = \theta_{\text{cath}}, \phi_Q = \pi/2)$ until $\theta_Q(y,z)$ returns, from its minimum, to θ_{cath} and the upper section is generated by integrating (B.19) from this point on until $\frac{dy}{dz} = 0$. However, as shown before, (B.21) is undefined at the start point of the integration. To find $\frac{dy}{dz}$ at the start point, consider the ray $\hat{\mathbf{t}} = (\cos\phi_i \sin\theta_i, \sin\phi_i \sin\theta_i, -\cos\phi_i)$ of Section B.1 (see Figure B.4) which is subjected to the conditions (B.14) and (B.15). The angle ϕ_i is easily derived from (B.14) and from (B.15) one obtains a quadratic in $\frac{dy}{dz}$ of which the relevant root is

$$\frac{dy}{dz} = \frac{\cos\theta_i \sin\theta_{\text{cath}} - \sin\phi_i \sin\theta_i \cos\theta_{\text{cath}} + \sqrt{\sin^2\phi_i \sin^2\theta_i + \cos^2\theta_i}}{\sin\phi_i \sin\theta_i \sin\theta_{\text{cath}} + \cos\theta_i \cos\theta_{\text{cath}}}. \qquad \text{(B.24)}$$

Thus $\frac{dy}{dz}$ is specified at the start point of the integration and the profile can be generated for case (iii).

Bibliography

[1] R. Davis *et al.*, in *Second International Workshop on Neutrino Telescopes*, Venice, 13–15 February 1990, edited by M. Baldo Ceolin, University of Padavo.

[2] K.S. Hirata *et al.*, Phys. Rev. Lett. **65**, 1297 (1990).

[3] A.I. Abazov *et al.*, Phys. Rev. Lett. **67**, 3332 (1991).

[4] A. Cisneros, Astrophys. Space Sci. **10**, 87 (1971).

[5] C.S. Lim and W.J. Marciano, Phys. Rev. D **37**, 1368 (1988).

[6] J.N. Bahcall and R. Ulrich, Rev. Mod. Phys. **60**, 297 (1988).

[7] S. Turck-Chieze, S. Cahen, M. Casse and C. Doom, Astrophys. J. **335**, 415 (1988).

[8] D.A. VandenBerg, Ap. J. Suppl. **51**, 29 (1983).

[9] Y. Lebreton and A. Maeder, Astr. Ap. **161**, 119 (1986).

[10] S. Cahen, C. Doom, in *'86 Massive Neutrinos in Astrophysics and Particle Physics*, ed. O. Fackler and J. Tran Thanh Van, (Gif sur Yvette, France: Editions Frontieres), p. 83 (1986).

[11] I.J. Sackman *et al.*, Ap. J. **360**, 727 (1990).

[12] A.N. Cox *et al.*, Ap. J. **353**, 698 (1990).

[13] J.N. Bahcall, *Neutrino Astrophysics*, Cambridge Univ. Press, Cambridge (1989).

[14] Y. Elsworth *et al.*, Nature **347**, 536 (1990).

[15] B. Pontecorvo, Sov. JETP **26**, 984 (1968).

[16] V. Gribov and B. Pontecorvo, Phys. Lett. B **28**, 493 (1969).

[17] S.P. Mikheyev and A.Yu. Smirnov, Sov. J. Nucl. Phys. **42**, 913 (1986).

[18] S.P. Mikheyev and A.Yu. Smirnov, Nuovo Cimento C **9**, 17 (1986).

[19] L. Wolfenstein, Phys. Rev. D **17**, 2369 (1978).

[20] L. Wolfenstein, Phys. Rev. D **20**, 2634 (1979).

[21] D.H. Perkins, *Introduction to High Energy Physics*, Addison-Wesley Publishing Company, Wokingham, U.K., (1987).

[22] R.G. Winter, Nuovo Cimento Lett. **30**, 101 (1981).

[23] H.A. Bethe, Phys. Rev. Lett. **56**, 1305 (1986).

[24] S.J. Parke, Phys. Rev. Lett. **57**, 1275 (1986).

[25] R. Davis Jr., J.C. Evans, V. Radeka and L.C. Rogers, in *Neutrino 72: Proceedings of Europhysics Conference*, edited by A. Frenkel and G. Marx, (Budapest: OMKDK Technoinform), (1972).

[26] J.K. Rowley, B.T. Cleveland and R. Davis Jr., in *Solar Neutrinos and Neutrino Astronomy*, edited by M.L. Cherry, W.A. Fowler and K. Lande (New York: American Institute of Physics) Conference Proceedings No. 126, p. 1 (1985).

[27] T. Kirsten *et al.*, in *Neutrino 90: Proceedings of the 14th International Conference on Neutrino Physics and Astrophysics*, (Geneva: Cern), 10-15 June 1990; Nuclear Physics B (Proc. Suppl.) 19 (1991).

[28] K.S. Hirata *et al.*, Phys. Rev. D **38**, 448 (1988).

[29] K.S. Hirata *et al.*, Phys. Rev. Lett. **63**, 16 (1989).

[30] G. 't Hooft, Phys. Lett. B **37**, 195 (1971).

[31] G.T. Ewan *et al.*, *Sudbury Neutrino Observatory Proposal*, SNO-87-12, October 1987.

[32] S.D. Ellis and J.N. Bahcall, Nucl. Phys. A **114**, 636 (1968).

[33] J.N. Bahcall, K. Kubodera and S. Nozawa, Phys. Rev. D **38**, 1030 (1988).

[34] Page II.2 of *Review of Particle Properties*, Edited by G.F. Bertsch *et al.*, Phys. Lett. B **239**, 1 (1990).

[35] I. Frank and I. Tamm, C. R. Acad. Sci. USSR **14**, 109 (1937).

[36] R.J. Boardman, private communication (Thesis to be submitted 1992).

[37] L.P. Boivin *et al.*, Appl. Opt. **25**, 877 (1986).

[38] W.F. Davidson, C.X. Dodds and J. Zwinkels, Annexe 2 to the Sudbury Neutrino Observatory Proposal, SNO-87-12.

[39] E. Bonvin, SNO Scientific and Technical Report, SNO-STR-91-046.

[40] R.C. Allen, G. Buhler and H.H. Chen, Annexe 7 to the Sudbury Neutrino Observatory Proposal, SNO-87-12.

[41] P. Skensved and B.C. Robertson, SNO Scientific and Technical Report, SNO-STR-91-06.

[42] E.W. Beier and W. Frati, SNO Scientific and Technical Report, SNO-STR-88-87.

[43] W.R. Nelson *et al.*, SLAC-Report-265, Stanford Linear Accelerator Center, December 1985.

[44] M. Bercovitch *et al.*, Annexe 15 to the Sudbury Neutrino Observatory Proposal, SNO-87-12.

[45] E.D. Earle and P.Y. Wong, Annexe 1 to the Sudbury Neutrino Observatory Proposal, SNO-87-12.

[46] J.R. Leslie, SNO Scientific and Technical Report, SNO-STR-91-017.

[47] R.J. Boardman, M.D. Lay, N.W. Tanner and D.L. Wark, SNO Scientific and Technical Report, SNO-STR-91-033.

[48] E.D. Earle *et al.*, Annexe 12 to the Sudbury Neutrino Observatory Proposal, SNO-87-12.

[49] W.T. Welford and R. Winston, *High Collection Non-imaging Optics*, Academic Press, 1989.

[50] R.K. Luneburg, *Mathematical Theory of Optics*, Univ. of California Press, Berkeley, 1964.

[51] H. Timan, Revue Technique Thompson, **8**, (1976).

[52] C. Ghosh and B.P. Varma, *Optical Properties of Bialkali Photocathodes*, Conference Proceedings.

[53] M. Born and E. Wolf, *Principles of Optics*, Pergamon Press, 1964, p. 627-630.[1]

[54] M. Born and E. Wolf, *ibid*, p. 613.

[55] W. Greschat, H. Heinrich and P. Romer, Adv. in Electronics and Electron Phys., **40A**, 397 (1976).

[56] T.H. Chyba and L. Mandel, Journ. Opt. Soc. Am. B **5**, 1305 (1988).

[57] O. Heavens, *Optical Properties of Thin Solid Films*, London, 1955, p. 76-79.

[58] G. Wallis, Ann. Physik, **17**, 401 (1956).

[59] A.H. Sommer,*Photoemissive Materials*, Robert E. Kreiger Publishing Company, New York, 1980, p. 88.

[60] T.J. Radcliffe and J.R. Leslie, *Efficiency of Photomultiplier Tubes as a Function of Angle of Incidence*, private communication.

[61] R.J. Boardman, SNO Scientific and Technical Report, SNO-STR-91-063.

[62] E. Shiles, T. Sasaki, M. Inokuti and D.Y. Smith, Phys. Rev. B, **22**, 1612 (1980).

[63] C. Waltham, S. Gil, L. McGarry and A. Poon, SNO Scientific and Technical Report, SNO-STR-91-081.

[64] P. Thornewell and N. Jelley, SNO Scientific and Technical Report, SNO-STR-91-075.

[65] J. Barton, SNO Scientific and Technical Report, SNO-STR-90-9.

[66] P. Trent, SNO Scientific and Technical Report, SNO-STR-90-60.

[67] P. Trent, SNO Scientific and Technical Report, SNO-STR-90-127.

[68] P. Trent, SNO Scientific and Technical Report, SNO-STR-91-038.

[69] X. Zhu, B. Sur, H. Lee and A.B. McDonald, SNO scientific and Technical Report, SNO-STR-91-065.

[70] L. Holland, *Vacuum Deposition of Thin Films*, Chapman and Hall Ltd., London, 1970.

[71] J.W. Swaine Jr. and R.C. Plumb, Jour. Appl. Phys. **33**, 2378 (1962).

[72] A. Rabl, Appl. Opt. **15**, 1871 (1976).

[1] In this (3rd) edition there is a missprint in the equation for photocathode transmissivity which is corrected in later editions.